

NITROGEN LINE SPECTROSCOPY IN O-STARS



Jorge G. Rivero González

NITROGEN LINE SPECTROSCOPY IN O-STARS

Dissertation

an der
Ludwig–Maximilians–Universität (LMU) München

Ph.D. Thesis

at the
Ludwig–Maximilians–University (LMU) Munich

submitted by

Jorge G. Rivero González

born on 21st July 1984 in Las Palmas de Gran Canaria, Spain

Munich, July 26th 2012

1st Evaluator: Priv. Doz. Dr. Joachim Puls

2nd Evaluator: Prof. Dr. Barbara Ercolano

July 26th 2012

Contents

Contents	vii
List of Figures	xiv
List of Tables	xvi
Zusammenfassung	xvii
Abstract	xix
1 Introduction	1
1.1 Massive star evolution	1
1.1.1 Overview	2
1.1.2 Evolution with mass loss and rotation	6
1.2 Motivation of this thesis	12
1.3 Overview of the chapters of this thesis	14
2 Atmospheric codes	16
2.1 Overview	16
2.2 Basic assumptions for modeling stellar atmospheres of hot stars	16
2.2.1 Non-local thermodynamic equilibrium	17
2.2.2 Stellar winds	19
2.2.3 Line-blocking/blanketing	20
2.3 A description of the atmospheric code FASTWIND	21
2.3.1 FASTWIND v10.1	22
2.3.2 Application of FASTWIND	23
3 Model atoms for NLTE line formation computations in stellar atmospheres – A nitrogen model atom	24
3.1 Construction of a comprehensive model atom	24
3.1.1 Model atom structure	24
3.1.2 Input atomic data	25
3.2 The nitrogen model atom – Implementation into FASTWIND	29
3.2.1 N II model ion	29
3.2.2 N III model ion	30
3.2.3 N IV model ion	34

3.2.4	N v model ion	35
3.3	Diagnostic nitrogen lines in the optical	37
4	Nitrogen III emission line formation revisited	41
4.1	Introduction	42
4.2	N III emission lines from O-stars - status quo	44
4.3	Dielectronic recombination	46
4.3.1	The N III emission triplet at $\lambda\lambda 4634\text{-}4640\text{-}4642$	46
4.3.2	Implementation into FASTWIND	46
4.3.3	Implicit vs. explicit method	51
4.4	N III (emission) line formation	53
4.4.1	Comparison with the results from MH	53
4.4.2	Models with full line-blanketing	56
4.4.3	The impact of wind effects	60
4.5	Comparison with results from CMFGEN	62
4.6	Coupling with O III	64
4.7	Influence of various parameters	69
4.8	Summary and conclusions	72
5	Surface nitrogen abundances for O-stars in the Large Magellanic Cloud	75
5.1	Introduction	76
5.2	Understanding the N IV $\lambda 4058/\lambda 6380$ line formation	77
5.3	Stellar sample and observations	83
5.3.1	The stellar sample	83
5.3.2	Observations	85
5.4	Analysis	85
5.4.1	Methodology	85
5.4.2	Model calculations and grids	86
5.4.3	Determination of stellar and wind parameters	88
5.4.4	Nitrogen abundances and micro-turbulences	91
5.4.5	Additional considerations	93
5.5	Comments on the individual objects	94
5.5.1	Late O- and B-supergiants/giants	95
5.5.2	O-stars	96
5.6	Discussion	103
5.6.1	Comparison with results from Mok07	103
5.6.2	Overlap with B-star nitrogen analyses	104
5.6.3	Nitrogen abundances	105
5.7	Summary	107
6	The earliest O-stars	109
6.1	Introduction	110
6.2	Code and model grid	111
6.3	N III/N IV emission lines – parameter-dependence	112
6.3.1	N III emission line formation: EUV line-blocking vs. wind-strength	112

6.3.2	$N_{IV}\lambda 4058$ – dependence on background abundance	115
6.3.3	$N_{IV}\lambda 4058$ – dependence on nitrogen abundance	117
6.4	Predictions on the N_{IV}/N_{III} emission line ratio	118
6.4.1	Overview	118
6.4.2	Basic considerations	120
6.5	Comparison with results from CMFGEN	124
6.6	Analysis of a sample of LMC/SMC early-type O-stars	130
6.6.1	The stellar sample	130
6.6.2	Observational data	130
6.6.3	Analysis	132
6.6.4	Comments on the individual objects	134
6.6.5	Comparison with results from Massey et al.	137
6.7	Discussion	138
6.7.1	Nitrogen abundances	138
6.7.2	Effective temperatures vs. spectral types	138
6.7.3	N_{IV}/N_{III} emission line ratio	142
6.7.4	N_{V}/N_{IV} line ratio	144
6.7.5	Caveats for low-metallicity stars	146
6.7.6	SMC Of-stars	147
6.8	Summary and conclusions	148
7	Summary and outlook	152
7.1	Summary	152
7.2	Outlook	156
A	Testing the N_{II} model ion	159
B	Comparison of line profiles with results from CMFGEN	165
B.1	Comparison of N_{II}/N_{III} line profiles	165
B.2	Comparison of H/He/N line profiles for models with different nitrogen abundances	172
C	Line fits for individual objects	179
C.1	Line fits for the LMC sample	179
C.2	Line fits for the LMC/SMC early O-star sample	190
	Bibliography	203
	Acknowledgements	221
	Curriculum Vitae	223

List of Figures

1.1	Schematic picture of the CNO cycle	9
3.1	Grotrian diagrams for the N II model ion	31
3.2	Grotrian diagrams for the N III model ion	33
3.3	Grotrian diagrams for the N IV model ion	35
3.4	Grotrian diagram for the N V model ion	36
4.1	Grotrian diagram displaying the important transitions involved in the formation of emission at N III λ 4634-4640-4642.	45
4.2	Comparison between photoionization cross-sections from the OPACITY project and the Seaton (1958) approximation	47
4.3	Illustration of the consistency between different methods used to implement the dielectronic recombination process into FASTWIND	52
4.4	Reproduction of the former predictions on N III λ 4097 and λ λ 4640/42 by Mihalas & Hummer (1973)	54
4.5	Comparison of FASTWIND N III line profiles from model ‘T3740’ with ‘pseudo line-blanketing’, using different atomic data sets	55
4.6	Illustration of the effects from new atomic data and realistic line-blanketing on the N III λ 4097 and λ λ 4640/42 line profiles	56
4.7	Illustration of the effects from a realistic treatment of line-blocking/blanketing on the EUV radiation temperatures and the departure coefficients for important levels regarding the triplet emission for model ‘T3735’	57
4.8	Fractional net rates to and from level 3p and level 3d, for model ‘T3735’ with pseudo and full line-blanketing	58
4.9	Illustration of the consistency between FASTWIND predictions for N III λ 4097 and λ λ 4640/42, using realistic line-blanketing with results from TLUSTY	59
4.10	Illustration of the impact of realistic line-blanketing/blocking and mass-loss on the N III λ 4097 and λ λ 4640/42 line profiles	61
4.11	Fractional net rates to and from level 3p and level 3d for model ‘T3735’ (full line-blanketing) with and without mass-loss.	62
4.12	N III λ λ 4634-4640-4642 for three versions of model \S 6a, as calculated by CMFGEN to evaluate the impact of the overlapping of N III and O III resonance lines	66
4.13	NLTE departure coefficients for three versions of model \S 6a, as calculated by CMFGEN to evaluate the impact of the overlapping of N III and O III resonance lines	66

4.14	Line source functions for the N III/O III resonance lines at 374 Å, for two versions of model s6a, as calculated by CMFGEN	67
4.15	Illustration of the effect from different abundances and nitrogen abundances on the λ4097 and λλ4640/42 line profiles	70
4.16	Illustration of the effect from different background abundances on the λ4097 and λλ4640/42 line profiles	71
5.1	Simplified Grotrian diagram displaying the most important transitions involved in the N IV emission line problem	78
5.2	Equivalent width of N IVλ4058 and N IVλ6380 as a function of T_{eff} . Impact of wind-strength and surface gravity	79
5.3	Departure coefficients, fractional net rates, and line profiles for N IVλ4058/λ6380 and involved processes, for model ‘A4540’	80
5.4	Departure coefficients and line profiles for N IVλ4058/λ6380, for the dense-wind model ‘E4540’	82
5.5	Observed and synthetic line profiles for N11-072	97
5.6	Observed and synthetic line profiles for N11-032	99
5.7	Observed and synthetic line profiles for BI237	101
5.8	Nitrogen abundances derived for our LMC sample, analyzed as a function of O-star spectral type and helium content	105
5.9	Nitrogen abundance vs. projected rotational speed for our LMC sample (‘Hunter-plot’). Population synthesis from Brott et al. (2011b), shown as a density plot in the background	106
6.1	Observed and synthetic strategic line profiles for HD 64568	113
6.2	Equivalent width of N IIIλ4640 as a function of T_{eff} , for MW and SMC models at $\log g = 4.0$ and mass-loss rates scaled according to Z , for solar nitrogen content and for the theoretically expected maximum nitrogen enrichment	114
6.3	Equivalent width of N IIIλ4640 and N IVλ4058 as a function of T_{eff} , for MW and SMC models, for fixed $\log g$ and nitrogen content but different wind-strengths	116
6.4	Equivalent width of N IVλ4058 as a function of T_{eff} for models with fixed $\log g$ and background abundance but different nitrogen content and wind-strength	117
6.5	Illustration of the effect from a different nitrogen abundance on the radiation temperature and departure coefficients for important levels regarding the N IVλ4058 emission, for model ‘A4540’.	118
6.6	Iso-contours of the N IV/N III emission line ratio in the T_{eff} - $\log g$ plane for Galactic, LMC, and SMC models.	121
6.7	Dependence of N IV/N III on wind-strength, for LMC models with solar nitrogen content	122
6.8	Dependence of N IV/N III on nitrogen abundance, for a fixed wind-strength and three different background metallicities: Galactic, LMC, and SMC	123
6.9	Illustration of the behavior of N IVλ4058 as a function of abundance for weak-wind models, as predicted by FASTWIND and CMFGEN.	126
6.10	Comparison between FASTWIND and CMFGEN predictions for the equivalent width ratio N IV/N III	126
6.11	Nitrogen abundance ‘analysis’ of CMFGEN model d4v by means of FASTWIND	129

6.12	Effective temperatures as a function of spectral type, for LMC and SMC O-stars analyzed within this work	139
6.13	Effective temperatures as a function of observed and theoretical N IV/N III emission line ratio, for our sample of early O-stars	143
6.14	Effective temperatures as a function of observed and theoretical N V/N IV line ratio, for our sample of early O-stars	146
A.1	Comparison of electron temperature and electron density for FASTWIND and TLUSTY models	161
A.2	Comparison of important optical N II line profiles for a model with $T_{\text{eff}} = 20$ kK and $\log g = 3.0$ as calculated by different atmospheric codes and using different atomic data sets	162
A.3	As Fig. A.2, but for $T_{\text{eff}} = 20$ kK and $\log g = 2.5$	162
A.4	As Fig. A.2, but for $T_{\text{eff}} = 24$ kK and $\log g = 3.0$	163
A.5	As Fig. A.3, but for $T_{\text{eff}} = 24$ kK and $\log g = 2.75$	163
A.6	As Fig. A.3, but for $T_{\text{eff}} = 27.5$ kK and $\log g = 3.5$	164
A.7	As Fig. A.3, but for $T_{\text{eff}} = 27.5$ kK and $\log g = 3.0$	164
B.1	Comparison of N II line profiles from FASTWIND and CMFGEN, for model d10v	165
B.2	As Fig. B.1, but for model d8v.	166
B.3	As Fig. B.1, but for model s10a.	166
B.4	As Fig. B.1, but for model s8a.	167
B.5	Comparison of N III line profiles from FASTWIND and CMFGEN, for model d10v	167
B.6	As Fig. B.5, but for model d8v.	168
B.7	As Fig. B.5, but for model d6v.	168
B.8	As Fig. B.5, but for model d4v.	169
B.9	As Fig. B.5, but for model d2v.	169
B.10	As Fig. B.5, but for model s10a.	170
B.11	As Fig. B.5, but for model s8a.	170
B.12	As Fig. B.5, but for model s6a.	171
B.13	As Fig. B.5, but for model s4a.	171
B.14	As Fig. B.5, but for model s2a.	172
B.15	Comparison of H/He/N spectra from CMFGEN and FASTWIND for model d4v, for a high nitrogen content and different T_{eff}	173
B.16	Comparison of N spectra from CMFGEN and FASTWIND for model d4v, for a solar nitrogen content	174
B.17	Comparison of N spectra from CMFGEN and FASTWIND for model d2v, for a solar nitrogen content and different T_{eff}	174
B.18	Comparison of H/He/N spectra from CMFGEN and FASTWIND for model d2v, for a high nitrogen content and different T_{eff}	175
B.19	Comparison of H/He/N spectra from CMFGEN and FASTWIND for model s4a, for a high nitrogen content	176
B.20	Comparison of N spectra from CMFGEN and FASTWIND for model s4a, for a solar nitrogen content	177

B.21	Comparison of N spectra from CMFGEN and FASTWIND for model s2a, for a solar nitrogen content	177
B.22	Comparison of H/He/N spectra from CMFGEN and FASTWIND for model d4v, for a high nitrogen content	178
C.1	Observed and synthetic N line profiles for N11-029	179
C.2	Observed and synthetic N line profiles for N11-036	180
C.3	Observed and synthetic N line profiles for N11-008	180
C.4	Observed and synthetic N line profiles for N11-042	181
C.5	Observed and synthetic N line profiles for N11-033	181
C.6	Observed and synthetic N line profiles for N11-026	182
C.7	Observed and synthetic N line profiles for N11-031	182
C.8	Observed and synthetic N line profiles for N11-038	183
C.9	Observed and synthetic N line profiles for Sk-66° 100	183
C.10	Observed and synthetic N line profiles for N11-045	184
C.11	Observed and synthetic N line profiles for BI253	184
C.12	Observed and synthetic N line profiles for N11-060	185
C.13	Observed and synthetic N line profiles for Sk-70° 69	185
C.14	Observed and synthetic N line profiles for N11-051	186
C.15	Observed and synthetic N line profiles for N11-058	186
C.16	Observed and synthetic N line profiles for Sk-66° 18	187
C.17	Observed and synthetic N line profiles for N11-065	187
C.18	Observed and synthetic N line profiles for N11-066	188
C.19	Observed and synthetic N line profiles for N11-068	188
C.20	Observed and synthetic N line profiles for N11-061	189
C.21	Observed and synthetic N line profiles for N11-123	189
C.22	Observed and synthetic N line profiles for N11-087	190
C.23	Observed and synthetic H/He/N line profiles for R136-040	191
C.24	Observed and synthetic H/He/N line profiles for LH 81:W28-23	192
C.25	Observed and synthetic H/He/N line profiles for LH 101:W3-24	193
C.26	Observed and synthetic H/He/N line profiles for LH 81:W28-5	194
C.27	Observed and synthetic H/He/N line profiles for R136-018	195
C.28	Observed and synthetic H/He/N line profiles for LH 90:ST 2-22	196
C.29	Observed and synthetic H/He/N line profiles for Sk-67° 22	197
C.30	Observed and synthetic H/He/N line profiles for LH 101:W3-19	198
C.31	Observed and synthetic H/He/N line profiles for Sk-65° 47	199
C.32	Observed and synthetic H/He/N line profiles for AV 435	200
C.33	Observed and synthetic H/He/N line profiles for AV 177	201
C.34	Observed and synthetic H/He/N line profiles for NGC 346-355	202

List of Tables

1.1	Nuclear reactions involved in the CNO-cycle	11
3.1	Electronic configurations and term designations of our N II model ion	30
3.2	Electronic configurations and term designations of our N III model ion	32
3.3	Electronic configurations and term designations of our N IV model ion	34
3.4	Electronic configurations and term designations of our N V model ion	36
3.5	Diagnostic nitrogen lines in the optical spectra of early B- and O-type stars, together with potential blends	38
4.1	Model grid as used by Mihalas & Hummer (1973) and in our test series for studying the N III emission line problem	53
4.2	Oscillator strengths for the ‘two electron transition’ as used by Mihalas & Hummer (1973) and within our newly developed nitrogen model atom	53
4.3	Stellar and wind parameters of our model grid used to compare synthetic N II/N III profiles from FASTWIND and CMFGEN	63
4.4	Summary of the important transitions, atomic data, and different calculations performed to address the impact of the N III and O III resonance lines in the formation of emission at N III $\lambda\lambda$ 4634-4640-4642	65
5.1	Basic information about our LMC O-star sample	84
5.2	Fundamental parameters for the LMC sample	87
5.3	Differences between the fundamental parameters derived within this work and previous studies	90
5.4	Helium and nitrogen abundances for the LMC sample	92
5.5	Comparison between nitrogen abundances derived within this work and previous studies	104
6.1	Coverage of fundamental parameters of the model grid used within this work	112
6.2	The Walborn et al. (2002) classification scheme for spectral types O2-O4	119
6.3	Stellar and wind parameters of models used to compare synthetic H/He/N line profiles from FASTWIND and CMFGEN	125
6.4	Basic information about sample stars analyzed within this study	131
6.5	Fundamental parameters derived for our early O-star sample	133
6.6	Observed and predicted line-strength ratios for N IV/N III and N V/N IV, for the O2-O4 stars analyzed within this work	145
A.1	Basic information about different tests performed for the N II model ion	160

Zusammenfassung

Ziel vorliegender Arbeit ist es, die quantitative Spektroskopie optischer Stickstofflinien von O-Sternen zu ermöglichen, um damit das Verständnis massereicher Sterne, insbesondere ihrer heißesten Vertreter, zu verbessern. In diesem Zusammenhang hat sich Stickstoff als Schlüsselement herausgestellt, sowohl bezüglich seines Potentials als Temperaturindikator, als auch als derzeit bestes Testwerkzeug, die vorhergesagten Effekte rotationsinduzierter Mischung in massereicher Sterne zu überprüfen und weitergehende Einschränkungen an deren Entwicklung zu ermöglichen.

Für diese Studie wurde der NLTE (nicht lokales thermodynamisches Gleichgewicht) Atmosphären- und Spektrumsynthesecode FASTWIND (Santolaya-Rey et al. 1997; Puls et al. 2005) verwendet, und ein neues, teilweise auf älteren Arbeiten basierendes Stickstoffmodellatom entwickelt, das die Ionisationsstufen N II bis N V umfasst. Darüber hinaus wurde der dielektronischen Rekombinationsmechanismus in FASTWIND implementiert, da dieser Code bislang derartige Prozesse nicht berücksichtigen konnte.

Im ersten Teil vorliegender Arbeit wurde der Linienentstehungsprozess strategischer Stickstoffemissionslinien (N III λ 4634-4640-4642 und N IV λ 4058) unter Berücksichtigung von 'line-blocking/blanketing' und der Präsenz stellarer Winde detailliert untersucht. Im Gegensatz zu den Resultaten der wegweisenden Untersuchung der N III-Triplett-Entstehung durch Mihalas & Hummer (1973), die auf viel einfacheren Atmosphärenmodellen basierte, erwies sich in unserer Studie der Einfluss der dielektronischen Rekombination nur von untergeordneter Bedeutung. Tatsächlich wird die Linienemission durch den stellaren Wind kontrolliert (sog. Swings-Mechanismus), und zwar solange der Wind stark genug ist, ein signifikant anwachsendes Geschwindigkeitsfeld schon in der photosphärischen Entstehungsregion zu erzeugen. Bei späteren O-Spektraltypen kann die Emission auch durch eine O III Resonanzlinie, die im EUV mit der N III Resonanzlinie überlappt, affektiert werden. Die Emission von N IV λ 4058 kann in ähnlicher Weise beschrieben werden. Auch hier ist der dominierende Prozess eine starke Depopulation des unteren Zustands des Linienüberganges, die als Funktion der Windstärke anwächst. Resonanzlinien spielen allerdings kaum eine Rolle.

Unter Verwendung der aktualisierten FASTWIND-Version wurden Stickstoffhäufigkeiten für eine Stichprobe erheblichen Umfangs von LMC (Große Magellansche Wolke) O-Sternen bestimmt. Stellare und Windparameter der Stichprobenobjekte wurden durch Linienfits von Wasserstoff, Helium und Stickstoff gewonnen. Der Großteil der Stichprobe zeigte sich als stark stickstoffangereichert, und wir fanden eine klare Korrelation von Stickstoff- und Heliumhäufigkeit. Durch einen Vergleich der Stickstoffhäufigkeiten als Funktion der projizierten Rotationsgeschwindigkeiten mit maßgeschneiderten Entwicklungsrechnungen konnten wir eine Vielzahl von hochangereicherten, aber langsam rotierenden Objekten identifizieren, die zufolge der Standardtheorie der Rotationsmischung nicht existieren sollten. Unser Befund steht in Übereinstimmung mit einem der grundlegenden Resultate des 'VLT-FLAMES survey on massive stars' (Evans et al. 2006), das auf ähnliche Diskrepanzen bei B-Sternen

hinweist. Die Entdeckung starker Stickstoffanreicherung für den Großteil unserer Stichprobe deutet darauf hin, dass eine effiziente Mischung schon während sehr früher Entwicklungsphasen von LMC O-Sternen auftreten muss.

Im letzten Teil dieser Arbeit untersuchten wir die Anwendbarkeit des Klassifikationsschemas von Walborn et al. (2002) für sehr frühe O-Sterne, das hauptsächlich auf dem Verhältnis der Linienstärken der $N\text{ IV}\lambda 4058$ und $N\text{ III}\lambda 4640$ Emissionslinien beruht. Dieses Schema wurde schon innerhalb einer Vielzahl von Studien benutzt, galt aber bislang als kontrovers. Mit unserer Arbeit konnten wir erste theoretische Voraussagen für dieses Linienverhältnis – in Abhängigkeit diverser Parameter – treffen, und stellten diese Vorhersagen den Resultaten einer Analyse von frühen LMC/SMC O-Sternen gegenüber. Obwohl wir eine monotone Beziehung zwischen dem $N\text{ IV}/N\text{ III}$ Emissionslinienverhältnis und der Effektivtemperatur fanden (sofern alle anderen Parameter unverändert bleiben), deuten unsere Untersuchungen auf zusätzliche Abhängigkeiten hin, insbesondere von der *Stickstoffhäufigkeit*. Die Beziehung zwischen dem *beobachteten* Linienverhältnis und der Effektivtemperatur - für eine gegebene Leuchtkraftklasse – zeigte sich tatsächlich als recht monoton innerhalb unserer Stichprobe, und konsistent mit unseren Vorhersagen. Die Streuung innerhalb einer spektralen Unterklasse wird dabei hauptsächlich durch Häufigkeitseffekte verursacht. Zusammenfassend lässt sich sagen, dass das Walborn et al. Klassifikationsschema eine aussagefähige Beziehung zwischen Spektraltyp und Effektivtemperatur ermöglicht, sofern man die Leuchtkraftklasse unabhängig ableiten kann.

Abstract

This work aims at enabling quantitative optical nitrogen line spectroscopy in O-stars, in order to improve our knowledge about these objects, particularly their earliest spectral subtypes. To this end, nitrogen has proven to be a key element, both in terms of its potential to infer effective temperatures, and for being the best tracer for testing the effects of rotational mixing in massive stellar models, allowing us to further constrain the evolution of massive stars.

To accomplish this study, we used the NLTE (non local thermodynamic equilibrium) atmosphere/spectrum synthesis code FASTWIND (Santolaya-Rey et al. 1997; Puls et al. 2005), and developed a new nitrogen model atom, partly based on older work, comprising the ionization stages N II to N V. Moreover, we incorporated the dielectronic recombination mechanism into FASTWIND, which was previously unable to deal with this process.

We performed an extensive investigation on the line-formation process of strategic nitrogen emission lines such as N III $\lambda\lambda$ 4634-4640-4642 and N IV λ 4058, accounting for a complete treatment of line blocking/blanketing effects and the presence of a wind, as it is possible when using a state-of-the-art atmospheric code. Contrasted to the results from the seminal work on the N III triplet formation performed by Mihalas & Hummer (1973), based on much simpler model atmospheres, our study implies that dielectronic recombination plays only a secondary role under Galactic conditions. Rather, the emission is controlled by the stellar wind (Swings mechanism), as long as the wind is powerful enough to enable a significantly accelerating velocity field already in the photospheric formation region. For later spectral O-subtypes, the strength of the emission might be also affected by an O III resonance line overlapping with the N III resonance line in the EUV. Concerning the emission at N IV λ 4058, we suggest a rather similar mechanism. Also in this case, the dominating process is the strong depopulation of the lower level of the transition, which increases as a function of the wind-strength. Unlike the N III triplet emission, however, resonance lines do not play a role for typical mass-loss rates and below.

Using the updated version of FASTWIND and our new model atom, we derived nitrogen abundances for a substantial O-star sample in the Large Magellanic Cloud (LMC). Stellar and wind parameters of our sample stars were determined by line profile fitting of hydrogen, helium and nitrogen lines, exploiting the corresponding ionization equilibria. The bulk of our sample stars turned out to be strongly nitrogen-enriched, and a clear correlation of nitrogen and helium enrichment was found. By comparing the nitrogen abundances as a function of projected rotation velocity with tailored evolutionary calculations, we identified a considerable number of *highly* enriched, but slowly rotating object, which should not exist according to standard theory of rotational mixing. Our findings support the basic outcome of previous B-star studies within the VLT-FLAMES survey on massive stars (Evans et al. 2006) which pointed to similar discrepancies. The detection of strong nitrogen enrichment in the bulk of our sample stars indicates that efficient mixing takes place already during the very early

phases of stellar evolution of LMC O-stars.

In the last part of this thesis, we concentrated on the applicability of the Walborn et al. (2002) classification scheme for very early O-stars, which is primarily based on the relative strengths of the N IV λ 4058 and N III λ 4640 emission lines. This scheme has already been used in a variety of studies, but is still disputed for various reasons. We provided first theoretical predictions on the N IV λ 4058/N III λ 4640 emission line ratio in dependence of different parameters, and confronted these predictions with results from an analysis of a sample of early-type LMC/SMC O-stars. Though we found a monotonic relationship between the N IV/N III emission line ratio and the effective temperature, all other parameters being equal, our predictions indicate additional dependencies on other important stellar parameters, most significantly, *the nitrogen abundance*. The relation between the *observed* N IV/N III emission line ratio and the effective temperature, for a given luminosity class, turned out to be quite monotonic for our sample stars, and to be fairly consistent with our model predictions. The scatter within a spectral subtype is mainly produced by abundance effects. Our findings suggest that the Walborn et al. classification scheme is able to provide a meaningful relation between spectral type and effective temperature, as long as it is possible to discriminate for the luminosity class.

Chapter 1

Introduction

Massive stars are vital in many major fields of present-day astrophysical research. They are the brightest stars, visible even at extreme distances in the local Universe (Kudritzki et al. 2008), and also perceptible at high red-shift, in the integrated light of star-forming galaxies. They comprise objects over a wide range of masses, from roughly ten solar masses (M_{\odot}) up to a few hundreds of M_{\odot} (e.g., R136a1, the most massive star ever observed, with approximately $265 M_{\odot}$, see Crowther et al. 2010).

Even though the number of massive stars in the Universe is quite low compared to low-mass objects, and their typical lifetimes are much shorter, only a few million years, they have been proven to be of crucial impact. Due to their input of (ionizing) radiation, wind-energy and momentum, and nuclear processed matter on their environments, massive stars are the main drivers for the dynamical and chemical evolution of their surroundings and the interstellar medium (ISM), therefore being fundamental for the evolution of galaxies in the present cosmos. In addition, there is evidence that massive stars are able to trigger star-formation in molecular clouds, either by means of their extreme ionizing radiation, e.g., Gritschneider et al. (2009); Marquez-Lugo & Phillips (2010), or via their extremely violent deaths, i.e., core-collapse supernovae (SNe, e.g., Getman et al. 2009). Moreover, in the distant Universe, the spectra of young galaxies are shaped by hot, massive stars. The very first generation of these objects ('First Stars', see Johnson et al. 2008 for a review on this topic) is thought to be responsible for the re-ionization of the early Universe (e.g., Bromm et al. 2001; Morales & Wyithe 2010), at least in part (Matteucci & Calura 2005), and for the first enrichment of metals (Bromm & Larson 2004; Bromm et al. 2009). Furthermore, the most energetic processes in the Universe, gamma-ray bursts (GRB), are suspected to result from the final collapse of a massive star to a black hole (at least the 'long-duration' GRBs). A deeper knowledge about massive stars and their evolution is therefore a prerequisite for improving our understanding of the Universe as a whole.

1.1 Massive star evolution

Stellar evolution strongly depends on the initial mass of a star. This parameter determines its final fate, either in terms of a spectacular SN explosion that leaves behind a black hole or a neutron star, or by having a more 'modest' death, by ejecting its outer layers to form a planetary nebula and producing a white dwarf. The former scenario is associated with high-mass objects, and the latter with lower-mass ones. The 'high-mass' range is defined by stars with $M_{\text{init}} > 8M_{\odot}$ ¹ at the beginning of their lives, i.e.,

¹ Corresponding to spectral types earlier than B2, see Massey et al. (2001).

at the main sequence (MS). In the following, we concentrate on the evolutionary scenario for massive single stars². We provide an overview of the different evolutionary stages during their lifetimes, and discuss the most important physical processes that are crucial for the evolution of massive stars.

1.1.1 Overview

The different stages of the life of a star are unavoidably linked to the fusion processes occurring in its core. In order to balance the gravitational force - whose ultimate goal is to produce the stellar collapse - nuclear fusion in the stellar core produces an internal pressure gradient that is able to counteract the gravitational effect.

Stars enter the MS when their core temperature are high enough to fuse hydrogen into helium, producing the energy needed for counteracting the gravitational collapse. This phase lasts for typically 90% of their lifetime. With increasing initial mass, the interior temperature rises as well. One of the most important consequence is that for stars more massive than $1.3 M_{\odot}$, the CNO-cycle becomes the dominant energy production mechanism, rather than the p-p chain, e.g., the Sun. As the hydrogen is transformed into helium, the luminosity of the star increases, owing to an enhanced mean molecular weight³, whilst its radius (R_*) is increased and its effective temperature (T_{eff}) is diminished. The hydrogen in the core is rapidly consumed (10^6 to a few 10^7 yr), and, when the amount of hydrogen is no longer sufficient to maintain the structure in equilibrium, the star begins to contract until the central H-burning phase is over. At this stage, there is H-burning in a shell around the core. Then, as the central regions contract, the outer layers expand, producing again an increase in R_* and a lower T_{eff} , at a roughly constant luminosity. The core contracts until the structure reaches the thermal conditions⁴ ($T_c \sim 10^8$ K) required for efficient helium burning into carbon. At the same time, H is still burning in a shell around the core. The amount of time needed for the contraction of the core to reach the latter temperature is a function of the total mass, i.e., the more massive a star is, the faster it reaches the required temperature. In later evolutionary stages of high-mass stars (which occur on much faster time-scales than the He-burning), first carbon ($T_c \sim 0.3 - 1.2 \cdot 10^9$ K), then neon ($T_c \sim 1.2 - 1.9 \cdot 10^9$ K), oxygen ($T_c \sim 1.5 - 2.6 \cdot 10^9$ K), and finally silicon ($T_c \sim 2.3 \cdot 10^9$ K) become the main energy sources of the star, while less advanced burning stages continue in shells around the core, the so-called onion-like structure. After the silicon-burning stage, the core of the star is mainly composed of iron. This element has the highest binding energy per nucleon. Therefore, no further energy can be supplied by nuclear fusion, and the iron core collapses, resulting in a violent SN explosion or a GRB, which distributes most of the processed material of the star into the ISM, enabling the chemical enrichment of a new generation of stars and planets.

Typically, stellar evolution theory uses the Hertzsprung-Russell diagram (HRD) to compare evolutionary predictions with observed quantities of actual stars. The HRD was first introduced by Russell (1913) based on work by Hertzsprung (1911). The basic idea was to use two of the star's most directly observable characteristics, namely its (absolute) magnitude and spectral type. Often, a slightly modified version of the HRD is provided, defined in terms of the analogous quantities, but with more physical meaning, luminosity (L_*) and T_{eff} . This diagram could be used, among other important objectives, for characterizing the lifetime of a star, which is associated with different locations in this

² For an overview on the binary evolution, we refer to Vanbeveren et al. (1998) and Langer et al. (2008).

³ The H-burning luminosity depends on μ as $L_{\text{H}} \propto \mu$, all other parameters being equal.

⁴ As an exemplary case, in the following all core temperatures of the subsequent burning stages are provided for the mass-range $15-30 M_{\odot}$.

diagram. Mostly in dependence on its initial mass (but also on its chemical composition and rotational velocity, see Sect. 1.1.2), a star follows a unique track through the HRD, connecting all the different varieties of massive stars as defined by their evolutionary stages.

Various types of high-mass stars

Before we continue with our overview on massive single star evolution, in the following we briefly describe the different types of massive stars and their relation throughout their stellar life.

OB stars. ‘Normal’ high-mass stars in the H-burning evolutionary-phase (MS) have O or early-B spectral type, with luminosity class V (dwarfs) for B-type stars. The *O dwarf stars* have typically masses between 15 and 90 M_{\odot} , and effective temperatures between 30,000 and 55,000 K. They are extremely luminous objects ($\sim 5 \cdot 10^4 - 10^6 L_{\odot}$). The spectra of these stars display dominant absorption (and, under certain circumstances, emission) lines from H I and He II, as well as highly ionized stages of several metals (Si IV, N III/N IV/N V, O III/O IV, C III/C IV). He I lines are present as well, though they are very weak (or even absent) in the hottest O-stars. *Early B-type dwarfs* (B0-B2) are cooler ($T_{\text{eff}} \sim 22,000 \dots 28,000$ K) and less massive (between 8 and 12 M_{\odot}). Their spectra show neutral helium lines, which are most prominent at B2, and moderate hydrogen Balmer lines. Metal lines from ‘low’ ionization stages (mostly singly ionized) are ubiquitous, e.g., from silicon, carbon, oxygen, and nitrogen. Both O- and B-stars produce a sufficient amount of Lyman continuum radiation to create H II regions around them. They are usually found in OB associations, loose aggregates typically containing 10-100 massive stars, see Briceño (2009) and references therein.

Blue Supergiants (BSG). This evolutionary phase starts as the former O and early B-type stars begin to burn helium in their cores, leaving the MS. Their spectral types are late B and early A supergiants. It is thought that B-supergiants could also be regarded as a late phase of stellar evolution where hydrogen is being burned at the same time both in the core and in a shell around it. They are extremely luminous objects, and constitute the brightest stars in the Universe at visual light, with absolute magnitudes up to $M_v = -10$. For moderately massive stars this is a transition phase before evolving redwards to the Red Supergiant phase. They could also be blue-loop objects (see below). Extremely massive ($M > 60 M_{\odot}$) as well as ‘mildly’ massive stars ($M < 25 M_{\odot}$) do not experience this phase in their post-MS evolution (see below). Interestingly, evolutionary stellar models predict a gap in the HRD for massive stars between $\sim 10 M_{\odot}$ and $\sim 25 M_{\odot}$ at the end of MS, which extends till the supergiant region, the so-called Blue Hertzsprung Gap (BHG). However, the BHG is not actually observed, and a rather continuous distribution from MS stars to supergiants, with a maximum density in the A-supergiant domain, has been observed in the Galaxy as well as the Magellanic Clouds, see Maeder (1999a) and references therein. Binarity has been proposed to explain this observational discrepancy (Vanbeveren et al. 1998).

Yellow Supergiants (YSG). These objects are evolved helium-burning massive stars that represent a short period during their total lifetimes, as they horizontally cross the HRD from the blue side to the red supergiant stage or from the red back to the blue. Their spectral types are typically F0-G9. The yellow supergiants are among the brightest stars in our Galaxy, but their identification is difficult because they can be masked by the presence of foreground stars, of similar magnitudes and colors. To

discriminate these stars, radial velocity measurements are used in nearby galaxies (e.g., Neugent et al. 2010).

Red Supergiants (RSG). They constitute an He-burning evolutionary phase in the lives of moderately massive stars (see below). They have the largest physical sizes of any star, and their very cool effective temperatures (spectral types K-M) lead to a spectrum that is dominated by molecular absorption lines. They are the final result of a nearly horizontal evolution across the HRD, after their blue predecessors have left the MS and crossed the ‘yellow void’, passing through the yellow supergiant phase. In some cases ($10 M_{\odot} \leq M < 25 M_{\odot}$), the RSG phase is the terminal stage for massive stars before exploding as a SN. In other, more massive cases (up to $M \sim 40 M_{\odot}$), this stage comprises only a small fraction of their lifetimes, before they evolve back to the blue again, either to a blue supergiant or a Wolf-Rayet star. Levesque (2010) recently reviewed the latest advances in our understanding of these objects.

Luminous Blue Variables (LBV). These objects represent a short-lived ($\sim 10^4 - 10^5$ yr) evolutionary phase, and are interpreted as a transition stage between O-type and WN stars, in which the stars are subject to significant temperature changes. They are stars of high intrinsic luminosity ($10^6 L_{\odot}$) at or near the top of the empirical HRD. LBVs are generally close to the Eddington limit. They are discriminated by two different types: giant eruptions with magnitude changes of the order of 3-5 during which the bolometric luminosity most certainly increases (e.g., Eta Carinae), and eruptions of 1-2 magnitudes at approximately constant bolometric luminosity, often observed on time scales of years to decades (e.g., S Doradus variables). Their spectra typically show prominent emission lines, often with P Cygni profiles when observed at sufficiently high resolution. Their characteristic temperatures and mass-loss rates are $T_{\text{eff}} \sim 7,000 \dots 30,000$ K and $\dot{M} \sim 10^{-5} \dots 10^{-4} M_{\odot} \text{yr}^{-1}$, respectively. A detailed review on these objects can be found in Vink (2009).

Wolf-Rayet stars (WR). In most cases, they are the ‘bare cores’ of initially ‘normal’ massive stars, which are devoid of their outer layers because of extreme stellar winds. There is about one WR-star for 10^8 stars in our Galaxy. Typically, they have masses between $8-25 M_{\odot}$, high mass-loss rates ($\dot{M} \sim 5 \cdot 10^{-6} \dots 10^{-4} M_{\odot} \text{yr}^{-1}$) and occur in young associations. Their spectra are dominated by strong emission lines. Visual spectra classification of WR stars is based on emission line strengths and line ratios. WR-stars can be broadly divided into nitrogen-rich WN stars and carbon rich WC stars. The basic difference between the two subtypes is believed to be that the N-enrichment in the WN stars is merely a product of the previous H-burning phase, whereas the C in WC stars is a sign of He-burning. As a result, WC stars are thought to be more evolved than the WN stars. The late WN (WNL) are more luminous and H-rich than the early ones (WNE) with almost no H left. There is a similar designation for early and late WC stars, being WCL and WCE, respectively. An extreme case of WCEs are the WO stars, which have higher O/C ratios. WR-stars have been recently reviewed by Crowther (2007).

Very schematically, the evolutionary scenarios for massive single stars at solar metallicity (Z_{\odot}) can be described, according to Maeder & Meynet (2010), by the following sequences:

$M > 90 M_{\odot}$: O - Of - WNL - WNE - WCL - WCE - SN

$M > 60-90 M_{\odot}$: O - Of/WNL \leftrightarrow LBV - WNL (H poor) - WCL-E - SN

$M > 40\text{-}60 M_{\odot}$: O - BSG - LBV \leftrightarrow WNL - (WNE) - WCL-E - SN

or

O - BSG - LBV \leftrightarrow WNL - WCL-E - WO - SN

$M > 30\text{-}40 M_{\odot}$: O - BSG - RSG - WNE - WCE - SN

or

O - BSG - RSG - OH/IR \leftrightarrow LBV?

$M > 25\text{-}30 M_{\odot}$: O - (BSG) - RSG - BSG (blue loop) - RSG - SN

$M > 10\text{-}25 M_{\odot}$: O - RSG (Cepheid loop for $M < 15 M_{\odot}$) - RSG - SN

The OH/IR designation refers to M-type supergiants with detectable ejected dust shell, which are strong sources of maser emission, e.g., Schuster et al. (2006). The \leftrightarrow character indicates back and forward motions between two stages. Note that the limits between the various scenarios depend both on metallicity (Z) and rotation (see below). Roughly, we might separate three major paths of massive star evolution:

- **In the range 40-60 M_{\odot} and above:** These objects spend their entire lifetimes in the blue part of the HRD. After leaving the MS, they typically evolve to a BSG, and experience a short phase as an LBV. Then, they lose their envelope to become a WR star. If they are massive enough ($M > 75 M_{\odot}$), they could evolve directly to a WR-star from the MS, owing to a strong stellar wind. Finally, they explode as a SN.
- **In the range 30-40 M_{\odot} :** These stars evolve in the HRD from the MS to the red, in the sequence BSG to RSG. They only lose a fraction of their envelopes during the MS. In the RSG stage, they further evolve, lose their envelopes and return to the blue part of the HRD, to become a WR-star and finally explode as a SN.
- **In the range 10-30 M_{\odot} :** After leaving the MS, these stars experience a rapid development to the RSG phase, where they spend most of their He-burning lifetime. In the RSG-phase, the outer convective zone penetrates deep enough into the star, and nuclear processed matter can be transported to the stellar surface - the so-called first dredge-up, preventing the mass extension of the convective He-core.

Objects within the range of 25-30 M_{\odot} pass through a brief BSG phase before they experience one or more blue-loops, when they proceed back and forth from RSG to BSG phases. Their ultimate stage is a RSG phase, before they end their lives with a SN explosion.

Objects within the range of 10-25 M_{\odot} , cross the 'Cepheid instability strip', where they pulsate rapidly and are observed as Cepheids, during their blueward evolution along the blue-loop. They cross again this region of the HRD during their final redward evolution to the RSG phase. These stars also end up as a supernova.

Discrepancies between observational results and stellar evolutionary models

The modeling of massive star evolution sensitively depends on the details of the physical effects which are considered. For instance, a comparison of the observed HRD with predictions from the standard theory of stellar evolution *at constant mass*, i.e., without mass loss (e.g., Kippenhahn & Weigert 1990), showed that this theory failed to match the observations. In particular, such evolutionary models violate the so-called empirical Humphreys-Davidson limit (Humphreys & Davidson 1979),

by predicting a large number of high-mass, high luminous core He-burning RSGs which were not found in the observations.

A first step to circumvent these problems was taken by including the effects of mass loss. Both the Geneva group (Schaller et al. 1992; Schaerer et al. 1993; Charbonnel et al. 1993; Meynet et al. 1994) and the Padova group (Alongi et al. 1993; Bressan et al. 1993; Fagotto et al. 1994a,b,c; Girardi et al. 1996) were finally able to provide stellar evolutionary models for different metallicities including mass loss. They succeeded to explain the lack of very bright RSGs since the luminosity of a star evolving with mass-loss is lower than for constant-mass evolution. One of the biggest achievement of including mass-loss in stellar models was a better agreement with the observed number ratio of WR-stars to O stars at different metallicities, e.g., Maeder & Meynet (1994).

Despite these improvements, there were still a number of observational findings which could not be explained, such as the so-called 'mass discrepancy' between the spectroscopically determined and evolutionary predicted stellar masses (Groenewegen et al. 1989; Herrero et al. 1992, 2000), or the observed abundance anomalies in several OB-stars, mostly referring to a high helium and nitrogen enrichment (Gies & Lambert 1992; Herrero et al. 1992, 2000).

The inclusion of rotation, considered as a second-order effect for a long time, was the next logical step. Big efforts were made to develop stellar evolutionary models accounting for both mass loss and rotation (Meynet & Maeder 2000; Heger & Langer 2000; Heger et al. 2000; Maeder & Meynet 2001a). These models were able – at least basically – to explain the aforementioned abundance anomalies, where the consideration of initially fast rotators favors the rotational mixing of nuclear processed elements from the interior towards the stellar surface.

However, the appearance of additional observational discrepancies, mostly in the context of the VLT-FLAMES Survey of Massive Stars (Evans et al. 2005, 2006, hereafter FLAMES-I) indicated that, even with the inclusion of rotational mixing, there were – and still are – problems to reconcile observational findings with theoretical predictions. Most likely, other physical processes need to be considered as well, e.g., *binarity* (e.g., Langer et al. 2008; Sana et al. 2009, 2011) and/or *magnetic fields* (e.g., Maeder & Meynet 2003, 2004, 2005; Morel et al. 2008; Maeder et al. 2009).

Building on the effort performed by different research groups during the past years, in the following we concentrate in more detail on the evolution of massive stars with mass loss and rotation. We highlight the importance of both effects regarding the evolution of massive stars, and we comment on their basic benefits as well as the most important caveats.

1.1.2 Evolution with mass loss and rotation

As it turned out in recent years, the detailed physics and evolution of massive stars are dominated by the effects from both *mass loss* and *rotation*. These quantities are able to modify all the outputs of stellar evolution: lifetimes, evolutionary tracks in the HRD, chemical yields, final stellar masses, etc.

Because of their high or even extreme luminosities, all massive stars display stellar winds⁵. Regarding hot stars (all varieties of massive stars, except for RSGs and YSGs), such winds are mainly driven by radiative line acceleration, since there are numerous spectral lines with high interaction probability close to the stellar flux maximum. Massive stars are heavily influenced by mass loss due to their strong radiative-driven stellar winds, especially during their evolution in the core H-burning and the WR-phases. The stellar winds are able to remove most of the initial stellar mass, tearing apart

⁵ For an introduction into stellar winds of various kinds see Lamers et al. (1999), whilst for the present state of the physics and observations of stellar winds *from hot massive stars* we refer to the review by Puls et al. (2008).

their envelopes and, thus, exposing their bare cores (WR stars) in the latest stages of their lives. The importance of an accurate determination of mass-loss rates was already quantified by Meynet et al. (1994). These authors stated that even a change of only a factor of two in the mass-loss rates of massive stars would have dramatic effects on their overall evolution.

One of the major consequences of stellar rotation, on the other hand, is the rotationally-induced mixing of elements synthesized in the core towards the stellar surface, which is capable to change the chemical composition of the outer layers of the stars.

Moreover, both effects are inevitably connected. On the one hand, rotation affects the stellar wind. Mass loss from rapidly rotating stars might become significantly increased. Rapid rotation induces anisotropic mass loss, (mostly) predicted to be stronger over the poles than in equatorial regions (e.g., Maeder 1999b; Cranmer & Owocki 1995; Petrenz & Puls 2000). On the other hand, mass-loss tends to remove angular momentum from the star, slowing down its rotation rate (Langer 1998).

Basic assumptions

Physically, the origin of both effects is rooted in the large ratio between temperature and density in massive stars, T/ρ . First, this enhances the ratio of radiation to gas pressure, which scales as T^3/ρ , favoring the presence of radiation-driven stellar winds. Second, a high T/ρ -ratio also favors rotational mixing, since mixing by shear turbulence scales as thermal diffusivity, K , and behaves like $K \propto T^3/\rho^2$. Finally, the velocity of meridional circulation scales with the luminosity to mass ratio, L/M , favoring mixing and the transport of angular momentum in the stellar interior in massive stars.

To account for both effects in the evolutionary calculations, a variety of approximations are used. The main physical assumptions adopted for the treatment of mass-loss and stellar rotation in the models by the Geneva group⁶ have been summarized by Maeder & Meynet (2010): (i) For differentially rotating stars, the stellar structure equations (Meynet & Maeder 1997) are defined by considering the case of ‘shellular’ rotation, where the angular velocity, Ω , is a function of radius alone (e.g., Zahn 1992). (ii) For treating the internal transport of chemical elements and angular momentum, the effects of shear diffusion (Zahn 1992; Maeder 1997), meridional circulation (Maeder & Zahn 1998), and their interactions with horizontal turbulence (Talon & Zahn 1997) are considered. (iii) Mass-loss effects are accounted for, using the theoretical mass-loss rates as provided by Vink et al. (2000, 2001) for OB-star winds, and by Nugis & Lamers (2000) for WR-star winds. (iv) The effects of rotation on mass loss are accounted following Maeder & Meynet (2001a).

Important model results

Rotating vs. non-rotating models. The effects induced by rotation on the stellar models have been described in detail by Heger & Langer (2000), Maeder & Meynet (2000), and Meynet & Maeder (2000). In the following, we briefly summarize the most important ones.

Rotation modifies the evolutionary tracks mainly through the following physical effects: rotation lowers the effective gravity (centrifugal acceleration!), enlarges the convective cores and smoothes the chemical gradients in the convective zone, enhances the mass-loss rates, and distorts the stellar photosphere, i.e., rotation induces deviations from spherical symmetry. This leads to the following consequences:

⁶ Similar assumptions are used in the models by Langer and co-workers, with certain differences regarding the coupling of mass loss and rotation, see point (iv) below.

- Rotating stars have larger convective cores compared to non-rotating stars, recovering former results achieved using the ad hoc approximation of convective overshooting (see Maeder & Mermilliod 1981; Maeder & Meynet 1989).
- On and near the Zero Age Main Sequence (ZAMS), distortions of the stellar photosphere due to rotation produce a small shift of the tracks towards lower effective temperatures. Rotational mixing transports ‘fresh’ hydrogen into the convective core, slowing down its decrease in mass during the MS. This effect produces a more massive He-core at the end of the H-burning phase, resulting in tracks at lower T_{eff} .
- Rotating tracks become more luminous than non-rotating ones. Rotational mixing transports helium and other H-burning products into the radiative envelope. The He-enrichment diminishes the opacity, leading to an enhancement of the stellar luminosity.
- Rotation increases the MS lifetimes with respect to non-rotating models (up to about 40%).
- Stellar masses determined from evolutionary tracks for non-rotating stars are always larger than those deduced from rotating models, thus solving at least part of the mass discrepancy mentioned above. Typically, the mass lost by stellar winds during the MS is enhanced by 45-75% in rotating models with an initial rotational velocity $v_{\text{ini}} = 300 \text{ km s}^{-1}$. Additionally, the higher luminosities reached by the rotating models and their longer MS lifetimes contribute into producing smaller final masses.

Metallicity. Maeder & Meynet (2001b) studied the impact of different metallicities for rotating stellar models. They concentrated on comparing low- Z models, appropriate for the Small Magellanic Cloud (SMC, $Z = 0.2 Z_{\odot}$), with corresponding Galactic models. Most of the above effects were also found at lower metallicity. The main conclusion of this work can be summarized as follows: since at low Z the mass-loss rates become diminished ($\dot{M} \propto (Z/Z_{\odot})^{0.72}$, cf. Mokiem et al. 2007b), the removal of angular momentum during the stellar evolution is much lower. Moreover, there is an efficient outward transport of angular momentum by meridional circulation as well. Thus, a much larger fraction of the stars at lower Z reach ‘break-up’ velocities (critical rotation, with zero effective gravity), and rotation may thus be a dominant effect at low Z . Another important consequence of a lower metallicity is that the gradient of the internal rotation, $\Omega(r)$, becomes steeper, because of the higher densities in the outer layers and the higher compactness of the star at low Z . This favors the occurrence of more mixing at lower Z .

Rotation-induced mixing. One of the major effects of including rotation in stellar evolutionary models for single massive stars is rotation-induced mixing: CNO-cycle processed material from the interior of massive stars can reach the stellar surface at early evolutionary stages. In particular, this enhances the surface N/C ratios, as observed for OB-stars (Gies & Lambert 1992; Herrero et al. 1992, 2000). Nitrogen enhancements (together with carbon depletion to a lesser extent) produced by rotational mixing are more important during the MS, whilst the enrichment during the post-MS evolution is rather inefficient. The (relative) N/C ratios are also affected by the background metallicity, as already mentioned, being larger in lower- Z environments⁷.

⁷ Such larger N/C enrichments have been confirmed, e.g., by abundance determinations in the SMC, e.g., Venn & Przybilla (2003).

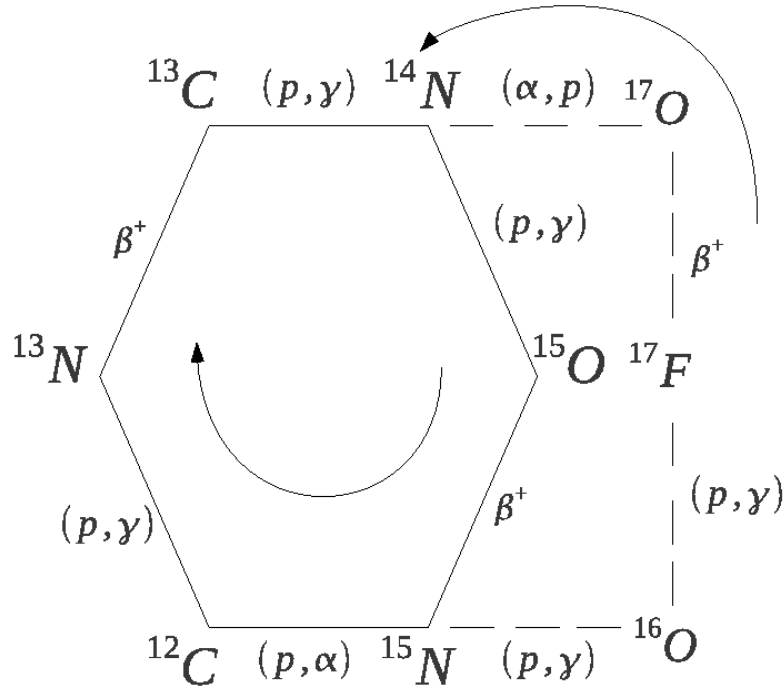


Figure 1.1: Schematic picture of the CNO cycle. The main CN cycle is represented by the hexagon (solid lines), whereas the secondary NO cycle is represented by the dashed lines. Detailed information about the involved reaction network is provided in Table 1.1. The compact notation $X(a,b)Y$ means that the nucleus X captures the particle labeled by "a" and emits the particle labeled by "b", resulting in the nucleus Y . In this diagram, β^+ indicates a beta plus decay (positron emission). Arrows indicate the sequence of the different nuclear reactions for both cycles according to Table 1.1. Figure adapted from Maeder (2009).

This scenario is rather different from the one for non-rotating models, where CNO-processed material appears at the surface only during the RSG stage, after the first dredge-up has occurred. Such non-rotating models were not able to explain the observed N/C ratios. However, the consideration of rotation allowed to reconcile the observational results with the theoretical predictions (at least basically, but see below).

Surface abundances of CNO-processed material are expected to change most notably. Also, other elements should show alterations due to rotational mixing, though sometimes to a lesser extent. For instance, helium has already a considerably initial surface abundance, and the expected enhancement relative to this initial abundance should be rather small. As discussed by Brott et al. (2011a), the surface abundances of boron, sodium, fluorine, and aluminum should change as well. Among all these elements, the nitrogen surface abundance is expected to be the most affected, even for relatively slow rotators, making this element one of the best tracers for testing the treatment and the effects of rotational mixing in massive stellar models.

The latter consequence is largely related to the nature of the CNO-cycle itself. As mentioned in

Sect. 1.1.1, the CNO-cycle is the dominant nuclear energy source for high-mass stars. While CNO-burning itself is catalytic, i.e., the total number of C, N, and O nuclei is not changed, the concentration of the different isotopes could be modified, leading to a buildup of nitrogen at the expense of carbon and, to a much lesser extent, oxygen.

The CNO-cycle is a combination of mainly two independent cycles: the basic CN-cycle, and a secondary NO-loop. Figure 1.1 displays a schematic picture of the cycle, and important data on the corresponding reaction network are provided in Table 1.1.

At the initial phase of the CN-cycle, most of the initial C nuclei are converted into ^{14}N . The follow-up nuclear reaction, $^{14}\text{N} + ^1\text{H} \rightarrow ^{15}\text{O} + \gamma$ (in compact notation: $^{14}\text{N}(p,\gamma)^{15}\text{O}$, see caption Fig. 1.1), is the slowest within the CN-cycle, acting as a ‘bottleneck’” Therefore, ^{14}N becomes the most abundant isotope. While ^{14}N ‘waits’ to be transformed into ^{15}O , it can be mixed from the lower envelope into the stellar surface, favored by the formation of a strong mean molecular weight gradient produced during the MS.

The (relative) importance of the NO-cycle is quantified by the branching ratio between the proton captures by ^{15}N , producing either $^{15}\text{N}(p,\gamma)^{16}\text{O}$ or $^{15}\text{N}(p,\alpha)^{12}\text{C}$, which is on the order of 10^{-3} . Thus, the amount of ^{16}O produced by proton captures is negligible, i.e., approximately 10^3 cycles are required before a significant number of CN nuclei are transferred to the NO chain. Nevertheless, even though there is a low production of oxygen through this channel, the NO-loop allows the ^{16}O nuclei to take part in the process as well, as they are transformed into nitrogen via the NO cycle. The timescales for the ON nuclei produced at the NO-loop to be transferred into the CN-cycle are rather long as well, $\tau \sim 10^8$ years. As a result, the CN-cycle falls into equilibrium fairly quickly, and is largely decoupled from the slower NO cycle.

To summarize, the nitrogen enhancement comes (mostly) from the carbon destruction via the CN-cycle, leaving the oxygen content almost constant. Only at later stages oxygen is also depleted. The resulting changes among the CNO elements caused by the different burning channels are in such a way that, overall, the final surface abundance of C and O are decreased, whereas nitrogen becomes enhanced. Therefore, the nitrogen surface abundance turns out to be one of the best tracers to quantitatively test the efficiency of rotational mixing at early stages of stellar evolution.

Observations vs. theory

For the past years, there have been different projects aimed to observe a statistically significant sample of massive stars, allowing for *quantitative* conclusions, e.g., FLAMES-I; the VLT-FLAMES Tarantula survey (Evans et al. 2010); the Galactic O-Star Spectroscopic Survey (Maíz-Apellániz et al. 2004); the OWN survey (Barbá et al. 2010); the IACOB survey (Simón-Díaz et al. 2011); the Northern Massive Dim Stars Survey (Pellerin et al. 2012). For instance, the FLAMES-I survey enabled to measure the surface abundances of light elements as well as the projected rotational velocities from about 700 O- and B-stars in the Galaxy and the Magellanic Clouds, comprising both slow and fast rotators. Previous work on abundance determinations in OB stars (e.g., Gies & Lambert 1992; Herrero et al. 1992, 2000) was mostly restricted to slowly rotating objects (with $v \sin i < 50 \text{ km s}^{-1}$).

One of the major outcomes of the analysis of the FLAMES-I survey posed (and still poses) a considerable challenge for the theory of rotational mixing. Indeed, the derivation of nitrogen abundances for a large sample of B-stars over a large range of projected rotational velocities led to unexpected results, which partly even contradicted predictions from rotating single star models: within the population of Large Magellanic Cloud (LMC) core-hydrogen burning objects, a significant number of both

Table 1.1: Nuclear reactions involved in the two main loops of the CNO-cycle, together with approximate timescales τ at $T_c = 25 \cdot 10^6$ K. Data taken from Maeder (2009).

				Approx. τ
CN	$^{12}\text{C} + ^1\text{H}$	\longrightarrow	$^{13}\text{N} + \gamma$	10^3 yr
	^{13}N	\longrightarrow	$^{13}\text{C} + e^+ + \nu_e$	420 s
	$^{13}\text{C} + ^1\text{H}$	\longrightarrow	$^{14}\text{N} + \gamma$	$2.9 \cdot 10^2$ yr
	$^{14}\text{N} + ^1\text{H}$	\longrightarrow	$^{15}\text{O} + \gamma$	$9.4 \cdot 10^4$ yr
	^{15}O	\longrightarrow	$^{15}\text{N} + e^+ + \nu_e$	120 s
	$^{15}\text{N} + ^1\text{H}$	\longrightarrow	$^{12}\text{C} + ^4\text{He}$	3.7 yr
NO	$^{15}\text{N} + ^1\text{H}$	\longrightarrow	$^{16}\text{O} + \gamma$	$4.6 \cdot 10^3$ yr
	$^{16}\text{O} + ^1\text{H}$	\longrightarrow	$^{17}\text{F} + \gamma$	$5.0 \cdot 10^6$ yr
	^{17}F	\longrightarrow	$^{17}\text{O} + e^+ + \nu_e$	66 s
	$^{17}\text{O} + ^1\text{H}$	\longrightarrow	$^{14}\text{N} + ^4\text{He}$	$3.1 \cdot 10^6$ yr

non-enriched fast rotators and highly enriched slow rotators were found (Hunter et al., 2008a, 2009b), together with a population of slowly rotating and highly enriched B-type supergiants (discussed by Vink et al. 2010). Independently, Morel et al. (2006) found a population of nitrogen-enhanced Galactic stars with intrinsically slow rotation. These results imply that standard rotational mixing might be less efficient than commonly thought, and might not even be the dominant mixing process (see below).

To obtain further insight into this matter, Brott et al. (2011b) recently performed a quantitative study trying to reproduce the physical properties of the LMC B-star sample from the FLAMES-I survey, using evolutionary models for single stars accounting for the effects of rotational mixing. To perform these simulations, the latter authors used a dense grid of models for MS LMC stars, as described in Brott et al. (2011a)⁸. These models were carefully calibrated in terms of initial abundances, convective core overshooting, and rotational mixing efficiency, using results from the FLAMES-I survey. The complete set was used as input for the population-synthesis code STARMAKER⁹, which interpolates the parameters of model stars of a specified initial mass, age, and initial rotation velocity within the grid. This allows to obtain the primary stellar parameters (T_{eff} , luminosity, radius, and $\log g$) as well as other quantities, namely: mass-loss rate, current rotational velocity, current stellar mass, and surface abundances of light elements.

In agreement with the earlier results by Hunter et al. (based on a more simple comparison), also the overall agreement between the more complex population synthesis and the observed sample turned out to be rather poor. While the models predicted that the bulk of the stars should consist of non-enriched slow rotators and enriched fast rotators, the observed objects were distributed over a larger range of both projected rotational velocities and nitrogen abundances. Again, the two problematic groups of observed non-enriched fast rotators and highly enriched slow rotators could not be reproduced, supporting the earlier results by Hunter et al.

⁸ The models used by Hunter et al. in their comparison with observations from the FLAMES-I survey were a sub-sample of these models.

⁹ Detailed information about the population synthesis code can be found in Brott et al. (2011b).

Additional effects. To explain these unexpected results, additional physical processes were invoked.

At first, **close binary evolution** was considered. Recent studies indicate that a significant fraction of massive stars is part of a binary system (e.g., Mason et al. 2009), with a binary fraction of above 50% in young clusters (Sana et al. 2008, 2009, 2011; Bosch et al. 2009). In close binary systems, the primary star (the one with the higher initial mass) may fill its Roche lobe during the MS evolution, transferring its stellar envelope to the companion. Owing to this process, and even neglecting rotational mixing, the surface nitrogen abundance of the companion star would become enhanced by a factor of 3 to 5 (Langer et al. 2008). In addition, subsequent rotational mixing of the mass-gainer would increase the abundance even further. Brott et al. (2011b), on the other hand, argued that close binary evolution, at the present stage of knowledge, is unlikely to be responsible for the slowly rotating nitrogen-rich population of observed stars in the FLAMES-I survey, since canonical mass transfer evolution leads to *rapidly rotating* nitrogen-enhanced objects. Even though the consideration of binary evolution may also increase the population of slowly rotating N-enhanced objects, as post-mass-transfer systems can spin down the accreting star (Langer et al. 2008), it is thus more likely that the population of fast rotating N-enhanced objects becomes increased, making the problem even worse. Nevertheless, further insight into this matter requires a comparison between observational findings and binary population synthesis models accounting also for non-conservative mass transfer¹⁰, which are just at the stage of their beginnings, e.g., de Mink et al. (2007, 2009); Sepinsky et al. (2009); Lajoie & Sills (2011).

Another possibility is that the highly enriched, slowly rotating population may be produced by effects of **magnetic fields**. During the past years, some evidence pointing in that direction has been accumulated. For instance, Morel et al. (2008) found evidence for magnetic fields in Galactic nitrogen-enriched slowly-rotating B-type dwarfs, and evidence for nitrogen enrichments in magnetic slowly rotating Galactic O-stars has been recently found by Martins et al. (2011a). A potential mechanism to explain this population of objects would be through *magnetic breaking* (e.g., Townsend et al. 2010), which slows down the stars, with rotational mixing occurring whilst the star is still a fast rotator. Moreover, since this process needs to occur on short time scales, Brott et al. (2011b) argued that this would explain the lack of highly enriched, but ‘mildly’ rotating objects as found by Hunter et al.

Brott et al. (2011b) invoked another potential mechanism to increase the population of slowly-rotating objects from non-enriched to enriched ones through the rise of magnetic bubbles carrying both magnetic flux and nitrogen from the core to the surface (building on a model from MacGregor & Cassinelli 2003).

Summarizing, magnetic fields may need to be considered to explain the observed nitrogen excess, but more work is certainly needed to enable quantitative conclusions. First steps into this direction were recently undertaken by Meynet et al. (2011), who calculated models with a simple description of magnetic breaking, leading both to slow rotation and to surface nitrogen enhancement (because of strong internal differential rotation).

1.2 Motivation of this thesis

As should have become apparent from the last sections, nitrogen has been proven to be a key element for testing and constraining the stellar evolution of massive stars. To further constrain the findings

¹⁰Models including rotation indicate that mass transfer may be significantly non-conservative, with only a fraction of the transferred material retained by the accretor while the remainder is ejected from the system, e.g., Petrovic et al. (2005).

accomplished by the FLAMES-I survey and to provide a general picture of massive star evolution, *these studies need to be extended to the O-type stars*. Because of their shorter lifetimes, the time-range where this enrichment takes place can be narrowed down, and one might be able to constrain the mixing scenario even better than it is possible from B-stars alone. In this respect, low-Z environments such as the LMC and SMC are an ideal testbed, because the nitrogen baseline abundances are low (Hunter et al. 2007), and even a strong enrichment is easier to measure/confirm than, for instance, in the Milky Way. Unfortunately, most previous abundance studies of massive stars are strongly biased toward intermediate and early type B-stars. Indeed, when inspecting the available literature, metallic abundances, in particular of nitrogen, are scarcely found for O-stars.

In addition, nitrogen also presents a promising potential for deriving effective temperatures in the very *early* O-star regime. At those hotter temperatures ($T_{\text{eff}} > 45$ kK), the usual diagnostics for deriving T_{eff} , the helium ionization equilibrium, begins to fail, owing to weak He I lines and rather insensitive He II. Instead, numerous prominent nitrogen lines of the N III/N IV/N V ionization stages are found in the O-star spectra, showing in most cases a remarkably sensitivity on the effective temperature.

The presence of line emission in the N III triplet at $\lambda\lambda 4634\text{-}4640\text{-}4642$ Å, in combination with the behavior of He II $\lambda 4686$, is used for classification purposes ('f'-features, see Walborn 1971b, Sota et al. 2011), and for discriminating O-stars with such line emission from pure absorption-line objects. Walborn et al. (2002) used the relative strength of the emission at both N III $\lambda\lambda 4634\text{-}4640\text{-}4642$ and N IV $\lambda 4058$ to spectroscopically discriminate the earliest O-stars, splitting the formerly degenerate O3 class into three different types, O2, O3, and O3.5, being O2 the new degenerate one instead. This scheme has been used in a variety of studies during the past years to classify spectra of early O-stars in the LMC and SMC (e.g., Walborn et al. 2004, Massey et al. 2004, 2005, 2009, Evans et al. 2006) and in the Milky-Way, e.g., Sota et al. (2011). However, these additional sub-types are not yet universally accepted (e.g., Massey et al. 2004, 2005).

Particularly, this classification scheme has been questioned for the same reason as the available information about surface nitrogen abundances in O-stars is scarce: the complexity of the line formation of some of these nitrogen lines, especially those that typically display emission in the O-star range, namely N III $\lambda\lambda 4634\text{-}4640\text{-}4642$ as well as N IV $\lambda 4058$. These lines have been suggested to be formed by photospheric NLTE processes rather than by emission in an extended atmosphere. The most important analysis of the N III emission problem, so far, was the seminal work by Mihalas & Hummer (1973), building on work by Bruccato & Mihalas (1971). These authors argued that the dielectronic recombination was the canonical explanation for the formation of the 'f'-features. On the other hand, regarding N IV $\lambda 4058$, there is no detailed analysis on its formation process to date.

To provide more insight into this matter, we started a project with the objective to enable quantitative nitrogen spectroscopy in O-type stars. The primary purpose was to analyze a large sample of early O-stars, and to determine both their temperatures and nitrogen abundances from the available nitrogen lines, exploiting the nitrogen ionization equilibrium. In addition, we intended to investigate whether the Walborn et al. (2002) classification scheme is able to provide a meaningful relation for discriminating the earliest O-stars. Finally, a comparison between our results and predictions from population synthesis models should allow us to test the efficiency of rotational mixing in early phases of the evolution of massive stars.

To perform these analysis, an investigation regarding the line-formation process of strategic nitrogen lines, such as N III $\lambda\lambda 4634\text{-}4640\text{-}4642$ and N IV $\lambda 4058$, using modern atmospheric codes, was required. For this objective, it was crucial to develop an improved, accurate nitrogen model atom

including a precise treatment of the dielectronic recombination process to face the N III emission line problem, and to implement this model atom into a suitable stellar atmosphere code in order to synthesize the corresponding spectra and to fit the observations.

1.3 Overview of the chapters of this thesis

In the following, we briefly present the content of the different chapters within this thesis.

Chapter 2: Atmospheric codes

We summarize important aspects that need to be considered to allow us for a reasonable description of the outer layers of massive stars. In addition, we describe FASTWIND, the NLTE atmosphere/spectrum synthesis code primarily used within this work.

Chapter 3: Model atoms for NLTE line formation computations – A nitrogen model atom

We briefly discuss the various ingredients needed for the construction of a comprehensive model atom, required for the numerical solution of a given NLTE problem. In particular, we describe the implementation of a new nitrogen model atom into the FASTWIND database.

Chapter 4: Nitrogen III emission line formation revisited

We concentrate on the formation of the optical N III emission lines at $\lambda\lambda 4634\text{-}4640\text{-}4642$, which are fundamental for the definition of the different morphological ‘f’-classes. Since the f-features are observed in the majority of O-stars and are strongly dependent on the nitrogen abundance, a thorough re-investigation of their formation process using modern atmosphere codes is required, in order to avoid wrong conclusions.

Chapter 5: Surface nitrogen abundances for O-stars in the Large Magellanic Cloud

The main goal of this chapter is twofold: (i) we investigate the N IV $\lambda 4058$ emission line formation and (ii) we derive nitrogen abundances for a substantial O-star sample in the Large Magellanic Cloud, and compare our findings with recent predictions from stellar evolutionary models.

Chapter 6: The earliest O-stars

In this chapter we perform a quantitative study of the atmospheric parameters of the earliest O-stars, by means of nitrogen line spectroscopy. Particularly, we concentrate on testing the Walborn et al. (2002) classification scheme on its capability of providing a reasonable relation between spectral types and effective temperatures. To this end, we investigate the theoretical N IV/N III emission line ratio, and the impact of different parameters on this ratio. Subsequently, our predictions are confronted with corresponding observational results, derived from an analysis of an early O-type sample of LMC/SMC stars.

Chapter 7: Summary and outlook

Finally, we summarize the major results achieved within this work and provide an outlook for future work.

Chapter 2

Atmospheric codes

2.1 Overview

Quantitative spectroscopy is one of the most common tools used to study stars in a comprehensive way. Since most of the knowledge about the physical parameters of these objects comes from the interpretation of stellar spectra, this method aims at describing the stellar spectra with high precision. The standard procedure is performed by fitting calculated synthetic spectra to observed ones in order to derive stellar parameters (effective temperatures T_{eff} , surface gravities $\log g$, microturbulence v_{mic}), wind-properties (mass-loss rates \dot{M} , terminal velocities v_{∞}), and the chemical composition of a star. Moreover, physical properties, such as luminosities L , masses M , and radii R_* , are calculated based on the aforementioned spectroscopic measurements. The accuracy of these analyses depends crucially on the extent to which model atmospheres are able to reproduce the physical processes that occur in the atmospheres of the stars, and on the goodness of the employed spectrum synthesis code.

For the particular case of hot stars, the numerical calculation of model atmospheres is an enormous task, since, apart from their intense radiation fields, a number of effects not present in the atmospheres of cooler, less massive stars have also to be accounted for. In the following, we summarize important aspects that must be considered in order to allow us for a reasonable description of the outer layers of massive stars. Finally, we describe FASTWIND, the atmospheric code primarily used within this work.

2.2 Basic assumptions for modeling stellar atmospheres of hot stars

The classical approach for modeling stellar atmospheres is usually based on certain ‘standard’ assumptions, namely: flux conservation, hydrostatic equilibrium, a one-dimensional (1D) plane-parallel stratification, and Local Thermodynamic Equilibrium (LTE) (e.g., Mihalas 1978).

These assumptions, originally intended for the study of cool stars, may need to be replaced/relaxed depending on the objective of the particular analysis. For instance, when analyzing the extended atmospheres of giants and supergiants, the spherical extension of the star must be accounted for rather than using a plane-parallel stratification. In particular the stellar spectral type is an important factor to clarify which assumptions are needed for a reliable modeling of each specific case. In general, for early-type stars, the *stellar wind* significantly influences most of the strategic spectral lines¹, and therefore, should be considered in the analysis, discarding the aforementioned hydrostatic assumption.

¹ This applies for all luminosity classes of OB-types, and at least for A supergiants.

Moreover, the intense radiation field and the low densities in the atmospheres of early-type stars, assuming typical conditions, make the assumption of LTE dubious for these objects. Rather, Non-Local Thermodynamic Equilibrium (NLTE) must be used.

In the following, we concentrate on the most important assumptions needed for successfully modeling the ‘windy’ atmospheres of early-type stars.

2.2.1 Non-local thermodynamic equilibrium

Since the photons are able to transport non-local information while propagating through the stellar atmosphere, the validity of LTE depends on whether the radiative transitions are in detailed balance or not, i.e., if every radiative process is exactly balanced by its inverse. On the contrary, collisions between massive particles (most frequently electrons in ionized matter) are controlled by the local conditions in the plasma, and, vice versa, collisions usually drive the stellar plasma towards LTE.

Massive stars display an intense radiation field because of their high surface temperatures. Besides, they have rather low densities, ρ , in their line- and continuum-forming regions. For objects not too close to the Eddington limit², the density in photospheric regions, which are the quasi-hydrostatic regions emitting most of the stellar light, depends mostly on the pressure scale height, H , and the column density, m ,

$$\rho(m) \approx \frac{1}{H} m \propto \frac{g}{T_{\text{eff}}} m \propto \frac{M_*/M_\odot}{(R_*/R_\odot)^2 T_{\text{eff}}/T_\odot} m, \quad (2.1)$$

with g the gravitational acceleration. Note that m is roughly proportional to any reference optical depth scale, τ . Thus, at a given m (or τ), the photospheric density of a typical late O-dwarf is a factor of 50 lower than in the Sun, assuming prototypical parameters of $10 M_\odot$, $10 R_\odot$ and $T_{\text{eff}} = 30,000$ K.

Collisional processes are diminished by the low particle densities. Consequently, they are less important in hot star atmospheres than in their cooler counterparts. In combination with the intense radiation field, which enhances the strength of radiative processes, the overall combined effect is that in the atmospheres of hot stars considerable departures from LTE can be expected.

Departures from LTE have an enormous impact on the modeling of stellar atmospheres. For instance, to define the thermodynamic state of a system, the Maxwellian velocity distribution and the Saha-Boltzmann equations (cf. Mihalas 1978) are sufficient under LTE conditions. Instead, when LTE conditions fail, a more general calculation must be performed which replaces the Saha-Boltzmann equations. The occupation numbers of the atomic levels, n_i , have to be calculated from the equations of *statistical equilibrium*, the so-called NLTE *rate equations*³

$$n_i \sum_{j \neq i} (R_{ij} + C_{ij}) = \sum_{j \neq i} n_j (R_{ji} + C_{ji}) \quad (2.2)$$

where R_{ij} and C_{ij} are the radiative and collisional rates, respectively, for the transitions from level i to j , including all bound-bound and bound-free processes. Transitions depopulating level i are represented by the left-hand side of Eq. 2.2, whereas the right-hand side describes the processes populating the latter level. Similar equations must be written for each level i of every ion k in every

² Beyond which the continuum radiation pressure would exceed the gravitational acceleration throughout the star.

³ These statistical equilibrium equations are customarily defined under the assumptions of steady state and that changes of n_i in a given unit volume due to macroscopic motions are much slower than the atomic transition time scales. Under typical atmospheric conditions, both assumptions can be safely employed owing to the very brief transition timescales.

volume of the stellar atmosphere, and they characterize the microscopic interaction between atoms, electrons, and photons.

The radiative upward rates are given by

$$R_{ij} = 4\pi \int \sigma_{ij} \frac{J_\nu}{h\nu} d\nu, \quad (2.3)$$

where σ_{ij} is the atomic cross-section for a given bound-bound or bound-free process, and J_ν is the mean intensity. The corresponding downward rate is

$$R_{ji} = 4\pi \left(\frac{n_i}{n_j} \right)^* \int \frac{\sigma_{ij}}{h\nu} \left(\frac{2h\nu^3}{c^2} + J_\nu \right) \exp(-h\nu/kT) d\nu, \quad (2.4)$$

with the asterisk denoting LTE populations. The first term of the latter equation corresponds to spontaneous emission, whereas the second one is due to stimulated emission.

For the collisional processes, which only depend on the the local value of electron temperature, T_e , and density, n_e , the upward rates are given by

$$C_{ij} = n_e \int \sigma_{ij}(v) f(v) v dv, \quad (2.5)$$

where $f(v)$ is the velocity distribution of the colliding particles, mainly electrons for early-type stars, given by the Maxwellian velocity distribution. Consequently, the collisional downward rates result from

$$C_{ji} = \left(\frac{n_i}{n_j} \right)^* C_{ij}. \quad (2.6)$$

Because the radiative rates depend on the radiation field, which in turn depends on the opacities and emissivities (which are functions of the occupation numbers), the rate-equations *for all levels* n_i have to be solved in parallel with the equations of radiative transfer for *all required frequencies*. To accurately determine the level populations, we basically need good knowledge of (i) the local temperatures and particle densities, (ii) the non-local radiation field, (iii) accurate cross-sections, and (iv) all transitions between atomic states. Items (i) and (ii) depend on the model atmosphere used for the NLTE calculations, whereas items (iii) and (iv) are related to the specific model atoms of the species involved in the calculations. We refer to Chapter 3 for a detailed description regarding the construction of comprehensive models atoms for NLTE calculations.

The set of rate equations for all levels form a linearly dependent system. In order to close the system, one of these equations must be replaced by another relation, typically the equation of *total number conservation*,

$$\sum_{i,k} N_{i,k} = \frac{\alpha_{el}}{\alpha_H} \left(\sum_i N_{i,H} + n_p \right), \quad (2.7)$$

with the summation extended over all levels of all ions of a given species, and α_{el}/α_H the fraction of all atoms and ions of a certain element relative to that of hydrogen.

The complete system of rate equations, in parallel with the equations of radiative transfer, is solved numerically within a delicate iteration scheme to avoid stagnation of the convergence process. In stellar atmosphere work, a powerful and widely used method to accomplish the latter is the Accelerated

Lambda Iteration (ALI), reviewed by Hubeny (1992). The basic idea is to split the so-called ‘A-operator’, relating the mean intensity and the source function, in order to avoid a full matrix inversion of the latter operator. Rather, an approximate operator (diagonal or tri-diagonal) is constructed and inverted instead.

NLTE line formation

Before we continue with our discussion of the basic assumptions regarding the modeling of stellar atmospheres of early-type stars, we highlight one important implication of NLTE-effects on the formation of spectral lines. Indeed, this implications will be fundamental for the theoretical studies performed within this work regarding the formation of specific nitrogen *emission lines* in O-stars (Chapters 4 and 5).

The strength of a spectral line may differ from the corresponding LTE predictions via two different (but coupled) ways, either because the line opacity has changed or because the line source function departs from the Planck function. Before we define the line source function, it is convenient to introduce the NLTE departure coefficient, $b_i \equiv n_i/n_i^*$, where n_i is the actual population density of a level i and n_i^* is the corresponding LTE value⁴. If $b_i \neq 1$, it is clear that there exists a departure from LTE. The line source function is the ratio of emissivity and opacity, and can be expressed in terms of departure coefficients. Assuming complete frequency distribution,

$$S_v^l = \frac{2h\nu^3}{c^2} \frac{1}{\frac{b_l}{b_u} e^{h\nu/kT} - 1}, \quad (2.8)$$

where b_l and b_u are the departure coefficients of the lower and upper level of the corresponding transition, respectively. When $h\nu > kT$ (Wien’s regime), as is the case for all UV and optical spectral lines in hot stars, the line source function can be approximated by

$$\frac{S_v^l}{B_v} \approx \frac{b_u}{b_l}, \quad (2.9)$$

where B_v is the Planck function. Analyzing the latter expression, we see that $S_v^l > B_v$ when $b_u > b_l$, i.e., the upper level of the transition is considerably overpopulated with respect to the lower one. Hence, the corresponding source function outweighs the continuum intensity at transition frequency ν_0 , and emission may occur in the line. This effect is responsible for explaining the possibility of emission in photospheric lines along with other lines being in absorption.

2.2.2 Stellar winds

Massive stars have (line-) radiation driven winds of various strength, primarily controlled by luminosity and metallicity. Any atmospheric code that is intended to reliably synthesize spectra to perform quantitative spectroscopy of massive stars needs to account for a consistent treatment of both photosphere and wind, at least if the lines/continua are formed outside the (quasi-) hydrostatic region.

To obtain a more precise idea for the maximum mass-loss rate, \dot{M} , for which a hydrostatic treatment is still possible, Puls (2009) provided an estimate valid at least for UV and optical lines,

$$\dot{M} \lesssim 6 \cdot 10^{-8} M_\odot \text{yr}^{-1} (R_*/10 R_\odot) (\nu_\infty/1000 \text{ km s}^{-1}). \quad (2.10)$$

⁴ Calculated by means of the Saha-Boltzmann equation.

with v_∞ the terminal velocity of the wind. This limit implies that hydrostatic models may be sufficient for the UV/optical spectroscopy of late O-dwarfs, B-stars until luminosity class II (for early sub-types) or Ib (for mid/late sub-types), and A-stars until luminosity class Ib.

The concept of a consistent treatment of photosphere and wind was first introduced by Gabler et al. (1989) by means of the so-called *unified* model atmospheres. These models are computationally expensive, basically due to the need of accounting for the Doppler shifts induced by the velocity-field. In most cases, the latter is either accomplished by solving the radiative transfer in the comoving frame (Mihalas et al. 1975, 1976), or by using the so-called Sobolev approximation (Sobolev 1960) which is only justified for those lines that are formed predominantly in the wind.

Unified model atmospheres can be constructed in two different ways. On the one hand, atmospheric codes such as WM-basic (Pauldrach et al. 2001) derive the complete stratification from a (self-) consistent approach, solving the hydrodynamic equations under the assumption of stationarity. On the other hand, an analytical description of the wind may be used. For instance, the velocity field can be described in terms of a so-called β velocity law,

$$v(r) = v_\infty \left(1 - \frac{R_t}{r}\right)^\beta, \quad (2.11)$$

which originates from a generalization of corresponding results from hydrodynamic solutions for line-driven winds. A smooth transition between the quasi-hydrostatic photosphere and the wind is needed, defined by the transition radius, R_t , which is located at roughly 10% of the sound speed. The density then follows from the equation of continuity,

$$\rho(r) = \frac{\dot{M}}{4\pi r^2 v(r)}. \quad (2.12)$$

In this approach, \dot{M} , v_∞ , and velocity field exponent β become input parameters for setting up the wind model as well as *fit parameters* in the quantitative spectroscopic analysis.

The density stratification of the photosphere is calculated as for a hydrostatic atmosphere but accounting for sphericity, from large optical depths until R_t , and can be *roughly* expressed by an exponential law with scale height H (see above). The corresponding velocity law follows again from using the continuity equation with mass-loss rate from above and photospheric density. Such an approach is used, e.g., by the atmospheric code FASTWIND.

2.2.3 Line-blocking/blanketing

Since spectral lines absorb radiation, the emergent flux may become significantly blocked in the extreme UV region, owing to the very large number of overlapping strong metal lines. This line blocking affects the overall shape of the emergent spectrum. Since the total flux has to be conserved, the blocked flux needs to be redistributed at other frequencies, typically in regions where few lines are present, i.e., at longer wavelengths. The process that produces such a redistribution of stellar flux is the so-called line blanketing. A significant fraction of photons is scattered back (or emitted in the backwards direction) and (partially) thermalized, increasing the electron temperature. This leads to a back-warming effect in the deeper layers of the photosphere. On the other hand, in the higher layers, the effect is the opposite, producing a surface cooling. Iron group species, especially the abundant number of Fe and Ni lines, are the dominant contributors to the blanketing effect.

Both LTE and NLTE models require a careful consideration of line-blocking/blanketing effects. Various techniques are applied to cope with this problem, using either statistical approaches, Opacity Distribution Functions (ODFs, suitable under LTE conditions, Kurucz 1979) and Opacity Sampling (OS, Pauldrach et al. 2001), or direct calculations, solving the problem line by line (Hillier & Miller 1998; Hubeny 1998, using model atoms consisting of super-levels connected by super-lines). FASTWIND, the atmospheric code used throughout this work and described in Sect. 2.3, employs a more approximate method based on a simple statistical approach to calculate suitable means of line opacities and emissivities (Puls et al. 2005).

One major consequence of accounting for line-blocking/blanketing effects is that line-blanketed models of hot stars have photospheric He ionization fractions similar to those from unblanketed models at higher effective temperature (see Repolust et al. 2004). Since effective temperatures for O-stars are typically determined by exploiting the He I/He II ionization equilibrium, the latter effect has led to a reduction of the corresponding effective temperature scales, e.g., Repolust et al. (2004); Massey et al. (2004, 2005, 2009); Martins et al. (2005a); Mokievich et al. (2007b). As we will show in Chapter 4, the consideration of a realistic treatment of line blocking/blanketing also turned out to be of crucial importance for addressing the formation mechanism that produces emission at N III $\lambda\lambda$ 4634-4640-4642.

2.3 A description of the atmospheric code FASTWIND

For this work we used a new, updated version (v10.1, see below) of the atmospheric code FASTWIND (see Santolaya-Rey et al. 1997 and Puls et al. 2005 for previous versions), developed by J. Puls and co-workers at the University Observatory Munich (USM) and collaborators from the Instituto de Astrofísica de Canarias (IAC).

FASTWIND calculates theoretical spectra of blue massive stars under the conditions of NLTE, spherical symmetry, line-blanketing, and mass-loss. The atmospheric code has been designed for optical/IR spectroscopic analysis of ‘normal’ hot stars with $T_{\text{eff}} \geq 8,500$ K (spectral types A to O). The synthetic spectra are calculated in a two-step process:

- (i) At first, FASTWIND calculates the atmospheric structure and solves the NLTE rate equations. To set up the atmospheric stratification, the code adopts a smooth transition between an analytical wind structure, described by a β -velocity law (Eq. 2.11), and a quasi-hydrostatic photosphere with a velocity law following from the equation of continuity (Eq. 2.12). This philosophy allows for the calculation of photospheric *and* wind lines with a similar degree of precision.

FASTWIND calculates the NLTE occupation numbers using a different treatment for the so-called explicit elements, which are used as diagnostic tools for quantitative spectroscopy, and the background elements, which are used to determine the background radiation field, accounting for line-blocking/blanketing effects. The explicit elements are typically H/He but also C, N, and O in early-type stars. They are treated by a full NLTE approach and a comoving frame radiative transfer. For these elements, a detailed description of all required atomic data in terms of a comprehensive model atom is needed. On the other hand, the rate equations for the background elements are calculated using some approximations. Most notably, a Sobolev line transfer was used for FASTWIND versions prior to v10. This approximate treatment agrees rather well with the ‘exact’ approach, but the derived occupation numbers are not well suited

for quantitative spectroscopy (Puls et al. 2005). The atomic data needed for the background elements are provided in a fixed way from the compilations by Pauldrach et al. (1998, 2001).

- (ii) The emergent profiles are calculated in a second step. Basically, the ‘formal integrals’ are solved using the occupation numbers from the explicit elements and the background opacities and emissivities from the converged NLTE solution.

The formal integral solves the radiative transfer on a radial micro-grid. Basic features are a separation between line and continuum transport, information about which line broadening mechanism needs to be applied (most important: Stark- and Voigt broadening), and, if necessary, a consistent treatment of non-coherent electron scattering. As for the atomic data for explicit elements, an external input file with all corresponding information needs to be provided.

2.3.1 FASTWIND v10.1

The current version of FASTWIND incorporates a variety of updates and improvements compared with previous versions. The most important ones are briefly described in the following.

As stated above, the background elements have been treated by means of the Sobolev approximation in previous versions. Although this is reasonable in the wind regime, the Sobolev approximation becomes doubtful in regions where the velocity field is strongly curved, which is the case in the transition zone between photosphere and wind. It has been checked that the induced errors are not important for the background radiation field, but they can have a certain influence on the temperature structure. Applying the Sobolev approximation in regions with a strong velocity field curvature results, on average, in too highly populated upper levels of line transitions (see, e.g., Santolaya-Rey et al. 1997). In turn, this leads to overestimated heating rates, which can result in too high temperatures in the transition region (and sometimes even below). To avoid this problem, the new FASTWIND version also treats the most important lines from the background elements in the comoving frame.

A second modification refers to the *photospheric* line acceleration. So far, this quantity (which is important for the photospheric density stratification – higher line acceleration, lower density) has been calculated from the Rosseland opacities, which is strictly justified only at high optical depths. In the new version, an additional iteration cycle for calculating the photospheric structure is performed, now by using the *flux-weighted* mean from the current NLTE opacities.

By calculating a large grid of OB-star models, and comparing with solutions from the previous FASTWIND version, it turned out that both improvements affect mostly dwarfs/giants in the effective temperature range $30 \text{ kK} \leq T_{\text{eff}} \leq 35 \text{ kK}$. In particular the optical He II lines become stronger, mostly because of the somewhat lower (electron-) densities. Interestingly, this is just the domain where previous FASTWIND solutions showed the strongest deviations from other codes (Simón-Díaz & Stasińska, 2008). The new structures excellently agree with results from, e.g., TLUSTY (Hubeny 1988; Hubeny & Lanz 1995). For dwarfs/giants with effective temperatures outside the ‘problematic’ region, and for all supergiants, the differences to previous results from earlier FASTWIND versions are small.

The last important improvement concerns the implementation of dielectronic recombination, both for the background and the explicit elements. We refer to Chapter 4 for a detailed description of the implementation process.

2.3.2 Application of FASTWIND

The major advantage of FASTWIND compared with other atmospheric codes with rather similar characteristics (e.g., CMFGEN, Hillier & Miller 1998; WM-basic, Pauldrach et al. 2001) is that it performs faster calculations. The parameter space to be investigated within the analysis of even one star is large, comprising effective temperature T_{eff} , gravity $\log g$, mass-loss rate \dot{M} , terminal velocity v_{∞} , velocity field parameter β , individual abundances, and global background metallicity Z . The need to obtain satisfactory fits for all diagnostic lines demands the calculation of model-grids, comprising large number of models, and therefore, involving an immense computational effort. Moreover, large surveys of hundreds of massive stars have been performed during the past years (e.g., the VLT-FLAMES survey of massive stars, Evans et al. 2006; the VLT-FLAMES Tarantula survey, Evans et al. 2010; the IACOB project, Simón-Díaz et al. 2011). All these surveys are intended to derive reliable stellar/wind parameters owing to sufficient statistics, provided by the large number of objects involved. Such an objective becomes only possible when using considerably fast codes, such as FASTWIND. Indeed, all O- and early B-stars from the VLT-FLAMES survey have been analyzed by means of quantitative hydrogen and helium line spectroscopy using this code (Mokiem et al. 2006, 2007a). Note that within the present work we re-analyze the former LMC O- and early B-star sample, using also nitrogen line spectroscopy (Chapter 5), and provide nitrogen abundances for the largest O-star sample analyzed so far. Regarding future work, also the O-stars from the VLT-FLAMES Tarantula and the IACOB survey will be analyzed by FASTWIND, following the prospects opened by our work.

Chapter 3

Model atoms for NLTE line formation computations in stellar atmospheres – A nitrogen model atom

3.1 Construction of a comprehensive model atom

A model atom is an approximation to the quantum-mechanical system of a real atom, and its interaction with radiation and with other particles in a plasma. Therefore, it is a compilation of atomic input data required for the numerical solution of a given NLTE problem. Basically, a model atom comprises information about (i) its structure, i.e., energy levels, statistical weights, and ionization potentials, and (ii) a description of the transitions between individual states, i.e., oscillator strengths, cross-sections for photo- and collisional ionization/excitation, etc.

In the following, we briefly discuss all different ingredients needed for the construction of a comprehensive model atom. For a more detailed description of the necessary steps, we refer to Przybilla (2010).

3.1.1 Model atom structure

Which ions should be included?

To study certain NLTE problems, the effective temperature is the fundamental parameter that determines which ions should be included in a model atom. The main ionization stage of the target species should be fairly represented, together with two or three minor ionic species. For instance, for an O4 dwarf ($T_{\text{eff}} \sim 45$ kK), the major ionization stage of nitrogen in the line-formation region is typically N IV but features of minor species such as N III (and to a lesser extent N V) are usually present. Therefore, a comprehensive nitrogen model atom designed to quantitatively study these kind of objects should include N III/N IV/N V plus the ground level of N VI. The inclusion of the latter simplified ion is intended to consider important ionizations/recombinations from/to N V. However, this approximation is only justified as long as there is a large energy gap between the ground state and the first excited level of the uppermost ion, to safely ignore transitions between excited N VI levels.

Number of levels

In order to keep a model atom robust, for each model ion it is recommended to include levels that are energetically higher than the minimum energy necessary to cope with a given problem. This ensures that the population of crucial levels involved in the problem are accurately represented, e.g., with respect to cascading processes involving high lying levels. In addition, another criterion concerning the inclusion of levels is related to the convergence of the behavior of departure coefficients, b_i , for increasing model complexity. Models with a low number of levels can show a different behavior at the line-formation region, resulting in inaccurate predictions, see Sigut & Lester (1996).

Another important consideration is that for many elements fine-structure states of a term may safely be combined into one level representing a ‘packed’ term with appropriate statistical weight. This approximation is well suited for levels that are fairly represented by LS-coupling. Sub-levels with small energy difference are strongly coupled by collisions, i.e., they are in relative LTE to each other. For levels with higher excitation energies it is also suggested to pack them since, in general, the energy separations of terms decrease with increasing principal quantum number n . Using this approximation, we ensure that the number of explicit NLTE levels to be treated in the complete model atom is not extremely large, even if we consider several ionization stages simultaneously. Otherwise, the execution times for the NLTE line-formation would become excessive, and special precautions were necessary to avoid numerical instabilities.

3.1.2 Input atomic data

As already mentioned in Chapter 2, the rate-equations *for all levels* n_i have to be solved in parallel with the equations of radiative transfer for *all required frequencies*. To accurately determine the level populations, we basically need a good knowledge of the local temperatures and particle densities, the non-local radiation field, accurate cross-sections, and all transitions between atomic states.

The two first items depend on the model atmosphere used for the NLTE calculations (see Chapter 2), whereas the remaining ones are related to the model atoms for the species involved in the calculations. So far, only a small amount of atomic data could be determined experimentally, and the bulk of the atomic data is provided from theoretical calculations, via *ab-initio* methods. Large databases of transition probabilities and cross-sections for photoionization and excitation via electron impact are available for the community, provided, e.g., by the OPACITY Project (OP, Seaton 1987; Seaton et al. 1994) and the IRON Project (IP; Hummer et al. 1993). *Ab-initio* data for radiative processes are usually available for transitions between levels up to $n \leq 10$. For excitation via electron collisions, explicit data are scarce, typically covering transitions up to $n \leq 4$, and biased towards selected ions of light elements and iron. The remainder of the data has to be calculated by means of different approximations.

In the following, we concentrate on the basic processes that should be considered for the construction of a comprehensive model atom, together with various approximations used for the implementation.

Radiative processes

The non-local character of the radiation field drives the stellar plasma to NLTE conditions, coupling the thermodynamic state of the plasma at different layers in the stellar atmosphere. Only specific radiative transitions are usually allowed. They obey selection rules, which describe the conditions

under which a radiative transition is permitted, e.g., electric dipole transitions between states from different spin systems are not allowed.

Radiative bound-bound transitions. The absorption/emission of photons can lead to excitations/de-excitations of electrons within an ion/atom, giving rise to spectral lines. The strength of the spectral lines is mainly determined by the number of absorbers (or emitters) and the line absorption cross-sections, which is given by

$$\alpha_{ij} = \frac{\pi e^2}{m_e c} f_{ij} \phi(\nu), \quad (3.1)$$

where e is the electron charge, m_e the electron mass, f_{ij} the oscillator strength, and $\phi(\nu)$ the line absorption profile. To calculate the contribution of radiative bound-bound transitions to the radiative rates, only the oscillator strengths of the transitions need to be provided as input atomic data.

Radiative bound-free transitions. Photoionization is the process in which an ion absorbs a photon with enough energy to excite a bound electron beyond the ionization threshold, leading to an ion with a higher ionization stage. The inverse process is the recombination.

Photoionization cross-sections are usually taken from *ab-initio* data from OP and IP. These cross-sections are typically computed by the R-matrix method using the close-coupling approximation and contain complex resonance structures (Seaton 1987). These resonances are either produced by autoionizing Rydberg series states or by double excited states, which produce the wide PEC (Photo-Excitation of the Core) resonances that are related to the dielectronic recombination processes, see below.

For excited levels with missing detailed data, ‘smooth’ (resonance free) photoionization cross-sections can be used, provided in terms of least square fittings from the non-linear form of the cross-section by Seaton (1958),

$$\alpha_{ik}(\nu) = \alpha_0 [\beta (\nu_0/\nu)^s + (1 - \beta) (\nu_0/\nu)^{s+1}] \quad (3.2)$$

with α_0 the cross-section at the threshold ν_0 , and fit parameters β and s .

Collisional processes

Inelastic collisions with particles can lead to excitation and ionization of atoms/ions as well. One of the most important characteristics of the collisional processes is that they drive the stellar plasma towards LTE conditions, because the velocity distribution in stellar atmospheres is usually Maxwellian. Typically, only electron collisions are considered since the thermal velocity and hence the collision frequency of heavy particles is much smaller.¹ Unlike radiative processes, collisions do not obey any selection rule. Therefore, collisions between all states within an atom/ion are possible *and need to be accounted for*.

¹ This is not the case for cool stars, especially for metal-poor objects, where hydrogen collisions may become the dominant thermalization process, which must not be neglected.

Collisional bound-bound transitions. The collisional rates are defined in terms of the effective collision strength via

$$C_{ij} = \frac{8.631 \cdot 10^{-6}}{T^{1/2} g_i} n_e e^{-u_0} \gamma. \quad (3.3)$$

The effective collision strength is

$$\gamma_{ij} = \int_0^\infty \Omega_{ij} \exp\left(-\frac{E_j}{kT}\right) d\left(\frac{E_j}{kT}\right), \quad (3.4)$$

where E_j is the electron's kinetic energy after the excitation has occurred, and Ω_{ij} is the collision strength, first introduced by Seaton (1953). It is a dimensionless quantity defined by the ratio of two areas (the cross-section Q and the square of the appropriate de Broglie wavelength), weighted by the statistical weight of the transition, g_i ,

$$\Omega_{ij} = \frac{4\pi g_i}{\lambda_i^2} Q(i \rightarrow j). \quad (3.5)$$

Thus, the *effective* collision strength is the thermally averaged collision strength Ω_{ij} .

Only few *ab-initio* data of collisional excitations are available, usually up to levels with $n = 3 \dots 4$, in terms of tabulations of the effective collision strength. For the bulk of the possible collisional transitions, approximations need to be used which give, at best, order-of-magnitude estimates. In the following, we refer to the two most commonly used ones:

- (i) In the radiatively permitted case, the collision rate C_{ij} might be calculated on the assumption that the collision cross-section is proportional to the oscillator strength of the transition. This scaling is the base of the van Regemorter (1962) approximation,

$$C_{ij} = 5.465 \cdot 10^{-11} n_e T^{1/2} [14.5 f_{ij} (I_H/E_0)^2] u_0 \exp(-u_0) \Gamma(u_0), \quad (3.6)$$

where E_0 is the threshold energy of the process, $u_0 = E_0/kT$, f_{ij} is the oscillator strength, I_H is the ionization energy of hydrogen, and $\Gamma(u_0)$ is the maximum of a slowly-varying function of temperature,

$$\Gamma(u_0) = \max[\bar{g}, 0.276 \exp(u_0) E_1(u_0)]. \quad (3.7)$$

The parameter \bar{g} is about 0.7 for transitions $n_l \rightarrow n_l'$, and about 0.2 for transitions $n_l \rightarrow n_l'$, $n' \neq n$. $E_1(x)$ is the first exponential integral.

- (ii) For the radiatively forbidden case, Allen (1973) provides a semi-empirical formula,

$$\begin{aligned} C_{ij} &= 5.465 \cdot 10^{-11} n_e T^{1/2} \exp(-u_0) \Gamma, \\ \Gamma &= \frac{\Omega}{g_i} \frac{I_H}{kT}, \end{aligned} \quad (3.8)$$

with the collision strength Ω (usually) being set to unity.

Collisional bound-free transitions. Collisional ionizations can² become a dominant factor for the coupling of high-lying levels to the continuum, whilst for the ground-state and low-lying levels they are rather inefficient because only few electrons have energies high enough to overcome the threshold for the reaction.

Cross-sections for ionization by electron impact are even less quantitatively known than the atomic data for the previously discussed processes. Experimentally, only ionization from the ground-state are usually covered, whilst on the theoretical side the situation is not much better. Nevertheless, reasonable approximations can be applied in the majority of cases. Collisional ionization cross-sections are usually calculated in terms of the photoionization cross-section at threshold, α_0 , using the Seaton (1962) formula. This yields a collisional rate

$$C_{ik} = 1.55 \cdot 10^{13} \alpha_0 \bar{g} n_e \frac{e^{-u_0}}{u_0 T^{1/2}}, \quad (3.9)$$

where the \bar{g} -factor is Z (charge) dependent, being 0.1, 0.2, and 0.3 for $Z=1$, $Z=2$, and $Z \geq 3$, respectively.

Other processes

For the construction of comprehensive model atoms to be used within the analysis of stellar atmospheres, the consideration of the above processes is sufficient in most cases.³ However, there are other processes that might be relevant in certain cases and might need to be considered as well, e.g., dielectronic recombination for the N III λ 4634-4640-4642 emission line formation problem, see Chapter 4.

Autoionization/Dielectronic recombination. If two electrons are excited within a complex atom/ion with several electrons, they can give rise to states with energies both below and above the ionization potential. States above the ionization limit, under certain selection rules, may preferentially autoionize to the ground state of the ion plus a free electron.

Thus the ionization from an initial bound state $A(i)$ to an ionized final state $A^+(f)$ can occur either directly,

$$h\nu_1 + A(i) \rightarrow A^+(f) + e^-, \quad (3.10)$$

or by a (different) transition from the initial bound state $A(i)$ to an intermediate doubly excited state \bar{A} above the ionization potential that finally autoionizes to $A^+(f)$.

$$h\nu_2 + A(i) \rightarrow \bar{A} \rightarrow A^+(f) + e^-. \quad (3.11)$$

Photoionizations of the latter kind are produced by strong resonances, involving Photo-Excitation of the Core (PEC) resonances (Yan & Seaton, 1987). In this case, the photoionization occurs due to intermediate resonant state(s) in the core of the atom leading to autoionization rather than in the direct ionization of an excited electron. In this respect, PEC resonances are particularly strong, because they correspond to a single electron transition in which the outer electron is a spectator and does not change, giving rise to wide resonances in the total photo-ionization cross-section (see Fig. 4.2), which are produced by the strong dipole coupling that exists among the involved states.

² For high enough densities.

³ For cool stars, hydrogen collisions are needed as well.

The inverse process is also possible, if an ion collides with an electron of sufficient energy, leading to a doubly excited state. Generally, the compound state will immediately autoionize again (large autoionization probabilities, $A^a \sim 10^{13} - 10^{14} \text{ s}^{-1}$). In some cases, however, a stabilizing transition occurs, in which one of the excited electrons, usually the one in the lower state, radiatively decays to the lowest available quantum state. This process is the dielectronic recombination, and can be summarized as the capture of an electron by the target leading to an intermediate doubly excited state that stabilises by emitting a photon rather than an electron.

Charge exchange. These reactions are collisional processes in which one or more electrons are transferred between atoms/ions,



with Y usually being H or He. This process is of major importance for cool stars.

3.2 The nitrogen model atom – Implementation into FASTWIND

In the following, we describe the implementation of a new nitrogen model atom into the FASTWIND database. The complete nitrogen model atom comprises the ionization stages N II to N V. The corresponding N II model ion was adapted from a previous one, developed by Becker & Butler (1989). Both N IV and N V model ions were adapted from the WM-basic atomic database (Pauldrach et al., 1994).

In the present work, we had no intention to develop a ‘perfect’ N II model, since most of our analyses deal with O-star spectra where N II becomes invisible, and particularly because N. Przybilla and co-workers have already constructed such a model (based on an earlier version, see Przybilla & Butler 2001) which will be incorporated into our code after release. However, a series of tests were performed to ensure the goodness of the latter model ion, see Appendix A. Different tests regarding N III/N IV/N V model ions are performed in Chapters 4, 5, and 6.

3.2.1 N II model ion

For the N II model ion, we considered 50 LS-coupled terms, up to principal quantum number $n = 4$ and angular momentum $l = 3$, where all fine-structure sublevels have been packed⁴. Detailed information about the selected levels is provided in Table 3.1. Three different spin systems are included (singlet, triplet, and quintet), and all of them are treated simultaneously. A Grotrian diagram for each system is presented in Fig. 3.1.

We account for some hundred permitted electric dipole radiative transitions. For the bulk of the transitions, oscillator strengths were taken from calculations performed by Becker & Butler (1989). However, for some transitions related to strong N II lines oscillator strengths were taken from NIST.⁵ Radiative intercombinations i.e., transitions between levels from different spin-systems, were neglected.

⁴ When calculating the final synthetic profiles we use, when necessary, the un-packed levels by assuming that n_i/g_i – with occupation number n_i and statistical weight g_i – is similar for each sub-level within a packed level, due to strong collisional coupling.

⁵ <http://www.nist.gov/physlab/data/asd.cfm>, firstly described in Kelleher et al. (1999)

Table 3.1: Electronic configurations and term designations of our N II model ion. The level numbers correspond to the entries in the Grotrian diagrams in Fig. 3.1 for the singlet, triplet, and quintet terms.

#	Configuration	Desig.	#	Configuration	Desig.
1	$1s^2 2s^2 2p^2$	$2p^2 \ ^3P$	26	$1s^2 2s^2 2p(2P^0) 4p$	$4p \ ^1P$
2	$1s^2 2s^2 2p^2$	$2p^2 \ ^1D$	27	$1s^2 2s^2 2p(2P^0) 4p$	$4p \ ^3D$
3	$1s^2 2s^2 2p^2$	$2p^2 \ ^1S$	28	$1s^2 2s^2 2p(2P^0) 4p$	$4p \ ^3P$
4	$1s^2 2s 2p^3$	$2p^3 \ ^5S^0$	29	$1s^2 2s^2 2p(2P^0) 4p$	$4p \ ^3S$
5	$1s^2 2s 2p^3$	$2p^3 \ ^3D^0$	30	$1s^2 2s^2 2p(2P^0) 4p$	$4p \ ^1D$
6	$1s^2 2s 2p^3$	$2p^3 \ ^3P^0$	31	$1s^2 2s 2p^2(4P) 3s$	$3s' \ ^5S$
7	$1s^2 2s 2p^3$	$2p^3 \ ^1D^0$	32	$1s^2 2s^2 2p(2P^0) 4p$	$4p \ ^1S$
8	$1s^2 2s^2 2p(2P^0) 3s$	$3s \ ^3P^0$	33	$1s^2 2s^2 2p(2P^0) 4d$	$4d \ ^3F^0$
9	$1s^2 2s^2 2p(2P^0) 3s$	$3s \ ^1P^0$	34	$1s^2 2s^2 2p(2P^0) 4d$	$4d \ ^1D^0$
10	$1s^2 2s 2p^3$	$2p^3 \ ^3S^0$	35	$1s^2 2s^2 2p(2P^0) 4d$	$4d \ ^3D^0$
11	$1s^2 2s^2 2p(2P^0) 3p$	$3p \ ^1P$	36	$1s^2 2s^2 2p(2P^0) 4d$	$4d \ ^3P^0$
12	$1s^2 2s^2 2p(2P^0) 3p$	$3p \ ^3D$	37	$1s^2 2s^2 2p(2P^0) 4f$	$4f \ ^1F$
13	$1s^2 2s 2p^3$	$2p^3 \ ^1P^0$	38	$1s^2 2s^2 2p(2P^0) 4f$	$4f \ ^3F$
14	$1s^2 2s^2 2p(2P^0) 3p$	$3p \ ^3S$	39	$1s^2 2s^2 2p(2P^0) 4d$	$4d \ ^1F^0$
15	$1s^2 2s^2 2p(2P^0) 3p$	$3p \ ^3P$	40	$1s^2 2s^2 2p(2P^0) 4f$	$4f' \ ^3G$
16	$1s^2 2s^2 2p(2P^0) 3p$	$3p \ ^1D$	41	$1s^2 2s^2 2p(2P^0) 4d$	$4d \ ^1P^0$
17	$1s^2 2s^2 2p(2P^0) 3p$	$3p \ ^1S$	42	$1s^2 2s^2 2p(2P^0) 4f$	$4f' \ ^1G$
18	$1s^2 2s^2 2p(2P^0) 3d$	$3d \ ^3F^0$	43	$1s^2 2s^2 2p(2P^0) 4f$	$4f' \ ^3D$
19	$1s^2 2s^2 2p(2P^0) 3d$	$3d \ ^1D^0$	44	$1s^2 2s^2 2p(2P^0) 4f$	$4f' \ ^1D$
20	$1s^2 2s^2 2p(2P^0) 3d$	$3d \ ^3D^0$	45	$1s^2 2s 2p^2(4P) 3s$	$3s' \ ^3P$
21	$1s^2 2s^2 2p(2P^0) 3d$	$3d \ ^3P^0$	46	$1s^2 2s 2p^2(4P) 3p$	$3p' \ ^3S^0$
22	$1s^2 2s^2 2p(2P^0) 3d$	$3d \ ^1F^0$	47	$1s^2 2s 2p^2(4P) 3p$	$3p' \ ^5D^0$
23	$1s^2 2s^2 2p(2P^0) 3d$	$3d \ ^1P^0$	48	$1s^2 2s 2p^2(4P) 3p$	$3p' \ ^5P^0$
24	$1s^2 2s^2 2p(2P^0) 4s$	$4s \ ^3P^0$	49	$1s^2 2s 2p^2(4P) 3p$	$3p' \ ^3D^0$
25	$1s^2 2s^2 2p(2P^0) 4s$	$4s \ ^1P^0$	50	$1s^2 2s 2p^2(4P) 3p$	$3p' \ ^5S^0$

Roughly one thousand collisional bound-bound transitions were considered, with corresponding rates using the van Regemorter approximation in the radiatively permitted case (Eq. 3.6) and following the semi-empirical expression by Allen (1973) in the forbidden one (Eq. 3.8). Radiative ionization cross-sections to the ground state and the first and second excited states of N III have been derived by Becker & Butler (1989), and adapted to the representation suggested by Seaton (1958), see Eq. 3.2. Collisional ionization cross-sections were calculated using the Seaton (1962) formula (Eq. 3.9).

3.2.2 N III model ion

Our N III model ion consists of 41 levels. LS-coupled terms up to principal quantum number $n = 6$ and angular momentum $l = 4$ have been considered. Table 3.2 provides detailed information about the selected levels. Like for the N II model ion, all fine-structure sub-levels have been packed into one LS-coupled term. Two spin systems (doublet and quartet) are present and treated simultaneously. A

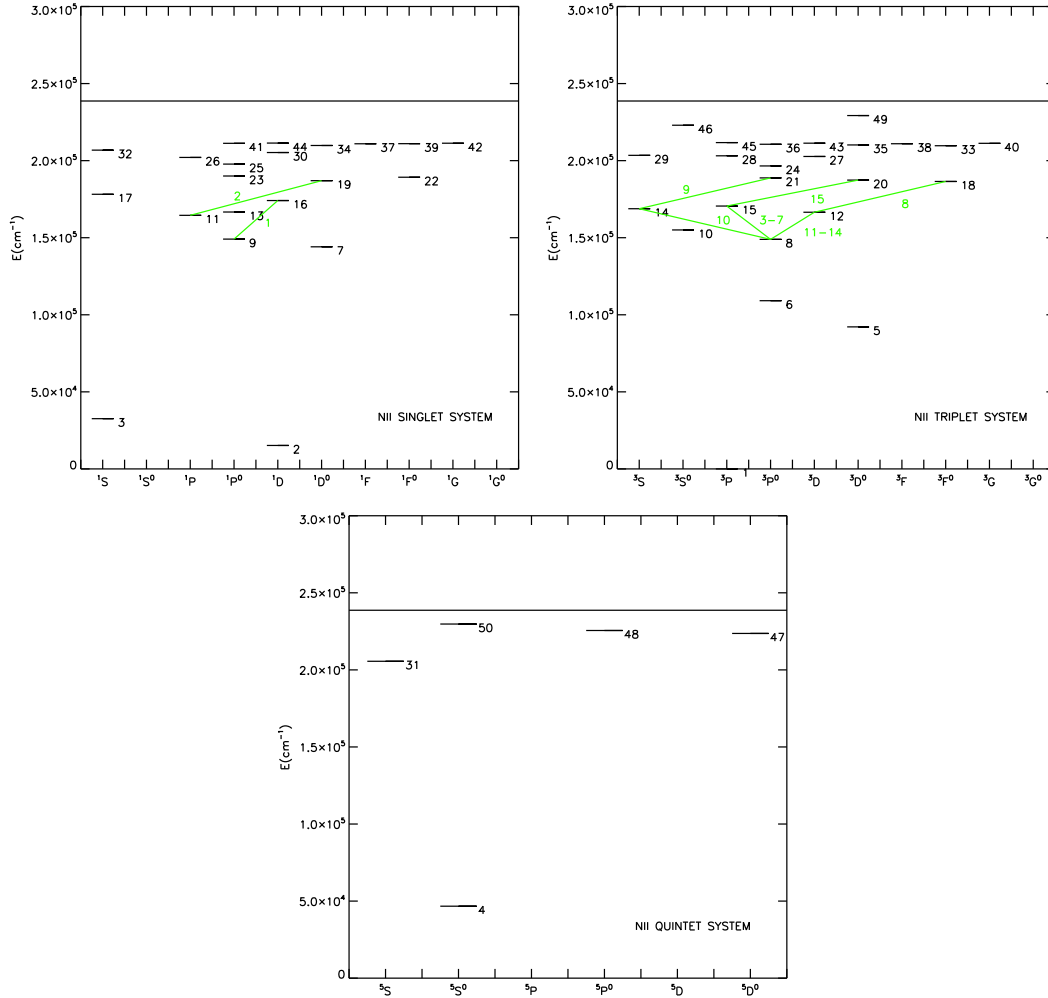


Figure 3.1: Grotrian diagrams for the N II singlet (upper panel; left), triplet (upper panel; right) and quintet (lower panel) systems. Level designations refer to Table 3.1. Important optical transitions are indicated by green lines, and numbers refer to entries in Table 3.5.

Grotrian diagram for each system is presented in Fig. 3.2.

All allowed electric dipole radiative transitions between the 41 levels are accounted for, giving rise to 193 transitions. Unlike for our (simplified) N II model, we account also for radiative intercombination transitions between the two spin system, with a total of 357 radiative bound-bound transitions. Oscillator strengths have been taken from NIST when possible, and else from the WM-basic database.⁶ NIST N III data are mostly from Bell et al. (1995), and from OPACITY project calculations by Fernley et al. (1999).

⁶ See Pauldrach et al. (1994). In brief, the atomic structure code SUPERSTRUCTURE (Eissner & Nussbaumer 1969; Eissner 1991) has been used to calculate all bound state energies in LS and intermediate coupling as well as related atomic data, particularly oscillator strengths including those for stabilizing transitions.

Table 3.2: Electronic configurations and term designations of our N III model ion. The level numbers correspond to the entries in the Grotrian diagrams, Fig. 3.2.

#	Configuration	Desig.	#	Configuration	Desig.
1	$1s^2 2s^2(1S) 2p$	$2p^2 P^0$	22	$1s^2 2s 2p(3P^0) 3p$	$3p^2 D$
2	$1s^2 2s 2p^2$	$2p^2 4P$	23	$1s^2 2s 2p(3P^0) 3p$	$3p^2 S$
3	$1s^2 2s 2p^2$	$2p^2 2D$	24	$1s^2 2s 2p(3P^0) 3d$	$3d^2 F^0$
4	$1s^2 2s 2p^2$	$2p^2 2S$	25	$1s^2 2s 2p(3P^0) 3d$	$3d^2 D^0$
5	$1s^2 2s 2p^2$	$2p^2 2P$	26	$1s^2 2s^2(1S) 5s$	$5s^2 S$
6	$1s^2 2p^3$	$2p^3 4S^0$	27	$1s^2 2s 2p(3P^0) 3d$	$3d^2 D^0$
7	$1s^2 2p^3$	$2p^3 2D^0$	28	$1s^2 2s 2p(3P^0) 3d$	$3d^2 P^0$
8	$1s^2 2s^2(1S) 3s$	$3s^2 S$	29	$1s^2 2s^2(1S) 5p$	$5p^2 P^0$
9	$1s^2 2p^3$	$2p^3 2P^0$	30	$1s^2 2s 2p(3P^0) 3d$	$3d^2 F^0$
10	$1s^2 2s^2(1S) 3p$	$3p^2 P^0$	31	$1s^2 2s^2(1S) 5d$	$5d^2 D$
11	$1s^2 2s^2(1S) 3d$	$3d^2 D$	32	$1s^2 2s 2p(3P^0) 3d$	$3d^2 P^0$
12	$1s^2 2s 2p(3P^0) 3s$	$3s^2 4P^0$	33	$1s^2 2s^2(1S) 5f$	$5f^2 F^0$
13	$1s^2 2s 2p(3P^0) 3s$	$3s^2 2P^0$	34	$1s^2 2s^2(1S) 5g$	$5g^2 G$
14	$1s^2 2s^2(1S) 4s$	$4s^2 S$	35	$1s^2 2s^2(1S) 6p$	$6p^2 P^0$
15	$1s^2 2s 2p(3P^0) 3p$	$3p^2 2P$	36	$1s^2 2s^2(1S) 6s$	$6s^2 S$
16	$1s^2 2s 2p(3P^0) 3p$	$3p^2 4D$	37	$1s^2 2s 2p(1P^0) 3s$	$3s^2 2P^0$
17	$1s^2 2s^2(1S) 4p$	$4p^2 P^0$	38	$1s^2 2s^2(1S) 6d$	$6d^2 D$
18	$1s^2 2s 2p(3P^0) 3p$	$3p^2 4S$	39	$1s^2 2s^2(1S) 6f$	$6f^2 F^0$
19	$1s^2 2s 2p(3P^0) 3p$	$3p^2 4P$	40	$1s^2 2s^2(1S) 6g$	$6g^2 G$
20	$1s^2 2s^2(1S) 4d$	$4d^2 D$	41	$1s^2 2s 2p(3P^0) 4s$	$4s^2 4P^0$
21	$1s^2 2s^2(1S) 4f$	$4f^2 F^0$			

With respect to bound-bound collisional transitions with rate coefficients C_{ij} , we account for roughly one thousand transitions between all levels. Three different implementations have been used.

- (i) For *all* collisions between the 11 lowest levels, $2s^2 2p$, $2s 2p^2$, $2p^3$, and $2s^2 3l$ ($l = s, p, d$), (including doublet and quartet terms), we use the collision strengths as calculated by Stafford et al. (1994), from the *ab-initio* R-matrix method (Berrington et al., 1987). These authors provide analytic fits to the effective collision strengths, γ , as a result of the collisions between all fine structure levels. The data have been fitted to a Chebyshev polynomial expansion of the form

$$\ln(\gamma) = \frac{1}{2}a_0 + \sum_{n=1}^N a_n T_n(x), \quad (3.13)$$

where T_n is the Chebyshev polynomial of the first kind of degree n and x is

$$x = 0.542519 \ln(T_e) - 5.620738 \quad (3.14)$$

when T_e is expressed in units of [K].

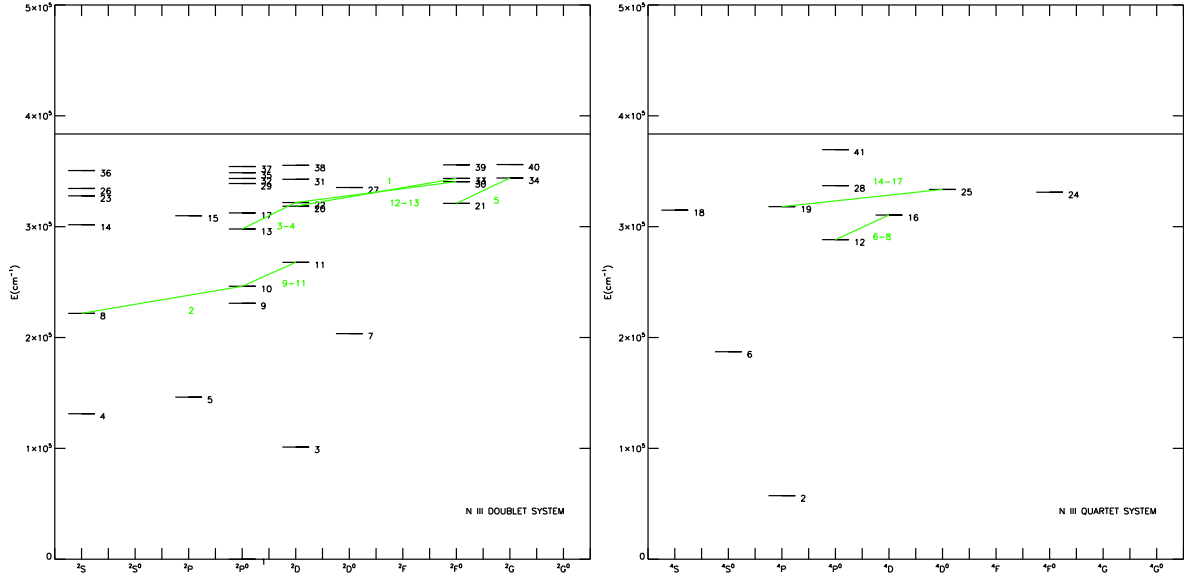


Figure 3.2: As Fig. 3.1, but for the N III doublet (left) and quartet (right) system. Level numbers refer to Table 3.2. Important optical transitions are indicated by green lines, and numbers refer to Table 3.5.

To adapt the data to our level structure, for each of our *packed* transitions among the LS-coupled terms the effective collision strengths for all corresponding fine structure components need to be summed up. Finally, the collision strength is related to the collisional rate coefficient via Eq. 3.3.

- (ii) For most of the optically allowed transitions between higher levels (i.e., from level 11 as the lower one on), the van Regemorter approximation (Eq. 3.6) is applied.
- (iii) For the optically forbidden transitions and the remainder of optically allowed ones, the semi-empirical formula from Allen (Eq. 3.8) is used.

Photoionization cross-sections have been taken from the OPACITY Project online atomic database TOPbase⁷ (Cunto & Mendoza 1992). These cross-sections have been computed by Fernley et al. (1999) by the R-matrix method using the close-coupling approximation and contain complex resonance structures, particularly PEC resonances (see Sect. 3.1.2).

For excited N III levels with no OPACITY data available ($5g\ ^2G$ and $6g\ ^2G$) and in those cases where we apply the ‘explicit’ method for dielectronic recombination (see Chapter 4), ‘smooth’ photoionization cross-sections are used, provided in terms of the Seaton (1958) approximation by Eq. 3.2. The required parameters are taken from the WM-basic atomic database. For most transitions, a reasonable consistency between these data and data from the OPACITY project has been found, cf. Fig. 4.2.

The most important dielectronic recombination and reverse ionization processes are treated by the ‘explicit’ method (in particular, recombination to the strategic 3d level). Corresponding atomic data (wavelengths and oscillator strengths of the stabilizing transitions) are from the WM-basic atomic database as well.

⁷ <http://cdsweb.u-strasbg.fr/topbase/topbase.html>

Table 3.3: Electronic configurations and term designations of our N IV model ion. The level numbers correspond to the entries in the Grotrian diagrams in Fig. 3.3.

#	Configuration	Desig.	#	Configuration	Desig.
1	$1s^2 2s^2$	$2s^2 \ ^1S$	26	$1s^2 2p(^2P^0_{3/2}) 3d$	$3d' \ ^1F^0$
2	$1s^2 2s 2p$	$2p \ ^3P^0$	27	$1s^2 2s 4p$	$4p \ ^1P^0$
3	$1s^2 2s 2p$	$2p \ ^1P^0$	28	$1s^2 2s 4d$	$4d \ ^3D$
4	$1s^2 2s 2p$	$2p \ ^3P$	29	$1s^2 2p(^2P^0_{3/2}) 3d$	$3d' \ ^3P^0$
5	$1s^2 2p^2$	$2p^2 \ ^1D$	30	$1s^2 2s 4d$	$4d \ ^1D$
6	$1s^2 2p^2$	$2p^2 \ ^1S$	31	$1s^2 2p(^2P^0_{3/2}) 3p$	$3p' \ ^1S$
7	$1s^2 2s 3s$	$3s \ ^3S$	32	$1s^2 2s 4f$	$4f \ ^3F^0$
8	$1s^2 2s 3s$	$3s \ ^1S$	33	$1s^2 2p(^2P^0_{3/2}) 3d$	$3d' \ ^1P^0$
9	$1s^2 2s 3p$	$3p \ ^1P^0$	34	$1s^2 2s 4f$	$4f \ ^1F^0$
10	$1s^2 2s 3p$	$3p \ ^3P^0$	35	$1s^2 2s 5s$	$5s \ ^3S$
11	$1s^2 2s 3d$	$3d \ ^3D$	36	$1s^2 2s 5s$	$5s \ ^1S$
12	$1s^2 2s 3d$	$3d \ ^1D$	37	$1s^2 2s 5p$	$5p \ ^3P^0$
13	$1s^2 2p(^2P^0) 3s$	$3s' \ ^3P^0$	38	$1s^2 2s 5p$	$5p \ ^1P^0$
14	$1s^2 2p(^2P^0_{3/2}) 3s$	$3s' \ ^1P^0$	39	$1s^2 2s 5d$	$5d \ ^3D$
15	$1s^2 2p(^2P^0_{1/2}) 3p$	$3p' \ ^1P$	40	$1s^2 2s 5d$	$5d \ ^1D$
16	$1s^2 2p(^2P^0) 3p$	$3p' \ ^3D$	41	$1s^2 2s 5g$	$5g \ ^1G$
17	$1s^2 2p(^2P^0_{3/2}) 3d$	$3d' \ ^3S$	42	$1s^2 2s 5g$	$5g \ ^3G$
18	$1s^2 2p(^2P^0_{1/2}) 3d$	$3d' \ ^1D^0$	43	$1s^2 2s 5f$	$5f \ ^3F^0$
19	$1s^2 2s 4s$	$4s \ ^1S$	44	$1s^2 2s 5f$	$5f \ ^1F^0$
20	$1s^2 2p(^2P^0) 3p$	$3p' \ ^3P$	45	$1s^2 2s 6s$	$6s \ ^3S$
21	$1s^2 2p(^2P^0) 3d$	$3d' \ ^3F^0$	46	$1s^2 2s 6s$	$6s \ ^1S$
22	$1s^2 2p(^2P^0_{3/2}) 3p$	$3p' \ ^1D$	47	$1s^2 2s 6p$	$6p \ ^3P^0$
23	$1s^2 2s 4p$	$4p \ ^3P^0$	48	$1s^2 2s 6p$	$6p \ ^1P^0$
24	$1s^2 2s 4s$	$4s \ ^3S$	49	$1s^2 2s 6d$	$6d \ ^3D$
25	$1s^2 2p(^2P^0) 3d$	$3d' \ ^3D^0$	50	$1s^2 2s 6g$	$6g \ ^3G$

Finally, the cross-sections for collisional ionization are derived as for the N II model ion, following the Seaton (1962) formula as given in Eq. 3.9.

3.2.3 N IV model ion

This model ion also consists of 50 LS-coupled terms, up to principal quantum number $n = 6$ and angular momentum $l = 4$, with all fine-structure sublevels packed into one term. Table 3.3 provides detailed information about the selected levels. Two spin systems (singlet and triplet) were treated simultaneously (Fig. 3.3). All allowed electric dipole radiative transitions between the 50 levels were considered, as well as radiative intercombinations, with a total of 520 transitions. Corresponding oscillator strengths were drawn from either NIST when available or otherwise from the WM-basic database. Furthermore, we considered roughly one thousand bound-bound collisional transitions be-

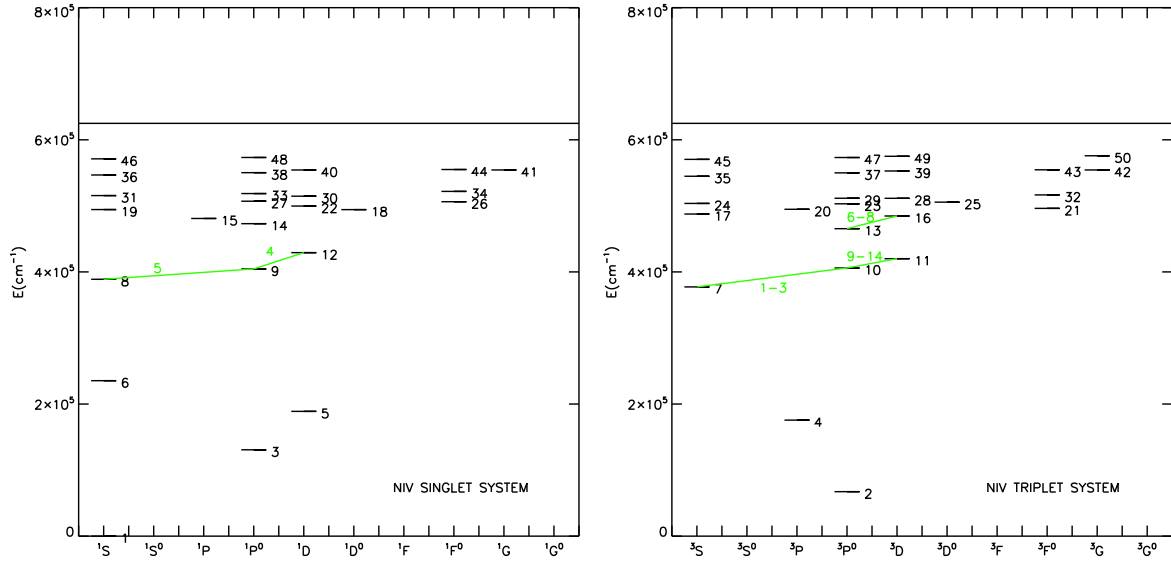


Figure 3.3: As Fig. 3.1, but for the N IV singlet (left) and triplet (right) system. Level numbers refer to Table 3.3. Important optical transitions are indicated by green lines, and numbers refer to entries in Table 3.5.

tween all levels, with effective collision strengths among the 12 lowest LS-states, $2s^2$, $2s\ 2p$, $2p^2$, and $2s\ 3l$, ($l=s,p,d$), comprising singlet and triplet terms, from R-matrix computations by Ramsbottom et al. (1994). These authors provide analytic fits to the effective collision strengths, γ , for collisions between all fine structure levels. Remaining transitions without detailed data as well as the collisional ionizations were treated as in N II.

Photoionization cross-sections were taken from calculations by Tully et al. (1990) from the OPACITY Project data. For excited levels without available OPACITY Project data ($5g\ ^1G$, $5g\ ^3G$, $6s\ ^1S$, and $6g\ ^3G$, see Table 3.3), resonance-free cross-sections were used, provided in terms of the Seaton (1958) approximation (Eq. 3.2) with parameters from the WM-basic database. Finally, the most important dielectronic recombination and reverse ionization processes were implicitly accounted for by means of exploiting the OPACITY Project photo cross-sections. Only for the few levels without these data we applied the ‘explicit’ method, using the stabilizing transitions on top of resonance-free photo cross-section (see Chapter 4), with corresponding data from WM-basic.

3.2.4 N v model ion

Our model of this lithium-like ion (one doublet spin system) consists of 27 levels, including LS-coupled and packed terms up to $n = 7$ and $l = 6$ (see Table 3.4 for details and Fig. 3.4 for a Grotrian diagram). All allowed electric dipole radiative transitions were accounted for, with a total number of 102 radiative bound-bound transitions and oscillator strengths from WM-basic. Collisional excitations and ionizations were treated as in N II, whilst photo cross-sections, in terms of the Seaton 1958 approximation (Eq. 3.2), were also taken from the WM-basic atomic database.

The resulting N II/III/IV/V model atom accounts for 178 LS-coupled energy levels, with more

Table 3.4: Electronic configurations and term designations of our N V model ion. The level numbers correspond to the entries in the Grotrian diagram Fig. 3.4.

#	Configuration	Desig.	#	Configuration	Desig.
1	1s ² 2s	2s ² S	15	1s ² 6s	6s ² S
2	1s ² 2p	2p ² P ⁰	16	1s ² 6p	6p ² P ⁰
3	1s ² 3s	3s ² S	17	1s ² 6d	6d ² D
4	1s ² 3p	3p ² P ⁰	18	1s ² 6f	6f ² F ⁰
5	1s ² 3d	3d ² D	19	1s ² 6g	6g ² G
6	1s ² 4s	4s ² S	20	1s ² 6h	6h ² H ⁰
7	1s ² 4p	4p ² P ⁰	21	1s ² 7s	7s ² S
8	1s ² 4d	4d ² D	22	1s ² 7p	7p ² P ⁰
9	1s ² 4f	4f ² F ⁰	23	1s ² 7d	7d ² D
10	1s ² 5s	5s ² S	24	1s ² 7f	7f ² F ⁰
11	1s ² 5p	5p ² P ⁰	25	1s ² 7g	7g ² G
12	1s ² 5d	5d ² D	26	1s ² 7h	7h ² H ⁰
13	1s ² 5f	5f ² F ⁰	27	1s ² 7i	7i ² I
14	1s ² 5g	5g ² G			

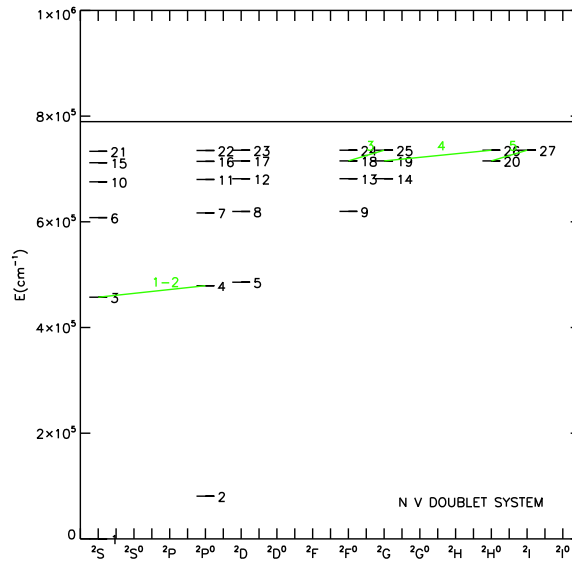


Figure 3.4: As Fig. 3.1, but for the N V model ion. Level numbers refer to Table 3.4. Important optical transitions are indicated by green lines, and numbers refer to entries in Table 3.5.

than 1100 radiative and more than 3800 collisional bound-bound transitions. To calculate the final synthetic profiles, we adopted Voigt profiles in the formal solution. Central wavelengths of the observed transitions are taken from NIST. Radiative damping parameters are from the Kurucz database,⁸ and collisional damping parameters (broadening by electron impact) are computed according to Cowley (1971).

3.3 Diagnostic nitrogen lines in the optical

Table 3.5 presents a set of 51 nitrogen lines visible in the optical (and adjacent) spectra of OB-stars, along with the position of potential blends. Included are the connected levels (for corresponding term designations, see Sect. 3.2) and multiplet numbers to provide an impression of how many independent lines are present. This set of lines (labeled by '+' in Table 3.5) is used for theoretical comparisons with different atmospheric codes (Chapters 4, 6 and Appendix A) as well as for analysis of stellar spectra by line profile fitting to observed spectra (Chapters 5 and 6).

Lines from N II (visible in the spectra of B and late O-stars) have been selected after careful comparisons with profiles calculated by N. Przybilla (priv. comm., see Appendix. A). Only one of the suggested lines, N II λ 3995, is completely isolated and remains uncontaminated even at high rotation rates. Moreover, this is one of the strongest N II lines located in the optical region, making it a good choice for deriving nitrogen abundances. Other useful lines are N II λ 5667 and λ 5679, where the former is moderately strong and the latter has roughly the same strength as N II λ 3995.

Prominent lines from N III, N IV, and N V are among the most well-known features in O-stars and can be used to infer nitrogen abundances as well as effective temperatures for the earliest subtypes from the reaction of the N IV/N V ionization equilibrium, see Chapters 5 and 6. In a similar line of reasoning, Walborn et al. (2002) used the N IV λ 4058 emission line in combination with N III λ 4634-4640-4642 to split the degenerate O3 spectral type (Walborn, 1971a) into three different types O2, O3, and O3.5, relying on the N IV/N III emission line ratio, see Chapter 6.

The set of N III lines can be split into five different groups. Lines that belong to the first group (#2,5,9-11 in Table 3.5), at λ 4097, 4379, and 4634-4640-4642 Å, are produced by cascade processes of the (doublet) series $1s^2 2s^2 nl$ with $n = 3, 4, 5$ and $l = s, p, d, f, g$, and additional (over-) population of the 3d level (level #11 in Table 3.2). The emission triplet at λ 4634-4640-4642 is typically used to discriminate O-stars with such line emission from pure absorption-line objects (Walborn 1971b). Seminal work carried out by Mihalas & Hummer (1973) suggested that emission at these lines is formed by a complex photospheric NLTE processes rather than by emission in an extended atmosphere. A deeper insight into this matter is provided in Chapter 4, where we also provide first predictions using state-of-the-art atmospheric codes. The second group (lines #6-8), λ 4510-4514-4518, results from transitions within the quartet system. We consider only the three strongest components of the corresponding multiplet, that are also the least blended ones. The third group (lines #1,3,4) represents three lines, at λ 4003, 4195, and 4200 Å, that are formed between higher lying levels within the doublet system. These lines are weaker than the ones from the previous two groups, but still worth to use them within a comparison of codes and also within a final abundance analysis. Note that N III λ 4195 and N III λ 4200 are located within the Stark-wing and the core of He II λ 4200, respectively, which requires a consistent analysis of the total line complex. Lines at λ 5320, 5327 Å (#12-13) and λ 6445, 6450, 6454, 6467 Å (#14-17) comprise the fourth and fifth group, respectively.

⁸ www.pmp.uni-hannover.de/cgi-bin/ssi/test/kurucz/sekur.html

The former set of lines is located in a spectral region that is rarely observed, and the latter comprises a multiplet from the quartet system, in the red part of the visual spectrum.

Table 3.5: Diagnostic nitrogen lines in the optical (and adjacent) spectrum of early B- and O-type stars, together with potential blends. Line numbers for N II, N III, N IV, and N V refer to important transitions as indicated in Figs. 3.1, 3.2, 3.3 and 3.4, respectively. Multiplet numbers for N II/N III are from Moore (1975), and for N IV/N V from Moore (1971). Lines used within the present work are labeled by ‘+’. Lower and upper levels of the transitions are denoted by a combination of ion and level number according to Tables 3.1, 3.2, 3.3, and 3.4, e.g., ‘N29’ means level #9 of N II.

Ion	Transition	Multiplet	Line	Wavelength(Å)	Blends	Used
N II	N29 - N216	12	1	3994.99	-	+
	N211 - N219	15	2	4447.03	O II λ 4446.81, 4447.67, 4448.19, O III λ 4447.79	+
	N28 - N215	5	3	4601.47	O II λ 4602.13, 4603.23, N III λ 4604.18	+
	N28 - N215	5	4	4607.16	O II λ 4609.44, 4610.20, N III λ 4605.16, Ne II λ 4606.70	+
	N28 - N215	5	5	4621.39	O II λ 4621.27, N III λ 4621.04, 4623.05, Si II λ 4621.72	+
	N28 - N215	5	6	4630.54	O III λ 4630.77, N III λ 4630.61, Si IV λ 4631.24	+
	N28 - N215	5	7	4643.09	O II λ 4641.81, 4643.89, N III λ 4641.85	-
	N212 - N218	19	8	5005.15	O III λ 5006.84	-
	N214 - N221	24	9	5007.33	O III λ 5006.84	-
	N28 - N214	4	10	5045.10	N II λ 5046.53	-
	N28 - N212	3	11	5666.63	C II λ 5662.47	-
	N28 - N212	3	12	5676.01	N II λ 5679.55	-
	N28 - N212	3	13	5679.55	N II λ 5676.01	-
	N28 - N212	3	14	5710.77	Si II λ 5707.20	-
	N215 - N220	28	15	5941.65	N II λ 5940.24, N III λ 5943.44	-
N III	N320 - N333	17	1	4003.58	O II λ 4007.46	+
	N38 - N310	1	2	4097.33	O II λ 4097.26, 4098.24, H δ λ 4101.74	+
	N313 - N322	6	3	4195.76	O II λ 4192.52, 4196.26, Si III λ 4195.59, He II λ 4200.00	+
	N313 - N322	6	4	4200.07	He II λ 4200.00	-
	N321 - N334	18	5	4379.11	O II λ 4378.03, 4378.43, C III λ 4379.47, N II λ 4379.59	+
	N312 - N316	3	6	4510.88	N III λ 4510.92, Ne II λ 4511.42	+
	N312 - N316	3	7	4514.86	O III λ 4513.83,	+

Table 3.5 – continued from previous page

Ion	Transition	Multiplet	Line	Wavelength(Å)	Blends	Used
N III					Ne II λ 4514.88, C III λ 4515.81, 4516.77	
	N312 - N316	3	8	4518.14	Ne II λ 4518.14, O III λ 4519.62	+
	N310 - N311	2	9	4634.14	Si IV λ 4631.24, O IV λ 4632	+
	N310 - N311	2	10	4640.64	O II λ 4638.86, Si III λ 4638.28	+
	N310 - N311	2	11	4641.85	O II λ 4641.81, 4643.39, N II λ 4643.08	+
	N322 - N330	21	12	5320.82	O II λ 5322.53	-
	N322 - N330	21	13	5327.18	-	-
	N319 - N325	14	14	6445.34	-	-
	N319 - N325	14	15	6450.79	C IV λ 6449.90	-
	N319 - N325	14	16	6454.08	O II λ 6457.05, N II λ 6457.68	-
	N319 - N325	14	17	6467.02	-	-
N IV	N47 - N410	1	1	3478.71	-	+
	N47 - N410	1	2	3482.99	-	+
	N47 - N410	1	3	3484.96	-	+
	N49 - N412	3	4	4057.76	C III λ 4056.06, 4059.56	+
	N48 - N49	2	5	6380.77	O III λ 6378.34, 6383.30, DIBs λ 6376.08,6379.32	+
	N413 - N416	5	6	5200.41	O IV λ 5198.22	-
	N413 - N416	5	7	5204.28	N IV λ 5205.15	-
	N413 - N416	5	8	5205.15	N IV λ 5204.28, O II λ 5206.65	-
	N410 - N411	4	9	7103.24	-	+
	N410 - N411	4	10	7109.35	-	+
	N410 - N411	4	11	7111.28	-	+
	N410 - N411	4	12	7122.98	-	+
	N410 - N411	4	13	7127.25	-	+
	N410 - N411	4	14	7129.18	-	+
	N V	N53 - N54	1	1	4603.73	N III λ 4604.18, 4605.16, N IV λ 4606.33
N53 - N54		1	2	4619.98	Si III λ 4619.66, N III λ 4621.04, 4623.05	+
N518 - N525		9	3	4943.17	O IV λ 4941.29	-
N519 - N526		10	4	4943.97	O IV λ 4941.29	-
N520 - N527		10.01	5	4945.29	-	-

N IV λ 4058 and N IV λ 6380 connect the ‘neighboring’ levels of the singlet series $1s^2 2s3l$ with $l = s, p, d$ (levels #8, 9, and 12 in Table 3.3). N IV λ 4058 (if present) is observed in emission in the majority of stars, and has been suggested to be formed by photospheric NLTE processes, in analogy to the N III triplet emission. Note that there is no detailed analysis of the line formation process. So far, only Taresch et al. (1997) and Heap et al. (2006) simulated the behavior of this line as a

function of effective temperature. Heap and collaborators found emission for this line using the plane-parallel atmospheric code TLUSTY (Hubeny 1988; Hubeny & Lanz 1995), which supports the idea that the emission is of photospheric origin and that velocity fields are not required to explain the basic effect. Other arguments for the photospheric origin of N IV λ 4058 are the agreement with other, absorption line profiles as a function of $v \sin i$, unshifted radial velocities, and lack of P Cygni profiles (N. Walborn, priv. comm.). In Chapter 5, we investigate the N IV λ 4058 line formation. Interestingly, N IV λ 6380 appears clearly in absorption in O-star spectra, and seems to play a similar role as the N III absorption lines at λ 4097 – 4103 in the N III emission line problem (see Chapter 4). We note that N IV λ 6380 can be significantly affected by the presence of two diffuse interstellar bands (DIBs) at λ 6376.08, 6379.32 (Herbig 1975; Krelowski et al. 1995), the latter of which is stronger if reddening is significant. Fortunately, the stars analyzed in this work are subject to low reddening, and these DIBs only minorly affect some of the observed N IV λ 6380 lines (e.g. N11-038, Fig. C.8).

As for the previous pair of N IV lines, N IV λ 6380 and N IV λ 4058, the N IV multiplets around 3480 Å and 7103-7129 Å are also formed between levels of the same series (here within the triplet system – levels #7, 10, and 11 in Table 3.3), and seem to mimic the behavior of these lines: at least in the earliest O-star regime they are prominent features, where the former multiplet appears in absorption and the latter in emission. Both line complexes are widely used in WR-star analyses, and the emission in the latter multiplet is a strong feature in most WR spectra. The lack of emission at this multiplet and also at N IV λ 4058 has been used for classification purposes in different WR-star studies (e.g., Negueruela & Clark 2005). Likewise, the multiplet around 3480 Å has been used by Walborn et al. (2004) to infer T_{eff} and nitrogen abundances for a set of O2 stars. The remaining N IV lines listed, N IV λ 5200 – 5204 – 5205, also belong to the triplet system, and appear, if present, in absorption for O-stars.

Finally, N V lines at λ 4603-4619 are produced by transitions between the fine-structure components of $3s \ ^2S$ and $3p \ ^2P^0$ (levels #3 and 4 in Table 3.4). These doublet lines are strong absorption features in the earliest O-stars, showing sometimes extended absorption in their blue wings or even pronounced P-Cygni profiles (e.g., N11-031, Fig. C.7), revealing that they can be formed in the wind. Therefore, mass-loss and wind-clumping will clearly influence the formation of these lines. Besides, we also list N V λ 4943 – 4945, which become important, (almost) isolated diagnostic lines in the spectra of very early, nitrogen rich O- and WNL-stars. Note that to use these lines, we would need to extend our N V model ion, including high-lying levels, to allow for cascading processes into the corresponding upper levels at $n = 7$, which are our present uppermost ones.

Chapter 4

Nitrogen III emission line formation revisited

This chapter is - to a major fraction - a copy of Rivero González, Puls, & Najarro (2011), *Astronomy & Astrophysics*, 536, A58. There are some revisions from the original version, to allow for a better clarity and consistency of this thesis: The information about the dielectronic recombination process and the N III model ion were moved to Chapter 3. Section 4.2 was extended for a better understanding of the 'Of' problem. The original Appendix A was incorporated into Sect. 4.3.2, whereas the original Appendix B was moved to Chapter 3. The original Appendix C corresponds to Appendix B.1 within this thesis.

Abstract. Evolutionary models of massive stars predict a surface enrichment of nitrogen, due to rotational mixing. Recent studies within the *VLT-FLAMES survey of massive stars* have challenged (part of) these predictions. Such systematic determinations of nitrogen abundances, however, have been mostly performed only for cooler (B-type) objects. For the most massive and hottest stars, corresponding results are scarce.

This is the first paper in a series dealing with optical nitrogen spectroscopy of O-type stars, aiming at the analysis of nitrogen abundances for stellar samples of significant size, to place further constraints on the early evolution of massive stars. Here we concentrate on the formation of the optical N III lines at $\lambda\lambda 4634\text{-}4640\text{-}4642$ that are fundamental for the definition of the different morphological 'f'-classes.

We implement a new nitrogen model atom into the NLTE atmosphere/spectrum synthesis code FASTWIND, and compare the resulting optical N III spectra with other predictions, mostly from the seminal work by Mihalas & Hummer (1973, *ApJ* 179, 827, 'MH'), and from the alternative code CMFGEN.

Using similar model atmospheres as MH (not blanketed and wind-free), we are able to reproduce their results, in particular the optical triplet emission lines. According to MH, these should be strongly related to dielectronic recombination and the drain by certain two-electron transitions. However, using realistic, fully line-blanketed atmospheres at solar abundances, the key role of the dielectronic recombinations controlling these emission features is superseded – for O-star conditions – by the strength of the stellar wind and metallicity. Thus, in the case of wind-free (weak wind) models, the resulting lower ionizing EUV-fluxes severely suppress the emission. As the mass loss rate is increased,

pumping through the N III resonance line(s) in the presence of a near-photospheric velocity field (i.e., the Swings-mechanism) results in a net optical triplet line emission. A comparison with results from CMFGEN is mostly satisfactory, except for the range $30,000 \text{ K} \leq T_{\text{eff}} \leq 35,000 \text{ K}$, where CMFGEN triggers the triplet emission at lower T_{eff} than FASTWIND. This effect could be traced down to line overlap effects between the N III and O III resonance lines that cannot be simulated by FASTWIND so far, due to the lack of a detailed O III model atom.

Since the efficiency of dielectronic recombination and ‘two electron drain’ strongly depends on the degree of line-blanketing/-blocking, we predict the emission to become stronger in a metal-poor environment, though lower wind-strengths and nitrogen abundances might counteract this effect. Weak winded stars (if existent in the decisive parameter range) should display less triplet emission than their counterparts with ‘normal’ winds.

4.1 Introduction

One of the key aspects of massive star evolution is rotational mixing and its impact. Evolutionary models including rotation (e.g., Heger & Langer 2000; Meynet & Maeder 2000; Brott et al. 2011a) predict a surface enrichment of nitrogen with an associated carbon depletion during the main sequence evolution.¹ The faster a star rotates, the more mixing will occur, and the larger the nitrogen surface abundance that should be observed.

Several studies (Hunter et al., 2008a, 2009b; Brott et al., 2011b) have challenged the predicted effects of rotational mixing on the basis of observations performed within the VLT-FLAMES survey of massive stars (Evans et al., 2006). These studies provide the first statistically significant abundance measurements of Galactic, LMC, and SMC B-type stars, covering a broad range of rotational velocities.

For the Galactic case, the mean B-star nitrogen abundance as derived by Hunter et al. (2009a) is in quite good agreement with the corresponding baseline abundance. For the Magellanic Clouds stars, however, the derived nitrogen abundances show clearly the presence of an enrichment, where this enrichment is more extreme in the SMC than in the LMC.² Theoretical considerations have major difficulties in explaining several aspects of the accumulated results: Within the population of (LMC) core-hydrogen burning objects, both unenriched fast rotators and highly enriched slow rotators have been found, in contradiction to standard theory, as well as slowly rotating, highly enriched B-supergiants (see below). Taken together, these results imply that standard rotational mixing might be not as dominant as usually quoted, and/or that other enrichment processes might be present as well (Brott et al., 2011b).

Interestingly, there exist only few rapidly rotating B-supergiants, since there is a steep drop of rotation rates below $T_{\text{eff}} \approx 20 \text{ kK}$ (e.g., Howarth et al. 1997). Recently, Vink et al. (2010) tried to explain this finding based on two alternative scenarios. In the first scenario, the low rotation rates of B-supergiants are suggested to be caused by braking due to an increased mass loss for $T_{\text{eff}} < 25 \text{ kK}$, related to the so-called bi-stability jump (Pauldrach & Puls, 1990; Vink et al., 2000). Since the reality of such an increased mass loss is still debated (Markova & Puls, 2008; Puls et al., 2010), Vink et al. (2010) discuss an alternative scenario where the slowly rotating B-supergiants might form an entirely

¹ Due to a rapid achievement of the CN equilibrium, whilst the oxygen depletion implied by the full CNO equilibrium is only found in rapidly rotating and more massive stars at later stages, e.g., Brott et al. 2011a.

² Baseline abundances for all three environments from H II regions and unevolved B-stars, see Hunter et al. (2007).

separate, non core hydrogen-burning population. E.g., they might be products of binary evolution (though this is not generally expected to lead to slowly rotating stars), or they might be post-RSG or blue-loop stars.

Support of this second scenario is the finding that the majority of the cooler (LMC) objects are strongly nitrogen-enriched (see above), and Vink et al. argue that “although rotating models can in principle account for large N abundances, the fact that such a large number of the cooler objects is found to be N enriched suggests an evolved nature for these stars.” A careful nitrogen analysis of their (early) progenitors, the O-type stars, will certainly help to further constrain these ideas and present massive star evolution in general. Note that one of the scientific drivers of the current VLT-FLAMES Tarantula survey (Evans et al., 2011) is just such an analysis of an unprecedented sample of ‘normal’ O-stars and emission-line stars.

Until to date, however, nitrogen abundances have been *systematically* derived only for the cooler subset of the previous VLT-FLAMES survey, by means of analyzing N II alone, whereas corresponding results are missing for the most massive and hottest stars. More generally, when inspecting the available literature for massive stars, one realizes that metallic abundances, in particular of the key element nitrogen, have been derived only for a small number of O-type stars (e.g., Bouret et al. 2003; Hillier et al. 2003; Walborn et al. 2004; Heap et al. 2006). The simple reason is that they are difficult to determine, since the formation of N III/N IV lines (and lines from similar ions of C and O) is problematic due to the impact of various processes that are absent or negligible at cooler spectral types.

One might argue that the determination of nitrogen and other metallic abundances of hotter stars could or even should be performed via UV wind-lines, since these are clearly visible as long as the wind-strength is not too low, and the line-formation is less complex and less dependent on accurate atomic models than for photospheric lines connecting intermediate or even high-lying levels. Note, however, that the results of such analyses strongly depend on the assumptions regarding and the treatment of wind X-ray emission and wind clumping (Puls et al. 2008 and references therein). A careful photospheric analysis, on the other hand, remains rather unaffected by such problems as long as X-ray emission and clumping do not start (very) close to the photosphere, and we will follow the latter approach, concentrating on optical lines.

This paper is the first in a series of upcoming publications dealing with nitrogen spectroscopy of O-type stars. The major objective of this project is the analysis of optical spectra from stellar samples of significant size in different environments, to derive the corresponding nitrogen abundances which are key to our understanding of the early evolution of massive stars. In the present study, we will concentrate on the formation of the optical N III emission lines at $\lambda\lambda 4634\text{-}4640\text{-}4642$, which are fundamental for the definition of the different morphological ‘f’-classes. During our implementation of nitrogen into the NLTE-atmosphere/line formation code FASTWIND (Puls et al., 2005) it turned out that the canonical explanation in terms of dielectronic recombination (Mihalas & Hummer, 1973) no longer or only partly applies when modern atmosphere codes including line-blocking/blanketing and winds are used to synthesize the N III spectrum. Since the f-features are observed in the majority of O-stars and strongly dependent on the nitrogen abundance, a thorough re-investigation of their formation process is required, in order to avoid wrong conclusions.

This chapter is organized as follows: First, (Sect. 4.2) we recapitulate previous explanations for the N III triplet emission, in particular the standard picture as provided by Mihalas & Hummer (1973). In Sect. 4.3 we discuss the dielectronic recombination process and its implementation into FASTWIND. In Sect. 4.4 we investigate the dependence of the triplet emission on various processes. We compare

our results with corresponding ones from the alternative code CMFGEN (Hillier & Miller, 1998) in Sect 4.5, and discuss the impact of coupling with O III via corresponding resonance lines in Sect. 4.6. The dependence of the emission strength on specific parameters is discussed in Sect. 4.7, and Sect. 4.8 provides our summary and conclusions.

4.2 N III emission lines from O-stars - status quo

The presence of emission in the N III triplet at $\lambda\lambda 4634\text{-}4640\text{-}4642$ Å, in combination with the behaviour of He II $\lambda 4686$, is used for classification purposes and to discriminate O-stars with such line emission from pure absorption-line objects. Walborn (1971b) introduced the following classes: ((f)), weak N III emission and strong He II absorption (e.g., λ Ori); (f), N III in emission and He II in weak absorption (e.g., HD 15558); f, both N III and He II in emission (e.g., λ Cep); f⁺, both lines and Si IV $\lambda\lambda 4089 - 4116$ in emission (e.g., HD 15570).³

The importance of the N III emission lines in the spectra from Of stars leads to questioning their formation mechanism and to their relation with stellar/atmospheric parameters. Seminal work on this topic has been performed by Bruccato & Mihalas (1971) and Mihalas & Hummer (1973). As pointed out in the former investigation, the emission lines originate in the stellar atmosphere and not in an “exterior shell” (see also Heap et al. 2006 for more recent work), as suggested for emission lines from objects of different nature, e.g., emission lines formed in the solar corona.

The most plausible explanation is by invoking NLTE effects (see also Sect. 2.2.1). In NLTE, line emission occurs when the corresponding source function is sufficiently large at formation depths, i.e., larger than the continuum intensity at transition frequency ν_0 . Such a large source function becomes possible if the upper level of the transition is (considerably) overpopulated with respect to the lower one, i.e., if $b_u > b_l$ (with b_u and b_l the corresponding NLTE departure coefficients of upper and lower level). Note that both quantities can lie below unity.

For the N III triplet produced by the $2s^2(1S) 3p\ 2P^0 - 2s^2(1S) 3d\ 2D$ transitions (see Fig. 4.1), such a mechanism should result in a (relative) overpopulation of the upper level, $3d\ 2D$. In the early work about Of stars, the fluorescence mechanism developed by Bowen (1935) has been suggested to trigger such an overpopulation, where this mechanism had been originally invoked to explain the presence of O III and N III emission lines in nebular spectra. Many authors (Swings & Struve 1940; Swings 1948; Oke 1954) argued against the relevance of the Bowen mechanism in Of stars, because of the lack of O III emission lines at $\lambda\lambda 3340, 3444, 3759$ Å which are connected to the involved levels.

An alternative suggestion is due to Swings (1948) and relies on an intense continuum that may directly (i.e., without involving oxygen) pump the resonance transition $2p\ 2P^0 - 3d\ 2D$ (thus producing the required overpopulation, $b_{3d} > b_{3p}$) as well as $2p\ 2P^0 - 3s\ 2S$, while the transition $2p\ 2P^0 - 3p\ 2P^0$ is radiatively forbidden. The implied overpopulation of level $3s\ 2S$ due to pumping may then explain why the transitions $3s\ 2S - 3p\ 2P^0$ at $\lambda\lambda 4097\text{-}4103$ are always in absorption ($b_{3s} > b_{3p}$). Without such pumping of the 3s level, an auxiliary draining mechanism for the 3p level is needed, since otherwise an overpopulation, $b_{3p} > b_{3s}$, would occur due to cascade processes. This overpopulation would imply the presence of emission at $\lambda\lambda 4097\text{-}4103$, which is not observed in Of stars.

Indeed, the anomalous ‘two electron transitions’ $2p^2\ (^2S, ^2P, ^2D) - 3p\ 2P^0$ with transition probabilities comparable to the $3p \rightarrow 3s$ one electron transition have been identified by Nikitin & Yakubovskii

³ Recently the f⁺ designation has become obsolete since the Si IV emission at $\lambda\lambda 4089 - 4116$ is now established as a common feature in normal O-type spectra (Sota et al., 2011).

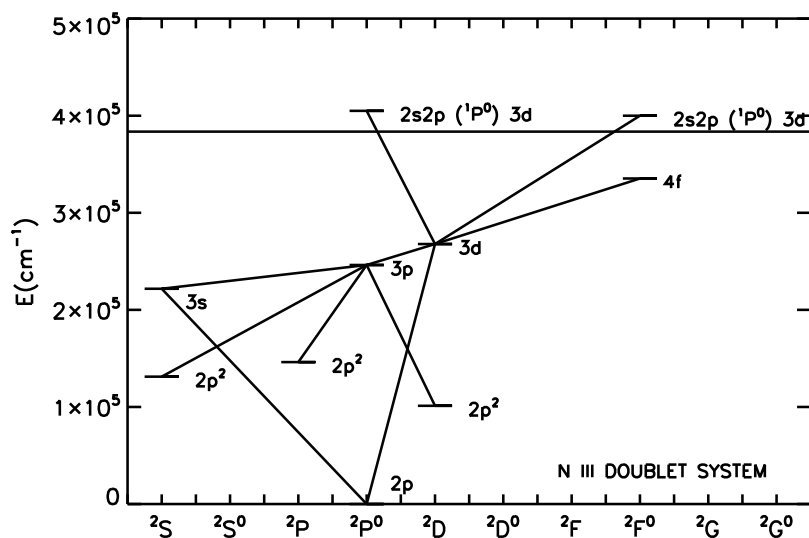


Figure 4.1: Grotrian diagram displaying the transitions involved in the N III emission lines problem. The horizontal line marks the N III ionization threshold. The N III $\lambda\lambda 4634$ - 4640 - 4642 triplet is formed by the transitions $3d \rightarrow 3p$, while the absorption lines at $\lambda\lambda 4097$ - 4103 are due to the transitions $3p \rightarrow 3s$. An effective drain of $3p$ is provided by the ‘two electron transitions’ $3p \rightarrow 2p^2$ (2S , 2P , 2D). The levels above the ionization limit are the autoionizing levels that feed level $3d$ via dielectronic recombination (Sect. 4.3.1). Cascade processes ($4f \rightarrow 3d$) can overpopulate the $3d$ state as well. The Swings mechanism involves the resonance transitions $2p \rightarrow 3s$ and $2p \rightarrow 3d$. Note that the (energetic) positions of the autoionizing niveaus have been shifted upwards for clarity.

(1963) as potentially important draining processes. Calculations by Bruccato & Mihalas (1971) showed that the presence of these draining processes is sufficient to ensure both the overpopulation of the $3d$ 2D level (relative to $3p$) and preventing the overpopulation of the latter relative to $3s$, which would produce the unwanted emission at $\lambda\lambda 4097$ - 4103 . Thus, these ‘two electron transitions’ play a key role in the N III emission.

As already pointed out by Bruccato & Mihalas (1971), there is a problem for the Swings mechanism when applied to Of stars. The $2p \rightarrow 3s$ and $2p \rightarrow 3d$ resonance lines are expected to be much more opaque than $3p \rightarrow 3s$ and $3d \rightarrow 3p$, and should be consequently in detailed balance in the line forming region. That would mean no pumping and no overpopulation of $3d$ relative to $3p$ (but see Sect. 4.4.3).

The problem became (preliminary) solved when Bruccato & Mihalas (1971) suggested a third potential mechanism. They realized the existence of a large number of autoionizing levels that either connect directly to the $3d$ state or to levels that can cascade downwards to $3d$. Hence, the latter state may become strongly overpopulated by *dielectronic recombination* (‘DR’, see Sect. 4.3).

The most important analysis of the N III emission lines problem until now has been carried out by (Mihalas & Hummer, 1973, ‘MH’), building on the work by Bruccato & Mihalas (1971). They used static, plane-parallel models trying to explain the effect for O((f)) and O(f) stars. As a final result, they were able to reproduce the N III $\lambda\lambda 4634$ - 4640 - 4642 emission lines at the observed temperatures

and gravities in parallel with absorption at $\lambda\lambda 4097 - 4103$, by overpopulating level 3d primarily via *dielectronic recombination*. The subsequent $3d \rightarrow 3p$ cascade produces the emission. The strong drain $3p \rightarrow 2p^2$ via ‘two electron transitions’ enhances the overpopulation of 3d relative to 3p by depopulating 3p and prevents emission in the $3p \rightarrow 3s$ lines. According to the authors, the Swings mechanism has little importance for these stars, though for Of stars it might become influential when expanding envelopes are present (note that at that time there were no models allowing for extended atmospheres). Until to date, dielectronic recombination is the canonical explanation for the formation of the f-features.

4.3 Dielectronic recombination

4.3.1 The N III emission triplet at $\lambda\lambda 4634-4640-4642$

As pointed out by Mihalas (1971), there are two important autoionizing series in the N III ion, of the form $2s2p(^1P^0)nl$ and $2s2p(^3P^0)nl$, along with few bound double excitation states with similar configuration. Since states of the form $2s2pnl$ are directly coupled to $2s^2nl$ states, they are of great importance. In the following, we consider only the states from the singlet series, because the transitions from the triplet series to $2s^2nl$ states are not electric dipole allowed transitions in LS coupling.

The singlet series comprises only two bound configurations, $2s2p3s$ and $2s2p3p$, whilst the $2s2p3d$ configuration lies only 1.6 eV above the ionization potential and is of major importance, since the low position in the continuum produces strong dielectronic recombination,

$$2s^2(^1S) (\text{N IV}) + e^- \rightarrow 2s2p(^1P^0)3d(^2P^0, ^2F^0). \quad (4.1)$$

Note that the core electron transition (see above), $2s^2(^1S) \rightarrow 2s2p(^1P^0)$, is equivalent to the resonance transition in N IV. Thus, any $2s^2(^1S)nl \rightarrow 2s2p(^1P^0)nl$ transition gives rise to strong, broad resonances (see Fig. 4.2), unless the $2s2p(^1P^0)nl$ state is truly bound.

The autoionizing states (Eq. 4.1) can stabilize via two alternative routes, either

$$2s2p(^1P^0)3d(^2P^0, ^2F^0) \rightarrow 2s2p(^1P^0)3p(^2S, ^2P, ^2D) + h\nu, \quad (4.2)$$

that end in the doubly excited bound configuration mentioned above, or the one that might overpopulate the upper level of the transition $3d \rightarrow 3p$,

$$2s2p(^1P^0)3d(^2P^0, ^2F^0) \rightarrow 2s^23d(^2D) + h\nu, \quad (4.3)$$

thus playing a (potential) key role in the N III triplet emission. The latter route is displayed in the upper part of Fig. 4.1.

4.3.2 Implementation into FASTWIND

Dielectronic recombination and its inverse process have been implemented into FASTWIND in two different ways, to allow us to use different data sets. Specifically, we implemented

- (i) an *implicit method* where the contribution of the dielectronic recombination is already included in the photoionization cross-sections. This method needs to be used for data that has been calculated, e.g., within the OPACITY project (Cunto & Mendoza, 1992) and

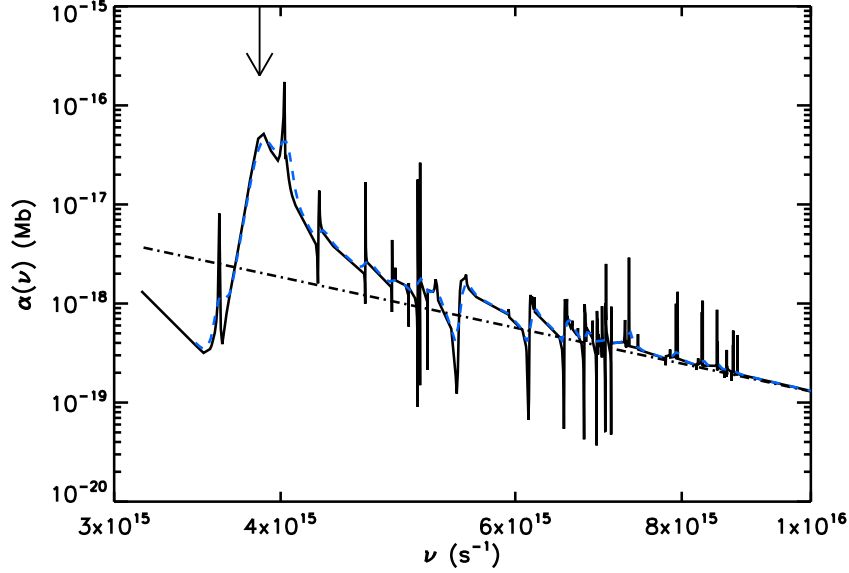


Figure 4.2: Comparison of the ‘raw’ cross-section from the OPACITY project (black), and the smoothed one (grey/blue), for the $3d\ ^2D$ state of N III. Note the numerous complex resonances. An example for a PEC resonance, being much broader than the usual Rydberg resonances, is marked by the vertical arrow. Dashed: corresponding resonance-free data in terms of the Seaton (1958) approximation from WM-basic.

- (ii) an *explicit method* using resonance-free photoionization cross-sections in combination with explicitly included stabilizing transitions from autoionizing levels. This method will be used when we have information regarding transition frequencies and strengths of the stabilizing transitions.

Photoionization cross-sections from the OPACITY project data include the contributions of dielectronic recombination and will be used within the implicit method. All these cross-sections display complex resonances (where the largest and widest ones are the PEC resonances), which somewhat complicate the implementation of this method. Since some of the resonances are quite narrow, care must be taken when sampling the cross-sections. If performing a straightforward calculation, the radiative transfer would need to be solved at each point of the fine-frequency grid required by the resonances in the ‘raw’ data, which would increase the computational effort considerably. To circumvent the problem we implemented a method that is also used in WM-basic (Pauldrach et al., 2001) and in CMFGEN (Hillier & Miller, 1998) (see also Bautista et al. 1998). The raw OPACITY project cross-sections are smoothed (Fig. 4.2) to adapt them to the standard continuum frequency grid used within the code, which has a typical resolution of a couple of hundred km s^{-1} . To this end, the data are convolved with a Gaussian profile of typically $3,000\ \text{km s}^{-1}$ width, via a Fast Fourier Transform. This convolution ensures that the area under the original data remains conserved, and that all resonances are treated with sufficient accuracy. By means of this approach, the ionization and recombination rates should be accurately represented, except for recombination rates at very low temperatures, where the recombination coefficient is quite sensitive to the exact location of the resonance (see Hillier & Miller 1998).

In the present work we implemented dielectronic recombination into FASTWIND, which, so far, could not (or only approximately) deal with this process. To this end, new rates (both for the dielectronic recombination and for the inverse process) had to be inserted into the system of the rate equations.

Explicit method

To calculate these rates for the ‘explicit method’, we follow the formulation as provided by Nussbaumer & Storey (1983). In compact notation, the dielectronic recombination for an element X and charge $m + 1$ proceeds via



where p is a parent state of the $m + 1$ times ionized element X, a is an autoionizing state and b is a bound state. We denote the initial state of expression 4.4, composed of the recombining ion and the free electron, as a continuum state c . We refer to the first process as dielectronic capture and to its inverse as autoionization. In general, dielectronic captures and autoionizations link state a to a large number of continuum states c .

As a final result,⁴ Nussbaumer & Storey (1983) could express the dielectronic recombination coefficient between autoionizing state a and bound state j , $\alpha_{\text{DR}}(aj)$, as

$$n_e N_k^{m+1} \alpha_{\text{DR}}(aj) = b_a (n_a^m)^* A_{aj}^{\text{R}}, \quad (4.5)$$

with A_{aj}^{R} the corresponding radiative transition probability for the stabilizing transition (Einstein coefficient for spontaneous emission, corrections for induced emission will be applied below), total ion density N_k^{m+1} (element k), $(n_a^m)^*$ the LTE population of state a with respect to the actual (NLTE) ground-state population of the next higher ion and the actual electron density, and b_a the related NLTE departure coefficient.

The last quantity can be expressed in terms of (i) the autoionization coefficient(s), A_{ac}^a , between state a and all possible compound-states c that can form a , (ii) the radiative transition probabilities, A_{ai}^{R} , between state a and all possible bound and autoionizing states with lower energy i to which state a can decay, and (iii) the departure coefficients of the contributing parent levels, b_p (here with respect to the ground-state of the same ion, n_1^{m+1})

$$b_a = \frac{n_a^m}{n_a^{m*}} = \frac{\sum_c b_p A_{ac}^a}{\sum_c A_{ac}^a + \sum_i A_{ai}^{\text{R}}}. \quad (4.6)$$

Usually, the autoionizing probabilities for state a are much larger than the radiative probabilities for decay, and often there is only one parent level, namely the ground-state of ion $m + 1$, $n_p = n_1^{m+1}$, i.e., $b_p = 1$. Under these conditions (which are similar for excited parent levels assumed to be in LTE with respect to the ground level), $b_a \rightarrow 1$, and *the dielectronic rate depends only on the LTE population of state a and the radiative transition probability A_{aj}^{R}* . All dependencies on the autoionization probabilities have ‘vanished’, and we need only the value of $(n_a^m)^*$ that can be derived from the Saha-equation and the ground-state population of ion $m + 1$, without including the autoionizing levels into the rate equations.

⁴ See also Mihalas 1978 for a simplified derivation.

In stellar atmospheres, one needs (in addition to the spontaneous emission to level j) to account for stimulated emission as well, i.e.,

$$A_{aj}^R \rightarrow A_{aj}^R + B_{aj}\bar{J} = A_{aj}^R \left(1 + \frac{c^2}{2h\nu^3}\bar{J} \right), \quad (4.7)$$

with B_{aj} the Einstein coefficient for stimulated emission and \bar{J} the scattering integral (profile weighted, frequency integrated mean intensity) for the stabilizing transition. Since the important resonances are broad, the scattering integrals might be replaced by the mean intensities, J_ν , of the pseudo-continuum (i.e., including all background opacities/emissivities) at the frequency of the stabilizing line.

Finally, we can define the total dielectronic rate to level j from any possible autoionizing state a^i ,

$$n_e N_k^{m+1} \sum_i \alpha_{\text{DR}}(a^i j) \approx n_e n_1^{m+1} \frac{1}{g_k} C_i T^{-3/2} \times \sum_i g(a^i) \exp(-E_{a^i}/kT) A_{a^i j}^R \left(1 + \frac{c^2}{2h\nu_{ij}^3} \bar{J}_{ij} \right), \quad (4.8)$$

which might need to be augmented by departure coefficients b_{a^i} inside the rhs sum if the parent levels are not the ground-state or not in LTE with respect to the ground-state. The inverse upward rate involves only the line process(es),

$$n_j^m \sum_i B_{ja^i} \bar{J}_{ij} = n_j^m \sum_i \frac{c^2}{2h\nu_{ij}^3} A_{a^i j}^R \frac{g(a^i)}{g_j} \bar{J}_{ij}, \quad (4.9)$$

with B_{ji} the Einstein-coefficient(s) for absorption. It is easy to show that for LTE conditions ($n_j^m = (n_j^m)^*$ and Planckian radiation in the lines) the upward and downward rates cancel each other exactly, as required for thermalization.

Though we have followed here the derivation by Nussbaumer & Storey (1983), our final results for the downward and upward rates are identical with the formulation as used by Mihalas & Hummer (1973) in their investigation.

These rates have been implemented into FASTWIND and are used whenever the ‘explicit method’ is applied. The only input parameters that need to be specified in the atomic data input file are the transition frequencies and the oscillator-strengths for the stabilizing lines, f_{ja} , which relate to the products $g_a A_{aj}^R$ via

$$g_a A_{aj}^R = \frac{8\pi^2 e^2}{m_e c^3} \nu_{aj}^2 g_j f_{ja}. \quad (4.10)$$

For convenience and for consistency with the formulation of ‘normal’ recombination rates, the quantity $(n_a^m)^*$ is expressed in terms of the LTE-population (with respect to actual ionization conditions) of the lower, stabilizing level $(n_j^m)^*$,

$$(n_a^m)^* = (n_j^m)^* \frac{g_a}{g_j} \exp(-h\nu_{aj}/kT), \quad (4.11)$$

so that the downward rate (for a specific autoionizing level a) can be expressed as

$$n_e N_k^{m+1} \alpha_{\text{DR}}(aj) = [b_a] (n_j^m)^* \frac{8\pi^2 e^2}{m_e c^3} \nu_{aj}^2 f_{ja} \exp(-h\nu_{aj}/kT) \left(1 + \frac{c^2}{2h\nu_{aj}^3} \bar{J}_{aj} \right). \quad (4.12)$$

Summation over all contributing autoionizing states yields the final rate.

In this explicit method, the rates for dielectronic recombinations and inverse processes are calculated in a separate step and then added to the rates involving resonance-free photoionization cross-sections alone. In our model atom (Chapter 3), we use such cross-sections defined in terms of the Seaton approximation (Eq. 3.2), which, together with the data for the stabilizing transitions, have been taken from the WM-basic atomic database. Note that we consider processes both from/to ground-states as well as from/to excited states within ion $m + 1$, so far on the assumption that the autoionizing levels are in LTE (i.e., without including these levels into the model atom and rate equations).

Implicit method

Within the implicit method, the DR contribution is already contained within the ‘conventional’ recombination rates, $(n_j/n_k)^* R_{kj}$, to yield a total number of recombinations

$$n_k \left(\frac{n_j}{n_k} \right)^* R_{kj} := n_j^* R_{kj}. \quad (4.13)$$

As usual, n_k is the actual population of the recombining ion in state k and $(n_j/n_k)^*$ the LTE population ratio of the considered level to which the process recombines (either directly or via the intermediate doubly excited state). R_{kj} is defined as

$$R_{kj} = 4\pi \int_{\nu_0}^{\infty} \frac{\alpha_{jk}(\nu)}{h\nu} \left(\frac{2h\nu^3}{c^2} + J_\nu \right) e^{-h\nu/kT} d\nu \quad (4.14)$$

with mean intensity J_ν and total photoionization cross-section (including resonances), $\alpha_{jk}(\nu)$.

In the following, we show that this formulation is consistent with the rates derived above. We split the cross-section into a resonance-free contribution, and a contribution from the resonances,

$$\alpha_{jk}(\nu) = \alpha_{jk}^{\text{no.res}}(\nu) + \alpha_{jk}^{\text{res}}(\nu). \quad (4.15)$$

The total recombination rate is then the sum of direct and dielectronic recombination,

$$n_j^* R_{kj} = n_j^* (R_{kj}^{\text{dir}} + R_{kj}^{\text{DR}}), \quad (4.16)$$

with

$$n_j^* R_{kj}^{\text{DR}} = n_j^* 4\pi \int_{\text{res}} \frac{\alpha_{jk}^{\text{res}}(\nu)}{h\nu} \left(\frac{2h\nu^3}{c^2} + J_\nu \right) e^{-h\nu/kT} d\nu. \quad (4.17)$$

The resonances are narrow enough so that most of the frequency dependent quantities can be drawn in front of the integral, evaluated at the average position of the resonances i ,

$$n_j^* R_{kj}^{\text{DR}} \approx n_j^* \sum_i \frac{4\pi}{h\nu_{ij}} \frac{2h\nu_{ij}^3}{c^2} e^{-h\nu_{ij}/kT} \left(\int_{\text{res}(i)} \alpha_{ji}^{\text{res}}(\nu) \left(1 + \frac{c^2}{2h\nu_{ij}^3} J_\nu \right) d\nu \right). \quad (4.18)$$

The integral over the cross-sections of the resonances corresponds to the cross-section of the stabilizing transitions,

$$\frac{4\pi}{h\nu_{ij}} \int_{\text{res}(i)} \alpha_{ji}^{\text{res}} d\nu = B_{ji} = \frac{4\pi}{h\nu_{ij}} \frac{\pi e^2}{m_e c} f_{ji}, \quad (4.19)$$

with Einstein-coefficient B_{ji} and oscillator-strength f_{ji} . Likewise,

$$\int_{\text{res}(i)} \alpha_{ji}^{\text{res}} J_{\nu} d\nu \propto f_{ji} \bar{J}_{ij}.$$

Then, indeed, we recover the result from Eq. 4.12 (explicit formulation),

$$n_j^* R_{kj}^{\text{DR}} = n_j^* \sum_i \frac{8\pi^2 e^2}{m_e c^3} v_{ij}^2 f_{ji} \exp(-hv_{ij}/kT) \left(1 + \frac{c^2}{2hv_{ij}^3} \bar{J}_{ij} \right), \quad (4.20)$$

if the autoionizing levels are in or close to LTE. Note that this is a necessary condition for the implicit method to yield reliable results,⁵ otherwise one has to use exclusively the explicit approach and to include the autoionizing levels into the model atom and rate equations.

The proof that the rates for the inverse photoionization process, calculated either by the implicit method (using total photoionization cross-sections) or via rates from resonance-free cross-sections plus rates involving the excitation of the second electron, are consistent, is analogous and omitted here.

Consistency check

To check the consistency of our implementation of implicit and explicit DR treatment, we carried out the following test. First, to ensure consistent *data*, we derived the oscillator strength corresponding to the wide PEC resonance in the total photoionization cross-section (Fig. 4.2) by integrating over the cross-section and applying Eq. 4.19.⁶ The resulting value ($f = 0.45$, which is somewhat smaller than the data provided by the WM-basic database, $f = 0.60$) was then used within the explicit method, at the original wavelength (which coincides with the position of the resonance). As displayed in Fig. 4.3 for the case of model ‘T3740’ with ‘pseudo line-blanketing’ (see Sect. 4.4.1), both methods result in very similar line profiles for the N III emission triplet, proving their consistency. Figure 4.3 also displays the strong reaction of the N III triplet when the oscillator strength is either increased or diminished by a factor of two.

4.3.3 Implicit vs. explicit method

Though under similar assumptions both methods achieve similar results, there are certain advantages and disadvantages that are summarized in the following (see also Hillier & Miller 1998).

The implicit method has the advantage that for states that can autoionize in LS coupling their contribution to dielectronic recombination (and the inverse process) is already included within the photoionization data. There is no need to look for both the important autoionizing series to each level and the oscillator strengths of the stabilizing transitions. On the other hand, there are also disadvantages. Narrow resonances are not always well resolved, and, if the resonance is strong, the dielectronic recombination rate from such a resonance could become erroneous. Besides, the positions of the resonances are only approximate. If line coincidences are important, this can affect the transfer and the corresponding rates. Hillier & Miller (1998) suggested to avoid the implicit approach for those

⁵ Which has been used to calculate the total cross-sections as provided by, e.g., the OPACITY Project.

⁶ Of course, the underlying contribution responsible for direct ionization needs to be subtracted.

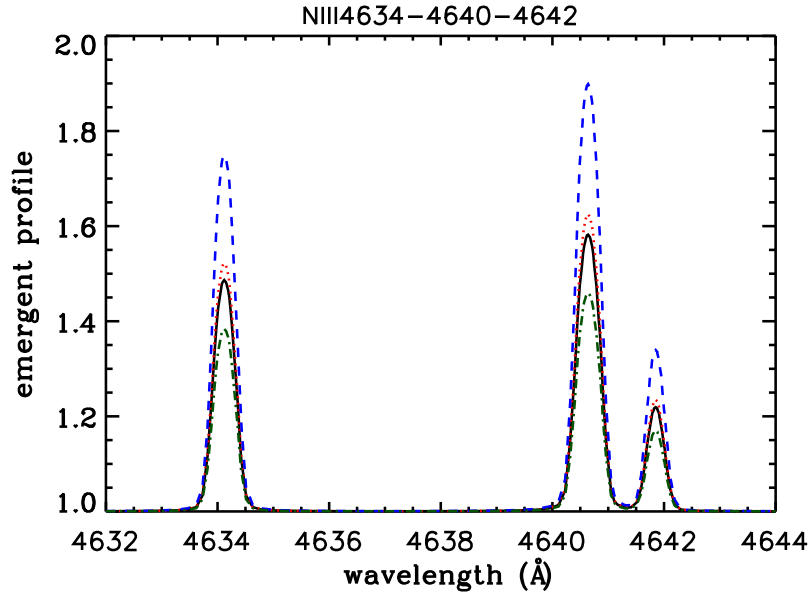


Figure 4.3: Consistency of implicit and explicit method. Comparison of N III $\lambda\lambda 4634-4640-4642$ profiles from model ‘T3740’, for calculations using a different treatment of DR to the 3d level. Implicit method (solid/black), explicit method (dotted/red), explicit method with oscillator strength for the stabilizing transition increased (dashed/blue) and decreased (dashed-dotted/black) by a factor of two.

transitions where dielectronic recombination is an important mechanism. In our new N III model ion (Chapter 3) we have followed their advice. Finally, dielectronic recombination rates calculated by the implicit method are inevitably based on the assumption that the autoionizing levels are in LTE with respect to the ground state of the next higher ion.⁷ In the rare case that this were no longer true, the implicit method cannot be used. Then, the autoionizing levels need to be included into the model atom, and all transitions need to be treated explicitly.

The explicit method has the theoretical advantage that resonances can be inserted at the correct wavelength if known. (Though one has to admit that resonance positions will never be very accurate. For the PECs this does not matter though.) Often, however, the profile functions for the resonances are difficult to obtain (which, on the other hand, are included in the implicit approach). The width of these Fano profiles is set by the autoionization coefficients, which, frequently, are not available. To overcome this problem, we follow the approach by MH and assume the resonance to be wide (which is true for the most important PEC-resonances), such that we can use the mean intensity instead of the scattering integral when calculating the rates, and become independent of the specific profile. When line coincidences play a role, this might lead to certain errors though.

⁷ This will almost always be the case, otherwise the states are more or less bound.

Table 4.1: Model grid used by Mihalas & Hummer (1973) and in our test series. The mass-loss rates provided in the last row (in units of $10^{-6} M_{\odot} \text{yr}^{-1}$) refer to our tests of wind effects (Sect. 4.4.3) alone. All other tests have been performed with negligible \dot{M} .

Model T	3233	3540	3533	3740	3735	4040	4035	4540	5040
$T_{\text{eff}}(\text{kK})$	32.5	35.0	35.0	37.5	37.5	40.0	40.0	45.0	50.0
$\log g$	3.3	4.0	3.3	4.0	3.5	4.0	3.5	4.0	4.0
\dot{M}	1.0	0.35	1.82	0.58	3.16	0.93	5.3	8.05	17.5

Table 4.2: Oscillator strengths for the ‘two electron transition’ as used by Mihalas & Hummer (1973) and within our new atomic model.

Transition	f_{lu} (MH)	f_{lu} (used in this work)
$2p^2 \ ^2D - 3p \ ^2P^0$	$2.50 \cdot 10^{-4}$	$4.38 \cdot 10^{-3}$
$2p^2 \ ^2S - 3p \ ^2P^0$	$2.00 \cdot 10^{-4}$	$1.31 \cdot 10^{-2}$
$2p^2 \ ^2P - 3p \ ^2P^0$	$2.40 \cdot 10^{-2}$	$4.02 \cdot 10^{-4}$

4.4 N III (emission) line formation

In the following, we describe the results of an extensive test series regarding our newly developed N III model ion (Sect. 3.2.2). In particular, we check if the triplet appears in emission in the observed parameter range, and if the $\lambda 4097$ line remains always in absorption. Note that these lines should be strongly correlated, i.e., the stronger the emission in the triplet, the weaker the absorption at $\lambda 4097$, since both transitions share the level 3p (Fig. 4.1). A change in the corresponding departure coefficient leads to a change in both lines. For example, if b_{3p} becomes diminished due to a more efficient drain by the ‘two electron transitions’ (see Sect. 4.2), this leads to more emission at $\lambda\lambda 4634\text{-}4640\text{-}4642$ and to less absorption at $\lambda 4097$, due to less cascading.

For all tests, we calculated model-grids that cover the same stellar parameters (O-type dwarfs and (super-) giants) as used by MH, listed in Table 4.1. All tests have been performed by means of FASTWIND, using our *complete* nitrogen model atom.

4.4.1 Comparison with the results from MH

First, we test if we are able to reproduce the MH-results for O((f)) and O(f) stars. To this end, we need to invoke (almost) identical conditions, regarding both atmospheric and atomic models. Thus, we modified our N III ionic model, replacing part of our new data with those used by MH (‘mixed’ ionic model). In particular, we replaced data for dielectronic recombination (to the three draining levels, $2p^2$ (2D , 2S , 2P), to level 3d, and to few higher important levels – #14, 17, 20 and 21, see Table 3.2), the oscillator strengths for the ‘two electron transitions’ (Table 4.2), and the photoionization cross-sections for all levels below 3d (the cross-sections for the latter did already agree).

Consistent with the MH-models, a nitrogen abundance of $[\text{N}]^8 = 8.18$ was adopted. This is a

⁸ $[\text{A}] = \log \text{A}/\text{H} + 12$, with A/H the number density of element A with respect to hydrogen

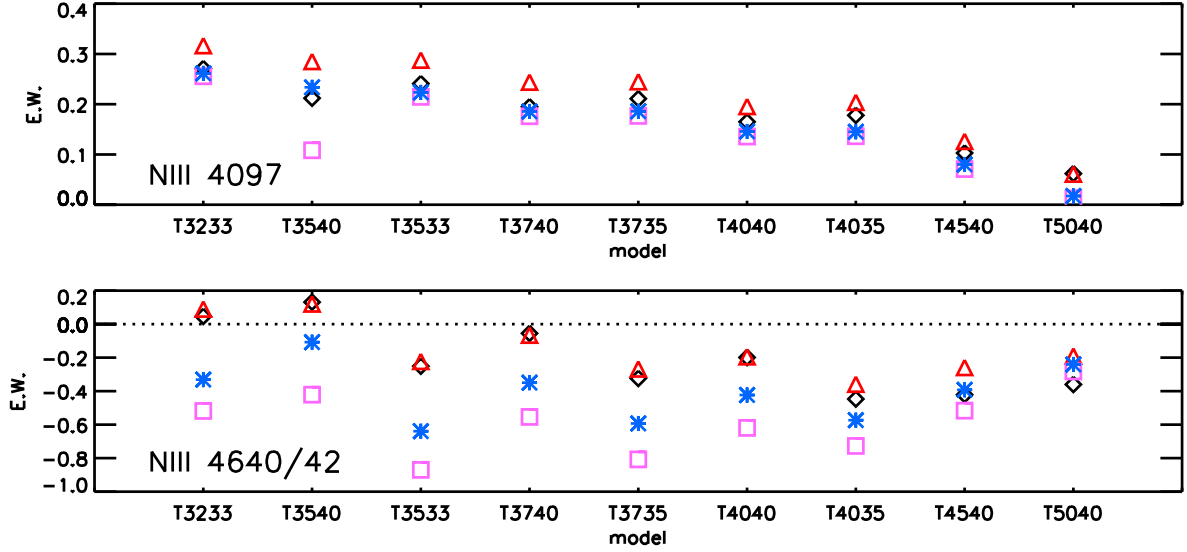


Figure 4.4: Comparison of equivalent widths (EW) for N III $\lambda 4097$ and $\lambda\lambda 4640/42$. All atmospheric models calculated with ‘pseudo line-blanketing’ (see text). Black diamonds: results from MH; red triangles: new FASTWIND calculations with ‘mixed’ N III ionic model (new level structure, but important transition data from MH); purple squares: new FASTWIND calculations with new N III model; blue asterisks: as squares, but DR-contribution to 3d level diminished by a factor of two. Here and in the following, positive and negative EWs refer to absorption and emission lines, respectively.

factor of 2.5 larger than the solar one, $[N_{\odot}] = 7.78$ (Asplund et al., 2005).⁹ To account for the absence of a wind in their models, a negligible mass-loss rate of $\dot{M} = 10^{-9} M_{\odot} \text{yr}^{-1}$ was used.

Though line-blocking/blanketing could not be included into the atmospheric models in 1973, MH realized its significance and tried to incorporate some important aspect by means of a ‘pseudo-blanketing’ treatment. The N III photoionization edge (at 261 Å) lies very close to the He II ground state edge (at 228 Å) in a region of low continuum opacity and high emergent flux (if no line-blanketing due to the numerous EUV metal-lines is present), and would cause severe underpopulation of the N III ground state if the blanketing effect is neglected, as shown by BM71. MH argued that heavy line-blanketing and much lower fluxes are to be expected in this region. To simulate these effects, they extrapolated the He II ground-state photoionization cross-section beyond the Lyman-edge up to the N III edge, using a ν^{-3} extrapolation. To be consistent with their approach, we proceed in the same way by including this treatment into FASTWIND (see Fig. 4.7).

Figure 4.4 displays the comparison between the resulting equivalent widths from the MH models (black symbols) and our models using the conditions as outlined above (red triangles). Overall, the agreement for $\lambda\lambda 4634-4640-4642$ is satisfactory,¹⁰ and slight differences are present only for the hottest models. In agreement with the MH results, our profiles turn from absorption into emission around $T_{\text{eff}} \sim 37,000$ K for dwarfs and at $T_{\text{eff}} \sim 33,000$ K for (super-)giants. As well, the $\lambda 4097$

⁹ Asplund et al. (2009) provide a slightly larger value, $[N_{\odot}] = 7.83 \pm 0.05$, where this difference is irrelevant in the following context.

¹⁰ Here and in the following, we only display the total equivalent widths of the $\lambda\lambda 4640/4642$ components; the behavior of $\lambda 4634$ is analogous.

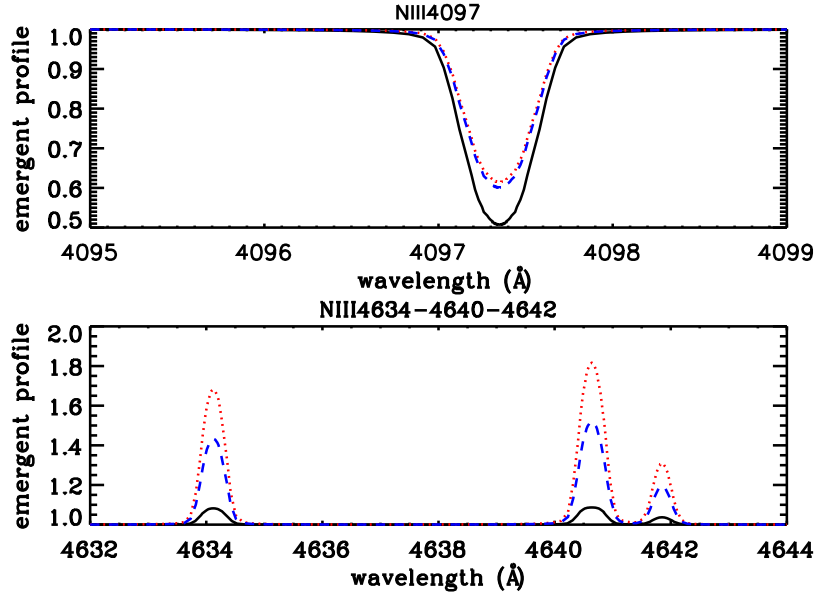


Figure 4.5: Comparison of FASTWIND N III line profiles from model ‘T3740’ with ‘pseudo line-blanketing’, using different atomic data sets. Solid (black): ‘mixed’ N III model (see text); dotted (red): new N III model; dashed (blue): new N III model, but DR-contribution to 3d level diminished by a factor of two.

line is always in absorption throughout the grid, though our calculations predict moderately more absorption in this line. All lines show the same trend in both sets, and the remaining differences might be attributed to still somewhat different atomic data.¹¹

We note already here that in all cases the emission is more pronounced in low-gravity objects. In high-gravity objects (dwarfs) part of the emission is suppressed because of higher collisional rates ($\propto n_e$), driving the relative populations towards LTE.

After demonstrating that we can (almost) reproduce the profiles calculated by MH when similar conditions are applied, the next step is to investigate the effect of the new N III atomic data implemented during the present work. In fact, this leads to much more triplet emission, see Figs. 4.4 (purple squares) and 4.5 (dotted profiles). Even for the coolest models, where MH still obtain weak absorption, our calculations result in strong emission. This big difference is produced by larger DR rates into 3d and a larger drain of 3p by the ‘two electron transitions’, due to larger oscillator strengths (see Table 4.2).¹² Note also that the $\lambda 4097$ line becomes weaker, in accordance with the correlation predicted above.

The reaction of the emission strength on the dielectronic data also allows us to check the validity of the implementation of dielectronic recombination by the explicit method, described in Sect. 4.3.2, particularly the dependence on the oscillator strength of the stabilizing transition(s). Figures 4.4 (blue asterisks) and 4.5 (dashed) show the reaction of the triplet lines if we diminish the oscillator strength

¹¹Number of levels, collisional data and LTE assumption concerning the quartet system levels by MH.

¹²A similar effect has already been noted by MH when they increased the corresponding oscillator strengths in their atomic model.

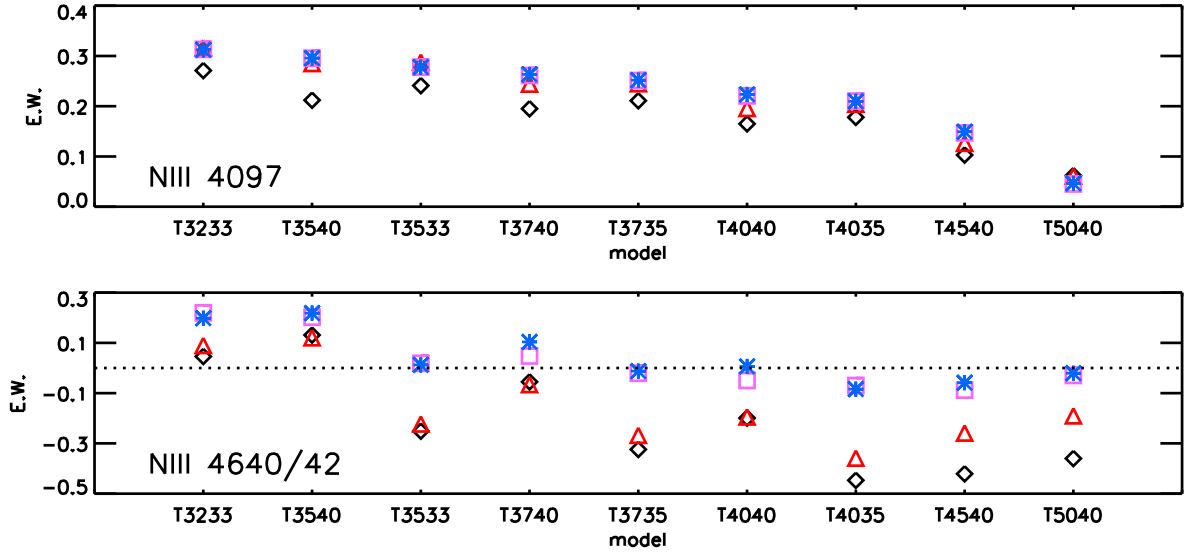


Figure 4.6: Comparison of equivalent widths (EW) for N III $\lambda 4097$ and $\lambda\lambda 4640/42$. Diamonds and triangles as Fig. 4.4. Purple squares: new results using new atomic data and realistic line-blanketing; blue asterisks: as squares, but DR-contribution to 3d level set to zero.

of the strongest stabilizing transition to 3d by a factor of two. This reduction leads to a significantly weaker emission throughout the whole grid, and a slight increase in the absorption strength of $\lambda 4097$. For a further test on the consistency between implicit and explicit method, see Sect. 4.3.2.

4.4.2 Models with full line-blanketing

In their study, MH could not consider the problem for realistic atmospheres accounting for a consistent description of line-blocking/blanketing, simply because such atmospheric models did not exist at that time. To investigate the differential effect on the N III emission lines, we calculated the same grid of models, now including full line-blanketing¹³ as incorporated to FASTWIND, and compare with the MH calculations (Fig. 4.6, purple squares vs. black diamonds, respectively).

Astonishingly, the triplet emission almost vanishes throughout the whole grid. This dramatic result points to the importance of including a realistic treatment of line-blanketing when investigating the emission line problem in Of stars. It further implies, of course, that the new mechanism preventing emission in line-blanketed models needs to be understood, and that an alternative explanation/modeling for the observed emission must be found.

Let us first investigate the ‘inhibition effect’, by considering model ‘T3735’ that displays one of the largest reactions. The most important consequence of the inclusion of line-blocking/blanketing is the decrease of the ionizing fluxes in the EUV. Figure 4.7 (left panel) displays corresponding radiation temperatures as a function of wavelength, for the ‘pseudo line-blanketed’, simple model constructed in analogy to MH (dashed) and the fully line-blanketed model (solid).

Indeed, the presence of substantially different ionizing fluxes around and longward of the N III

¹³Using background metallicities corresponding to the ‘older’ solar abundances from Grevesse & Sauval (1998), but keeping $[N] = 8.18$.

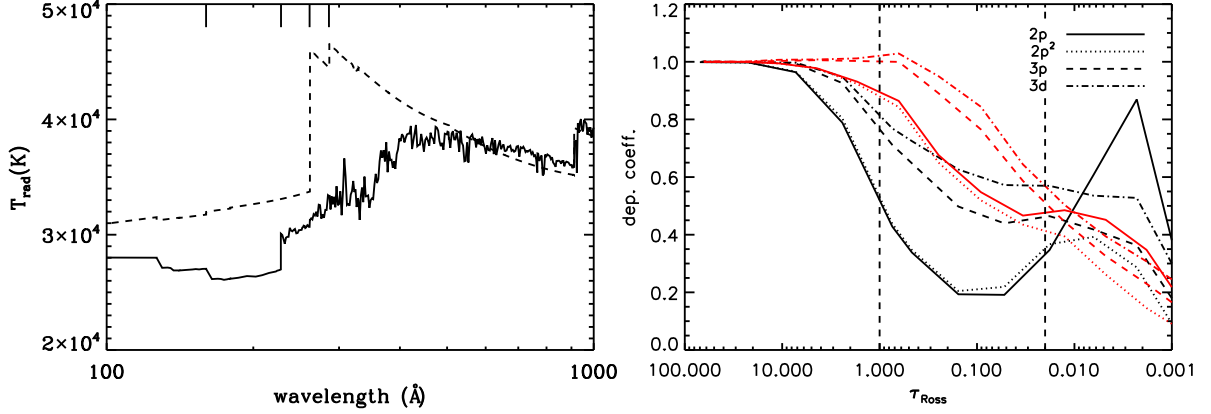


Figure 4.7: Left panel: EUV radiation temperatures for model ‘T3735’ with pseudo (dashed) and full (solid) line-blanketing. Important ionization edges are indicated as vertical markers. From left to right: N IV, He II, N III (ground-state), and N III $2p^2 \ ^2D$. Right panel: Departure coefficients for important levels regarding the triplet emission, for model ‘T3735’ with pseudo (black) and full (red) line-blanketing (level 2p is the ground-state). The formation region of the triplet lines is indicated by vertical dashed lines. See text.

edge is the origin of the different triplet emission, via two alternative routes. For part of the cooler models (not the one displayed here), significantly higher radiation temperatures in the N III continuum ($\lambda < 261 \text{ \AA}$) of the ‘pseudo line-blanketed’ models lead to a strong ground-state depopulation. Moreover, the ground-state and the $2p^2$ levels are strongly collisionally coupled, from the deepest atmosphere to the line-forming region of the photospheric lines. Thus, the ground-state and the $2p^2$ levels react in a coupled way. If the ground-state becomes depopulated because of a strong radiation field, the $2p^2$ levels become underpopulated as well, giving rise to a strong drain from level 3p and thus a large source-function for the triplet lines. Corresponding models including a realistic line-blocking (with lower EUV-fluxes) cause much less depopulation of the ground-state and the $2p^2$ levels, thus suppressing any efficient drain and preventing strong emission in the triplet lines.

For hotter models, e.g., model ‘T3735’ as considered here, the operating effect is vice versa, but leads to the same result. In the simple, MH-like model, the $2p^2$ levels become strongly depopulated in a direct way, because (i) the ionizing fluxes at the corresponding edges ($\lambda > 261 \text{ \AA}$) are extremely high (the ‘pseudo line-blanketing extends ‘only’ until 261 \AA), and (ii) because also a strong ionization via doubly excited levels is present, again due to a strong radiation field at the corresponding transition wavelengths around $290\text{--}415 \text{ \AA}$. Due to the depopulation of the $2p^2$ levels, the coupled ground-state becomes depopulated as well.

On the other hand, the depopulation via direct and ‘indirect’ ionization from $2p^2$ does not work for consistently blocked models, because of the much lower ionizing fluxes. Insofar, the extension of the He II ground-state ionization cross section by MH, to mimic the presence of line-blocking, was not sufficient. They should have extrapolated this cross-section at least to the edge of the lowest $2p^2$ level. In this case, however, they would have found much lower N III emission, too low to be consistent with observations.

In Fig. 4.7 (right panel), we compare the corresponding departure coefficients. Black curves refer to the simple, ‘pseudo line-blanketed’ model, and red curves to the corresponding model with full

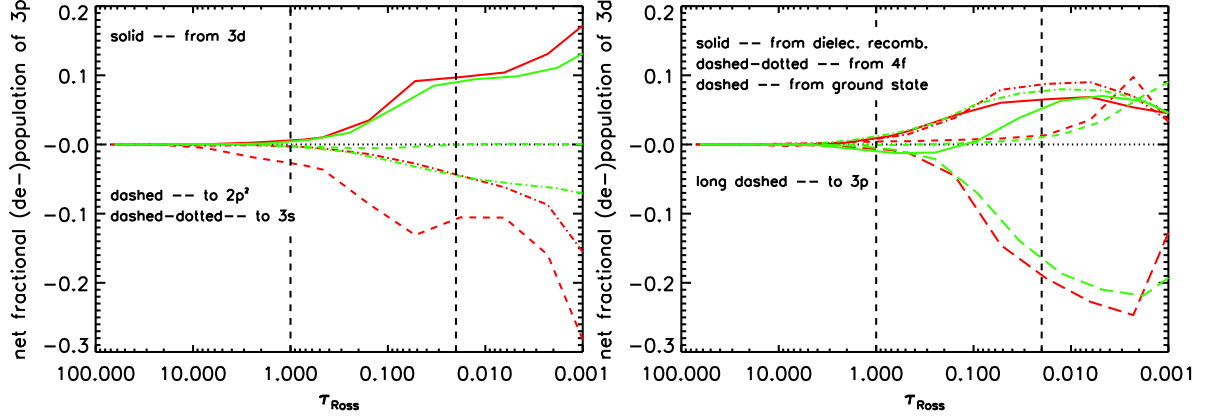


Figure 4.8: Fractional net rates to and from level 3p (left panel) and level 3d (right panel), for model ‘T3735’ with pseudo (red) and full (green) line-blanketing. The formation region of the triplet lines is indicated by vertical dashed lines.

line-blocking/-blanketing. Obviously, both models display strongly coupled ground and $2p^2$ states in the formation region of photospheric lines (here: $\tau_{\text{Ross}} \geq 0.02$), where these states are much more depopulated in the simple model.

For the conditions discussed so far, a significant depopulation of $2p^2$ is a prerequisite for obtaining strong emission lines in the optical: only in this case, an efficient drain $3p \rightarrow 2p^2$ due to cascading processes can be produced. The consequence of different draining efficiencies becomes obvious if we investigate the run of b_{3p} (dashed). In the pseudo-blanketed model, this level becomes much more depopulated relative to 3d (dashed-dotted), leading to much stronger triplet emission than in the full blanketed model.

The impact of the different processes can be examined in detail if we investigate the corresponding net rates responsible for the population and depopulation of level 3p (Fig. 4.8, left panel). In this and the following similar plots, we display the dominating individual net rates (i.e., $n_j R_{ji} - n_i R_{ij} > 0$ for population, with index i the considered level) as a fraction of the total population rate.¹⁴

Indeed, there is a dramatic difference in the net rates that depopulate level 3p via the ‘two electron’ drain (dashed). Whereas for the ‘pseudo line-blanketed’ model the net rate into $2p^2$ is the dominating one (resulting from the strong depopulation of $2p^2$), this rate almost vanishes for the model with full line-blanketing. In contrast, the other two important processes, the population by 3d (solid) and the depopulation into 3s (dashed-dotted) are rather similar. Consequently, 3p becomes less depopulated compared to 3d in the fully blanketed models. Moreover, since the (relative) depopulation into 3s remains unaffected, and 3p has a larger population (see Fig. 4.7), level 3s becomes stronger populated as well. Thus, the blanketed models produce more absorption in $\lambda 4097$ (cf. Fig. 4.6 with Fig. 4.4, squares in upper panels).

Since in the older MH-models the triplet emission is also due to the strong population of 3d via DR (Fig. 4.8, right panel, red solid), we have to check how the presence of full line-blocking affects this process. In this case, the net-rate from DR (green solid) becomes even negative in part of the line forming region, i.e., the ionization via intermediate doubly excited states partly outweighs the

¹⁴Which in statistical equilibrium is identical to the total depopulation rate.

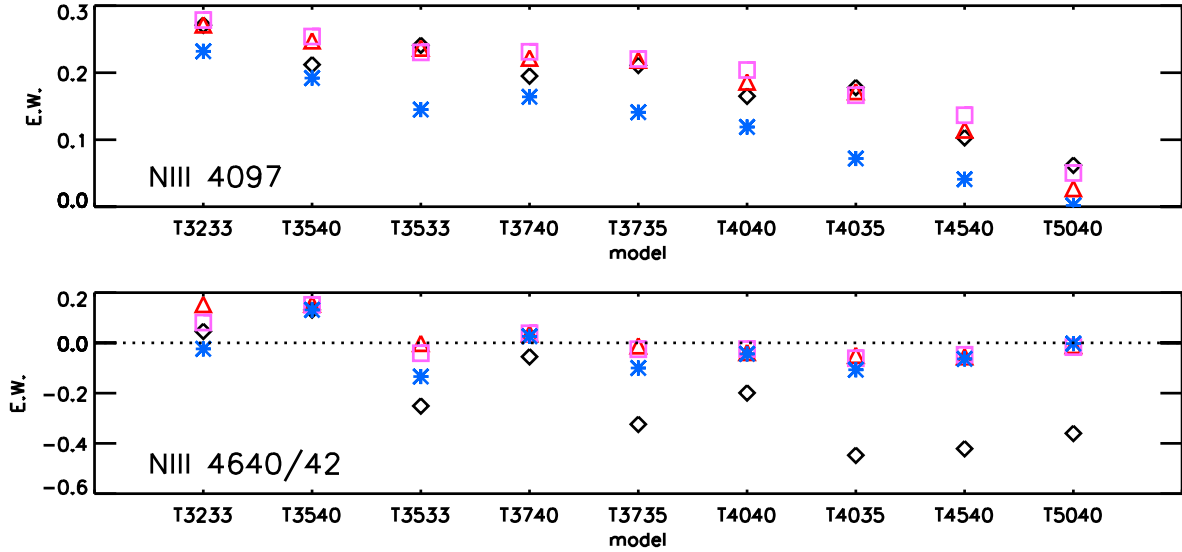


Figure 4.9: Comparison of equivalent widths for N III $\lambda 4097$ and $\lambda\lambda 4640/42$. Black diamonds as in Fig. 4.4 (original results from MH). Other models with $[N]=7.92$. Blue asterisks from TLUSTY (OSTAR2002), red triangles from FASTWIND, using new atomic data and realistic line-blanketing; purple squares: as triangles, but with temperature and electron stratification from TLUSTY. For details, see text.

dielectronic recombination. This difference originates from two effects: (i) the photospheric electron densities in the older models are larger, because of missing radiation pressure from metallic lines. Higher electron densities imply higher recombination rates. (ii) In the fully blanketed models, the radiation field at the frequency of the main stabilizing transition to 3d (777 \AA) is slightly higher (see left panel on Fig. 4.7), which leads to more ionization. Consequently, DR plays only a minor (or even opposite) role in the fully blocked models, contrasted to the MH case. In the blocked models, the major population is via the 4f level (dashed-dotted). Note also that the Swings mechanism, i.e., a population via the resonance line at 374 \AA (dashed), does not play any role in photospheric regions, as already argued by BM71 and shown by MH.

For a final check about the importance of DR to level 3d in models with full line-blanketing, we tested its impact by switching off the main stabilizing transition. From Fig. 4.6 (blue asterisks), it is obvious that the effect indeed is marginal throughout the whole grid. *Thus, a correct treatment of line-blocking seems to suppress both the efficiency of the draining transitions and the dielectronic recombination*, and we have to ask ourselves how the observed triplet emission is produced, since the presence of line-blocking cannot be argued away.

Before tackling this problem, in Fig. 4.9 we compare our results (red triangles) with those from TLUSTY (Hubeny 1988; Hubeny & Lanz 1995)¹⁵ (blue asterisks), as provided by the OSTAR2002 grid¹⁶ (Lanz & Hubeny 2003; see also Heap et al. 2006). Contrasted to all other similar plots, we used an abundance of $[N] = 7.92$, to be consistent with the TLUSTY grid. Obviously, our FASTWIND results

¹⁵A code that assumes plane-parallel geometry, hydrostatic and radiative equilibrium, and calculates line-blanketed NLTE model atmospheres and corresponding synthetic profiles. Due to its restrictions, only objects with negligible winds can be analyzed.

¹⁶Equivalent widths from own integration.

for the N III emission lines in dwarfs match exactly those from TLUSTY, whereas our results for supergiants display somewhat less emission (or more absorption). On the other hand, the absorption line at $\lambda 4097$ is systematically stronger in all our models, which points to different oscillator strengths. To rule out potential differences in the atmospheric stratification, we calculated an additional grid with temperature and electron structure taken from TLUSTY, smoothly connected to the wind structure as calculated by FASTWIND. Corresponding results are displayed by purple squares, and differ hardly from those based on the original FASTWIND structure, except for model T3233 where the differences in T and n_e are larger than elsewhere. The remaining discrepancies for supergiants can be explained by somewhat higher EUV fluxes in the TLUSTY models, favouring more N III triplet emission. Nevertheless, the disagreement between FASTWIND and TLUSTY is usually much weaker than between these two codes and the results by MH, which underpins our finding that the triplet emission becomes strongly suppressed in fully blanketed models.

4.4.3 The impact of wind effects

So far, one process has been neglected, namely the (general) presence of winds in OB-stars. Note that MH had not the resources to reproduce O-stars with truly “extended” atmospheres. Regarding their O(f) and O((f)) objects, on the other hand, there was no need to consider wind effects, because the observed N III triplet emission could be simulated by accounting for DR and ‘two-electron’ drain alone. Actually, MH pointed out that in Of-supergiants (with denser winds) the Swings mechanism could play a crucial role in the overpopulation of 3d: Velocity fields are able to shift the resonance lines into the continuum, allowing them to become locally more transparent, and deviations from detailed balance and strong pumping might occur.

With the advent of new atmospheric codes, we are now able to investigate the general role of winds, and to explain how the emission lines are formed within such a scenario. To this end, we have re-calculated the model grid from Table 4.1, now including the presence of a wind. Prototypical values for terminal velocity and velocity-field exponent have been used, $v_\infty = 2,000 \text{ km s}^{-1}$, $\beta = 0.9$, and mass-loss rates were inferred from the wind-momentum luminosity relationship (WLR) provided by Repolust et al. (2004), which differentiates between supergiants and other luminosity classes. Clumping effects have been neglected, but will be discussed in Sect. 4.7. For a summary of the adopted mass-loss rates, see Table 4.1.

With the inclusion of winds now, we almost recover the emission predicted in the original MH calculations (Fig. 4.10). Less emission is produced only for the two hottest models, where the inclusion of a wind has no effect. For all other models, however, the wind effect is large, both for the supergiants and for the dwarfs with a rather low wind-density.

To understand the underlying mechanism, we inspect again the fractional net rates, now for the wind-model ‘T3735’ (Fig. 4.11). Obviously, the wind induces a significant overpopulation of the 3d level via the ground state rather than the dielectronic recombination, just in the way as indicated above. Due to the velocity field induced Doppler-shifts, the resonance line(s) become desaturated, the rates are no longer in detailed balance, and considerable pumping occurs because of the still quite large radiation field at 374 \AA and the significant ground-state population (larger than in the MH-like models). Interestingly, this does not only happen in supergiants, as speculated by MH, but also in dwarfs (at least those with non-negligible mass-loss rate), because the velocity field sets in just in those regions where the emission lines are formed.¹⁷

¹⁷An analogous desaturation through velocity field induced Doppler shifts in stars with low mass loss rates was found by

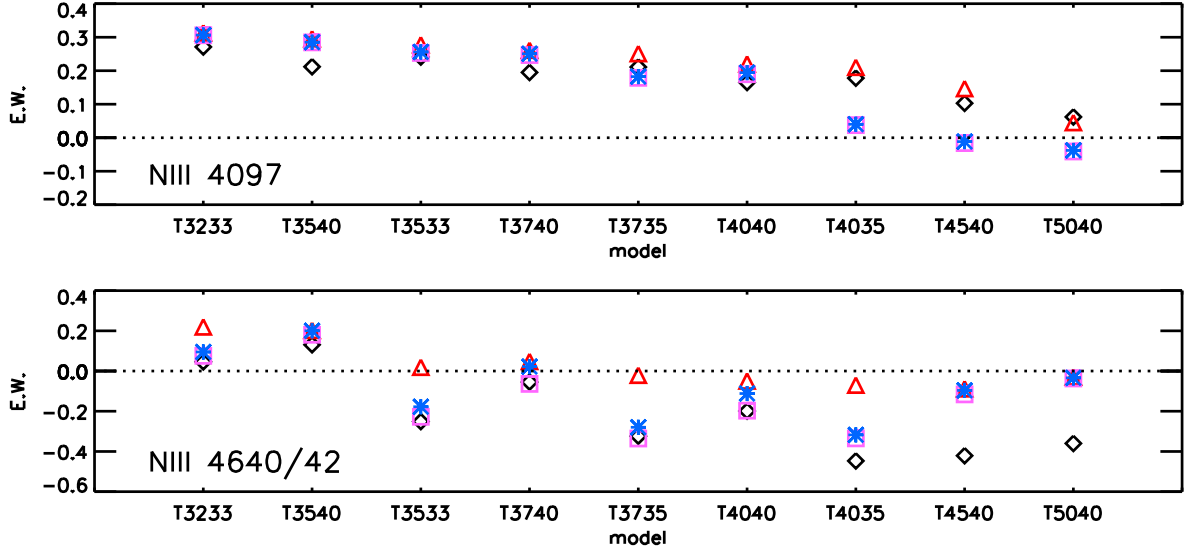


Figure 4.10: Comparison of equivalent widths (EW) for N III λ 4097 and $\lambda\lambda$ 4640/42. Black diamonds as in Fig. 4.4 (results from MH). Red triangles: new results using new atomic data, realistic line-blanketing, no winds; purple rectangles: new results using new atomic data, realistic line-blanketing and winds with a mass-loss rate according to the wind-momentum luminosity relation provided by Repolust et al. (2004); blue asterisks: as purple, but with DR contribution to 3d level set to zero.

The impact of the wind on the population of the 3p level is not as extreme, and the ‘two electron transition’ drain remains as weak as for the wind-free model. Thus, the presence of emission relies mostly on the overpopulation of the 3d level.

Again, we test the (remaining) influence of dielectronic recombination by switching off the stabilizing transition to 3d. Though there is a certain effect, the change is not extreme. Note also that the net rate from dielectronic recombination is larger in the wind model than in the wind-free model, see Fig. 4.11 (green solid line). Nevertheless, we conclude that dielectronic recombination plays, if at all, only a secondary role in the overpopulation of the 3d level when consistent atmospheric models are considered. *The crucial process is pumping by the resonance lines.*

The reaction of λ 4097 on velocity field effects is more complex. On the one side, there is still the cascade from 3p to 3s, giving rise to a certain correlation. On the other, the resonance line to 3s (at 452 Å) becomes efficient now, and can either feed (as argued in Sect. 4.2) or drain level 3s, in dependence of its optical depth. Under the conditions discussed here, the resonance line is pumping at cooler temperatures, with a zero net effect on the strength of λ 4097 (since the cascade from 3p becomes somewhat decreased, compared to wind-free models). At higher temperatures, the resonance line becomes optically thin,¹⁸ because of a lower ground-state population, and level 3s can cascade to the ground-state. Thus, the absorption strength of λ 4097 might become significantly reduced, which explains, e.g., the strong deviation of model ‘T4035’ from the MH predictions. For this and the hotter models, λ 4097 is very weak, and even appears in (very weak) emission for model ‘T5040’.

¹⁸Najarro et al. (1996) in the He I resonance lines of B giants.

¹⁸Note that the oscillator strength is more than a factor of 10 lower than that of the resonance line feeding 3d.

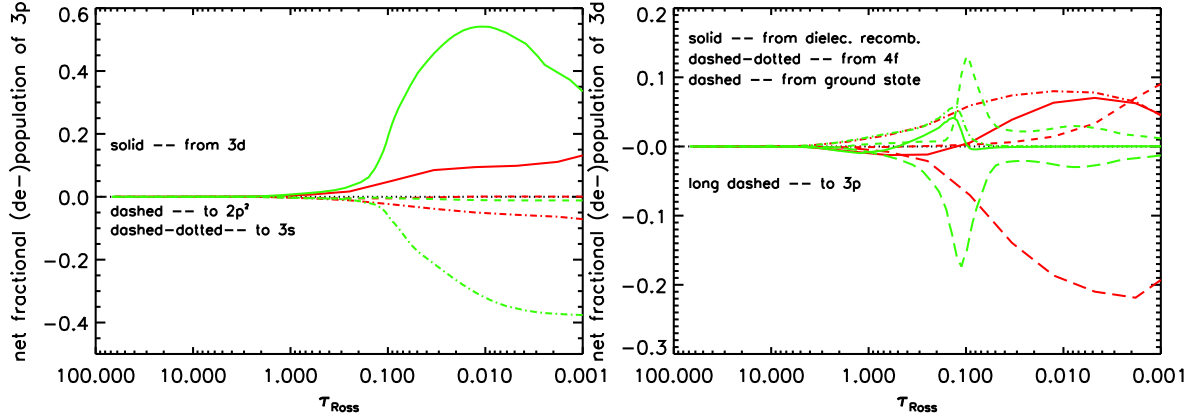


Figure 4.11: Fractional net rates to and from level 3p (left) and level 3d (right), for model ‘T3735’ (full line-blanketing) with no wind (red) and with wind (green).

4.5 Comparison with results from CMFGEN

In this section, we compare the results from our FASTWIND models with corresponding ones from CMFGEN, a code that is considered to produce highly reliable synthetic spectra, due to its approach of calculating all lines (within its atomic database) in the comoving frame. For this purpose, we used a grid of models for dwarfs and supergiants in the O and early B-star range, which has already been used in previous comparisons (Lenorzer et al., 2004; Puls et al., 2005; Repolust et al., 2005). FASTWIND models have been calculated with three ‘explicit’ atoms, H, He and our new N atom. Stellar and wind parameters of the grid models are listed in Table 4.3, with wind parameters following roughly the WLR for Galactic stars. The model designations correspond only coarsely to spectral types and are, with respect to recent calibrations (Repolust et al., 2004; Martins et al., 2005a), somewhat too early. All calculations have been performed with the ‘old’ solar nitrogen abundance, $[N] = 7.92$ (Grevesse & Sauval, 1998), and a micro-turbulence $v_{\text{turb}} = 15 \text{ km s}^{-1}$.

For the comparison between FASTWIND and CMFGEN results, we consider useful diagnostic N II (to check the cooler models) and N III lines in the blue part of the visual spectrum, see Table 3.5 in Chapter 3.

Although most of the N III lines listed in Table 3.5 are (usually) visible in not too early O-type spectra, their diagnostic potential for abundance determinations is different. The lines at $\lambda\lambda 4510$ - 4514 - 4518 (from the quartet system) are certainly the best candidates to infer abundances, since they are quite strong and their formation is rather simple. Also the N III triplet itself provides valuable information. Due to its complex formation – when in emission – and additional problems (see below and Sect 4.6), these lines should be used only as secondary diagnostics, whenever possible. The remaining N III lines in the blue part of the visual spectrum are rather weak and/or strongly blended with adjacent lines (see Table 3.5). In particular, the (theoretically) very interesting transition $3p \rightarrow 3s$, N III $\lambda 4097$, is located within the Stark-wing of H_{δ} . Thus, these lines should be used preferentially as a consistency check, and employed as a direct abundance indicator only at low rotation. Lines in the yellow part of the optical (‘group four’, see Sect. 3.3) have not been considered by us so far, since our observational material does not cover this spectral range, and we are not able to judge their diagnostic value for O-type stars. Finally, lines from ‘group five’ in the red are usually rather weak,

Table 4.3: Stellar and wind parameters of our model grid used to compare synthetic N II/N III profiles from FASTWIND and CMFGEN. The grid is a subset of the grid presented by Lenorzer et al. (2004).

Luminosity class V						
Model	T_{eff} (K)	R_* (R_{\odot})	$\log g$ (cgs)	\dot{M} ($10^{-6} M_{\odot} \text{yr}^{-1}$)	v_{∞} (km s^{-1})	β
d2v	46100	11.4	4.01	2.52	3140	0.8
d4v	41010	10.0	4.01	0.847	2850	0.8
d6v	35900	8.8	3.95	0.210	2570	0.8
d8v	32000	8.0	3.90	0.056	2400	0.8
d10v	28000	7.4	3.87	0.0122	2210	0.8
Luminosity class I						
Model	T_{eff} (K)	R_* (R_{\odot})	$\log g$ (cgs)	\dot{M} ($10^{-6} M_{\odot} \text{yr}^{-1}$)	v_{∞} (km s^{-1})	β
s2a	44700	19.6	3.79	12.0	2620	1.0
s4a	38700	21.8	3.57	7.35	2190	1.0
s6a	32740	24.6	3.33	3.10	1810	1.0
s8a	29760	26.2	3.21	1.53	1690	1.0
s10a	23780	30.5	2.98	3.90	740	1.0

and might be used only in high S/N spectra of slowly rotating stars.

A detailed comparison between the various N II (for the later subtypes) and N III lines from FASTWIND and CMFGEN is provided in Appendix B.1. Overall, the following trends and problems have been identified.

For models d10v, d8v, and s10a (Figs. B.1, B.2, and B.3, respectively), the agreement of the N II lines is almost perfect. For model s8a (Fig. B.4), on the other hand, big discrepancies are found. Most of our lines are much stronger than those from CMFGEN, because of the following reason. Within the line-forming region, the electron density as calculated by FASTWIND is a factor of ≈ 8 higher than the one as calculated by CMFGEN, thus enforcing higher recombination rates from N III to N II, more N II and thus stronger lines. This is the only model with such a large discrepancy in the electron density (e.g., the electron densities from models s10a and s6a agree very well), and the reason for this discrepancy needs to be identified in future work. Nevertheless, this discrepancy would not lead to erroneous nitrogen abundances: When analyzing the observations, a prime diagnostic tool are the wings of the hydrogen Balmer lines that react, via Stark-broadening, sensitively on the electron density. After a fit of these wings has been obtained, one can be sure that the electron stratification of the model is reasonable (though the derived gravity might be erroneous then). With a ‘correct’ electron density, however, the abundance determination via N II should be no further problem.

Let us concentrate now on the N III lines, beginning with the triplet $\lambda\lambda 4634\text{-}4640\text{-}4642$ and accounting for the fact that at cooler temperatures the $\lambda 4642$ component is dominated by an overlapping O II line (see Table 3.5). Except for the dwarf model d6v and the supergiant models s8a and s6a, both codes predict very similar absorption (for the cooler models) and emission lines, thus underpinning the results from our various tests performed in Sect. 4.4. Interestingly, our emission lines for the hottest dwarfs (d4v and d2v, Figs. B.8 and B.9) are slightly stronger than those predicted

by CMFGEN, a fact that is not too worrisome accounting for the subtleties involved in the formation process.

What *is* worrisome, however, is the deviation for models d6v, s8a and s6a (Figs. B.7, B.11 and B.12). Whereas FASTWIND predicts only slightly refilled absorption profiles for all three models, CMFGEN predicts almost completely refilled (i.e., $EW \approx 0$) profiles for d6v and s8a, and well developed emission for s6a.

We investigated a number of possible reasons for this discrepancy. At first, the difference in electron density for model s8a (see above) could not explain the strong deviations. At least for our FASTWIND models, dielectronic recombination does not play any role, and we checked that this is also the case for the CMFGEN models, by switching off DR. As it finally turned out, the physical driver that overpopulates the 3d level in CMFGEN in the considered parameter range is a coupling with the O III resonance line at 374 Å, which is discussed in the next section.

With respect to N III $\lambda 4097$, we find a certain trend in the deviation between FASTWIND and CMFGEN absorption profiles. Both for dwarfs and supergiants, our line is weaker at cooler temperatures, similar at intermediate ones and stronger at hotter temperatures.

For N III $\lambda 4379$, the CMFGEN models predict more absorption for models with $T_{\text{eff}} \leq 35,000$ K, because of an overlapping O II and C III line. For hotter models, the presence of O II is no longer important, but there is still a difference for $\lambda 4379$, going into emission at the hottest temperatures.

For the quartet multiplet at $\lambda \lambda 4510\text{-}4514\text{-}4518$, we find a similar trend as for $\lambda 4097$. For dwarfs, the lines are weaker at cooler temperatures, similar at d6v and stronger in absorption at d4v. Likewise then, the emission at d2v is weaker than in CMFGEN. For supergiants, the situation is analogous, at least for all models but the hottest one where both codes predict identical emission.

Finally, lines $\lambda 4003$ and $\lambda 4195$ (note the blueward Si III blend at hotter temperatures) show quite a good agreement for both dwarfs and supergiants, with somewhat larger discrepancies only for models d4v and s4a.

In summary, the overall agreement between N II and N III profiles as predicted by FASTWIND and CMFGEN is satisfactory, and for most lines and models the differences are not cumbersome. Because of the involved systematics, however, abundance analyses might become slightly biased as a function of temperature, if performed either via FASTWIND or via CMFGEN. Additionally, we have identified also some strong deviations, namely with respect to N II line-strengths for supergiants around $T_{\text{eff}} \approx 30$ kK,¹⁹ and regarding the emission strengths of the N III triplet, for models d6v, s8a, and s6a.

4.6 Coupling with O III

After numerous tests we were finally able to identify the origin of the latter discrepancy. It is the overlap of two resonance lines from O III and N III around 374 Å (for details, see Table 4.4) that is responsible for the stronger emission in CMFGEN models compared to the FASTWIND results. Whereas this process is accounted for in CMFGEN, our present FASTWIND models cannot do so, because oxygen is treated only as a background element, and no exact line transfer (including the overlap) is performed. We note that this is not exactly the Bowen (1935) mechanism as mentioned in Sect. 4.2, since this mechanism involves also the overlap between another O III resonance line and the He II Ly- α line at 303 Å, which does not play a strong role in our CMFGEN models as we have convinced

¹⁹Rooted within a different stratification of electron density.

Table 4.4: Overlapping N III and O III resonance lines around 374 Å. Packed levels/transitions and overlapping (‘coupled’) ones. ‘low’ = lower term/level, ‘up’ = upper term/level, g_l and g_u corresponding statistical weights. ‘Ratio’ indicates the opacity ratio between overlapping and packed lines. Individual components at 374.20...374.44 Å for N III (3 components) and at 373.80...374.43 Å for O III (6 components). Note that 0.01Å correspond to 8 km s^{-1} . Data from NIST database.

transition(s)	λ (Å)	low	g_l	up	g_u	gf	ratio
N III (packed)		$2p \ ^2P^0$	6	$3d \ ^2D$	10	2.5	
N III coupl. comp.	374.434	$2p \ ^2P^0_{3/2}$	4	$3d \ ^2D_{5/2}$	6	1.5	0.60
O III (packed)		$2p^2 \ ^3P$	9	$3s \ ^3P^0$	9	0.72	
O III coupl. comp.	374.432	$2p^2 \ ^3P_2$	5	$3s \ ^3P^0_1$	3	0.06	0.14

ourselves.²⁰ Here, only the coupling between N III and O III at 374 Å is decisive.

In the following we discuss some details of the process, by means of the CMFGEN model S6A that displays the largest difference to the FASTWIND predictions. For a further investigation, we ‘decoupled’ N III from O III by setting the corresponding oscillator strength of the transition O III $2p^2 \ ^3P_2 \rightarrow 3s \ ^3P^0_1$ to a very low value, and compared the results with those from the ‘coupled’ standard model. Figure 4.12 shows that the well developed emission lines from the standard models switch into absorption, and become very similar to the corresponding FASTWIND profiles (Fig. B.12). On the other hand, discarding DR by neglecting the resonances in the photo cross-sections from level 3d had almost no effect on the profiles, in accordance with our previous arguments. (Actually, without resonances there is even more emission than before, which shows that for this model the ionization via doubly excited levels outweighs DR.)

Figure 4.13 displays the corresponding NLTE departure coefficients for the N III ground state, level 3p and level 3d. Because of the superlevel approach, there is no difference²¹ between level $3d \ ^2D_{5/2}$ (coupled to O III) and $3d \ ^2D_{3/2}$ (not coupled). Whilst the ground state and the 3p level remain similar for all three models (standard, ‘decoupled’ and ‘coupled’ with resonance-free photo cross-section for 3d), level 3d becomes much stronger overpopulated in the two ‘coupled’ models, compared to the ‘decoupled’ one.

The origin of this stronger overpopulation becomes obvious from Fig. 4.14. The upper panel displays the source functions of the N III/O III resonance lines for the ‘decoupled’ and ‘coupled’ case (again, no difference for individual components, due to the superlevel approach). For the ‘decoupled’ case, the N III source function is significantly lower than the O III one, whereas for the ‘coupled’ standard model both source functions are identical, at a level very close to the ‘decoupled’ O III case. These changes are visualized in the lower panel: because of the line overlap, the N III source function increases by a factor up to 1.35 (in the line forming region of the optical triplet lines), whereas O III decreases only marginally.

The source function equality itself results from the strong coupling of the two resonance lines and the fact that both of them are optically thick from the lower wind on, with similar opacities

²⁰ Insofar, the O III lines at $\lambda \lambda 3340, 3444, 3759$ mentioned in Sect. 4.2 remain in absorption.

²¹ Assumed to be balanced by collisions.

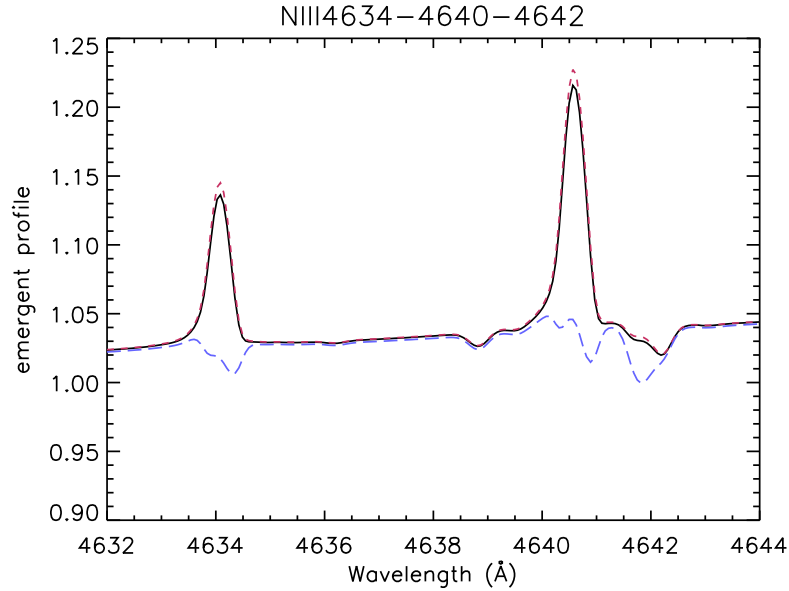


Figure 4.12: N III $\lambda\lambda$ 4634-4640-4642 for three versions of model s6a , as calculated by CMFGEN. Solid black: standard version; Dotted/red: photo cross-sections for level 3d without resonances (i.e., no DR); dashed/blue: N III resonance line at 374 Å forbidden to be affected by O III. For the latter model, the optical triplet lines remain in absorption!

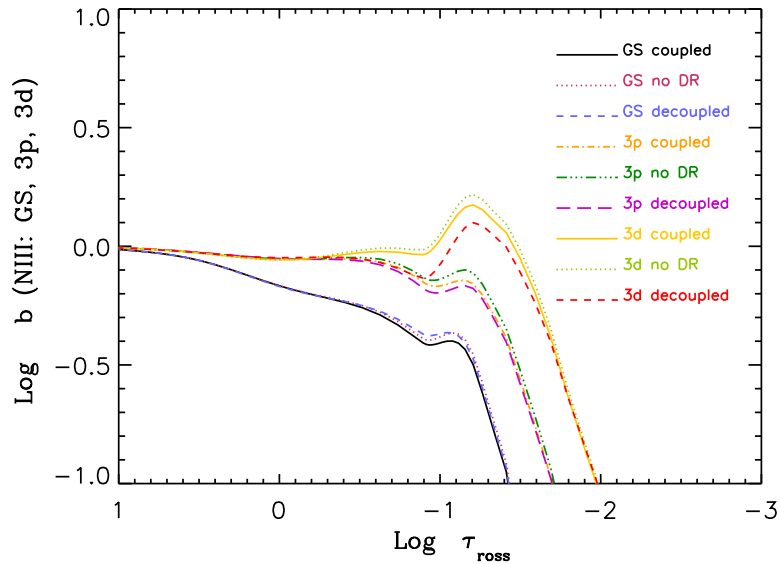


Figure 4.13: NLTE departure coefficients for three versions of model s6a , as calculated by CMFGEN. Lower group of curves: N III ground state; intermediate group: level 3p, upper group: level 3d. See text.

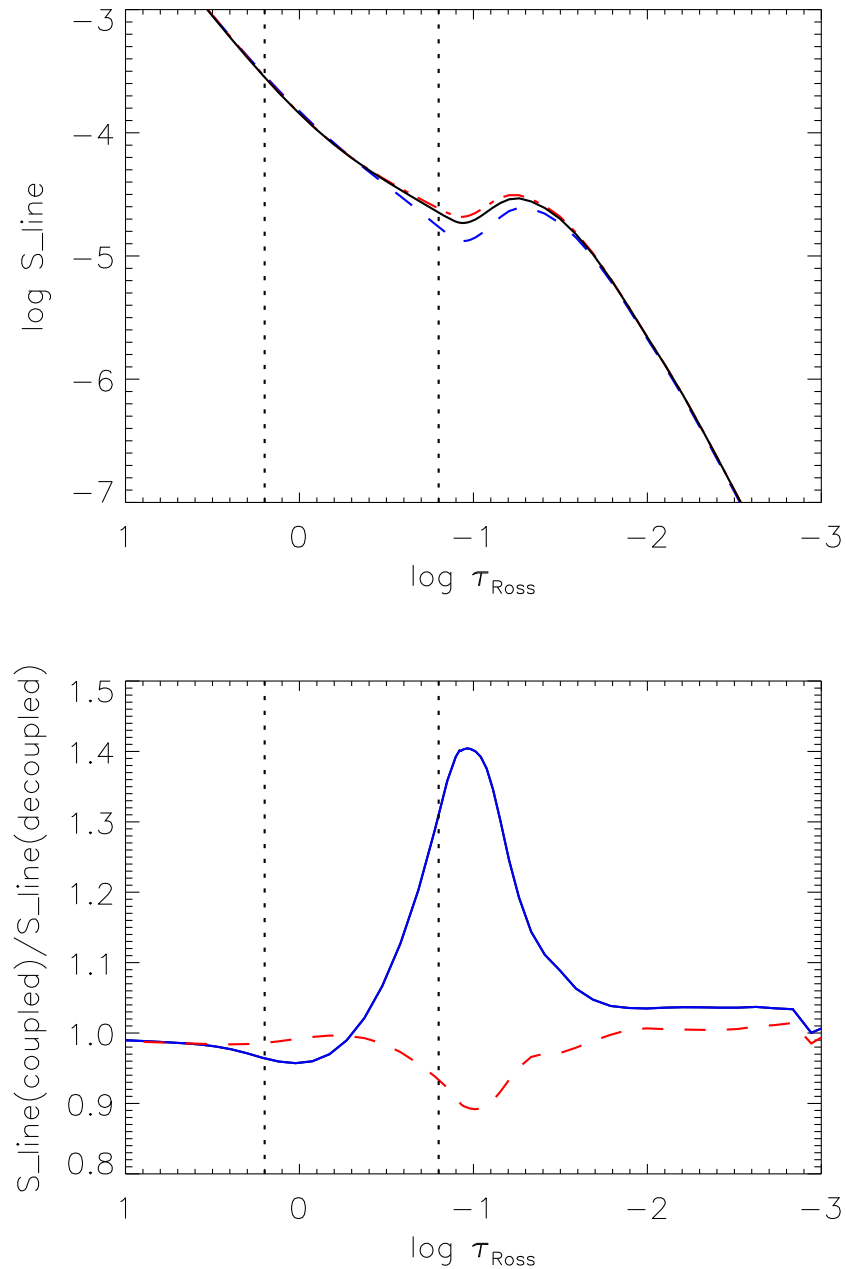


Figure 4.14: Line source functions for the N III/O III resonance lines at 374 \AA , for two versions of model s6a, as calculated by CMFGEN. *Upper panel:* N III ‘decoupled’ (dashed/blue); O III ‘decoupled’ (dashed-dotted/red); N III and O III ‘coupled’ (solid, identical). *Lower panel:* Source function ratios. Solid: N III (‘coupled’)/N III (‘decoupled’); dashed: O III (‘coupled’)/O III (‘decoupled’). The optical triplet lines are formed in the range indicated by the dotted lines.

(proportional to the product of cross-section, ionization fraction and abundance).²² It can be shown that the magnitude of the coupled source function mostly depends on those processes that determine the individual source functions in addition to the mean line intensity. This can be easily seen by using the Sobolev approximation,

$$\bar{J} = (1 - \beta)S + \beta_c I_c, \quad (4.21)$$

with scattering integral \bar{J} , local and core escape probabilities β and β_c , and core intensity I_c (Sobolev, 1960). In case of overlapping lines, the source function S and the opacities need to account for all components with appropriate weights.

We now assume that the individual source functions (for the packed levels) can be approximated by

$$S_N \approx \bar{J} + \delta_N, \quad S_O \approx \bar{J} + \delta_O, \quad (4.22)$$

where δ_N and δ_O correspond to the additional source terms (mostly from cascades to the upper levels), and the well-known factor²³ in front of \bar{J} has been approximated by unity.

\bar{J} includes the contributions from all transitions between the fine structure components, $\bar{J} = \sum g f_i \bar{J}_i / \sum g f_i$, exploiting the fact that the reduced occupation numbers for the fine structure levels are equal, $n_i/g_i = n_j/g_j$.

Let us first consider the case of no fine structure splitting, i.e., the overlapping resonance lines should be the only ones connecting the upper and lower levels. Without line overlap, we obtain the well-known result (solving for Eqs. 4.21 and 4.22 in parallel)

$$S_N^{\text{decoup}} = \frac{\beta_{c,N} I_c + \delta_N}{\beta_N}, \quad S_O^{\text{decoup}} = \frac{\beta_{c,O} I_c + \delta_O}{\beta_O}. \quad (4.23)$$

Likewise, but accounting for the line overlap and assuming $\beta \ll 1$ for both components, we find

$$\begin{aligned} S_N^{\text{coup}} &\approx S_O^{\text{coup}} \approx \frac{\beta_c I_c}{\beta} + \frac{\delta_N}{\beta_N} + \frac{\delta_O}{\beta_O} \approx \\ &\approx S_N^{\text{decoup}} + \frac{\delta_O}{\beta_O} \approx S_O^{\text{decoup}} + \frac{\delta_N}{\beta_N}, \end{aligned} \quad (4.24)$$

Thus, the coupled source functions are larger than in the decoupled case, but (almost) independent on the ratio of their contribution. (In the above equation, the first term of the sum does not depend on any specific opacity as long as the lines – coupled or decoupled – remain optically thick).

For the case of two multiplet lines from both N III and O III, with one of each overlapping, the corresponding result for the packed levels reads

$$S_N^{\text{coup}} \approx S_O^{\text{coup}} \approx \frac{\beta_c I_c}{\beta} + \frac{1}{3} \left(\frac{\delta_N}{\beta_N} + \frac{\delta_O}{\beta_O} \right), \quad (4.25)$$

where the escape probabilities β_N and β_O refer to the total opacity arising from both multiplet lines, and the factor ‘1/3’ can be traced down to the fact that three (optically thick) lines participate in total, two single lines from N III and O III, and one coupled line complex.

²²In the formation region of the optical lines, the opacity ratio between the N III and O III resonance lines ranges from roughly 5 for the coolest models to 0.5 for the hottest ones.

²³Corresponding to $(1-\epsilon)$ in a two-level atom, with ϵ roughly the ratio of collisional to spontaneous radiative rate coefficient, for the downward transition.

The corresponding source functions for the decoupled case with packed levels would read

$$S_{\text{N}}^{\text{decoup}} = \frac{\beta_{\text{c}} I_{\text{c}}}{\beta} + \frac{1}{2} \frac{\delta_{\text{N}}}{\beta_{\text{N}}}, \quad S_{\text{O}}^{\text{decoup}} = \frac{\beta_{\text{c}} I_{\text{c}}}{\beta} + \frac{1}{2} \frac{\delta_{\text{O}}}{\beta_{\text{O}}}, \quad (4.26)$$

(the factor of two arising from two participating multiplet lines), and a comparison with Eq. 4.25 shows that in most cases the coupled source function would lie in between the corresponding ones that neglect the line overlap. Again, our result is (almost) independent of the opacity ratio between the overlapping N III and O III lines but also independent of the weights of the individual lines within each multiplet.²⁴

Generalization to more multiplet lines is straightforward, and our analytic result compares well to the actual case where the N III and O III source functions for the coupled case are identical and lie in between the values for the decoupled situation, see Fig. 4.14, upper panel.

Thus, whenever the source function of the O III λ 374 line is significantly larger than the one from N III, a decent effect on the emission strength of the optical triplet lines is to be expected. This situation is particularly met around $T_{\text{eff}} = 30$ to 33 kK, since in this region the upper level of the O III line is significantly populated by cascades from higher levels.

First test calculations with a simplified oxygen model atom performed by FASTWIND confirm the general effect, but realistic results cannot be provided before a detailed model atom has been constructed. Let us note, however, that most of the other optical N III lines are barely affected by the resonance line coupling, and that these lines can be used for diagnostic purposes already now.

In Chapter 5 we derive nitrogen abundances for LMC O-stars from the VLT-FLAMES survey of massive stars. Though there are only few objects in the critical temperature range, at least for one object, N11-029 (O9.7Ib), we encountered the problem that the observed, refilled N III triplet (EW \approx 0) could not be reproduced by FASTWIND, though with CMFGEN. We interpret this problem as due to the resonance line overlap, but stress also the fact that other diagnostic lines enable a satisfactory abundance analysis.

4.7 Influence of various parameters

Let us finally investigate the influence of important parameters on the strength of the optical emission lines. We stress that the following results have an only qualitative, differential character, as long as the coupling with O III has not been accounted for, at least in the range $T_{\text{eff}} \lesssim 35\text{kK}$.

Nitrogen abundance. Figure 4.15 displays the reaction on a variation of nitrogen abundance and mass-loss rate. All models have been calculated with background abundances following Asplund et al. (2005). The (purple) squares correspond (almost, except for the background) to our previous results for $[\text{N}] = 8.18$ (0.4 dex larger than the solar value), and mass-loss rates according to Table 4.1. Reducing the nitrogen abundance to solar values, $[\text{N}] = 7.78$, results in considerably less emission (black diamonds), which is a consequence of the fact that the relative overpopulation of the 3d level decreases significantly when the formation depth proceeds inwards. The influence on N III λ 4097, on the other hand, is less extreme, and follows the standard trend that a higher abundance results in stronger absorption lines.

²⁴As long as $\beta \ll 1$.

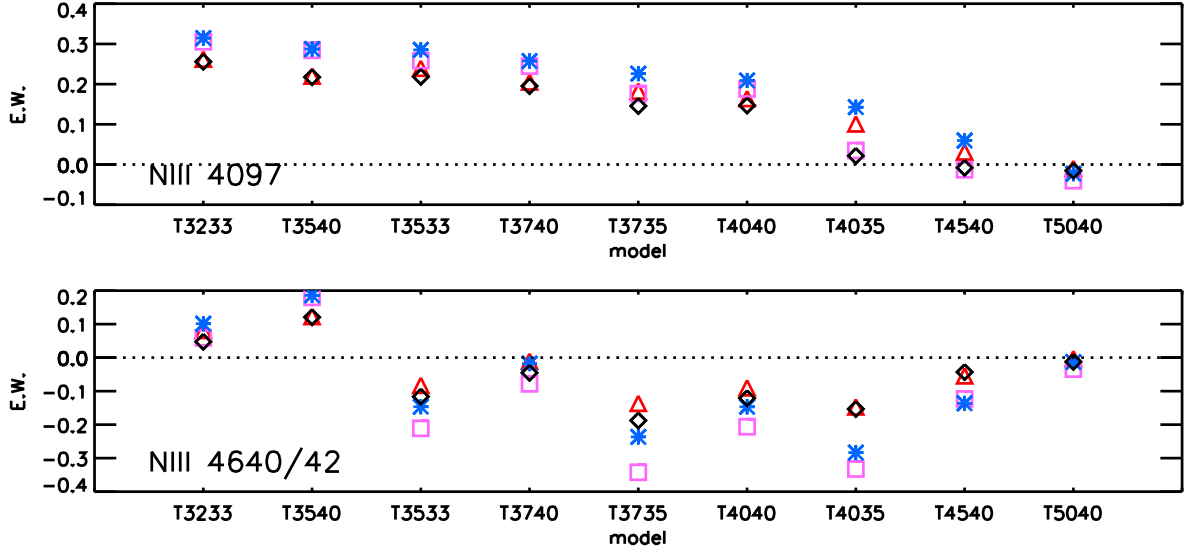


Figure 4.15: Comparison of equivalent widths (EW) for N III $\lambda 4097$ and $\lambda\lambda 4640/42$ for models with different nitrogen abundances and wind-strengths. Black diamonds: $[N] = 7.78$, mass-loss rates as in Table 4.1. Red triangles: as black diamonds, but with half the mass-loss rate. Purple squares: $[N] = 8.18$, mass-loss rates as in Table 4.1. Blue asterisks: as purple squares, but with half the mass-loss rate. All background abundances are solar (Asplund et al., 2005).

Mass-loss rates. Also in Fig. 4.15, asterisks (for $[N] = 8.18$) and triangles (for $[N] = 7.78$) correspond to a situation where the mass-loss rates have been decreased, by a factor of two compared to Table 4.1. Whereas the effect for the enriched models is significant, the models with solar nitrogen abundance are much less affected, though the predicted emission is still much stronger than for models without a wind at all, cf. Fig. 4.10 (triangles).

The origin of this different behaviour is, again, rooted in the specific run of the relative overpopulation of level 3d. For a large nitrogen abundance, the formation takes place in a region where the overpopulation increases quickly with increasing mass-loss rate, whereas for a lower abundance (deeper formation) it remains rather constant over a certain range of formation depths, such that a moderate change in \dot{M} has much less effect. Figures 4.13 and 4.14 (upper panel), with a formation region corresponding to $[N] = 7.92$, visualize the general situation (irrespective of whether coupling with O III is important or not): an increase of the nitrogen abundance shifts the formation depth to the right (towards lower τ_{Ross}), where the departure coefficient of level 3d and the source function display a ‘bump’, due to the large velocity gradient, inducing very strong pumping by the resonance line(s). A decrease of the wind-strength, on the other hand, shifts the position of the bump to the right, while (almost) preserving the formation depth with respect to τ_{Ross} . Thus, in case of a large nitrogen abundance the strong overpopulation is lost when \dot{M} decreases, leading to a corresponding loss of emission strength. For a lower abundance, however, the formation takes place in a region where the overpopulation displays a ‘plateau’, and a reduction of \dot{M} , i.e., a shift of the bump to the right, has a much weaker effect.

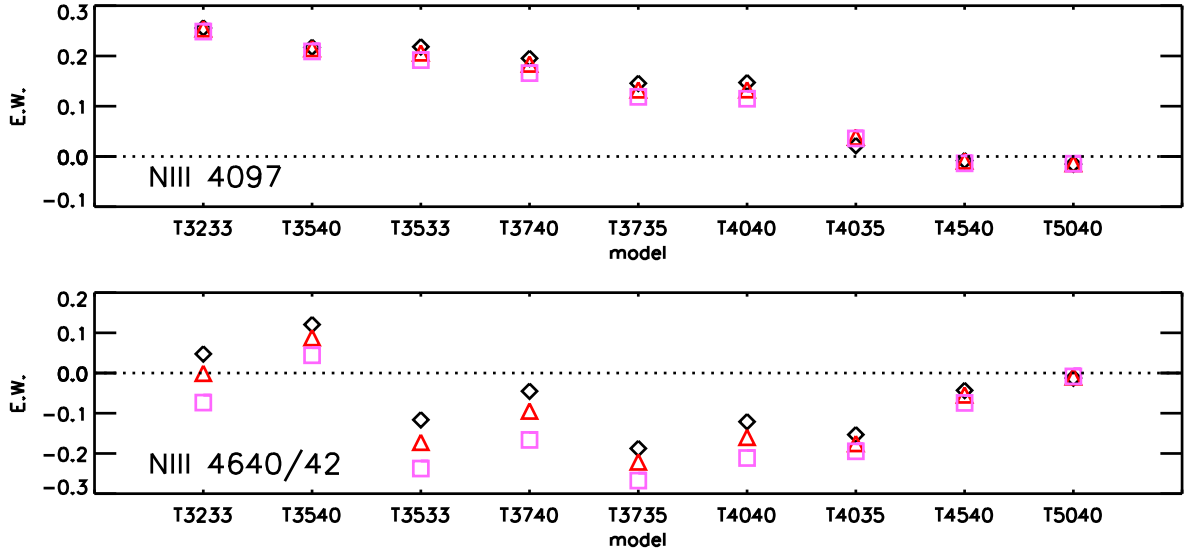


Figure 4.16: Comparison of equivalent widths (EW) for N III $\lambda 4097$ and $\lambda\lambda 4640/42$ for models with different background abundances, $[N] = 7.78$ and mass-loss rates as in Table 4.1. Black diamonds: $Z/Z_{\odot} = 1.0$; red triangles: $Z/Z_{\odot} = 0.5$; purple squares: $Z/Z_{\odot} = 0.2$. Background abundances scaled to solar abundance pattern from Asplund et al. (2005).

Wind clumping. Since the N III emission lines of O-stars are formed in the middle or outer photosphere,²⁵ wind clumping has no direct effect on their strength, as long as the photosphere remains unclumped (which is most likely the case, e.g., Puls et al. 2006; Sundqvist et al. 2011; Najarro et al. 2011). Only if the transition region wind/photosphere were clumped, such direct effects are to be expected, due to increased recombination and optically thick clumps affecting the resonance lines (Sundqvist et al., 2011). Indirect effects, however, can be large, since clumpy winds have a lower mass-loss rate than corresponding smooth ones. Since typical \dot{M} reductions are expected to be on the order of 2...3 when accounting for micro- and macro-clumping (Sundqvist et al. 2011 and references therein), Figure 4.15 (asterisks vs. squares and triangles vs. diamonds) gives also an impression on the expected effects when clumping were in- or excluded in the spectrum synthesis.

Background abundances. Figure 4.16 displays the effects when only the background abundances are varied, while, inconsistently, the nitrogen abundance is kept at its solar value and the wind-strengths correspond to the Galactic WLR. Diamonds refer to solar composition, triangles to $Z/Z_{\odot} = 0.5$ (roughly LMC) and squares to $Z/Z_{\odot} = 0.2$ (roughly SMC). In line with our reasoning from Sect. 4.4.2, the emission increases significantly when the background abundances decrease, due to reduced line-blocking. Note that for objects with unprocessed nitrogen this effect might be compensated by a lower nitrogen abundance, and, even more, because of lower wind-strengths ($\dot{M} \propto (Z/Z_{\odot})^{0.7}$, Mokiem et al. 2007b). Note also that the correlation between triplet emission and $\lambda 4097$ absorption strength has become rather weak, due to the influence of the resonance line connected to level 3s (see Sect. 4.4.3). Let us finally stress that because of the strong dependence of emission line strength

²⁵Only for a very large nitrogen abundance or mass-loss rate, ('slash stars' or Wolf-Rayets) the formation takes place in the wind.

on line-blocking, a sensible assumption on the atmospheric iron abundance is required, due to its dominating effect on the EUV fluxes.

4.8 Summary and conclusions

In this chapter, we concentrated on a re-investigation of the N III $\lambda\lambda 4634\text{-}4640\text{-}4642$ emission line formation. Previous, seminal work by MH has suggested that the formation mechanism of these emission lines in O((f)) and O(f) stars is dominated by two processes: the overpopulation of the 3d level via dielectronic recombination, and the strong drain of the 3p level (towards $2p^2$) by means of the ‘two electron transitions’.

To account for the dielectronic recombination process in our new N III model, we tested two different implementations. Within the implicit method, the contribution of dielectronic recombination is included in the photoionization cross-sections (provided from OPACITY project data), whereas the explicit method uses resonance-free photoionization cross-sections and directly accounts for the different stabilizing transitions from autoionizing levels. Both methods have been implemented into FASTWIND, and the equivalence of both methods has been shown.

First tests were able to reproduce the results by MH quite well, after adapting our new atomic data to values as used by them. This result was achieved by applying similar assumptions, i.e., wind-free atmospheres and the same approximate treatment of line-blanketing. The triplet emission becomes even increased when using our new atomic data, mostly because of higher oscillator strengths for the ‘two electron transitions’.

After switching to fully line-blanketed models (still wind-free), however, the situation changes dramatically. Then, the strong emission present in the ‘pseudo line-blanketed’ models is lost (consistent with results from the TLUSTY OSTAR2002 grid). We have investigated this mechanism in detail, and shown that it is rooted in the overall lower ionizing EUV-fluxes (not only until the N III edge as assumed by MH), either directly or indirectly, and the strong collisional coupling of the ground state and the $2p^2$ levels. In any case, these levels become much less underpopulated in fully line-blanketed models, thus preventing an effective drain of the 3p level. We also questioned the role of dielectronic recombination regarding the overpopulation of the 3d level. After setting the DR contribution to the 3d level to zero, almost no reaction on the triplet lines was found throughout the whole model grid. Both results lead to the conclusion that, under realistic conditions of line-blocking/-blanketing with solar background abundances, both the drain and the dielectronic recombination lose their key role as assigned to them by MH.

This key role is now played by the stellar wind. Already MH suggested that the emission lines of Of stars (contrasted to O((f)) and O(f) stars) might be formed due to the Swings (1948) mechanism, an overpopulation of the 3d level by pumping through the corresponding resonance line in an “extended atmosphere”. This suggestion could not be proven though, since MH had not the tools to model such atmospheres. Nowadays, this is no longer a problem, and when we include the wind in our calculations (with mass-loss rates following the ‘unclumped’ Galactic WLR), it turns out that we obtain almost the identical emission as present in the original MH simulations (performed without wind and without realistic line-blanketing). By inspection of the net rates into and from the 3d level, we noticed how the wind induces the overpopulation of the 3d level via pumping from the ground state rather than by dielectronic recombination. A prerequisite of this process is that the wind-strength is large enough to display a significantly accelerating velocity field already in the photospheric formation region of the

triplet lines, to allow the resonance lines to leave detailed balance.

The most important implication of our study is that under Galactic conditions DR plays only a secondary role, both for O-stars with “compact” and with “extended” atmospheres, whereas the key process is the overpopulation due to the resonance line *in the presence of an accelerating velocity field*. Note that without such a velocity field the resonance line loses its impact though. Consequently, it is to be expected that hydrostatic NLTE codes, such as TLUSTY and DETAIL/SURFACE, will not be suited to quantitatively synthesize the N III triplet lines (and, to a lesser extent, also N III λ 4097, because of their interrelation), unless the wind-strength is significantly below the Galactic WLR or the background metallicity, Z , is much lower than the Galactic one (see Heap et al. 2006 who performed nitrogen diagnostics for SMC O-stars by means of TLUSTY). Note also that our results have been derived for O-star conditions only, and should be valid as long as the N III emission lines, to a major extent, are formed in the photosphere or in the transition region. For objects with significantly denser winds, e.g., WN-stars, our analysis would certainly need to be extended, since additional effects might be present or might even dominate.

In order to check our new model atom and the predictive power of FASTWIND, we performed first comparisons with results from the alternative model atmosphere code CMFGEN, for a small grid of O-type dwarfs and supergiants. For this objective we used a set of important N II and N III lines in the blue part of the visual spectrum. The overall agreement between both codes is mostly satisfactory, though some systematic deviations demand a further clarification in terms of a comparison with observations.

Within the range $30,000 \text{ K} \leq T_{\text{eff}} \leq 35,000 \text{ K}$, however, some major discrepancies have been found. Here, CMFGEN triggers the emission at $\lambda\lambda 4634\text{-}4640\text{-}4642$ earlier, i.e., at cooler temperatures, than calculations from FASTWIND. This effect could be traced down to the overlap of the N III resonance line (actually, one of its fine-structure components, at 374.43 \AA) with a resonance line from O III, which is of similar strength throughout the O-star domain. We studied this effect by means of the corresponding CMFGEN calculations (since FASTWIND lacks a detailed O III model), and also by analytic considerations.

As long as both resonance lines are optically thick, source function equality is achieved. Under most conditions, the ‘coupled’ source function lies in between the individual, ‘decoupled’ ones from N III and O III. In the critical temperature range now, the decoupled O III source function is predicted to be much larger than the N III one (due to substantial cascades from upper levels), and leads, after being coupled with N III, to significant values for the combined source function, beyond the decoupled N III case. Thus, the important 3d level becomes more pumped, and the triplet emission occurs at cooler temperatures than without coupling. When the coupling is neglected in CMFGEN, the predicted triplet emission vanishes and the profiles become similar to those from FASTWIND.

It might be suspected that the impact of the O III resonance line overlap introduces an additional parameter to be known when the nitrogen abundance shall be determined via the triplet lines, namely the oxygen abundance. As we have shown by our analytic considerations, however, this parameter remains rather unimportant²⁶ as long as both resonance lines are optically thick, which is true in the interesting parameter range. We have tested this prediction by lowering the O III oscillator strength in CMFGEN by a large factor (50), and found no difference in the coupled source function and triplet emission.

Summarizing, not only the N III resonance line itself is responsible for the (strong) triplet emis-

²⁶Except for certain differences in the EUV-fluxes etc.

sion, but also the overlapping O III resonance line, at least at later O-types. Indeed, for one corresponding object studied in Chapter 5, N11-029 (O9.7Ib), we encountered the problem that the observed N III triplet could not be reproduced by FASTWIND, though with CMFGEN, and we interpreted this problem as due to the resonance line overlap. Insofar, we need to incorporate this process into FASTWIND if we aim at deriving nitrogen abundances at cooler temperatures from the triplet lines alone. Fortunately, the contamination of the other optical lines by this process remains weak, so that these lines can be used already now, and the nitrogen abundance determination by FASTWIND is not hindered.

Our study implies two important consequences that need to be tested in future comparisons with observations.

- (i) Since the efficiency of DR and ‘two electron’ drain is strongly dependent on the degree of line-blanketing/blocking, we predict that in a metal-poor environment (e.g., in the Small Magellanic Cloud with $Z/Z_{\odot} \approx 0.2$) the emission becomes stronger again, due to less EUV line-blocking. On the other hand, in such a low- Z environment also the wind-strengths and the base-line nitrogen abundance become lower, and the combined effects need to be investigated in detail. In Chapter 6, we address which effect dominates the strength of the emission.
- (ii) As outlined above, the triplet lines from O-type stars are of photospheric origin and depend, via the N III (and O III) resonance lines, on the actual wind-strength (independent of clumping and X-ray properties), determining the onset of the accelerating velocity field. Thus, their emission strengths might be used to constrain the stellar mass-loss rate (after the line-formation has been shown to work reliably), if the nitrogen abundance can be derived independently from other lines. In particular, ‘weak-winded’ stars (e.g., Bouret et al. 2003; Martins et al. 2005b; Puls et al. 2008; Marcolino et al. 2009; Najarro et al. 2011) have a rather weak wind for their luminosity, being a factor of 10 to 100 thinner than predicted/observed for their counterparts with ‘normal’ winds. Thus, it might be suspected that weak-winded stars display much less emission than stars with ‘normal’ winds of similar type. This requires, that a) there are weak-winded stars also at intermediate O-types, and b) that the winds of their ‘normal’ counterparts are not strongly clumped, which would diminish also their emission because of lower-than-thought mass-loss rates.

Using the N III triplet as an independent mass-loss diagnostics would be somewhat similar to the corresponding application of the NIR Br_{α} -line (Najarro et al. 2011, see also Puls et al. 2008), but with the advantage that the emission strength of the triplet is a rather monotonic function of \dot{M} , whereas Br_{α} changes its behaviour from weak to normal winds considerably.

Chapter 5

Surface nitrogen abundances for O-stars in the Large Magellanic Cloud

This chapter is - to a major part - a copy of Rivero González, Puls, Najarro, & Brott (2012), *Astronomy & Astrophysics*, 537, A79. As for Chapter 3, there are some revisions from the original version, to allow for clarity and consistency: The original Sect. 2.1 was moved to Chapter 2, and the original Sects. 2.2 and 2.3 as well as the original Appendix A to Chapter 3. Appendix B and Sect 2.2.1 in the original paper are now covered in Appendix A of this thesis, and the original Appendix C corresponds to the present Appendix C.1.

Abstract. Nitrogen is a key element for testing the impact of rotational mixing on evolutionary models of massive stars. Recent studies of the nitrogen surface abundance in B-type stars within the *VLT-FLAMES survey of massive stars* have challenged part of the corresponding predictions. To obtain a more complete picture of massive star evolution, and to allow for additional constraints, these studies need to be extended to O-stars.

This is the second paper in a series aiming at the analysis of nitrogen abundances in O-type stars, to establish tighter constraints on the *early evolution* of massive stars. In this paper, we investigate the N IV λ 4058 emission line formation, provide nitrogen abundances for a substantial O-star sample in the Large Magellanic Cloud, and compare our (preliminary) findings with recent predictions from stellar evolutionary models.

Stellar and wind parameters of our sample stars were determined by line profile fitting of hydrogen, helium and nitrogen lines, exploiting the corresponding ionization equilibria. Synthetic spectra were calculated by means of the NLTE atmosphere/spectrum synthesis code FASTWIND, using a new nitrogen model atom. We derived nitrogen abundances for 20 O- and 5 B-stars by analyzing all nitrogen lines (from different ionization stages) present in the available optical spectra.

The dominating process responsible for emission at N IV λ 4058 in O-stars is the strong depopulation of the lower level of the transition, which increases as a function of \dot{M} . Unlike the N III triplet emission, resonance lines do not play a role for typical mass-loss rates and below. We find (almost) no problem in fitting the nitrogen lines, in particular the ‘f’ features. Only for some objects, where lines from N III/N IV/N V are visible in parallel, we need to opt for a compromise solution.

For five objects in the early B-/late O-star domain that have been previously analyzed by different methods and model atmospheres, we derive consistent nitrogen abundances. The bulk of our sample

O-stars seems to be strongly nitrogen-enriched, and a clear correlation of nitrogen and helium enrichment is found. By comparing the nitrogen abundances as a function of $v \sin i$ ('Hunter-plot') with tailored evolutionary calculations, we identify a considerable number of *highly* enriched objects at low rotation.

Our findings seem to support the basic outcome of previous B-star studies within the VLT-FLAMES survey. Owing to the low initial abundance, the detection of strong nitrogen enrichment in the bulk of O-stars indicates that efficient mixing takes place already during the very early phases of stellar evolution of LMC O-stars. For tighter constraints, however, upcoming results from the *VLT-FLAMES Tarantula survey* need to be waited for, which will comprise a much higher number of O-stars that will be analyzed based on similar methods as presented here.

5.1 Introduction

One of the main products of the VLT-FLAMES survey of massive stars¹ (hereafter FLAMES I) was the determination of light element abundances from statistically significant samples of Galactic, Large and Small Magellanic Cloud (LMC, SMC) B-stars, covering a broad range of rotational velocities.

The inclusion of rotational mixing into massive star evolution (e.g., Heger & Langer 2000; Meynet & Maeder 2000; Brott et al. 2011a) brought better agreement with spectroscopic analyses that provide evidence for a characteristic enrichment of helium and nitrogen in many early-type stars (reviewed by, e.g., Herrero 2003, Herrero & Lennon 2004 and Morel 2009). Several recent studies based on the nitrogen diagnostics performed within the FLAMES I survey have severely challenged the predicted effects, though. In this context, nitrogen is a key element for testing the predictions of rotational mixing, because it should become strongly enriched at the stellar surface of rapidly rotating stars already in fairly early evolutionary phases, whilst for slow rotation almost no enhancement should occur before the red supergiant phase. Indeed, a significant number of both un-enriched fast rotators and highly enriched slow rotators have been found within the population of LMC core-hydrogen burning objects (Hunter et al., 2008a, 2009b; Brott et al., 2011b).² These results imply that standard rotational mixing might not be dominant, and/or that other enrichment processes might be decisive as well (Brott et al., 2011b).

To further constrain these findings and to provide a general picture of massive star evolution, these studies need to be extended to O-type stars. Because of their shorter lifetimes, the time-range where this enrichment takes place can be narrowed down, and one might be able to constrain the mixing scenario even better than it is possible from B-stars alone. In this respect, the LMC is an ideal testbed, because the nitrogen baseline abundance is low and even a strong enrichment is easier to measure/confirm than, e.g., in the Milky Way.

Interestingly, most previous abundance studies of massive stars are strongly biased toward intermediate and early type B-stars. Indeed, when inspecting the available literature, metallic abundances, in particular of nitrogen, are scarcely found for O-stars. The situation for LMC objects is even worse, and data for only a few supergiants (Pauldrach et al. 1994; Crowther et al. 2002; Evans et al. 2004) and giants (Walborn et al. 2004) are available. One of the reasons for this lack of information is that the determination of nitrogen abundances is not trivial because of the complexity of N III/N IV line

¹ See Evans et al. 2006 for an introductory publication and Evans et al. 2008 for a brief summary on the outcome of this project

² As well as slowly rotating, highly enriched supergiants, discussed by Vink et al. (2010)

formation, which is related to the impact of various processes that are absent or negligible at cooler spectral types where N II is the dominant ion.

To provide more insight into this matter, we started a series of publications dealing with nitrogen spectroscopy in O-type stars. In the first paper of this series (Rivero González et al., 2011, hereafter Chapter 4), we concentrated on the formation of the optical N III emission lines at $\lambda\lambda 4634\text{--}4640\text{--}4642$, which are fundamental for the definition of the different morphological ‘f’-classes (Walborn, 1971b). It turned out that the canonical explanation in terms of dielectronic recombination (Mihalas & Hummer, 1973) no longer or only partly applies when modern atmosphere codes including line-blocking/blanketing and winds are used. The key role is now played by the stellar wind, which induces a (relative) overpopulation of the upper level of the transition, via pumping from the ground state rather than by dielectronic recombination as long as the wind-strength is powerful enough to enable a significantly accelerating velocity field already in the photospheric formation region.

The main goal of the present chapter is to provide nitrogen abundances for a considerable number of O-stars in the LMC. For this purpose, we used the corresponding sample from Mokiem et al. (2007a, hereafter Mok07), mostly based on observations within the FLAMES I survey. So far, this is the most comprehensive sample of O-stars studied in the LMC by means of quantitative hydrogen and helium line spectroscopy, and allows us to determine nitrogen abundances for a significant number of objects. However, its size is still not comparable with the amount of corresponding B-stars, and does not allow us to extend the B-star results (that challenged rotational mixing) toward the O-star domain in a statistically sufficient way. Instead, it will yield a first impression on potential problems. A statistically significant analysis will become possible within the VLT-FLAMES Tarantula survey (Evans et al. 2011, ‘FLAMES II’), which provides an unprecedented sample of ‘normal’ O-stars and emission-line stars.

This chapter is organized as follows. In Sect. 5.2, we study the formation of the N IV $\lambda 4058$ emission line in parallel with the N IV $\lambda 6380$ absorption line. Section 5.3 presents the stellar sample and the observations used within this study. The procedure to determine stellar and wind parameters together with nitrogen abundances is outlined in Sect. 5.4. In Sect. 5.5 we comment in detail on the individual objects. Sect. 5.6 provides a discussion of our results, and Sect. 5.7 summarizes our findings and conclusions.

5.2 Understanding the N IV $\lambda 4058/\lambda 6380$ line formation

In the following, we discuss the most important mechanisms that explain the presence of emission at N IV $\lambda 4058$, in particular the decisive role of mass-loss. Our analysis is based on the model-grid as described in Sect. 5.4.2, and refers to LMC background abundances plus a solar (Asplund et al., 2005) nitrogen abundance, $[N] = 7.78$,³ chosen to obtain pronounced effects.

All important levels and the corresponding transitions involved in the N IV emission problem are summarized in Fig. 5.1. A comparison with the analogous diagram for N III (Fig. 4.1) shows a number of similarities, but also differences. In addition to what has already been outlined, the upper level of the emission line ($3d \rightarrow 3p$) is fed by only weak dielectronic recombination, with almost no influence on the population of $3d$ (contrasted to the N III case), and there is no resonance line connected to $3d$ (which turned out to be crucial for N III). Instead, the *lower* level of $\lambda 4058$, $3p$, is connected with the

³ Roughly 0.9 dex above the LMC baseline abundance, $[N]_{\text{baseline}} = 6.9$, following Hunter et al. (2007).

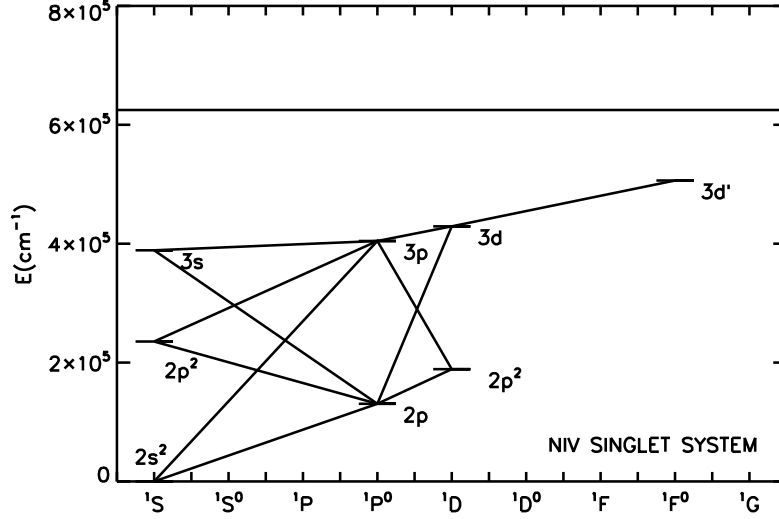


Figure 5.1: Simplified Grotrian diagram displaying the most important transitions involved in the N IV emission line problem. The horizontal line marks the N V ionization threshold. N IV $\lambda 4058$ is formed by the transition $3d \ ^1D \rightarrow 3p \ ^1P^0$, while the absorption line at $\lambda 6380$ originates from the transition $3p \ ^1P^0 \rightarrow 3s \ ^1S$. An efficient drain of 3p is provided by the ‘two-electron’ transitions $3p \ ^1P^0 \rightarrow 2p^2 \ ^1S, \ ^1D$. Cascade processes from $3d' \ ^1F^0$ and pumping from $2p \ ^1P^0$ are the major routes to overpopulate the $3d \ ^1D$ state. See text.

ground-state. Similar to N III, on the other hand, there are two strong ‘two-electron’ transitions able to drain 3p, via $3p \ ^1P^0 \rightarrow 2p^2 \ ^1S, \ ^1D$.

Basic considerations

In agreement with the results from Heap et al. (2006), our simulations (see Fig. 5.2) show that N IV $\lambda 4058$ turns from weak absorption (around $T_{\text{eff}} \approx 37$ kK) into weak emission around $T_{\text{eff}} \approx 42$ kK, for models with (very) low mass-loss rate and $\log g = 4.0$. As usual, we define equivalent widths to be positive for absorption and to be negative for emission lines. We find a 2 kK difference with respect to the turning point, which can be attributed, to a major part, to the lower nitrogen content of our models and different background abundances. Toward hotter temperatures, the emission strength increases monotonically until a maximum around $T_{\text{eff}} \approx 53$ kK has been reached, after which the emission stabilizes and finally decreases. For lower gravities and/or higher mass-loss rates, the line turns into emission at lower T_{eff} , so that, for a given T_{eff} , the emission strength increases with decreasing $\log g$ and increasing mass-loss rate, \dot{M} . Since the *absorption* strength of N IV $\lambda 6380$ increases in a similar way (though with a much weaker impact of \dot{M} , and only until $T_{\text{eff}} \approx 50$ kK), both lines appear (for a given T_{eff}) as anti-correlated, at least for a wide range of temperatures. In contrast, the corresponding transitions of N III were found to be correlated (Chapter 4).

The behavior of both lines and the corresponding level structure implies an efficient drain of level 3p that enhances the emission at $\lambda 4058$ and also prevents emission/increases absorption at $\lambda 6380$,

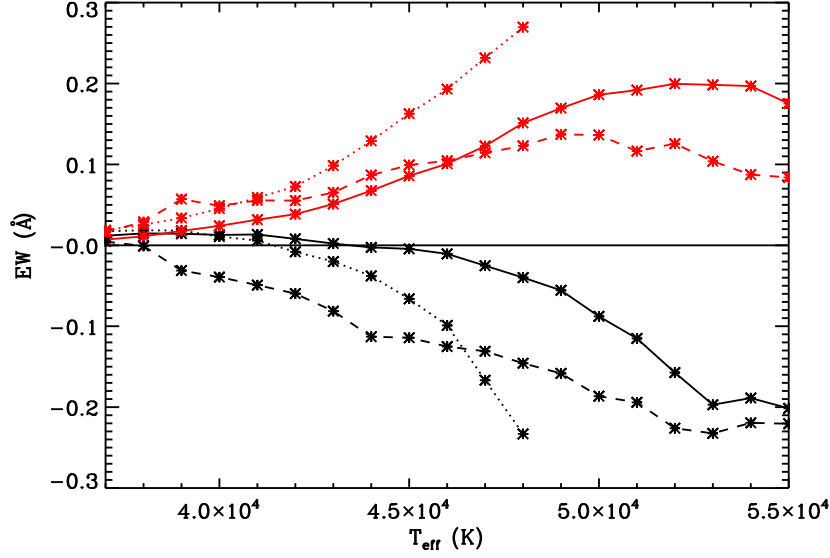


Figure 5.2: Equivalent width (positive for absorption) of N IV $\lambda 4058$ (black) and N IV $\lambda 6380$ (red) as a function of T_{eff} . Solid and dotted curves refer to low \dot{M} (model series ‘A’) with $\log g=4.0$ and 3.7 , respectively, and dashed curves to supergiant mass-loss rates (model series ‘E’), with $\log g=4.0$.

and is provided by the two ‘two-electron’ transitions $3p \rightarrow 2p^2 \ ^1D, \ ^1S$, similar to the case of N III.⁴

To investigate this mechanism in more detail and to avoid ‘contamination’ by wind effects, we concentrated at first on a low- \dot{M} model with decent emission at N IV $\lambda 4058$, with $T_{\text{eff}} = 45,000 \text{ K}$ and $\log g = 4.0$.⁵ In the upper panel of Fig. 5.3 we provide the NLTE departure coefficients, b , of involved levels, where black curves refer to our standard model. Obviously, level $3d$ is overpopulated with respect to $3p$ ($b_{3d} > b_{3p}$) over the complete line formation region. On the other hand, levels $2p^2 \ ^1D$, $2p^2 \ ^1S$, and $2p$ (the latter two not displayed) are (mostly collisionally) coupled to the ground state, which in itself is strongly depopulated, owing to fairly high ionizing fluxes (see below). This situation closely resembles the situation in N III, where strongly depopulated draining levels (for non-blocked models) favored a depopulation of the analogous level $3p$.

To further clarify the impact of the different processes, we investigated the corresponding *net rates* responsible for the population and depopulation of level $3p$ (Fig. 5.3, middle panel, black curves). As in Chapter 4, we display the dominating individual net rates (i.e., $n_j R_{ji} - n_i R_{ij} > 0$ for population, with index i the considered level) as a fraction of the *total* population rate. Indeed, the drain by level $2p^2 \ ^1D$ (dashed-dotted) and/or level $2p^2 \ ^1S$ (not displayed) are the most important processes that depopulate level $3p$ in the line formation region. In contrast, the resonance line does not contribute to any (de-)population of level $3p$, because it is (almost) in detailed balance (long dashed line).

To check the validity of our scenario, we calculated an alternative model where the two draining transitions were suppressed, by using very low oscillator strengths. Indeed, the upper panel of Fig. 5.3

⁴ Though in Chapter 4 we argued that in case of N III this mechanism becomes suppressed in realistic model atmospheres with near-solar background abundances.

⁵ At cooler T_{eff} , this line is in absorption because of a lower N IV ionization fraction implying deeper formation depths, which are closer to LTE.

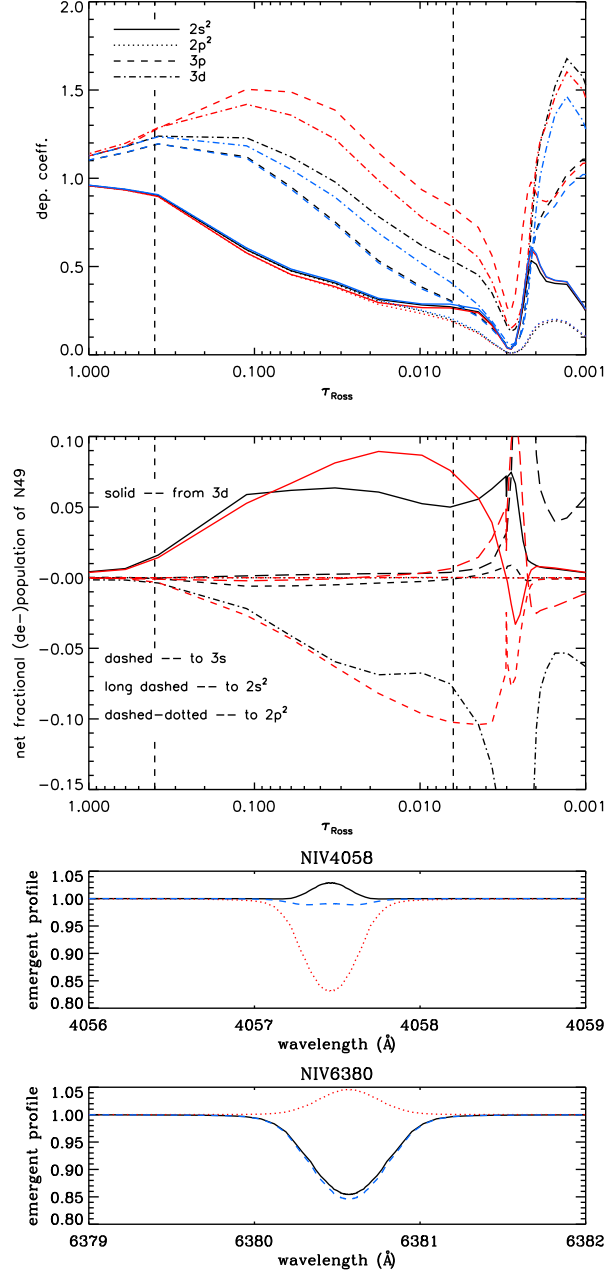


Figure 5.3: Departure coefficients, fractional net rates, and line profiles for N IV $\lambda 4058/\lambda 6380$ and involved processes, for model ‘A4540’. Designation for $2p^2$ refers to $2p^2 \ ^2D$ only since the other fine-structure component, $2p^2 \ ^2S$, behaves similarly. *Upper panel*: NLTE departure coefficients as a function of τ_{Ross} . The onset of the wind is clearly visible at $\tau_{\text{Ross}} \approx 0.003$. Black curves: standard model with $b_{3d} > b_{3p}$; red curves: draining transitions $3p \rightarrow 2p^2$ suppressed, leading to $b_{3d} < b_{3p}$; blue curves: transition $2p \rightarrow 3d$ suppressed. *Middle panel*: fractional net rates to and from $3p$, for the standard model (black) and the model with suppressed draining transitions (red). *Lower panel*: line profiles for N IV $\lambda 4058$ and $\lambda 6380$, for the three models displayed in the upper panel, with similar color coding.

(red curves) shows that now b_{3d} is smaller than b_{3p} , and $\lambda 4058$ becomes an absorption line (lower panel, red color). From the fractional net rates, we see that the preferred decay route has switched from $3p \rightarrow 2p^2$ (standard model, black) to $3p \rightarrow 3s$ (red, dashed), though level $3p$ retains a much higher population.

The upper level of $\lambda 4058$, $3d$, is predominantly fed by cascading from $3d' \ ^1F^0$, and also by pumping from level $2p$, whilst dielectronic recombinations are negligible. Suppressing the population from level $2p$ leads to less emission (Fig. 5.3, lower panel, blue colors), owing to a less populated level $3d$ (upper panel).

Let us now consider the behavior of the absorption line at $\lambda 6380$, resulting from the transition $3p \rightarrow 3s$, again by means of Fig. 5.3. As mentioned earlier, this line shows an anti-correlation⁶ with N IV $\lambda 4058$, in contrast to the behavior of the corresponding N III lines, which appear to be correlated. In Chapter 4 we argued that the latter correlation results from the proportionality of the level populations of $3p$ and $3s$. That is, when b_{3p} decreases (e.g., due to increased ‘two-electron’ drain), b_{3s} decreases in parallel due to less cascading, and the absorption at $\lambda 4097$ becomes weaker in concert with an increase in the triplet emission. Vice versa, an increase of $3p$ implies less emission of the triplet lines and more absorption at $\lambda 4097$, respectively.

This reaction requires the transition $3p \rightarrow 3s$ to be optically thin, dominated by spontaneous decays, which is no longer true for N IV $\lambda 6380$. Owing to a mostly significant optical depth, the radiative net rate is no longer dominated by spontaneous decays, but also depends on absorption and induced emission processes. Now, an increased population of $3p$ leads to less increase of b_{3s} ,⁷ and the absorption becomes *weaker* because of an increased source function $\propto b_{3p}/b_{3s}$. Vice versa, a decrease in the population of $3p$ leads to more absorption at $\lambda 6380$ in parallel with more emission at $\lambda 4058$. This behavior becomes particularly obvious if we investigate the reaction of the absorption line when suppressing the draining transitions. In this case, $3p$ becomes strongly overpopulated (Fig. 5.3, upper panel, red color), and $\lambda 4058$ goes into absorption whilst $\lambda 6380$ becomes an emission line, due to a significantly increased source function (more pumping than in the original scenario). We checked that if the absorption and stimulated emission terms in the $3p \rightarrow 3s$ transitions are neglected, $\lambda 6380$ displays more absorption instead, in accordance with our previous arguments.

Note, however, that this anti-correlation is not complete. If one changes processes that have an effect on $3d$ alone, e.g., the absorption strength of $\lambda 6380$ remains unaltered. Thus, by suppressing $2p \rightarrow 3d$, only b_{3d} is affected (upper panel, blue vs. black curves), and there is less emission at $\lambda 4058$ while the absorption at $\lambda 6380$ remains at the previous level (lower panel).

Summarizing, we interpret the different correlations between emission and absorption line-strength in N III and N IV as caused by optical depth effects in the $3p \rightarrow 3s$ transition. As long as this is optically thin, cascade effects dominate, and both lines appear to be correlated (N III). Higher optical depths introduce a counteracting ‘source-function effect’, and the lines become anti-correlated (N IV). The fairly high degree of such anti-correlation supports the importance of the draining transitions, because these are able to influence both the absolute population of the involved levels and their ratios in a very efficient way by providing additional decay channels for level $3p$.

⁶ When certain parameters/processes are changed for a given T_{eff} , e.g., the strength of the draining levels, the background opacities, etc.. The *overall* increase of these line-strengths as a function of T_{eff} is related to the increasing ionization fractions.

⁷ The net radiative rate (downward) is proportional to $A(1 - \bar{J}/S)$, with Einstein coefficient for spontaneous decay, A , scattering integral \bar{J} and source function, S .

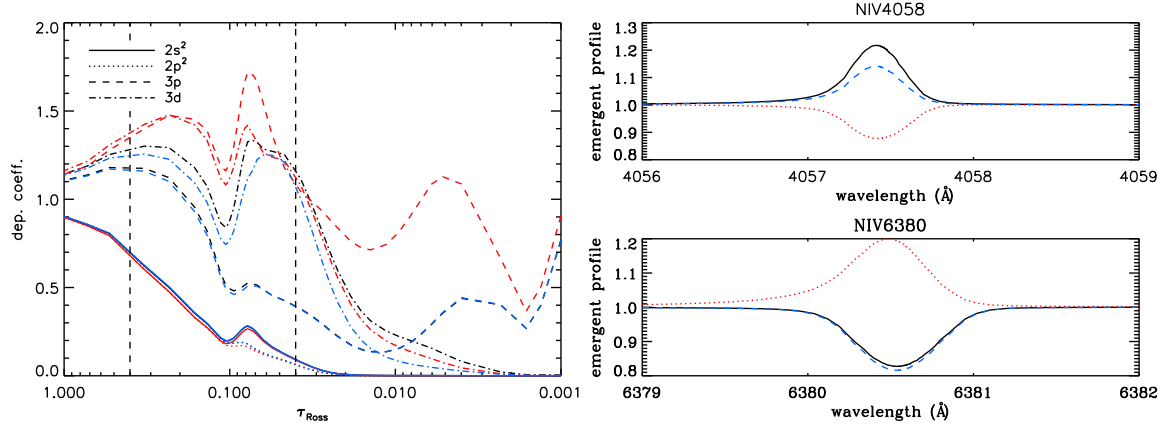


Figure 5.4: Departure coefficients (left) and line profiles for N IV λ 4058/ λ 6380 (right) for the dense-wind model ‘E4540’. Level designations, lines, and color coding as in Fig. 5.3.

The impact of wind effects

So far, we discussed the possibility of obtaining emission at N IV λ 4058 via solely photospheric NLTE processes. In Chapter 4, the presence of a wind (more accurately, a steep rise of the velocity field in the outer photosphere) turned out as crucial to explain the observed N III triplet emission in Of-stars, enabling an efficient pumping of the *upper* level by the corresponding resonance line. To investigate how the presence of a wind affects the emission at N IV λ 4058, we compared our previous model ‘A4540’ with model ‘E4540’, which has the same stellar parameters but a considerably higher, supergiant-like mass-loss rate. Indeed, the inclusion of such a strong wind has a pronounced effect. Comparing Fig. 5.4 (right panel) with Fig. 5.3, model ‘E4540’ (black) results in much more emission than ‘A4540’, increasing the equivalent width of λ 4058 from -7 to -114 mÅ. For higher T_{eff} the impact of \dot{M} also remains significant. The absorption line N IV λ 6380 is affected by the wind as well, though less pronounced. The absorption becomes slightly stronger (by 18% in the equivalent width), i.e., the anti-correlation discussed above is still present. This is valid not only for model ‘E4540’, but also for hotter models (Fig. 5.2), until the wind-emission begins to contaminate N IV λ 6380.

The origin of this stronger emission at λ 4058 becomes clear if one inspects the involved departure coefficients (Fig. 5.4, left panel, black curves). Again, the onset of the wind is clearly visible (at $\tau_{\text{Ross}} \approx 0.1$), now much deeper than in the ‘A’ model, and the line formation region is located in between $\tau_{\text{Ross}} \sim 0.40 \dots 0.04$. Compared to the ‘A’ model, ‘E4540’ displays a more advanced ground-state depopulation, where the ground-state remains coupled with the draining levels $2p^2$ as well as with level $2p$ (not displayed). This leads, particularly in the transition region between photosphere and wind, to an extreme depopulation of $3p$. Because level $3d$ becomes strongly overpopulated mostly because of feeding by $3d$ $^1F^0$ (which is severely overpopulated as well), the resulting line source function is quite high and partly even in inversion, which explains the pronounced emission at N IV λ 4058.

All these differences are caused by the onset of the wind. At first note that the N IV continuum ($\lambda < 160$ Å) is strongly coupled with the He II continuum. As already realized by Gabler et al. (1989), increasing mass-loss leads to more He II ground-state depopulation, to higher fluxes in the He II continuum and thus also to higher fluxes in the N IV continuum. Consequently, the N IV ground-state

becomes strongly depopulated, and the nitrogen ionization equilibrium switches from N IV (which is the dominant stage in the deeper photosphere) toward N V from the transition region on. This also favors the overpopulation of 3d by means of increased recombinations to high-lying levels with subsequent cascades via $3d^2\ ^1F^0$.

One might now argue that the inclusion of the wind could amplify the impact of the resonance transition(s) by producing deviations from detailed balance which would lead to strong pumping, similar to the case of N III. Unlike the situation in N III, however, this effect would lead to less line emission or even absorption at N IV λ 4058, because here the resonance line is connected to the lower level, 3p. But this effect is not present, however, because the resonance line is too strong (N IV is the dominant ion until the transition region) to leave detailed balance before the wind has reached a significant speed. Only then the resonance transition becomes dominant in populating level 3p, but this occurs already far beyond the formation region of N IV λ 4058. Close to the formation region, there is only a moderate population of 3p by the resonance line, similar to the population from 3d itself. Even this additional population is counteracted (even slightly overcompensated) by enhanced drain toward $2p^2$, not only in the formation region of λ 4058 but also in those outer regions where the resonance line strongly pumps.

These arguments are supported by the fact that N IV λ 6380 is only slightly affected by the wind, where the increased absorption results mostly from a diminished source function owing to a less populated 3p level. Performing the same tests as for the thin wind case, i.e., either suppressing the drain or suppressing the population of 3d via $2p \rightarrow 3d$, leads to similar results, as can be seen from the red and blue curves and profiles in Fig. 5.4, respectively.

We conclude that \dot{M} is a key parameter for modeling the N IV emission line, where in contrast to N III the basic mechanism (for typical mass-loss rates and below) is always caused by the depopulation of the lower level by the ‘two-electron’ transitions. This drain becomes stronger as a function of \dot{M} , because of increasing ionizing fluxes that lead to more ground-state depopulation.

5.3 Stellar sample and observations

5.3.1 The stellar sample

Table 5.1 lists our stellar sample that was drawn from the analysis of LMC O-/early B-stars by Mok07.

Three of the 28 stars from the original sample were discarded from the present analysis for two reasons. First, from our analysis we suspect that N11-004 and N11-048 might be (SB1) binaries, where the former object shows discrepant line shifts and for the latter we were unable to reproduce the observed He lines accurately (both shape and strength). A possible binarity of N11-048 was also suggested by Mok07 because of similar reasons. The other discarded star, Sk-67° 166, is the only object in the original sample that seems to be strongly evolved (helium content $Y_{\text{He}} = \text{N}(\text{He})/\text{N}(\text{H}) = 0.20 \dots 0.28$, Crowther et al. 2002 and Mok07, respectively), and has a very dense wind, with both H_{α} and He II λ 4686 in strong emission. We confirm the stellar/wind parameters as derived by Mok07 (almost perfect fit quality of H/He lines), but did not succeed in a reasonable fit for the nitrogen lines. A comparison with the analysis by Crowther et al. (2002) shows similar discrepancies. Because of this problem and because of its highly evolved evolutionary status, which does not match with all other objects in our sample, we decided to discard this object from our present analysis and will reconsider it in a future attempt.

Table 5.1: Sample stars used within this study along with spectral type, V-magnitude, interstellar extinction A_V , and absolute visual magnitude M_V . All quantities have been taken from Mok07. Primary identifications for N11 objects are from Evans et al. (2006). Identifications starting with "Sk", "BI", "P", and "LH" are from Sanduleak (1970), Brunet et al. (1975), Parker et al. (1992), and Walborn et al. (2002, 2004), respectively.

Star	Cross-IDs	Spectral Type	V	A_V	M_V
N11-026	-	O2 III(f*)	13.51	0.47	-5.46
N11-031	P3061/LH10-3061	ON2 III(f*)	13.68	0.96	-5.78
N11-038	P3100	O5 II(f ⁺)	13.81	0.99	-5.68
Sk-66° 100	-	O6 II(f)	13.26	0.34	-5.58
N11-032	P3168	O7 II(f)	13.68	0.65	-5.47
N11-045	-	O9 III	13.97	0.50	-5.03
BI253	-	O2 V((f*))	13.76	0.71	-5.45
BI237	-	O2 V((f*))	13.89	0.62	-5.23
N11-060	P3058/LH10-3058	O3 V((f*))	14.24	0.81	-5.07
Sk-70° 69	-	O5 V((f))	13.95	0.28	-4.83
N11-051	-	O5 Vn((f))	14.03	0.19	-4.66
N11-058	-	O5.5 V((f))	14.16	0.28	-4.62
Sk-66° 18	-	O6 V((f))	13.50	0.37	-5.37
N11-065	P1027	O6.5 V((f))	14.40	0.25	-4.35
N11-066	-	O7 V((f))	14.40	0.25	-4.35
N11-068	-	O7 V((f))	14.55	0.28	-4.23
N11-061	-	O9 V	14.24	0.78	-5.04
N11-123	-	O9.5 V	15.29	0.16	-3.37
N11-087	P3042	O9.5 Vn	14.76	0.62	-4.36
N11-029	-	O9.7 Ib	13.63	0.56	-5.43
N11-036	-	B0.5 Ib	13.72	0.40	-5.18
N11-008	Sk-66° 15	B0.7 Ia	12.77	0.84	-6.57
N11-042	P1017	B0 III	13.93	0.22	-4.79
N11-033	P1005	B0 III _n	13.68	0.43	-5.25
N11-072	-	B0.2 III	14.61	0.09	-3.98

The remaining sample consists of 20 O-stars, mostly giants or dwarfs, and 5 early B-type supergiants or giants. All B-stars and 15 O-stars are associated with the cluster N11, and the others are field stars. The early B-stars were included in our sample to allow for a comparison with previous analyses of such stars (Hunter et al., 2009b) and to check the consistency of different codes and methods in the transition region between O- and B-types (Sect. 5.6.2).

Table 5.1 gives information about spectral type, V-magnitude, interstellar extinction and absolute visual magnitude, and was taken from Mok07. Spectral types for N11 objects are based on Evans et al. (2006), slightly revised by Mok07 in collaboration with C. Evans (priv. comm.), and for the field stars from Walborn et al. (1995), and Massey et al. (1995, 2005). For the field star Sk-70° 69 we added the ((f)) designation because the present spectra show clear emission at N III $\lambda\lambda$ 4634-4640-4642 and He II λ 4686 in absorption.

5.3.2 Observations

Most of the observations (for objects denoted by ‘N11-’) have been carried out within the FLAMES I survey, and are described in detail in Evans et al. (2006). In brief, the data were obtained using the Fibre Large Array Multi-Element Spectrograph (FLAMES) at the VLT, for six wavelengths settings with an effective resolving power of $R \simeq 20,000$. The S/N ratios are in the ranges 50-200 for LMC objects. After sky subtraction, each wavelength range was co-added and normalized by means of a cubic spline.⁸ The final merged spectra cover two spectral ranges, 3850-4750 Å and 6300-6700 Å.

To improve the sampling in luminosity and temperature, Mok07 augmented the N11 sample by LMC O-type field stars, which were observed using the UVES spectrograph at the VLT as part of the ESO programs 67.D-0238, 70.D-0164, and 074.D-0109 (P.I. P. Crowther). Spectra were obtained for four different wavelength settings at an effective resolving power of $R \simeq 40,000$. The final product provides coverage between 3300-5600 Å and 6300-10400 Å for all stars except for Sk-70° 69, where ‘only’ the region between 3300-5600 Å and 6300-6700 Å had been observed. The typical S/N ratios achieved for all spectra lie in the range 60-80.

5.4 Analysis

5.4.1 Methodology

In an ideal world, we could have used the stellar and wind parameters as obtained by Mok07 from H/He lines, and simply derived the nitrogen abundances from atmospheric models with these parameters. Unfortunately, there are reasons to reanalyze all program stars. First, the present FASTWIND version (see Sect. 2.3.1) is somewhat different from the version used by Mok07, and the parameters need certain (mostly small) alterations to reach a similar fit quality to the H/He lines. Second, we used a somewhat different fitting strategy with respect to the ‘free’ parameters, which changes the optimum fit. In contrast to Mok07, we derived and fixed the projected rotational velocity, $v \sin i$, independently from the actual fitting procedure (Sect. 5.4.3), whereas Mok07 included $v \sin i$ as a free parameter in their fitting algorithm. Moreover, during our fit procedure we allowed for the presence of extra line-broadening (‘macro-turbulence’, v_{mac}), not considered by Mok07. Differences in $v \sin i$ and v_{mac} can lead to certain differences in the outcome of the fit, since the profile shapes might change (e.g., Fig. 4 in Puls 2008). Third, and most important, is that we now aim at a consistent fit for the H/He *and* nitrogen lines. Thus, and in the sense of a compromise solution (minimization of the differences between observed and synthetic spectra for *all* lines), different stellar parameters which result in a modest change of the fit quality of H/He alone⁹ can lead to a significant improvement with respect to the complete set of lines.

This is why we opted for an entire reanalysis, performed mostly by a simple ‘fit-by-eye’ method where we aimed to accomplish the best fit to the strategic lines by visual inspection (for a discussion, see Mokiem et al. 2005). Because we started from the parameter set as provided by Mok07 (highest ‘fitness’¹⁰ with respect to their assumptions), our new solution should be located at or close to the *global* maximum of the corresponding merit function as well and not only at a local one. Note that

⁸ We performed additional renormalizations for different wavelength ranges.

⁹ In particular at earliest spectral types the sensitivity of H/He on changes in the atmospheric parameters is quite weak.

¹⁰ Which quantifies the quality of the solutions resulting from a genetic algorithm optimization, see Mokiem et al. (2005) and references therein.

our derivation of nitrogen abundance and micro-turbulence for most of the cooler sample stars relies on a more objective method (Sect. 5.4.4).

Mok07 themselves used an automated fitting method (developed by Mokiem et al. 2005) based on a genetic algorithm optimization routine to obtain the stellar/wind parameters by evolving a population of FASTWIND models over a course of generations, until the best fit to H/He is found. Seven free parameters were considered to obtain the highest ‘fitness’: effective temperature, T_{eff} , surface gravity, $\log g$, helium content, Y_{He} , projected rotational velocity, $v \sin i$ (see above), micro-turbulent velocity, v_{mic} , mass-loss rate, \dot{M} , and velocity-field exponent, β .

5.4.2 Model calculations and grids

All models used within this analysis were calculated with FASTWIND, augmented by a few CMFGEN models for comparison purposes (Sect. 5.5). For these calculations, H, He, and N were treated as explicit elements. A description of our H/He model atoms can be found in Puls et al. (2005), and our nitrogen model atom is described in Chapter 3.

To allow us to study the combined reaction of all diagnostic H/He/N lines on variations of the stellar/wind parameters and nitrogen abundances, and also for understanding the N IV $\lambda 4058$ emission line process (Sect 5.2), we generated a grid of models.¹¹ The grid was constructed using various nitrogen abundances centered at the solar value $[\text{N}] = 7.78$ (from $[\text{N}] = 6.98$ to 8.58 with step size 0.2 dex and including the LMC nitrogen baseline abundance, $[\text{N}]_{\text{baseline}} = 6.9$), and a background metallicity, $Z = 0.5Z_{\odot}$, corresponding roughly to the *global* metallic abundance of the LMC (cf. Mokiem et al. 2007b). The individual abundances of the background elements (in terms of mass fractions) are scaled by the same factor with respect to the solar abundance pattern (see Massey et al. 2004).

For a given Z the grid is three-dimensional with respect to T_{eff} , $\log g$, and $\log Q$, where Q is the so-called wind-strength parameter (or optical depth invariant), $Q = \dot{M}/(v_{\infty}R_{*})^{1.5}$. This parameter allows us to condense the dependence on \dot{M} , terminal velocity, v_{∞} , and stellar radius, R_{*} , into one representative quantity.¹² The grids cover the temperature range from 25 to 55 kK (with increments of 1 kK), and a gravity range between 3.0 and 4.5 (with increments of 0.2 dex). For $\log Q$, the different wind strengths are denoted by a letter (from ‘A’ to ‘E’), with $\log Q = -14.0, -13.5, -13.15, -12.8, -12.45$, respectively, if \dot{M} is calculated in $M_{\odot}\text{yr}^{-1}$, v_{∞} in km s^{-1} , and R_{*} in R_{\odot} . Models with quantifier ‘A’ correspond to thin winds, resulting in lines that are (almost) unaffected by the wind, whereas ‘E’-models correspond to a significant wind-strength typical for O-type supergiants. Other parameters were adopted as follows: a solar helium abundance, $Y_{\text{He}} = 0.10$; v_{∞} as a function of the photospheric escape velocity, v_{esc} (see Kudritzki & Puls 2000); the stellar radius, R_{*} , as a function of spectral type and luminosity class, corresponding to prototypical values; the velocity field exponent, β , from empirical values (Kudritzki & Puls 2000), with $\beta = 0.8$ for O-stars, and higher values toward later types; and the micro-turbulence, $v_{\text{mic}} = 10 \text{ km s}^{-1}$.

¹¹Following the basic philosophy described by Puls et al. (2005).

¹²Relying on the fact that the wind-emission from recombination dominated (i.e., ρ^2 -) processes remains unaffected as long as the wind-strength parameter does not vary (see Puls et al. 1996, 2005).

Table 5.2: Fundamental parameters for the LMC sample, assuming unclumped mass-loss. For stars with two entries, see text. Brackets around v_∞ : derived from scaling via v_{esc} . Asterisks following v_{mic} : value obtained in parallel with nitrogen abundance.

Star	ST	Secondary T_{eff} diag.	T_{eff} (kK)	$\log g$ (cgs)	$\log g_{\text{true}}$ (cgs)	R_* (R_\odot)	$\log L_*$ (L_\odot)	Y_{He}	v_{mic} (km s^{-1})	$v \sin i$ (km s^{-1})	v_{mac} (km s^{-1})	\dot{M} ($10^{-6} M_\odot \text{yr}^{-1}$)	β	v_∞ (km s^{-1})
N11-026	O2 III(f*)	N III/N IV/N V	49.0	4.00	4.00	11.3	5.82	0.10	10.0	72	60	1.56	1.08	[3120]
		N IV/N V	52.0	4.10	4.10	11.0	5.89					1.49		
N11-031	ON2 III(f*)	N III/N IV	47.8	3.95	3.95	13.4	5.92	0.11	10.0	71	60	2.02	1.08	3200
		N IV/N V	56.0	4.00	4.00	12.2	6.12					2.20		
N11-038	O5 II(f ⁺)	N III/N IV	40.5	3.70	3.71	14.0	5.67	0.08	10.0	100	50	1.21	0.98	[2600]
Sk-66° 100	O6 II(f)	N III/N IV	39.0	3.70	3.71	13.7	5.59	0.19	10.0	59	60	0.83	1.27	2075
N11-032	O7 II(f)	N III/N IV	36.0	3.50	3.51	13.6	5.44	0.09	10.0	60	70	0.97	0.80	[1920]
N11-045	O9 III	-	32.3	3.32	3.33	12.0	5.15	0.07	10.0	64	80	0.69	0.80	[1550]
BI253	O2 V((f*))	N IV/N V	54.8	4.18	4.20	10.7	5.97	0.08	10.0	230	-	1.53	1.21	3180
BI237	O2 V((f*))	N IV/N V	53.2	4.11	4.12	9.7	5.83	0.09	10.0	140	-	0.62	1.26	3400
N11-060	O3 V((f*))	N III/N IV/N V	48.0	3.97	3.97	9.5	5.63	0.12	10.0	68	40	0.51	1.26	[2740]
		N IV/N V	51.0	4.10	4.10	9.2	5.71					0.48		
Sk-70° 69	O5 V((f))	N III/N IV	42.3	3.93	3.94	9.1	5.38	0.14	10.0	131	-	0.43	0.80	2750
N11-051	O5 Vn((f))	N III/N IV	41.4	3.70	3.83	8.6	5.42	0.08	10.0	350	-	0.41	0.80	[2110]
N11-058	O5.5 V((f))	N III/N IV	40.8	3.75	3.76	8.4	5.24	0.10	6.0*	62	60	0.01	1.00	[2470]
Sk-66° 18	O6 V((f))	N III/N IV	39.7	3.76	3.76	12.2	5.52	0.14	10.0	75	40	1.08	0.94	2200
N11-065	O6.5 V((f))	N III/N IV	41.0	3.85	3.85	7.4	5.14	0.13	10.0	60	50	0.05	1.00	[2320]
N11-066	O7 V((f))	N III/N IV	37.0	3.70	3.71	7.9	5.02	0.10	10.0	59	50	0.14	0.80	[2315]
N11-068	O7 V((f))	N III/N IV	37.0	3.70	3.71	7.5	4.98	0.10	10.0	30	50	0.13	1.12	[3030]
N11-061	O9 V	-	34.0	3.55	3.55	11.5	5.20	0.09	5.0	54	80	0.52	0.80	[1900]
N11-123	O9.5 V	-	34.3	4.20	4.21	5.4	4.56	0.09	10.0	115	-	0.08	0.80	[2890]
N11-087	O9.5 Vn	-	32.7	4.04	4.08	8.8	4.90	0.10	10.0	260	-	0.11	0.80	[3030]
N11-029	O9.7 Ib	N II/N III	29.0	3.20	3.21	15.8	5.20	0.08	10.0	46	60	0.28	1.23	[1580]
N11-036	B0.5 Ib	N II/N III	25.8	3.11	3.11	15.5	4.98	0.08	12.1*	39	40	0.11	0.80	[1710]
N11-008	B0.7 Ia	N II/N III	26.3	3.00	3.00	29.5	5.57	0.10	4.7*	46	60	0.62	1.30	[2390]
N11-042	B0 III	N II/N III	29.2	3.59	3.59	11.9	4.97	0.08	5.0	21	25	0.19	1.19	[2310]
N11-033	B0 III _n	-	26.7	3.20	3.34	15.7	5.05	0.10	5.0	256	-	0.25	1.03	[1540]
N11-072	B0.2 III	N II/N III	29.8	3.70	3.70	8.1	4.67	0.10	2.7*	14	10	0.25	1.30	[2100]

5.4.3 Determination of stellar and wind parameters

The different steps performed in our analysis can be summarized as follows, and are detailed in the next sections.

First, we determined $v \sin i$ for each object. Then we used the results from Mok07 in combination with our model grid to roughly constrain the stellar (T_{eff} , $\log g$, $[\text{N}]$) and wind-strength parameters ($\log Q$), by inspecting the synthetic and observed H/He and nitrogen line profiles (Y_{He} , β and v_{mic} already specified within the grid.) During this step, we determined the extra line-broadening parameter, v_{mac} , by reproducing the profile shape of the weaker lines.

Subsequently, the stellar/wind parameters, now including Y_{He} and β , were fine-tuned by calculating a grid of much higher resolution around the initial guess and adopting v_{∞} from Mok07. After the fundamental parameters were fixed and, in case, v_{mac} was adjusted, we fitted the nitrogen abundance using two different methods (for cooler and hotter objects, respectively), and also updated v_{mic} , which Mok07 solely derived from H/He lines. In certain cases, we needed to re-adapt the stellar/wind parameters to obtain the (almost) final solution. Now, we were able to calculate the stellar radius from M_V and the synthetic fluxes, and to update the mass-loss rate to its final value by scaling with the new radius. A final consistency check with the new \dot{M} and R_* values was performed to ensure the stability of our results.

Tables 5.2 and 5.4 list all quantities derived in this way, and Table 5.3 yields the main differences between our and the Mok07 results. Note that these quantities refer to unclumped winds, whilst in Sect. 5.4.5 we discuss the impact of wind clumping.

Projected rotational velocities and macro-turbulence. Before we were able to perform the actual (fine-)analysis, we needed to constrain the line broadening parameters, i.e., $v \sin i$ and v_{mac} (v_{mic} was - when possible - inferred in parallel with the nitrogen abundances, see Sect 5.4.4). As outlined above, Mok07 derived $v \sin i$ directly from their automated fitting method from the H/He lines. It is more suitable to use metal lines, because these are not affected by Stark-broadening. Only in case of high rotational velocities or high temperatures, where metallic lines are blended or are very weak, He I lines might be used. Therefore, we derived $v \sin i$ from scratch, employing the Fourier method (Gray, 1976), as implemented and tested in the OB-star range by Simón-Díaz et al. (2006) and Simón-Díaz & Herrero (2007). This method has the advantage to easily discriminate the rotational contribution from other broadening mechanisms that affect the line shapes. In dependence of temperature and rotational velocity of the star, we used lines from O II, N II, C II, and Si III for B- and late O-type stars. For earlier O-types, higher ionization states are predominant, and mostly N III/N IV and Si IV lines were considered, together with He I lines for the earliest types.

To finally reproduce the actual profile shape, some extra line-broadening was needed in most cases, conventionally called macro-turbulence. Though the physical origin of this broadening still remains to be proven, there are some strong indications that it is associated with (high order, non-radial) stellar pulsations (Aerts et al. 2009; Simón-Díaz et al. 2010). To account for this effect, we used a radial-tangential description of v_{mac} to fit the profile *shapes* of nitrogen (and partly helium) lines, using our first estimates on the stellar and wind parameters (see above) and the new $v \sin i$ values. For the fastest rotators of our sample, however, corresponding values could not be constrained, because high $v \sin i$ produce either too weak nitrogen lines, or these lines, together with He I lines, loose their sensitivity to distinct changes in v_{mac} .

As expected, most of our $v \sin i$ values turn out to be systematically lower than those provided by

Mok07 (Table 5.3), by typically 30-40%. The derived range of v_{mac} values is consistent with results from similar investigations, e.g., Dufton et al. (2006); Simón-Díaz et al. (2006); Lefever et al. (2007); Markova & Puls (2008); Simón-Díaz et al. (2010). The uncertainty of our estimates is typically on the order of $\pm 10 \text{ km s}^{-1}$, being larger for stars with relatively low rotational speeds.

Effective temperatures. This parameter is mostly constrained by the He I/He II ionization equilibrium. For this purpose, we primarily used He I $\lambda\lambda$ 4471, 4713, 4387 and He II $\lambda\lambda$ 4200, 4541. In most cases, we did not meet the so-called He I singlet problem (Najarro et al., 2006). As a consistency check on T_{eff} and especially for the hotter stars, where the He I lines can no longer serve as an efficient temperature indicator, we made additional use of the nitrogen ionization equilibrium by means of the lines listed in Table 3.5. For B- and late O-stars, we investigated N II/N III, for mid O-stars N III/N IV, and for early O-stars N IV/N V or even - in a few cases -N III/N IV/N V (see Table 5.2 for the specific diagnostics applied to a particular object). To this end, we either used our coarse grid or our specific ‘fine-grid’ models, with a similar gridding of nitrogen abundances ($[\text{N}] = 6.9 \dots 8.58$). By exploiting this additional information, i.e., roughly ‘fitting’ the nitrogen lines of different ions at a unique abundance, we were able to fine-tune T_{eff} (and also some of the other parameters, see below). For objects where only lines from one ionization stage are present (N11-033, 045, 061, 087, 123), this consistency check only allows for fairly weak constraints, if at all.

We estimate a typical uncertainty for T_{eff} according to the grid resolution, $\Delta T_{\text{eff}} \approx 1 \text{ kK}$. For N11-066 and N11-068 we are only able to provide rough estimates on the stellar parameters, consistent with the nitrogen ionization equilibrium, and we adopt a larger error, $\Delta T_{\text{eff}} \approx 2 \text{ kK}$. For some problematic stars, N11-026, N11-031, and N11-060, we consider an even larger error, about 4 kK, in agreement with Mok07 (see Sect. 5.5).

Surface gravities. We derived $\log g$ using the classical approach from the Stark-broadened wings of the Balmer lines, basically H_γ and H_δ , which should be uncontaminated by wind-emission. As for T_{eff} , we used nitrogen lines as a final consistency check. These surface gravities need to be corrected for stellar rotation, applying a centrifugal correction (see Repolust et al. 2004 and references therein). The estimated error for $\log g$ is 0.1 dex.

Helium abundances. To ensure the reliability of the final parameters, especially T_{eff} and $\log g$, and for our discussion on the abundance enrichment, we needed to revisit the helium line fits, because inconsistent helium abundances can influence these parameters. A small subgrid was constructed around the stellar parameters derived in previous steps, for different Y_{He} , from 0.08 (corresponding to the approximate LMC baseline abundance, see Sect. 5.6) to 0.14, in steps of 0.02. A rough estimate on the error is half this stepsize.

Terminal velocities cannot be reliably derived from the optical, and were adopted from Mok07. For the field stars, values have been inferred from UV P Cygni profiles by Massa et al. (2003) and Massey et al. (2005). The terminal velocity of Sk-66° 18 was measured by Mok07 using UV O VI lines. For the FLAMES N11 stars, only N11-031 could be analyzed with respect to this parameter by Walborn et al. (2004). For all other stars, v_∞ has been estimated from v_{esc} , following Kudritzki & Puls (2000).

Table 5.3: Differences between the fundamental parameters as derived here and by Mok07. Positive values indicate higher values from this study. Dashes: no difference compared to the Mok07 analysis. The comparison for N11-031 is made with respect to the cooler solution (see Sect. 5.5).

Star	ΔT_{eff} (kK)	$\Delta \log g$ (cgs)	ΔY_{He}	$\Delta v \sin i$ (km s^{-1})	$\Delta \log \dot{M}$ ($10^{-6} M_{\odot} \text{yr}^{-1}$)	$\Delta \beta$
N11-026	-4.3	-	-0.01	-37	-0.06	-
N11-031	2.8	0.10	0.01	-45	-0.28	0.19
N11-038	-0.5	-0.02	-0.02	-45	-0.10	-
Sk-66° 100	-	-	-	-25	-0.03	-
N11-032	0.8	0.05	-	-36	0.08	-0.23
N11-045	-	-	-	-41	0.10	-
BI253	1.0	-	-0.01	39	-0.10	-
BI237	-	-	-0.01	14	-0.10	-
N11-060	2.3	0.05	-	-38	-0.01	-
Sk-70° 69	-0.9	0.06	-0.03	-	-0.38	0.02
N11-051	-1.0	-0.05	-	17	-0.39	0.20
N11-058	-0.5	-0.14	-	-23	-1.18	-0.42
Sk-66° 18	-0.5	-	-	-7	-	-
N11-065	-0.7	-0.04	-0.04	-23	-0.86	0.20
N11-066	-2.3	-0.17	-0.01	-12	-0.47	-
N11-068	-2.9	-0.43	-	-24	-0.42	-
N11-061	0.4	0.04	-	-33	0.39	-1.00
N11-123	-0.5	-0.02	-	5	-	-
N11-087	-	-	-	-16	-0.10	-
N11-029	-0.4	-0.03	0.01	-31	0.22	-0.40
N11-036	-0.5	-0.20	-	-15	-	-
N11-008	0.3	0.02	-	-35	0.09	-0.57
N11-042	-1.0	-0.10	-0.02	-21	-0.02	-
N11-033	-0.5	-0.01	0.02	-	0.02	-
N11-072	-1.0	-0.08	-0.02	-	0.02	0.46

Velocity field exponent β . The sample used in this study does not contain any star whose wind is so dense that H_{α} is in emission, therefore an accurate determination of this parameter is difficult¹³ for optical spectroscopy. We applied the following philosophy. If the combination \dot{M} - β provided by Mok07 resulted in reasonable H_{α} -fits, we kept β . Otherwise, we set β to prototypical values, $\beta = 0.8 \dots 1.30$, depending on spectral type and results from earlier analyses performed in our group. Moreover, for some of the sample stars, N11-008, N-029, N11-058, and N11-061, the automated fitting method used by Mok07 resulted in quite high values for β (e.g., N11-061: $\beta=1.8$), whilst for N11-051 a rather low value, $\beta = 0.6$, was inferred. We consider these values as either unphysical or indicating a substantial amount of wind clumping. In all these cases, we modified β as outlined above (see also Sect. 5.5).

¹³If not impossible, because of the \dot{M} - β degeneracy (e.g., Markova et al. 2004) and effects from wind clumping (e.g., Puls et al. 2006).

Mass-loss rates were derived from fitting the synthetic H_α profiles to the observations, given β (see above). Usually He II $\lambda 4686$ was used as a consistency check. It turned out that for many sample stars we were unable to successfully fit both lines at the same \dot{M} , because He II $\lambda 4686$ showed more absorption than consistent with the observations when H_α was fitting. This might indicate a certain problem regarding He II $\lambda 4686$ in the new FASTWIND version, or some impact of wind clumping. The problem needs to be investigated in the future, but has no impact on the present study.

Another consistency check for \dot{M} is provided by the nitrogen lines, particularly by the N III and N IV emission lines (and sometimes also by the N V doublet), which are strongly affected by the wind strength. In the case of two stars, N11-058 and N11-065, which showed quite good line fits to H, He and N, the synthetic N IV $\lambda 4058$ profile displayed weak emission, whereas the observed one was clearly in weak absorption. Consistency could be achieved by lowering \dot{M} until this line could be acceptably fitted, leaving the remaining nitrogen lines and H_α almost unaltered. In both cases it turned out that H_α was already almost insensitive to reductions in \dot{M} . Other stars that showed a similar problem, N11-051, Sk-66° 18, and Sk-66° 100, could not be ‘cured’ by this approach because there a reduced value of \dot{M} was no longer consistent with (unclumped!, see Sect. 5.4.5) H_α .

Because H_α is in absorption in all our objects, which leads to the well-known \dot{M} - β degeneracy, we estimated quite a large error on \dot{M} , namely plus/minus a factor of two, which is typical in this situation (e.g., Markova et al. 2004). The impact of the error in R_* is negligible here, as outlined in the next paragraph.

Stellar radii. Because the effective temperatures derived within this work are different from those of Mok07 (overall, these differences are modest, except for N11-026, N11-031, and N11-068, see Table 5.3), this leads to different theoretical fluxes and thus to different stellar radii. Similar to Mok07, we followed Kudritzki (1980) and Herrero et al. (1992), and calculated the ‘new’ radii from the theoretical Eddington fluxes and the (de-reddened) absolute magnitudes from Table 5.1.

Once the radii were redetermined, \dot{M} needed to be modified as well to preserve the fit quality of H_α , which depends on the optical depth invariant Q (see above). Contrasted to the case of Galactic objects, where the error of M_V (because of unknown distances) dominates the error budget of \dot{M} , this plays a secondary role in our sample, owing to sufficiently well-known distances and the fairly large error introduced by the \dot{M} - β degeneracy.

5.4.4 Nitrogen abundances and micro-turbulences

After determining the stellar and wind parameters and their uncertainties (some fine-tuning may still be necessary), we are now in a position to derive the nitrogen abundances and the corresponding micro-turbulent velocities, v_{mic} . Because the latter parameter significantly affects the strength of both He and metal lines and thus the implied abundances, it is useful to determine both quantities in parallel.

To carry out this analysis, we calculated a fine grid of typically 25 models by combining different abundances centered at the rough estimates derived in Sect. 5.4.3 with five different values for $v_{\text{mic}} = 0, 5, 10, 15, 20 \text{ km s}^{-1}$.

When possible (see below), we used a ‘curve of growth’ method based on the equivalent widths of the lines, which has been applied in the past years to different sets of B-stars to obtain various metallic abundances (e.g., Urbaneja 2004; Simón-Díaz et al. 2006; Markova & Puls 2008). In brief, this method uses synthetic and observed equivalent widths including uncertainties from *all* considered

Table 5.4: Helium and nitrogen abundances for the LMC sample with stellar parameters from Table 5.2. $[N]$ is our best-fitting value, $\Delta[N]$ the corresponding uncertainty, and $\Delta[N]^{\text{cl}}$ the change in $[N]$ (always positive) if clumping with $f_{\infty} = 0.1$ is included in the models (Sect. 5.4.5). Values displayed in italics were derived by the ‘curve-of-growth’ method. Literature values are from Walborn et al. (2004) for N11-031 and from Hunter et al. (2009b) for the B-stars and N11-029. When two entries are provided, the first one corresponds to our preferred solution, except for N11-031 where we consider both solutions to be possible.

Star	$\nu \sin i$	Y_{He}	$[N]$	$\Delta[N]$	$\Delta[N]^{\text{cl}}$	Literature
N11-026	72	0.10	7.80 ¹	+0.40	0.25-0.30	-
			7.75 ²	+0.40		
N11-031	71	0.11	7.83 ¹	± 0.15	-	8.00 \pm 0.18
			8.30 ²	± 0.15		
N11-038	100	0.08	7.85	± 0.15	0.05-0.10	-
Sk-66° 100	59	0.19	8.48 ³	± 0.15	-	-
N11-032	60	0.09	7.87	± 0.15	0.05-0.10	-
N11-045	64	0.07	6.98	± 0.20	-	-
BI253	230	0.08	7.90	± 0.15	0.15-0.20	-
BI237	140	0.09	7.38	± 0.15	0.05-0.10	-
N11-060	68	0.12	8.20 ¹	+0.30	0.05-0.10	-
			8.15 ²	+0.30		
Sk-70° 69	131	0.14	8.05 ³	± 0.15	0.15-0.20	-
N11-051	350	0.08	7.58 ³	± 0.20	-	-
N11-058	62	0.10	8.09	± 0.15	-	-
Sk-66° 18	75	0.14	8.48 ³	± 0.15	-	-
N11-065	60	0.13	8.17 ³	± 0.15	0.05-0.10	-
N11-066	59	0.10	8.17	± 0.20	0.05-0.10	-
N11-068	30	0.10	7.85	± 0.20	0.05-0.10	-
N11-061	54	0.09	7.18	± 0.15	-	-
N11-123	115	0.09	7.00	± 0.15	-	-
N11-087	260	0.10	7.38	-0.20 ⁴	-	-
N11-029	46	0.08	7.43	± 0.15	-	7.10 \pm 0.35
N11-036	39	0.08	7.85	± 0.17	-	7.76 \pm 0.11
N11-008	46	0.10	8.08	± 0.11	-	7.84 \pm 0.11
N11-042	21	0.08	7.00	± 0.15	-	6.92 \pm 0.24
N11-033	256	0.10	7.28	-0.20 ⁴	-	-
N11-072	14	0.10	7.68	± 0.15	-	7.38 \pm 0.06

¹From N III/N IV, uncertainty from N V.

²From N IV/N V, uncertainty from N III.

³Improvement of N IV λ 4058 fit with weak clumping.

⁴Uncertainty of upper limit.

lines to derive a unique pair of abundance and v_{mic} (incl. errors). Results from these analyses are indicated by an asterisk in the v_{mic} -column of Table 5.2.

Unfortunately, this procedure was not applicable to the bulk of the sample stars because of various reasons, e.g., blending and diluted lines owing to fast rotation, almost invisible lines owing to low nitrogen content, and peculiarities in the observed lines from some of the stars with highly ionized nitrogen. All these problems will be commented on in Sect. 5.5, and we opted for a determination of the nitrogen abundance/micro-turbulence pair by means of a visual inspection of the fit quality, using the same fine grid as described above.

We estimated the errors in v_{mic} to be 3-5 km s^{-1} , both for the equivalent width and the visual method. To provide an impression of the impact of these errors on the derived nitrogen abundances, we note that a decrease in v_{mic} by 5 km s^{-1} leads to an increase of [N] by 0.05-0.07 dex. For the error associated to [N] when derived by ‘visual’ fitting, we decided to be quite conservative. Even though we are able to obtain quite good fits for the bulk of the stars implying an uncertainty of 0.1 dex, we instead adopt a higher value of 0.15 dex to roughly account for the additional dependence on the stellar and wind parameters. For two stars, N11-033 and N11-087, we can only provide an upper limit on the abundance, with an estimated uncertainty of 0.20 dex. This value is also adopted for N11-066, N11-068, and N11-045, N11-051. We were able to obtain only rough estimates for the stellar parameters of the first two stars and could only use one nitrogen multiplet for the latter two. Even larger uncertainties were derived for two ‘problematic’ stars, N11-026 and N11-060, see Sect. 5.5.

Table 5.4 lists the obtained nitrogen abundances together with their estimated errors. When available, corresponding literature values were added.

5.4.5 Additional considerations

Wind clumping

So far, we neglected wind clumping in our analysis. Because most of the nitrogen lines are formed in the intermediate or outer photosphere,¹⁴ at least for not too extreme winds as considered here, they should remain quite unaffected by *direct* clumping effects, though indirect effects could be important (see Chapter 4). Clumped winds have lower mass-loss rates compared to their unclumped counterparts by a factor of $1/\sqrt{f_{\text{cl}}}$ if the clumping factor f_{cl} is radially constant, which could influence both the N III and the N IV emission lines, because of their sensitivity on \dot{M} . Given the multitude of evidence for wind-clumping (e.g., Puls 2008 and references therein), it is necessary to examine the impact of clumping on our abundance determinations.

We adopted the parametrization as used by Hillier & Miller (1999) and Hillier et al. (2003),

$$f(r) = f_{\infty} + (1 - f_{\infty}) \exp(-v(r)/v_{\text{cl}}) \quad (5.1)$$

where $f(r)$ is the volume filling factor,¹⁵ f_{∞} its asymptotic value (if $v_{\infty} \gg v_{\text{cl}}$) and v_{cl} the velocity where the volume filling factor reaches values close to e^{-1} , if $f_{\infty} \ll 1$. To allow for maximum effects, we set $v_{\text{cl}} = 30 \text{ km s}^{-1}$, close to the sonic speed for O-stars, and concentrated on models with $f_{\infty} = 0.1$, corresponding to \dot{M} reductions by a factor of roughly 0.3 (consistent with recent investigations allowing for macro-clumping, see Sundqvist et al. 2011).

¹⁴Note that this might no longer be true for the N V doublet, e.g., N11-031.

¹⁵Which is, within the standard assumption of micro-clumping and a void inter-clump medium, the inverse of the clumping factor f_{cl} .

Because most of our sample stars display thin winds, no major reaction due to clumping is to be expected. Indeed, a value of $f_\infty = 0.1$ did not induce any noticeable change in the spectrum for the bulk of the stars.

For stars N11-038, 032, BI237, N11-060, 065, 066, and 068, mostly the N III triplet is affected (for BI237, also N V), requiring 0.05 to 0.1 dex more nitrogen to preserve the *previous* fit quality of these lines. Because on the other hand the other nitrogen lines remain unmodified, the inclusion of clumping did not change our [N]-values for these stars, but only improved or deteriorated the particular representation of the triplet lines.

For BI253 and Sk-70° 69, clumping of the considered amount has a stronger effect, particularly on the N III triplet, N IV λ 4058 and the N V doublet. Here, a clumping factor of $f_\infty = 0.1$ requires [N] to be increased by 0.15...0.20 dex.

Finally, for N11-026 and N11-031, the inclusion of clumping affects the stellar parameters as well. Owing to the lower \dot{M} , a hotter temperature (by 1 to 2 kK) is needed to preserve the He I fit. For N11-026, [N] needs to be considerably increased, by 0.25 to 0.3 dex. This is the only case where we encountered a significant effect. For N11-031, on the other hand, at least the ‘cool solution’ (see Sect. 5.5) remained at the previous nitrogen abundance.

In addition to these general effects, for a few stars, Sk-66° 100, Sk-70° 69, N11-051, Sk-66° 18 and N11-065, the inclusion of clumping (of a lesser degree than $f_\infty = 0.1$) favors a better fit to N IV λ 4058, see Sect 5.5.

Background abundances

One of the central results of Chapter 4 was that the N III triplet emission increases with decreasing background metallicity, Z , due to reduced line-blocking. In this investigation we assume, following Mokiem et al. (2007b), a *global* Z of the LMC, $Z = 0.5 Z_\odot$. Because this value is somewhat controversial, and a $Z = 0.4 Z_\odot$ might be appropriate as well (e.g., Dufour 1984), we need to test the impact of this difference on the derived nitrogen abundances.

Overall, the lower background Z does not produce any extreme changes. As expected, the triplet emission increases, requiring a roughly 0.05 dex lower abundance to recover the previous fits. Interestingly, we also found that N IV λ 4058 and the N III quartet lines tend to more emission and weaker absorption, respectively, but to a lesser extent. The effect on the remaining nitrogen lines is marginal. Note that a lower [N] value owing to lower background abundances would partly cancel the corresponding increase in the derived [N] because of moderately clumped winds.

5.5 Comments on the individual objects

In the following, we give specific comments on the individual objects, regarding peculiarities and problems found during our analysis. We distinguish between B-/late O-stars and (hotter) O-stars, and sort by luminosity class and spectral type, starting at the hotter side. All nitrogen line fits (including corresponding limits according to Table 5.4) are displayed in Appendix C.1, except for the objects N11-072, N11-032, and BI237 which were included in the main text, because they are exemplary for objects with different features. All spectra were corrected for radial velocity shifts.

We selected those lines that were clearly visible, at least in most cases. In particular, for $T_{\text{eff}} \leq 35$ kK, we used N II $\lambda\lambda$ 3995, 4447, 4601, 4607, 4621, 4630 and N III $\lambda\lambda$ 4003, 4097, 4195, 4379, $\lambda\lambda$ 4634-4640-4642, and $\lambda\lambda$ 4510-4514-4518. For $T_{\text{eff}} > 35$ kK, we analyzed the lines from

N III/N IV/N V: N III as before, N IV $\lambda\lambda$ 4058, 6380, and N V $\lambda\lambda$ 4603 – 4619 (see Table 3.5). Additionally, the N IV multiplets around 3480 Å and 7103-7129 Å were used for the field stars observed with UVES (except for Sk-70° 69 where only N IV λ 3480 is available).

5.5.1 Late O- and B-supergiants/giants

Supergiants

N11-029 – O9.7 Ib. This is the only O-supergiant within our sample. Because of its late nature, we discuss it here together with the B-supergiants. No major problem was encountered, and the largest difference with respect to Mok07 concerns the high $\beta = 1.63$ derived in their analysis. We opted for a lower value, $\beta = 1.23$, still at the limit of prototypical values. To compensate for this modification, \dot{M} needs to be somewhat increased.

Figure C.1 shows the best fit for the nitrogen lines. An abundance of $[N] = 7.43 \pm 0.15$ was inferred mainly from N II λ 3995 and the N III quartet lines. The bulk of the N II lines are not helpful because they are blended by O II (Table 3.5). This is also the case for most of the N III lines.

The most interesting feature, however, is the discrepancy for N III λ 4634,¹⁶ which shows an almost completely refilled profile but is predicted to be in absorption. To synthesize a profile with E.W. ≈ 0 would require a higher T_{eff} or a lower $\log g$, inconsistent with the He ionization equilibrium. This seems to be the first observational evidence for one of the problems discussed in Chapter 4. For a certain temperature range (around 30 to 35 kK), FASTWIND spectra predict too little emission in the N III triplet compared to results from CMFGEN, because of the (still) missing overlap effects between the N III and O III resonance lines around 374 Å (which are treated consistently in CMFGEN; for details, see Chapter 4).

For additional tests, we calculated a CMFGEN model at the same stellar/wind parameters and abundances as derived in the present analysis. As expected, the corresponding synthetic profiles are closer to the observations (though still not as refilled as observed). To check whether the oxygen abundance plays a significant role, two different abundances were considered, $[O] = 8.66$ and 8.30 dex (solar and factor two lower). In agreement with our theoretical argumentation from Chapter 4, this difference did not affect the predicted N III triplet emission strength.

N11-036 – B0.5 Ib. The largest difference to Mok07 is that we derive a lower value for $\log g$ (by 0.2 dex) as well as a lower T_{eff} (by 500 K), by exploiting He I/He II in parallel with the N II/N III ionization equilibrium.

The nitrogen lines are well fitted, both for N II and N III (Fig. C.2). The only discrepancy found relates to an underprediction of absorption strength in N II λ 4607, whereas the discrepancy at N II λ 4601 is caused by an O II blend. Quite a large enrichment is found, $[N] = 7.85 \pm 0.17$.

N11-008 – B0.7 Ia. Again, we adapted the fairly high velocity field exponent derived by Mok07, $\beta = 1.87$, to a more typical value of $\beta = 1.30$. We derived $v \sin i = 46 \text{ km s}^{-1}$, which is approximately half the value obtained by Mok07, and compensated by invoking a $v_{\text{mac}} = 60 \text{ km s}^{-1}$.

The best fitting abundance, $[N] = 8.08 \pm 0.11$ (Fig. C.3), was obtained by the ‘curve of growth method’, and yielded reasonable fits except for N II $\lambda\lambda$ 4447, 4621, and N III λ 4003, which are slightly overpredicted.

¹⁶Similar to N III λ 4640, which is strongly blended by O II.

Giants

N11-042 – B0 III. We derive a lower projected velocity than Mok07, $v \sin i = 21 \text{ km s}^{-1}$, as well as a lower T_{eff} , together with a corresponding decrease of $\log g$, for consistency with the N II/N III ionization equilibrium. For this cooler solution, the helium abundance needs to be lowered as well, $Y_{\text{He}} = 0.08$, close to the LMC He baseline abundance (see Sect. 5.6).

Owing to the low rotational speed, we were able to clearly inspect all N II and N III lines (Fig. C.4) which are fitted almost perfectly. The only discrepancy occurs at N III $\lambda 4097$, caused by a coincident O II line. We were able to see two strong O II absorption lines at both sides of N III $\lambda 4640$, and to the left of N III $\lambda 4379$ (where the former cannot be used for the diagnostics of similar stars with rapid rotation, N11-008, N11-029, N11-036, and N11-045).

A low nitrogen content was derived, $[\text{N}] = 7.00 \pm 0.15$, consistent with the low helium abundance.

N11-033 – B0 III_n. We find a slightly cooler T_{eff} compared to Mok07, and our helium line fits suggest $Y_{\text{He}} = 0.10$.

Owing to its rapid rotation, all nitrogen lines are severely diluted and almost ‘vanish’ from the spectrum (Fig. C.5), implying an upper limit of $[\text{N}] = 7.28$ from the N II lines.

N11-072 – B0.2 III. This object shows a very sharp-lined spectrum, with the lowest $v \sin i$ value within our sample. A consistent solution for nitrogen and helium suggests a slightly cooler T_{eff} (by 1 kK) and lower $\log g$ (by 0.1 dex). Our best fit indicates $Y_{\text{He}} = 0.10$.

As for the similar object N11-042, we were able to obtain a good fit from the ‘curve of growth’ method, with $[\text{N}] = 7.68 \pm 0.15$, and a rather low $v_{\text{mic}} = 2.7 \text{ km s}^{-1}$ (Fig. 5.5). Thus, and in contrast to N11-042, this object is clearly enriched. Note that N11-072 and N11-042 belong to different associations, LH-10 and LH-9, respectively.

5.5.2 O-stars

Giants

N11-026 – O2 III(*). This star is one of the four O2 stars in our sample, together with N11-031, BI237, and BI253, comprising the hottest objects. Unlike Mok07, we favor a cooler solution, $T_{\text{eff}} = 49 \text{ kK}$ (Mok07: 53 kK), and a somewhat lower \dot{M} . This comparably large difference for T_{eff} relies both on the better reproduction of He I $\lambda 4471$ and on the fit to the nitrogen lines, with three ionization stages visible (Fig. C.6). Mokiem et al. (2007a) considered this cooler solution as well (almost included in their error bars), which would have improved their fit to He I $\lambda 4471$, but argued in favor of the hotter one, accounting for the global fit quality. By considering nitrogen now, we find support for a lower T_{eff} , since for $T_{\text{eff}} \geq 50 \text{ kK}$ the N III lines vanish from the spectrum (cf. BI237 and BI253).

The derived nitrogen abundance results from a compromise solution, $[\text{N}] = 7.80$, where this value is also the lower limit. Moreover, we estimate quite a large uncertainty (upper limit) of 0.4 dex, arising from our difficulties to fit all three ionization stages in parallel. We favor a solution that provides a good fit for the N III quartet and the N IV lines, whereas a larger abundance, $[\text{N}] = 8.20$, is needed to fit the N V doublet. From Fig. C.6 it is clear that this large abundance (red) disagrees with the remaining nitrogen lines. Of course, we also tried a fit at hotter temperatures. At $T_{\text{eff}} = 52 \text{ kK}$ (close to the result by Mok07), $\log g = 4.1$ (which is still consistent with the Balmer line wings) and $\dot{M} = 1.5 \cdot 10^{-6} M_{\odot} \text{ yr}^{-1}$, it is possible to fit both N IV and N V, for quite a similar abundance, $[\text{N}] = 7.75$. At

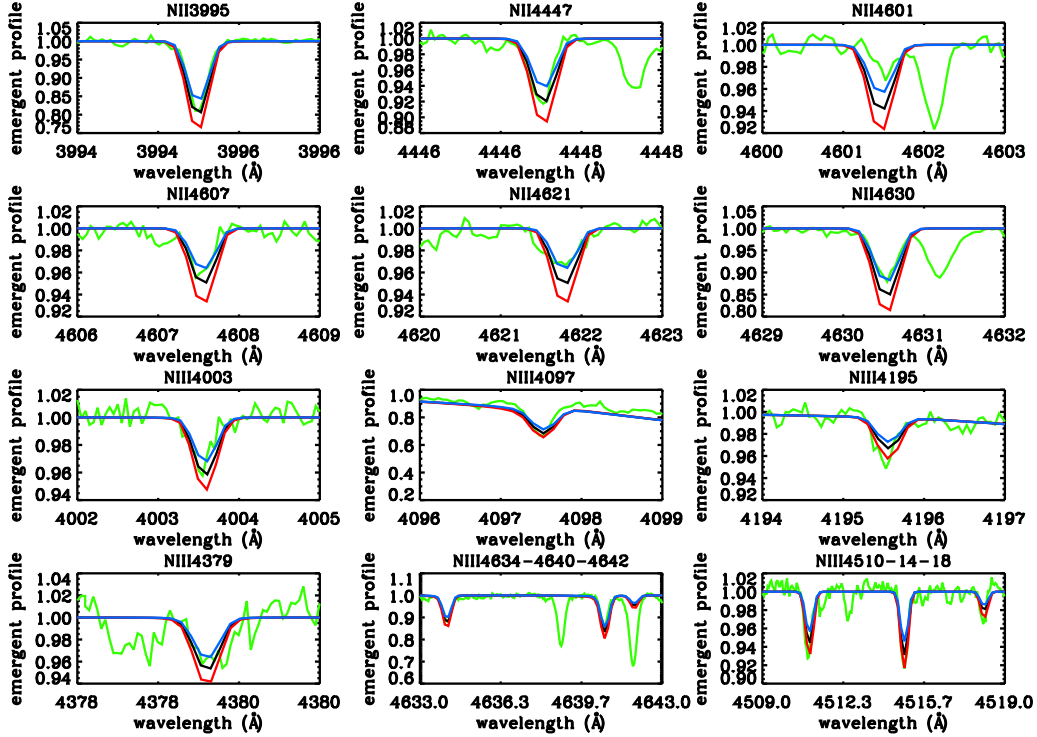


Figure 5.5: N11-072 - B0.2 III. Observed (green) and best-fitting optical nitrogen spectrum (black). Blue and red spectra correspond to synthetic line profiles with [N] at the lower and upper limit, respectively.

this temperature, however, all N III lines have vanished. To recover them we would need to increase the abundance again, also by 0.4 dex. Because of the poorer prediction of He I λ 4471 we opted for the cooler solution. Since in both cases the implied nitrogen abundances are similar, this does not lead to severe problems for our subsequent analysis, but requires larger error bars than typical.

N11-031 – ON2 III(f*). This star raised the most severe difficulties in our sample when trying to fit the nitrogen lines (Fig. C.7). Already its ‘ON’ designation indicates strong nitrogen features in its spectra, in this case N IV λ 4058, 3480 (for the latter, see Walborn et al. 2004), and the N V doublet lines. We were unable to consistently fit these strong features together with the remaining nitrogen lines. In contrast, N IV λ 6380 has almost the same strength as in N11-026.

When we tried to reproduce the (rather weak, but clearly visible) He I λ 4471 in parallel with N III and N IV λ 6380, we obtained $T_{\text{eff}} = 47.8$ kK, slightly cooler than N11-026, whilst Mok07 derived $T_{\text{eff}} = 45$ kK, excluding T_{eff} values higher than 47 kK based on the helium ionization analysis.

When, on the other hand, we tried to fit the problematic lines, we needed a much higher T_{eff} . A consistent fit for all N IV lines (including N IV λ 6380) together with those from N V requires $T_{\text{eff}} = 56$ kK, $\log g = 4.00$, and $\dot{M} = 2.2 \cdot 10^{-6} M_{\odot} \text{yr}^{-1}$, together with a very high abundance, $[\text{N}] = 8.30$. Clearly, this set of stellar parameters neither reproduces the N III lines nor the weak He I λ 4471. N11-031 has been previously analyzed by Walborn et al. (2004) and Doran & Crowther (2011) using the N IV/N V lines (without discussion of He I and N III). The former authors obtained quite similar pa-

rameters, $T_{\text{eff}} = 55$ kK, $\log g = 4.00$, and a somewhat lower $\dot{M} = 1.0 \cdot 10^{-6} M_{\odot} \text{yr}^{-1}$, presumably because of a clumped wind (though clumping has not been mentioned). At these parameters, they derived $[\text{N}] = 8.00 \pm 0.18$, which for our models would be still too low. Doran & Crowther (2011) only provided T_{eff} within their analysis, deriving $T_{\text{eff}} = 54.7$ kK for this object.

Because of the similarities with N11-026 (except for the two strong features), the fact that N IV $\lambda 6380$ ¹⁷ behaves ‘normally’ and that He I $\lambda 4471$ is clearly visible, the cooler solution with $[\text{N}] = 7.83 \pm 0.15$ cannot be discarded so far. We checked our synthetic spectra by independent CM-FGEN calculations. The results are quite similar, in particular the predicted N III emission lines are even slightly weaker than those produced by FASTWIND, again pointing to a cooler solution.

We also tried to attribute the problematic feature to the presence of X-rays by means of CM-FGEN calculations including typical X-ray strengths and distribution, but almost no effect on these lines was found (basically because the line forming region is still inside or close to the photosphere).

Of course, it would be helpful to consider N IV $\lambda 3480$ as well, which unfortunately is not included in our dataset. A by-eye comparison with the corresponding profile displayed in Walborn et al. (2004, their Fig. 1) showed that both our cooler and hotter solutions are compatible with this spectrum.¹⁸

Consequently, the nature of the strong N IV $\lambda 4058$ and N V doublet features remains open. Of course, binarity could be a plausible solution, where a cooler component could be responsible for He I and N III, and a hotter one for the intense N IV and N V lines. We note that this is the brightest ($M_V = -5.78$) object of the O-star sample and that other, previously thought single early O-stars, displaying both strong N V lines as well as the presence of He I in their optical spectra such as CygOB2-22 and HD 93129A, were subsequently resolved as binaries (Walborn et al. 2002, Nelan et al. 2004). Therefore, the binarity scenario for N11-031 needs to be clarified in future investigations.

Note, however, that the other ON-stars discussed by Walborn et al. 2004, LH64-16 and NGC 346-3, seem to display very similar features, though the presence of He I is not as clearly visible as in our spectrum for N11-031. Similar, but less dramatic, problems are also found for those other sample stars where we were able to analyze N III/N IV/N V in parallel, namely N11-026 and N11-060 (see below). While the presence of these discrepancies in all these objects may point toward a less likely binary scenario for N11-031, we note that the differences in T_{eff} for the two alternative solutions reach 8,000 K in N11-031, and remain at moderate 3,000 K for the other two objects analyzed here.

We will reconsider N11-031 and other ON-stars in future investigation to clarify how it is possible to have weak He I and N III in parallel with strong N IV and N V. For the remainder of this work, however, we discuss the results for N11-031 in terms of both the cool and the hot solution, without preferring either of them.

N11-038 – O5 II(f⁺). The parameter set derived for this star is quite similar to that of Mok07, with only slightly lower $Y_{\text{He}} = 0.08$ and $v \sin i = 100 \text{ km s}^{-1}$. This star displays a peculiar He I $\lambda 4471$ profile of triangular shape that could not be reproduced, even if invoking macro-turbulent broadening (as speculated by Mok07).

We obtained $[\text{N}] = 7.85 \pm 0.15$, similar to the case of N11-032, by means of quite a good fit to all lines from three ionization stages (Fig. C.8). Besides the peculiar He I $\lambda 4471$ profile, N IV $\lambda 6380$ shows contamination by the DIBs at $\lambda \lambda 6376.08, 6379.32$, and the N V $\lambda 4603$ absorption is much stronger than predicted, contrasted to the other component.

¹⁷Which turned out to be quite ‘reliable’ in the remaining objects, even for the hottest ones.

¹⁸Interestingly, our cooler solution predicts somewhat stronger absorption than the hotter one, even though the corresponding nitrogen abundance is significantly lower.

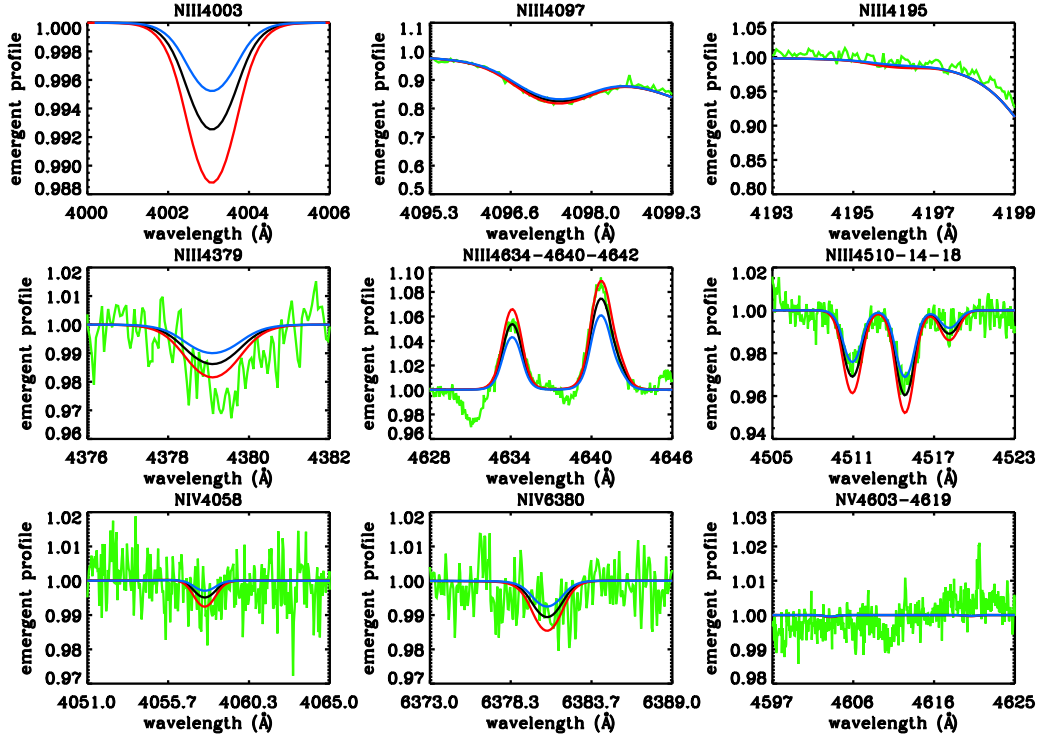


Figure 5.6: N11-032 - O7 II(f). Same color coding as Fig. 5.5. For this star, N III λ 4003 has not been observed.

Sk-66° 100 – O6 II(f) is one of the field stars within our sample. The inspection of the H/He fits suggests no major revision of the values provided by Mok07.

Figure C.9 shows the best fit to the nitrogen lines. An abundance of $[N] = 8.48 \pm 0.15$ was needed to obtain a consistent fit. This high value agrees well with the high He content found for this object, $Y_{\text{He}} = 0.19$. However, we also found some problems regarding the N IV fits, except for the multiplet around 3480 Å, where the fit is perfect. Interestingly, we were able to ‘cure’ these problems by invoking a clumped wind with $f_{\infty} = 0.2$, with no significant changes in the remaining nitrogen lines.

N11-032 – O7 II(f). No major problems were found for this star. Our solution is slightly hotter than in Mok07, and we preferred a typical β value for O-stars, $\beta = 0.80$.

An excellent fit is obtained for this star of the (f) category (Fig. 5.6), resulting in $[N] = 7.87 \pm 0.15$ for both the N III triplet and the quartet lines. The fit quality of N III λ 4097 is remarkable as well. Note that for this star N III λ 4003 has not been observed. Since the N IV lines are weak and quite noisy, we can only state that our simulations are consistent with the observations.

N11-045 – O9 III. Our analysis agrees well with that of Mok07. We confirm that a low He abundance (lower than the estimated LMC He baseline abundance) matches the observations.

The only clear N-abundance indicators are the N III quartet lines, since most other lines are weak and the spectrum is noisy (Fig. C.10). N III λ 4097 is also weakly visible, and consistent with the quartet lines. Around this T_{eff} , the N III triplet turns from absorption to emission, and thus this object

does not belong to the ‘f’ category. The absence of lines, the fact that the star does not display a fast (projected) rotation, and the very low helium content is consistent with the very low nitrogen abundance, $[N] = 6.98 \pm 0.20$. These findings suggest that this object is of unevolved nature.

Dwarfs

BI253 – O2 V((f*)). This was one of the stars that were used by Walborn et al. (2002) to define the O2 spectral type. A slightly hotter solution (by 1 kK, $T_{\text{eff}} = 54.8$ kK) than in Mok07 was obtained by using the N IV/N V ionization equilibrium. This star was also analyzed by Massey et al. (2005) and Doran & Crowther (2011). The former authors provide only a lower limit on T_{eff} and a consistently lower $\log g$ ($T_{\text{eff}} \geq 48$ kK and $\log g = 3.9$), both in agreement with the error bars by Mok07, whilst Doran & Crowther (2011) derive a somewhat cooler solution (by 2 kK) compared to our findings.

Figure C.11 shows that N IV $\lambda 6380$, N IV $\lambda 3480$, the N IV multiplet around 7120 Å (where we reproduce the observed emission), and the N V lines are nicely fitted, with $[N] = 7.90 \pm 0.15$. At this T_{eff} and \dot{M} , no N III is visible in the spectrum (see also our discussion on N11-031). The feature located around N III $\lambda 4634$ corresponds to O IV $\lambda 4632$. On the other hand, we were unable to reproduce the fairly broad emission of N IV $\lambda 4058$ (a higher $v \sin i$ is inconsistent with the remaining lines). For this star, we compared again with a CMFGEN model at similar parameters, in particular with the same $[N]$. Contrasted to our solution, the width of the N IV emission line could be fitted, whilst the other lines indicated either a hotter temperature or a higher abundance.

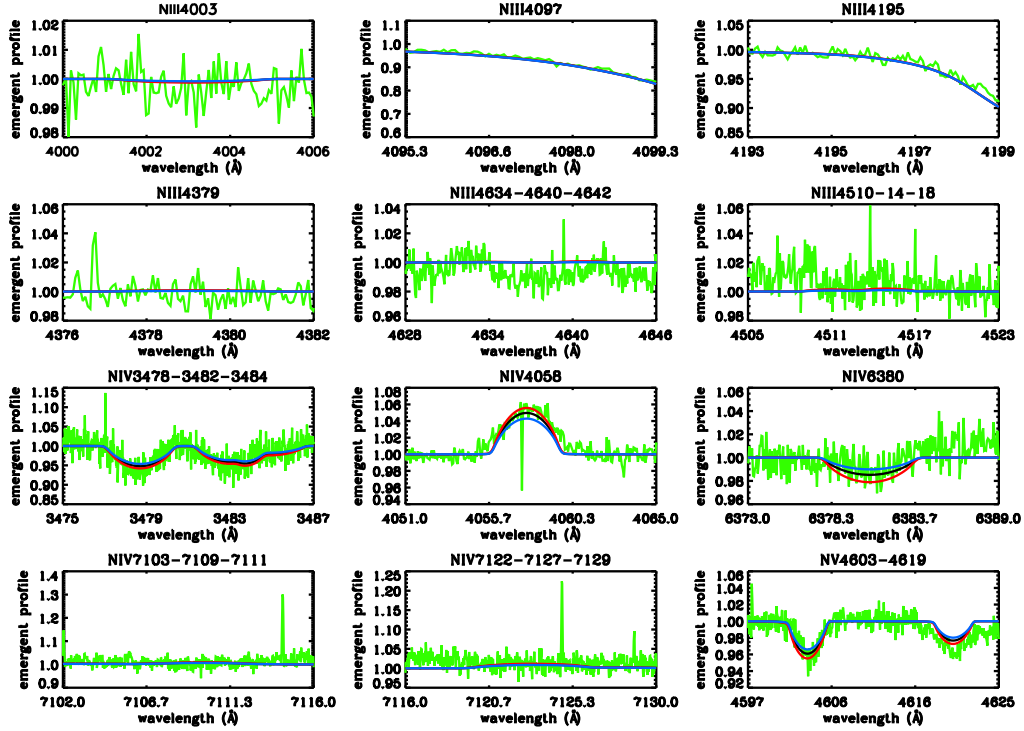
BI237 – O2 V((f*)). As for BI253, the nitrogen ionization equilibrium favours the hotter solution proposed by Mok07 ($T_{\text{eff}} = 53.2$ kK) rather than the cooler limit derived by Massey et al. (2005). Our result is also consistent with the work by Doran & Crowther (2011). This object is quite similar to BI253 with a somewhat thinner wind.

Figure 5.7 displays a good fit for the nitrogen lines. N IV $\lambda 4058$ does not show a broad profile as in BI253, and we are able to perform an excellent fit to this line. We derive a lesser enrichment than for BI253, with $[N] = 7.38 \pm 0.15$.

N11-060 – O3 V((f*)). With $T_{\text{eff}} = 48$ kK, which is about 2 kK hotter than in Mok07, we found a consistent description of H/He and nitrogen. As argued by Mok07, He I $\lambda 4471$ is similar to N11-031, and they derived a similar T_{eff} around 45 kK for both stars. Our findings indicate a higher value for both stars, indicating the internal consistency.

Again, we encountered the problem already met for N11-026 and N11-031, i.e., it is quite difficult to fit the lines from three different nitrogen ionization stages in parallel, see Fig. C.12. We opted for a compromise solution with $[N] = 8.20 \pm 0.30$, which is quite high but in line with the helium enrichment. Note that we also estimate quite a high upper limit, motivated by the following reasoning.

As for N11-026, we considered the impact of a hotter solution. With $T_{\text{eff}} = 51$ kK and $\log g = 4.1$, we are able to fit both N IV and N V at a similar abundance, $[N] = 8.15$. To recover the N III triplet lines at these hot temperatures, however, requires an increase of $[N]$ by roughly 0.3 dex. Thus, we are able to derive a quite similar nitrogen abundance for different T_{eff} , either using the N III/N IV or N IV/N V ionization equilibrium. The upper limit results from the condition to match either N V or N III, respectively.

Figure 5.7: BI237 - O2 V(f^*).

Sk-70° 69 – O5 V(f). For this field star, we had some problems to reconcile H/He and N at the parameters provided by Mok07. Our final solution is cooler by 1 kK, and we derived $Y_{\text{He}} = 0.14$ which is lower than the $Y_{\text{He}} = 0.17$ estimated by Mok07.

Figure C.13 presents the best fit for all nitrogen lines, for $[\text{N}] = 8.05 \pm 0.15$. There are only two disagreements: the ‘right’ wing of N III $\lambda 4634$ is predicted a bit too narrow, and N IV $\lambda 4058$ is predicted to be in very weak emission, contrasted to the observations. We consider the fit acceptable, particularly since in a clumped wind this weak emission becomes almost suppressed.

N11-051 – O5 Vn(f). This star is the fastest rotator in our sample, and we derived a slightly higher $v \sin i$ and cooler T_{eff} . We also used a prototypical value of $\beta = 0.8$ instead of the rather low $\beta = 0.6$ derived by Mok07, implying also a lower \dot{M} .

Unlike N11-033, where the fast rotation removes almost all information, this object shows the N III triplet in emission, which is quite well reproduced by our model, with $[\text{N}] = 7.58 \pm 0.20$ (Fig. C.14). At such high $v \sin i$, these lines are blended with C III $\lambda \lambda 4647 - 4650 - 4652$. Since carbon is not included in our calculations, it is not possible to predict the right wing of the blended profile. That the carbon triplet has the same strength as the N III one indicates that this star could belong to the newly defined Ofc category (Walborn et al., 2010; Sota et al., 2011), which seems to be strongly peaked at spectral type O5 for all luminosity classes.

The only problem of our fitting procedure is found for N IV $\lambda 4058$, predicted to be in slight emission and actually not present in the observed spectra. In contrast to N11-058 and N11-065, it was not possible to circumvent this discrepancy by lowering \dot{M} , since the fit to H $_{\alpha}$ becomes unacceptable then.

By means of a clumped wind with lower \dot{M} , on the other hand, we can fit both H_α and obtain a better result for N IV λ 4058, whilst not compromising the remaining nitrogen lines.

N11-058 – O5.5 V((f)). To find a consistent solution for all H, He, and N lines, a very low $\dot{M} = 0.01 \cdot 10^{-6} M_\odot \text{yr}^{-1}$ is required (similar to the case of N11-065), and also a low $\log g$ (0.14 dex lower than Mok07), which is still consistent with the Balmer line wings but appears to be fairly low for a dwarf.

This was the only O-star that could be analyzed by the ‘curve growth method’ with respect to [N] and v_{mic} . The derived value of $v_{\text{mic}} = 6 \pm 3 \text{ km s}^{-1}$ is lower than for the other O-stars, though such a difference does not drastically affect the derived abundance, as argued in Sect.5.4.4. Quite a large abundance, [N] = 8.09 ± 0.15 , was determined which fits all the lines (Fig. C.15).

Sk-66° 18 – O6 V((f)). Our estimates agree well with those from Mok07. As for Sk-66° 100, we found a very large nitrogen abundance, [N] = 8.48 ± 0.15 (Fig. C.16). Note that the N IV λ 4058 line is predicted in weak emission but appears in absorption. Again, lowering \dot{M} was not sufficient to cure this problem. A somewhat better fit to the this line was obtained for a weakly clumped wind with $f_{\text{cl}} = 2.3$, included in the figure.

N11-065 – O6.5 V((f)). Our best fit to the He lines indicates $Y_{\text{He}} = 0.13$, lower than the value derived by Mok07, $Y_{\text{He}} = 0.17$. As already discussed in Sect. 5.4.3, a satisfactory reproduction of N IV λ 4058 requires a very low $\dot{M} = 0.05 \cdot 10^{-6} M_\odot \text{yr}^{-1}$. Since this line clearly appears in absorption, whereas our model with \dot{M} from Mok07 predicts much too less absorption, we lowered \dot{M} , but were able to preserve the fit to H_α and the remaining nitrogen lines. By the inclusion of clumping we obtained an even better fit quality, with [N] = 8.17 ± 0.15 from N III and N IV (Fig. C.17).

N11-066 – O7 V((f)). T_{eff} and $\log g$ as derived by Mok07 turned out to be inconsistent with the N III/N IV ionization equilibrium. We had considerable problems to fit both N III and N IV lines at the same abundance, and particularly to reproduce the absorption within N IV λ 4058 and the N III quartet lines. To this end, a lower T_{eff} was mandatory, but only rough estimates using our coarse grid could be obtained, resulting in $T_{\text{eff}} = 37 \text{ kK}$ and $\log g = 3.7 \text{ dex}$, which are 2.3 kK and 0.17 dex lower than the values provided by Mok07, respectively. The gravity is somewhat low for a dwarf but still inside the error bars assigned by Mok07. With these values, we determined [N] = 8.17 ± 0.20 , see Fig. C.18, which seems rather large for $Y_{\text{He}} = 0.1$.

N11-068 – O7 V((f)). As for N11-066, we were only able to fit the H/He and N lines by means of the coarse grid. The differences to the results by Mok07 are significant, but still consistent with the observations and identical to those of N11-066 which has the same spectral type.

In contrast to N11-066, however, particularly the N III triplet shows weaker emission, and thus a lower [N] = 7.85 ± 0.20 has been found, see Fig. C.19.

N11-061 – O9 V. In contrast to Mok07, we chose a prototypical value for the velocity field exponent, $\beta = 0.8$, together with a higher value for \dot{M} . All H/He lines could be reproduced without difficulties.

The nitrogen analysis is quite similar to the case of N11-045, and we derived [N] = 7.18 ± 0.15 from N III alone (Fig. C.20).

N11-123 – O9.5 V((f)). Our parameters are very similar to Mok07, and Fig. C.21 shows our solution for N II/N III. Even though the rotation is not extreme, almost no nitrogen is visible, and the features overlapping with the ‘non-existent’ N II λ 4630 and N III λ 4640 are blends by O III and Si III, respectively. Thus, we infer a very low nitrogen content, $[N] = 7.00 \pm 0.15$, roughly corresponding to the LMC baseline abundance.

N11-087 – O9.5 Vn. For this rapid rotator we also found good agreement with Mok07. Because of rotation, all nitrogen lines are diluted into the continuum (Fig. C.22), and only an upper limit for $[N]$ could be estimated, $[N] = 7.38$.

5.6 Discussion

5.6.1 Comparison with results from Mok07

In our discussion of the derived results we first concentrate on a brief comparison with the findings by Mok07 (see Table 5.3). Except for a few cases, we derive somewhat cooler T_{eff} . To a certain extent, this might be attributed to the improved temperature structure in the new FASTWIND version, and also to the possibility to exploit the nitrogen ionization equilibrium. The most substantial changes concern N11-026 (4.3 kK cooler), and N11-031 (already the cooler solution is 2.8 kK hotter). For the earliest stars in our sample (two O2 dwarfs and two O2 giants), we determine a temperature range of $47.8 \leq T_{\text{eff}} \leq 54.8$, quite similar to Mok07, but now including N11-031, since we infer hotter solutions for this object. Massey et al. (2005) found a similar range, using two dwarfs and two giants. Gravities changed in parallel for most of the cases, with 0.10 and -0.43 dex as largest positive and negative difference, respectively. Stellar radii agree very well, even for the two stars with the most extreme changes in T_{eff} (less than 5% difference in R_*).

We derive \dot{M} values that are typically lower by less than a factor of two ($\Delta \log \dot{M} \approx -0.1 \dots -0.4$ dex), with a maximum change of -1.2 dex for N11-058 based on our analysis of the nitrogen lines. The resulting Y_{He} values agree well, except for two stars with differences considerably larger than the adopted errors. For both stars (Sk-70° 69 and N11-065) we find a lower helium content.

The largest differences relate to $v \sin i$ and v_{mic} . Differences around 30-40% in $v \sin i$ stress the importance of obtaining this parameter in a separate step, when using an automated fitting method. The substantial differences in v_{mic} , on the other hand, should not be taken too seriously. To a major part, v_{mic} has not been literally derived during this work, but was only adopted (as $v_{\text{mic}} = 10 \text{ km s}^{-1}$), where the resulting fit quality did not indicate any problems with this value, within $\pm 5 \text{ km s}^{-1}$. Only for four mostly cooler stars we were indeed able to infer more robust estimates, indicating quite a low $v_{\text{mic}} \approx 5 \text{ km s}^{-1}$. Note, however, that the latter value refers to nitrogen lines only, and inconsistencies in v_{mic} from H/He (used by Mok07) and metal lines have been found already in various studies.

Because the topic of a potential relation between v_{mic} and stellar type ($\log g!$) is of recent interest¹⁹ because it might indicate (together with other evidence) the presence of sub-surface convection (Cantiello et al., 2009), a more thorough investigation is certainly required. A derivation from light elements will become difficult for the hotter O-stars though, because of the restricted number of visible lines and the complex formation mechanism of the ubiquitous (photospheric) emission lines. Here, it

¹⁹E.g., Mok07 found a weak correlation for objects with $\log g \leq 3.6$; see also Kilian et al. (1991), Gies & Lambert (1992), Daflon et al. (2004) for similar results for Galactic B-stars and Hunter et al. (2007) for LMC B-stars.

Table 5.5: Comparison between nitrogen abundances derived by means of FASTWIND and by Hunter et al. (2009b), using their stellar parameters and N II diagnostics alone.

Star	Sp. Type	[N] t.w.	[N] Hunter
N11-029	O9.7 Ib	7.20	7.10
N11-036	B0.5 Ib	7.86	7.76
N11-008	B0.7 Ib	7.89	7.84
N11-042	B0 III	6.99	6.92
N11-072	B0.2 III	7.43	7.38

will become advantageous to exploit the information contained in the numerous UV Fe and Ni lines (e.g., Haser et al. 1998).

5.6.2 Overlap with B-star nitrogen analyses

To ensure the consistency between O-star nitrogen abundances from this (and upcoming) work and previous results from B-stars (using different codes, model atoms and analysis methods), a more thorough inspection of the cooler objects is certainly required. Indeed, we are able to compare with alternative nitrogen abundances from some overlapping objects (compiled by Hunter et al. 2009b, see Table 5.4), which are based on stellar parameters obtained by means of TLUSTY and using the Si III/Si IV ionization equilibrium (Hunter et al., 2007).

Hunter et al. (2007) already realized that their T_{eff} -values were somewhat lower than corresponding results from Mok07 (who used exclusively H and He), but also pointed out that T_{eff} estimates based on He II $\lambda 4541$ would agree much closer. This is even more true regarding our ‘new’ values, which lie in between the Hunter et al. estimates from Si and those from Mok07. These differences in T_{eff} derived either from metals or from H/He are somewhat disturbing because of their influence on the metallic abundances when using lines from one ionization stage only.

Still, Hunter et al. (2007) decided to keep their cooler solution to preserve the internal consistency of their analysis. Consequently, the nitrogen abundances derived in the present study are systematically higher because of our higher T_{eff} (leading to intrinsically weaker N II lines), with $\Delta T_{\text{eff}} \approx 1\text{kK}$ for N11-008 and N11-072, and $\approx 2\text{kK}$ for N11-036. For N11-042, the T_{eff} is quite similar, and for this object the derived [N]-values indeed overlap by better than 0.1 dex. For N11-029 our T_{eff} is quite similar as well, but we derive a 0.1 dex lower $\log g$, which leads to weaker N II lines.

To check our model atom and our diagnostic approach, we performed an additional analysis by reproducing the conditions adopted by Hunter et al. (2007), i.e., we used their stellar parameters (with negligible \dot{M} to mimic TLUSTY models) and N II lines only, within the ‘curve of growth’ method and adopting their N II equivalent widths and uncertainties. For N11-029 and N11-042, we could only perform a ‘by eye’ estimate because Hunter et al. considered one N II line alone. Corresponding results are compared in Table 5.5, and the agreement is almost excellent.

Therefore we conclude that the consistency of nitrogen abundances in the overlapping B- and O-star regime is satisfactory, and that the different codes and methods reasonably agree. However, there is a slight offset on the order of 0.1 to 0.2 dex, which we attribute mostly to different effective temperatures. Because our analysis is based on both N II and N III lines (in contrast to Hunter et al.), and was performed in parallel with the analysis of H/He, we prefer our values.

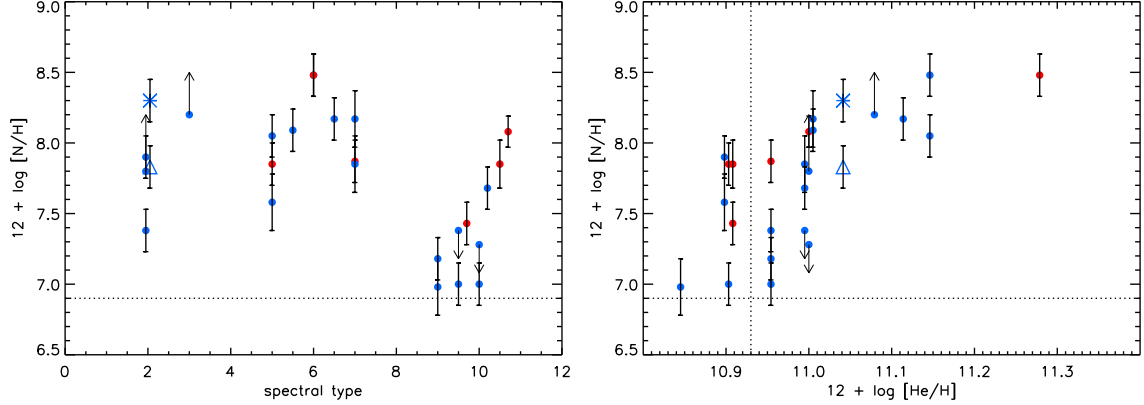


Figure 5.8: Nitrogen abundances derived for our LMC sample. Left panel: As a function of O-star spectral type (‘10-12’ correspond to B0-B2; for T_{eff} , see Table 5.2). Right panel: As a function of helium content, $12 + \log(\text{He}/\text{H}) = 12 + \log(Y_{\text{He}})$. Red: luminosity class I-II; blue: III-V. Arrows indicate upper or lower limits. Alternative solutions for N11-031 (see Sect. 5.5) are indicated by a triangle and an asterisk for the cooler and hotter solution, respectively. The estimated ($1-\sigma$) error for $\log(Y_{\text{He}})$ is 0.05 dex. The dotted lines indicate the LMC nitrogen (Hunter et al., 2007) and the average helium (see text) baseline abundances. Some objects were slightly shifted horizontally for clarity.

5.6.3 Nitrogen abundances

Figure 5.8 summarizes the basic outcome of our analysis by displaying the derived nitrogen abundances as a function of spectral type and helium content together with the LMC baseline abundance from Hunter et al. (2007). Evidently, there are only few cooler objects located close to the baseline, whereas the majority of the objects (independent of luminosity class!) is strongly enriched, with $[\text{N}]$ in between 7.5 and 8.1.²⁰ Five objects display extreme enrichment, with $[\text{N}]$ from 8.17 to 8.5, which is close to the maximum nitrogen content given by the CNO equilibrium value for nitrogen, $[\text{N}]_{\text{max}} \approx 8.5$. However, this is well above the enrichment reached for a $40 M_{\odot}$ star with an initial rotational velocity of 275 km s^{-1} (Brott et al., 2011a).

The right panel of Fig. 5.8 is more promising. There seems to be a strong correlation between the nitrogen and the helium enrichment, here displayed logarithmically. The LMC helium abundance should be located, in terms of number fraction, around $Y_{\text{He}} = 0.08\text{-}0.094$ corresponding to $[\text{He}] = 10.90\text{-}10.97$ (Russell & Dopita 1990; Maeder & Meynet 2001b; Vermeij & van der Hulst 2002; Peimbert 2003; Tsamis et al. 2003), and agrees quite well with our minimum values for the derived helium abundance. We found only five stars with considerably enriched nitrogen close to this value, three (super-)giants and two dwarfs, but note also the attributed uncertainty in helium content. Except for these objects, the correlation is almost perfect, and there is a certain clustering around the pair $[\text{He}]=11.0/[\text{N}]=8.0$.

A somewhat different view is provided in Fig. 5.9, which displays the so-called ‘Hunter-plot’, nitrogen-abundance vs. projected rotational speed, for all our sample stars with $T_{\text{eff}} \geq 29 \text{ kK}$. N-11 stars are indicated in black, field stars in blue. Circles, diamonds, and squares correspond to objects

²⁰Note that most stars have ‘normal’ or only moderately enriched helium abundances (see below) so that the high $[\text{N}]$ cannot be an effect of decreasing H content.

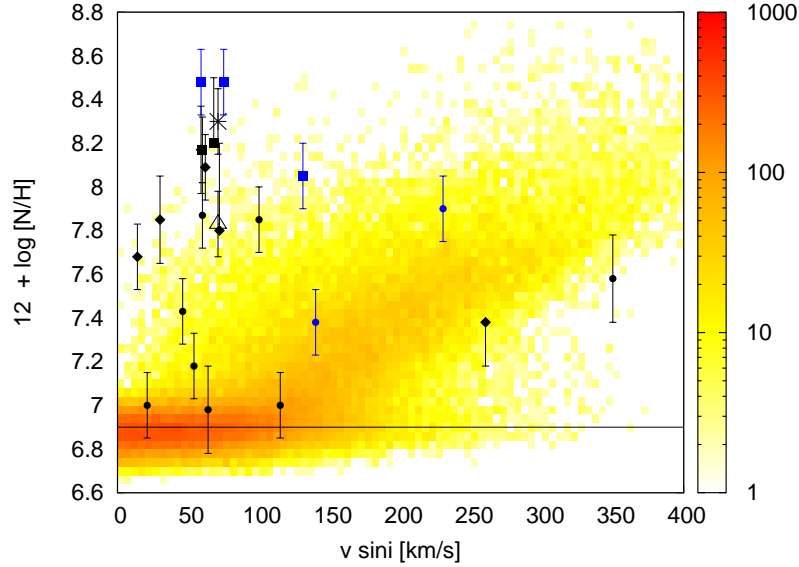


Figure 5.9: ‘Hunter-plot’ displaying the nitrogen abundance vs. projected rotational speed. Population synthesis from Brott et al. (2011b), for $T_{\text{eff}} \geq 29\text{kK}$ and a magnitude limit $V \leq 15.29$, shown as a density plot in the background. The color coding corresponds to the number of stars per bin, with binsize $5 \text{ km s}^{-1} \times 0.04 \text{ dex}$. Overplotted are data from this study. Black: N11 stars; blue: field stars. Circles, diamonds and squares correspond to objects with low, intermediate and strong helium enrichment, respectively (see text). Alternative solutions for N11-031 (intermediate He enrichment) as in Fig. 5.8.

with low ($Y_{\text{He}} < 0.1$), intermediate ($Y_{\text{He}} = 0.1$), and strong ($Y_{\text{He}} > 0.1$) helium enrichment, respectively.

The background of this figure consists of results from the recent population synthesis by Brott et al. (2011b), for all objects with $T_{\text{eff}} \geq 29 \text{ kK}$, and a magnitude limit (corresponding to our sample) of $V \leq 15.29$, shown as a density plot. The underlying simulation assumes a fairly broad Gaussian rotational velocity distribution as derived for LMC early-type stars, peaking at 100 km s^{-1} with a standard deviation of $\sigma = 140 \text{ km s}^{-1}$ (Hunter et al., 2008b, 2009b),²¹ and random inclinations.

Such diagrams ($[\text{N}]$ vs. $v \sin i$, compared with evolutionary calculations) have been presented the first time by Hunter et al. (2008a), to summarize the outcome of the B-star analyses within the FLAMES-I survey, and to investigate the predicted effects of rotational mixing. One of their major findings was the unexpected presence of a significant number of objects with slow rotation and high enrichment, not predicted by (single-star) theory, so-called ‘group 2’ objects.

In the O-star case now this problem becomes even more severe. We refrain here from a detailed statistical analysis, because there are too few investigated objects, and postpone this until the results from the FLAMES Tarantula survey (with more than 200 ‘useful’ O-stars) have become available.

Nevertheless, the trend is obvious. Roughly one third of the objects are located at positions where they should be expected (those at the baseline and the ‘diagonal’), another one-third is located at the predicted upper limit, and the last one-third (beyond $[\text{N}] = 8.0$) extends to very high values where

²¹Supergiants and stars above $25 M_{\odot}$ were discarded from their analysis to avoid effects from mass-loss-induced spin-down.

the predicted population density is almost zero. We note that the two objects with the highest [N] enrichment (≈ 8.5 dex, which is (incidentally?) just the maximum nitrogen content given by the CNO equilibrium value) are two field stars, Sk-66° 100 and Sk-66° 18, one O6 giant and another O6 dwarf. Both stars did not present any difficulties in the nitrogen analysis, which indicates a reasonable quality.

In terms of the original Hunter et al. sample, roughly two-thirds of our objects would be denoted by ‘group 2’.²² The corresponding number of objects is so large that inclination effects w.r.t. $v \sin i$ should be irrelevant. Interestingly, however, the corresponding He-abundances are in line with our findings. The first group has a low abundance (Fig. 5.9, circles), the second group mostly consists of enriched objects (diamonds), and the third one comprises objects with considerable He enrichment (squares). Accordingly, in parallel with the derived correlation between *observed* nitrogen and helium content, the discrepancy between observations and theory becomes the stronger the larger the He-abundance is.

In evolutionary models the amount of He transported to the surface is strongly controlled by the parameter f_μ , which describes the inhibiting effect of mean molecular weight gradients (in this case, the H-He gradient) on the transport of elements (see Heger & Langer 2000). The models of Brott et al. (2011a) have adopted $f_\mu = 0.1$, from an earlier calibration of Yoon et al. (2006). Lowering the sensitivity to the mean molecular weight barrier would increase mixing of nitrogen and helium to the surface, but would also reduce the minimum mass and velocity required for chemical homogeneous evolution in the models (see also the discussion in Heger & Langer 2000). Given the present values of [N] and Y_{He} , it might be possible to derive tighter constraints on f_μ in future work.

5.7 Summary

We investigated the N IV $\lambda 4058$ emission line formation, determined the nitrogen abundance of a sample of 25 LMC O- and early B-stars, and performed a first comparison with corresponding predictions from stellar evolution including rotational mixing. The results of this work can be summarized as follows.

- i) The dominating process responsible for the N IV line emission in O-stars is the strong depopulation of the lower level by the ‘two-electron’ transitions $3p \rightarrow 2p^2$, of (mostly) photospheric origin. This drain increases as a function of \dot{M} because of increasing ionizing fluxes (which are coupled to the He II continuum), which leads to more depopulation of the ground and the coupled $2p^2$ states. Resonance lines (as for the N III emission triplet) do not play a role for typical O-star mass-loss rates and below.

Because in addition to nitrogen there are many other elements that display optical line emission in the hot star regime (C, O, Si), it might be suspected that similar processes might be invoked because of similar electronic configurations/transitions.

- ii) To infer the nitrogen abundances, we redetermined the stellar and wind parameters by means of ‘by eye’ fits, starting with the values provided by Mok07, but exploiting in parallel the nitrogen ionization equilibrium and deriving $v \sin i$ in a first, separate step. Moreover, we accounted for extra line-broadening expressed in terms of v_{mac} . In addition to systematically lower $v \sin i$, we

²²In contrast to the B-star ‘group 2’ objects, however, the deviations between predictions and ‘observations’ for some of the objects are much more extreme.

also derived mostly lower T_{eff} (partly because of using an improved FASTWIND version) and thus $\log g$, but differences to Mok07 are generally small, except for few objects.

- iii) Based on these parameters, we derived nitrogen abundances mostly by varying the abundance and comparing with all nitrogen lines present in the spectrum. In a few cases, we were able to estimate $[\text{N}]$ and v_{mic} in parallel, by means of a curve-of-growth method.
- iv) Again in most cases, we found no problems in fitting the nitrogen lines, and reproduced the ‘f’ features quite well. Only for some of the (hotter) objects where lines from all three stages, N III, N IV and N V, are visible, we needed to aim at a compromise solution. Considerable problems were encountered for one star, N11-031 (ON2 III(f*)), where only either He I, N III and N IV λ 6380 (at cooler T_{eff}) or N IV and N V (at higher T_{eff}) could be fitted in parallel. The difference in the derived T_{eff} amounts to 8,000 K, which is far from satisfactory, and requires future effort to resolve the problem. A solution in terms of binarity, though somewhat unlikely, cannot be ruled out so far.
- v) For some cooler objects already analyzed by Hunter et al. (2007) by means of TLUSTY using N II lines alone, we found differences in $[\text{N}]$ on the order of 0.1 to 0.3 dex, with higher values from our analysis. These differences could be exclusively attributed to different stellar parameters, mostly T_{eff} . Overall, however, the nitrogen abundances in the overlapping B- and O-star domain are consistent within a reasonable error.
- vi) Within our sample, we found only three cooler objects close to the LMC nitrogen baseline abundance, $[\text{N}]_{\text{baseline}} = 6.9$. The majority of the analyzed O-stars (independent of luminosity class) seems to be strongly enriched, with $[\text{N}] = 7.5$ to 8.1. Five objects indicate an extreme enrichment, with $[\text{N}] = 8.17$ to 8.5.
- vii) There is a fairly good correlation between the derived nitrogen and helium surface abundances.
- viii) Comparing the nitrogen abundances as a function of $v \sin i$ with tailored evolutionary calculations, we found a significant number of highly enriched, low $v \sin i$ (‘group 2’) objects. Interestingly, the correlation between He and N becomes also visible in this comparison: Whilst most objects with unenriched He are located just in the region where the predicted population density is highest (accounting for selection effects), objects with enriched He are located at the upper limit of this distribution and above, and particularly those with the highest He enrichment lie well above this limit.

Owing to the low initial (baseline) nitrogen abundance, the detection of strong nitrogen enrichment in the bulk of O-stars might indicate that efficient mixing takes place already during the very early phases of stellar evolution of LMC O-stars. Nevertheless, it would be premature to draw firm conclusions from our results, because the sample size is still small. Upcoming results from the VLT-FLAMES Tarantula survey (which will be derived in a similar way as presented here, drawing from our experience) will enable a more complete view. In particular, the determination of O-star nitrogen abundances in the LMC will place very tight constraints on the early evolutionary phases of O-stars and thus on the theory of massive star evolution.

Chapter 6

The earliest O-stars

This chapter is a copy of Rivero Gonzalez, Puls, Massey, & Najarro (2012), accepted for publication in *Astronomy & Astrophysics*. The original Appendix A corresponds to Appendix B.2 of this thesis, whilst the content of the original Appendix B is covered by Sect. 6.6.4 and Appendix C.2.

Abstract. The classification scheme proposed by Walborn et al. (2002, *AJ*, 123, 2754), based primarily on the relative strengths of the N IV λ 4058 and N III λ 4640 emission lines, has been used in a variety of studies to spectroscopically classify early O-type stars. Owing to the lack of a solid theoretical basis, this scheme has not yet been universally accepted though.

We provide first theoretical predictions for the N IV λ 4058/N III λ 4640 emission line ratio in dependence of various parameters, and confront these predictions with results from the analysis of a sample of early-type LMC/SMC O-stars.

Stellar and wind parameters of our sample stars are determined by line profile fitting of hydrogen, helium and nitrogen lines, exploiting the helium and nitrogen ionization balance. Corresponding synthetic spectra are calculated by means of the NLTE atmosphere/spectrum synthesis code FASTWIND.

Though there is a monotonic relationship between the N IV/N III emission line ratio and the effective temperature, all other parameters being equal, theoretical predictions indicate additional dependencies on surface gravity, mass-loss, metallicity, and, particularly, *nitrogen abundance*. For a given line ratio (i.e., spectral type), more enriched objects should be typically hotter. These basic predictions are confirmed by results from the alternative model atmosphere code CMFGEN.

The effective temperatures for the earliest O-stars, inferred mostly from the nitrogen ionization balance, are partly considerably hotter than indicated by previous studies. Consistent with earlier results, effective temperatures increase with luminosity class for all spectral types. The relation between *observed* N IV λ 4058/N III λ 4640 emission line ratio and effective temperature, for a given luminosity class, turned out to be quite monotonic for our sample stars, and to be fairly consistent with our model predictions. The scatter within a spectral sub-type is mainly produced by abundance effects.

Our findings suggest that the Walborn et al. (2002) classification scheme is able to provide a meaningful relation between spectral type and effective temperature, as long as it is possible to discriminate for the luminosity class. In terms of spectral morphology, this might be difficult to achieve in low-*Z* environments such as the SMC, owing to rather low wind-strengths. According to our predictions, the major bias of the classification scheme is due to nitrogen content, and the *overall* spectral type- T_{eff} relation for low-metallicity (e.g., SMC) O-stars might be non-monotonic around O3.5/O4.

6.1 Introduction

Though important for the evolution of the early Universe and the present cosmos, massive stars are not as thoroughly understood as desirable to safely infer or predict their interaction with their surroundings, e.g., their input of (ionizing) radiation, wind-energy and momentum, and nuclear processed material.

Particularly uncertain is the situation for the earliest O-stars (earlier than O4, see below), both with respect to their physical parameters, and the relation between their spectroscopic definition and these parameters. Since the earliest O-type stars include the most massive stars in the Universe, i.e., the top end of the stellar initial mass function, such a lack of knowledge is intolerable. As pointed out by Massey et al. (2005), already a 10% uncertainty in the effective temperature, T_{eff} (which is still possible for the hottest stars to present date), results in a factor of two or more uncertainty in the Lyman flux, affecting our understanding of the ionization balance of H II regions and, e.g., the porosity of the interstellar medium (e.g., Oey & Kennicutt 1997; Oey 2006).

This large uncertainty is produced because the standard approach to derive T_{eff} , exploiting the He I/He II ionization equilibrium, fails in the earliest O-star regime. This is the result of rather insensitive He II lines to changes in T_{eff} , and quite weak strategic He I lines, with their equivalent widths falling below 200 mÅ, about the limit achievable with normal photographic emulsions in the 1970s. The apparent absence of He I was used by Walborn (1971a) to extend the criteria defined by Conti & Alschuler (1971) for discriminating O-stars to the O3 spectral type, which then displayed a degeneracy with respect to effective temperature. This degeneracy was partially broken by Kudritzki (1980) and Simon et al. (1983) who used better photographic data to detect He I in the spectra of some O3 stars, but even today with modern CCDs and high S/N the detection of He I is not always achievable. To circumvent this problem Walborn et al. (2002) suggested to use the N IV λ 4058/N III λ 4640¹ (hereafter N IV/N III) emission line ratio as the primary classification criterion for the earliest spectral types, instead of the He I/He II absorption line ratio. By means of this criterion, the former O3 class was split into three different types O2, O3, and O3.5, being O2 the degenerate one instead.

This scheme has been used in a variety of studies during the past years to classify spectra of early O-stars in the Large and Small Magellanic Clouds (LMC and SMC) (e.g., Walborn et al. 2004, Massey et al. 2004, 2005, 2009, Evans et al. 2006) and in the Milky-Way, e.g., Sota et al. (2011). However, these additional sub-types are not (yet) universally accepted. In particular Massey et al. (2004, 2005) criticized that relying on the relative strengths of the optical nitrogen emission lines lacks a solid theoretical basis, since the (photospheric) line emission is the result of complex NLTE processes.

To provide more insight into this and related matter, we started a series of publications dealing with nitrogen spectroscopy in O-type stars. In the first paper of this series (Rivero González et al. 2011, hereafter Chapter 4), we concentrated on the formation of the emission at N III λ 4634-4640-4642. In the follow-up paper (Rivero González et al. 2012, hereafter Chapter 5), we investigated the N IV λ 4058 emission line formation, and applied our accumulated knowledge to derive nitrogen abundances for an LMC O-star sample.

The primary goal of the present Chapter is a quantitative study of the atmospheric parameters of the earliest O-stars, by means of nitrogen line spectroscopy and building on the results from our previous work within this series. Particularly, we concentrate on testing the Walborn et al. (2002) classification scheme on its capability of providing a reasonable relation between spectral types and

¹ The individual components N III λ 4640.64-4641.85 become blended for a projected rotational velocity $v \sin i \geq 40 \text{ km s}^{-1}$.

effective temperatures. To this end, we investigate the theoretical N IV/N III emission line ratio, and the impact of different parameters on this ratio. Subsequently, our predictions are confronted with corresponding observational results, derived from an analysis of an early O-type sample of LMC/SMC stars.

This Chapter is organized as follows. In Sect. 6.2, we describe the tools used within this work, the atmospheric code FASTWIND and a suitable model grid. Open questions from our previous studies regarding the formation of the N III and N IV emission lines are addressed in Sect. 6.3. Section 6.4 presents first theoretical predictions on the N IV/N III emission line ratio. In Sect. 6.5, we compare our results and predictions with corresponding ones from the alternative atmospheric code CMFGEN (Hillier & Miller 1998). The stellar sample and the observations used within this study as well as the procedure to determine stellar/wind parameters together with nitrogen abundances are presented in Sect. 6.6. Finally, we provide a discussion of our results in Sect. 6.7, and summarize our findings and conclusions in Sect. 6.8.

6.2 Code and model grid

All calculations within this work were performed by means of the NLTE atmosphere/spectrum synthesis code FASTWIND (Santolaya-Rey et al. 1997; Puls et al. 2005), using the recently updated version v10.1 (see Sect. 2.3.1). Most results presented here (except for the fine-tuned fits in Sect. 6.6) are based on a model-grid, with H, He, and N as ‘explicit’ elements. Corresponding model atoms have been described in Puls et al. (2005) (H/He) and Chapter 3 (N), and Table 6.1 provides the coverage of important grid parameters. Details of the basic grid were already provided in Chapter 5, and only its ‘hot’ range ($T_{\text{eff}} \geq 35\text{kK}$) was used for our current analysis. This subgrid has been extended to cover a broader range in background metallicity, $Z = 1, 0.5, 0.2 Z_{\odot}$, associated with the Milky Way (MW), Large Magellanic Cloud (LMC), and Small Magellanic Cloud (SMC), respectively. Moreover, we increased the sampling with respect to $\log g$, and also the coverage of the wind-strength parameter (or optical depth invariant), $Q = \dot{M}/(v_{\infty}R_*)^{1.5}$, towards larger values, resulting in 6 model series of different wind-strength (from series A with $\log Q = -14.00$ to series F with $\log Q = -12.10$, for details see Table 6.1). Finally, the sampling in helium content, $Y_{\text{He}} = N_{\text{He}}/N_{\text{H}}$, and nitrogen abundance, $[\text{N}] = \log_{10}(N_{\text{N}}/N_{\text{H}}) + 12$, has been improved, for studying the reaction of important nitrogen lines on extreme changes in $[\text{N}]$ (Sects. 6.3.3 and 6.4.2), and for better constraining abundances in our analysis of LMC/SMC stars (Sect. 6.6). The current grid accounts for a total of 104,000 models.

The major potential of such a model-grid (besides theoretical investigations) is the possibility of obtaining rather precise estimates of stellar parameters within a reasonable amount of time (few minutes). With the advent of large stellar surveys, such as the VLT-FLAMES Tarantula survey (VTFS, Evans et al. 2011) or the IACOB project (Simón-Díaz et al. 2011), this will turn out to become a very useful tool. As an example for the present quality of our models, we show in Fig. 6.1 the comparison of a high resolution (resolving power $R = 48,000$), high S/N (≥ 150) spectrum of the Galactic O3 V((f*)) star HD 64568 (for details, see Markova et al. 2011) with the best fitting synthetic spectrum from our grid models. Obviously, the grid resolution is sufficient to achieve quite a fair representation of the observed spectrum, both with respect to H/He and N (note that lines from N III, N IV, and N V are present in parallel). Further analyzes of Galactic objects will be performed in a forthcoming paper.

Table 6.1: Model-grid used within this work: coverage of fundamental parameters. For T_{eff} and $\log g$ coverage, see also asterisks in Fig. 6.6. Other model parameters adopted as follows: wind terminal velocity, v_{∞} , as a function of the photospheric escape velocity, v_{esc} (see Kudritzki & Puls 2000); stellar radius, R_* , as a function of spectral type and luminosity class, corresponding to prototypical values; velocity field exponent, $\beta = 0.8$; and micro-turbulence, $v_{\text{mic}} = 10 \text{ km s}^{-1}$. Nitrogen baselines abundances (first entry in [N] range) have been drawn from Hunter et al. (2007).

Parameter	Range	Typical step size
T_{eff} (kK)	35.0 - 55.0	1.0
$\log g$ (cgs)	3.2, 3.5 - 4.2, 4.5	0.1
$\log Q^{\text{a}}/\text{series}$	-14.00/A, -13.50/B, -13.15/C -12.80/D, -12.45/E, -12.10/F	0.35
Y_{He}	0.08, 0.10 - 0.20	0.05
Galactic		
Z	Z_{\odot}	-
[N]	7.64, 7.78 - 8.98	0.2
LMC		
Z	$0.5Z_{\odot}$	-
[N]	6.90, 6.98 - 8.58	0.2
SMC		
Z	$0.2Z_{\odot}$	-
[N]	6.50, 6.78 - 8.38	0.2

^ain units of $M_{\odot}\text{yr}^{-1}/(\text{km s}^{-1}R_{\odot})^{1.5}$.

6.3 N III/N IV emission lines – parameter-dependence

Our previous studies on the formation of N III $\lambda\lambda 4634\text{-}4640\text{-}4642$ and N IV $\lambda 4058$ prompted a number of questions, which are investigated in the following. First we concentrate on the N III triplet emission in low- Z environments, to discriminate the counteracting effects of line blocking (less blocking – more emission) and mass-loss (less mass-loss – less emission) under these conditions. Subsequently, we study the impact of Z and [N] on N IV $\lambda 4058$.²

6.3.1 N III emission line formation: EUV line-blocking vs. wind-strength

In Chapter 4 we argued that, for Galactic conditions, the canonical explanation for the presence of emission at N III $\lambda\lambda 4634\text{-}4640\text{-}4642$ (related to dielectronic recombination, Mihalas & Hummer 1973) no longer or only partly applies if one accounts for the presence of line-blocking/blanketing and winds. The key role is now played by the stellar wind, as long as the wind-strength is large enough to enable a significantly accelerating velocity field already in the photospheric formation region of the resonance line(s) connected to the upper level of the involved transition. Furthermore, our study implied that particularly the efficiency of the ‘two electron’ drain (depopulating the lower

² For a detailed description of the formation process of N III and N IV emission lines, we refer to Chapter 4 and Chapter 5, respectively.

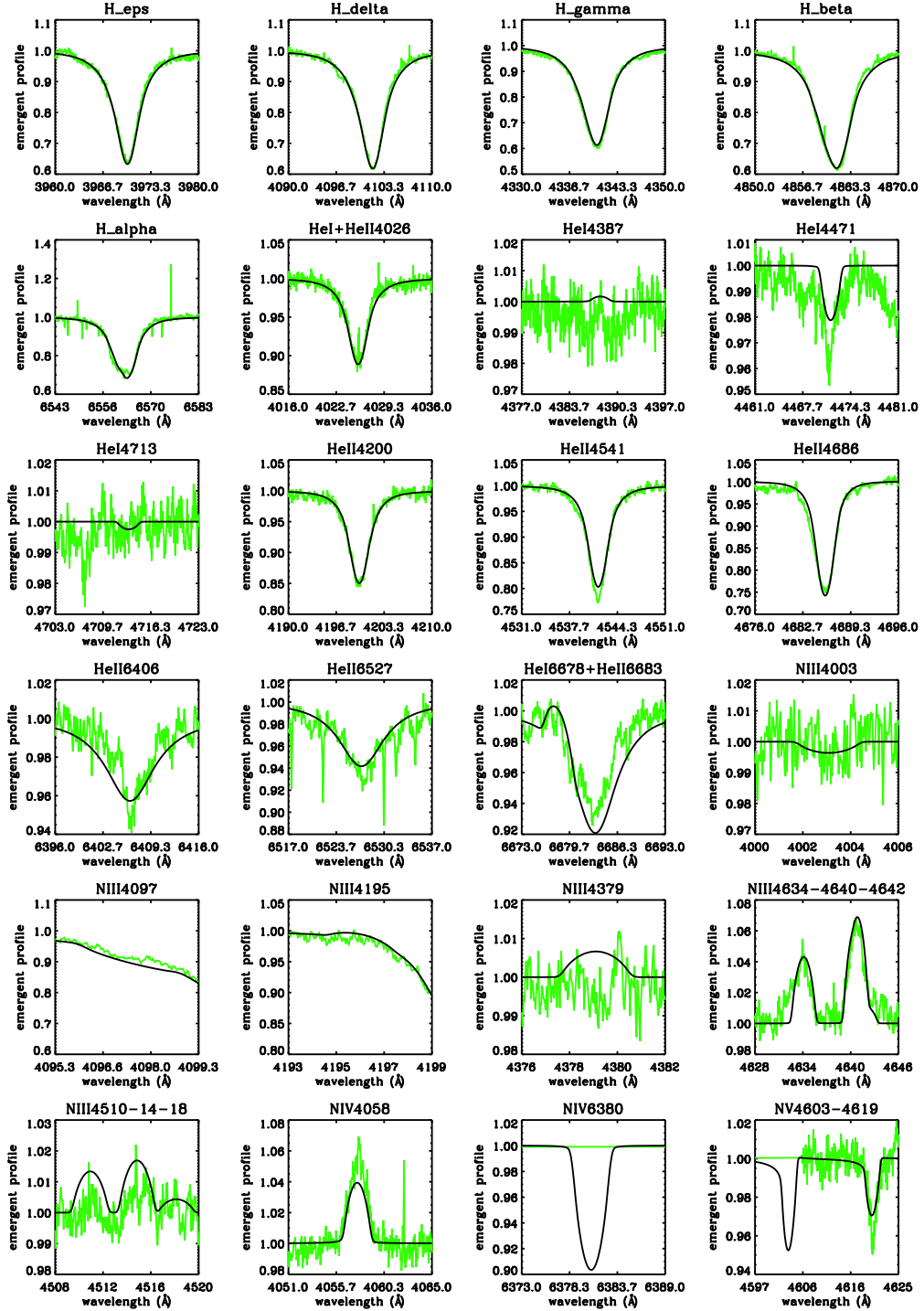


Figure 6.1: High resolution optical spectrum of the Galactic O3 V((f*)) star HD 64568 (green), compared with the best-fitting synthetic H/He/N spectrum from our grid (black, convolved with $v \sin i = 100 \text{ km s}^{-1}$, see Markova et al. 2011). N IV $\lambda 6380$ and N V $\lambda 4603$ not observed. Grid parameters: $T_{\text{eff}} = 48 \text{ kK}$, $\log g = 4.0$, $\log Q = -12.8$ (series D), $Y_{\text{He}}=0.1$, $[\text{N}] = 8.38$. Fine tuning of the parameters can improve the fit.

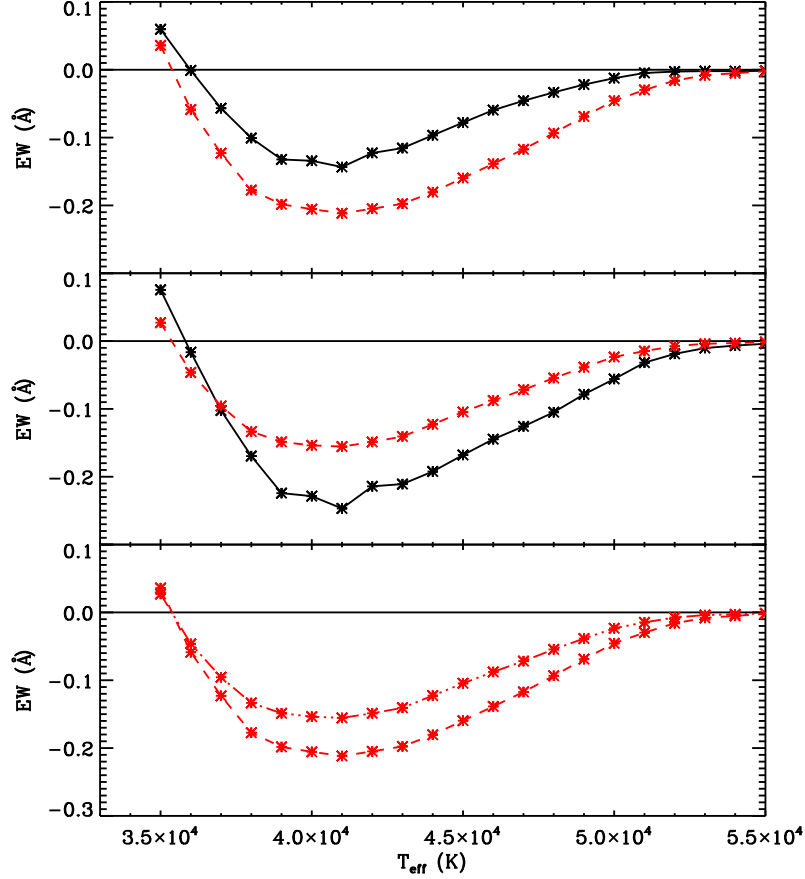


Figure 6.2: Equivalent width of N III λ 4640 as a function of T_{eff} , for MW and SMC models at $\log g = 4.0$ and mass-loss rates scaled according to Z (see text). Solid/black and dashed(-dotted)/red curves refer to MW series ‘E’ and SMC series ‘D’ models, respectively ($\Delta \log Q = -0.35$ dex). Upper panel: $[N] = 7.78$ for both Galactic and SMC models. Middle panel: comparison accounting for the theoretically expected maximum $[N]$ enrichment, drawn from tailored evolutionary calculations by Brott et al. (2011a): MW models with $[N] = 8.18$ and SMC models with $[N] = 7.58$. Lower panel: SMC series ‘D’ models, with $[N] = 7.58$ (dashed-dotted) and $[N] = 7.78$ (dashed). The line emission increases with increasing $[N]$.

level, see Chapter 4) is strongly dependent on the degree of EUV line-blocking, i.e., on Z . For a given wind-strength and nitrogen abundance, the emission should become stronger in low- Z environments, because of less blocking (see Fig 4.16). Nevertheless, this comparison might be unrealistic, since less blocking goes hand in hand with a lower wind-strength, which might (over-) compensate the discussed effect. Moreover, one might need to consider a lower nitrogen content, owing to a lower baseline abundance.

Here we investigate the combined effect. At first, we compare the behavior of the N III emission lines for two different Z environments (MW and SMC), applying a consistent scaling of $\log Q$, via

$\dot{M} \propto (Z/Z_{\odot})^{0.72}$ (clumping corrected, Mokiem et al. 2007b) and $v_{\infty} \propto (Z/Z_{\odot})^{0.13}$ (Leitherer et al., 1992). For the SMC with $Z/Z_{\odot} = 0.2$, this yields a reduction of $\log Q$ by -0.37 dex compared to the Galactic case, and corresponds well to the step size of $\Delta \log Q = 0.35$ used within our model grid. Thus, Galactic models from, e.g., series E need to be compared with SMC models from series D.

In Fig. 6.2 (upper panel), we compare the equivalent widths of N III $\lambda\lambda 4640.64, 4641.85^3$, in the following abbreviated by N III $\lambda 4640$, as a function of T_{eff} , for MW series E (black/solid) and SMC series D models (red/dashed). All models have the same gravity, $\log g = 4.0$, and the same nitrogen content, $[\text{N}] = 7.78$ dex (almost solar, Asplund et al. 2005, 2009). As usual, we define equivalent widths (hereafter EWs) to be positive for absorption and to be negative for emission lines. The result of this comparison is similar to our findings from Chapter 4. Even when we account for consistently scaled mass-loss rates, the low- Z models result in more emission. Thus, lower mass-loss rates associated with low- Z environments do not compensate the increase in emission strength due to a lower degree of line-blocking.

So far, we neglected the fact that a lower Z also implies a difference in the $[\text{N}]$ baseline abundance, which needs to be considered in a final comparison. In the middle panel of Fig. 6.2, we compare the same series of models as in the upper one, accounting now for more consistent abundances (MW: black/solid, SMC: red/dashed). Here we used $[\text{N}]$ values in agreement with the theoretically expected maximum enrichment as provided by Brott et al. (2011a), for MW and SMC models of $40 M_{\odot}$ and initial rotation velocities of 270 km s^{-1} . This roughly corresponds to models with $[\text{N}] = 8.2$ and 7.6 for the MW and SMC, respectively.⁴

It turns out that with the inclusion of more realistic abundance conditions, the increase of emission strength due to less blocking becomes strongly suppressed, and now the MW models display stronger emission than the SMC ones. This might explain the relatively low number of "f" objects among the SMC O-stars (see Sect. 6.7.6).

For convenience, the lower panel of Fig. 6.2 displays a direct comparison of SMC models with expected maximum enrichment ($[\text{N}] = 7.58$, dashed-dotted) and a solar nitrogen content ($[\text{N}] = 7.78$, dashed). Obviously, the emission strength of N III $\lambda 4640$ increases with increasing nitrogen content (see also Fig. 4.15).

6.3.2 N IV $\lambda 4058$ – dependence on background abundance

Though we studied the response of the N III triplet on different background abundances already in Chapter 4, a similar analysis for N IV $\lambda 4058$ is still missing. This is now done in Fig. 6.3, by means of our model-grid. We display models with thin winds (series A; solid) and with wind-strengths typical for Galactic supergiants (series E; dashed), and compare the impact of MW (black) and SMC (red) background abundances. All models have the same gravity, $\log g = 4.0$, and the same $[\text{N}] = 7.78$. To enable a better comparison, we show the effects for both N III $\lambda 4640$ (upper panel) and N IV $\lambda 4058$ (lower panel). We clearly see that N III $\lambda 4640$ is much more influenced by Z than N IV $\lambda 4058$, irrespective of wind-strength and T_{eff} . For LMC background abundances, $Z = 0.5$ (not displayed), the

³ The blue component of the triplet shows a similar behavior.

⁴ Unfortunately, there are only few abundances studies in the O-star regime to confirm these assumptions, and most of them are biased towards late O-types (reviewed by, e.g. Herrero 2003; Herrero & Lennon 2004; Morel 2009). Heap et al. (2006), following previous work by Bouret et al. (2003), found most of their 18 SMC sample stars to be enriched, and more than half of the sample displayed $[\text{N}] > 7.5$. Regarding Galactic objects, Martins et al. (2011b) (see also Martins et al. 2011a) recently found a typical enrichment by 0.4-0.6 dex above the Galactic baseline abundance, corresponding to $[\text{N}] \approx 8.0-8.2$.

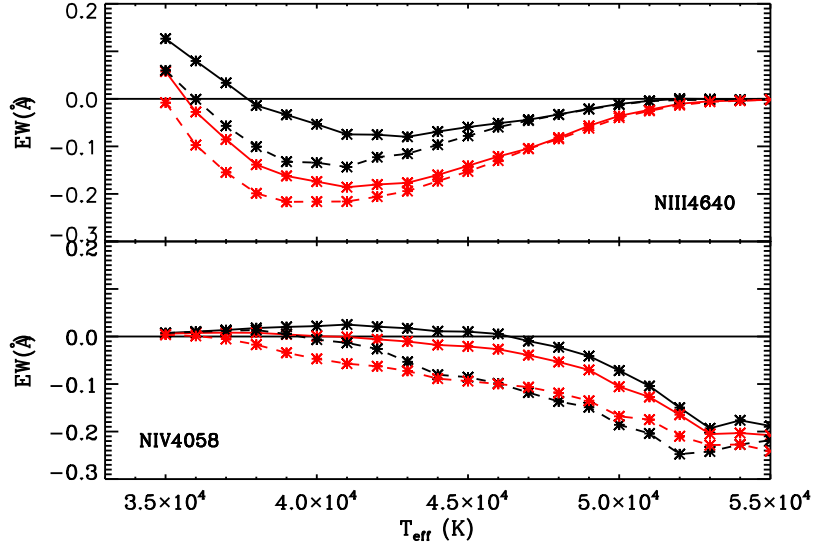


Figure 6.3: Equivalent width of N III λ 4640 (upper panel) and N IV λ 4058 (lower panel) as a function of T_{eff} , for MW (black) and SMC (red) models, at $\log g=4.0$ and $[N]=7.78$ dex. Solid lines: series A (thin winds), dashed lines: series E (prototypical for Galactic supergiants).

effect on N IV λ 4058 becomes almost negligible.

With respect to the formation of this line, all ‘A’ and also the ‘cooler’ ‘E’ models (with $T_{\text{eff}} \leq 45$ kK) behave as discussed in Chapter 5. A lower background Z induces a more depopulated ground state, owing to somewhat higher ionizing fluxes around the N IV edge at $\lambda = 160$ Å. Consequently, the drain of the lower level of the λ 4058 transition, $3p$, via the ‘two electron’ transitions becomes enhanced, and more emission is produced at lower Z . For ‘E’ models with $T_{\text{eff}} \geq 45$ kK the situation changes, and now the higher Z (MW) models produce slightly more emission: At higher T_{eff} and \dot{M} , the resonance line towards $3p$ (at $\lambda = 247$ Å) leaves detailed balance and $3p$ becomes pumped, stronger at low Z because of higher EUV fluxes. Thus, less emission at N IV λ 4058 is produced, compared to a Galactic environment.

Overall, however, background abundances have a weak effect on N IV λ 4058, much weaker than wind-strength effects (e.g., red solid vs. red dashed). This is related to the much higher sensitivity of the N IV continuum on mass-loss rate. Accordingly, also the helium content has a certain impact on the N IV emission strength, since this parameter controls the overall flux level of the He II continuum including the N IV edge. In particular, an increase of Y_{He} decreases the N IV emission strength.⁵

As already discussed above and in Chapter 4, N III λ 4640 reacts much stronger on different background abundances (e.g., upper panel of Fig. 6.3, black vs. red), and in a similar way for all mass-loss rates. Because of this different behavior, the (theoretical) N IV λ 4058/N III λ 4640 emission line ratio, studied in Sect. 6.4, is affected by metallicity.

Interestingly, the reaction of N III λ 4640 on \dot{M} becomes negligible for models with $T_{\text{eff}} \geq 46$ kK. At these temperatures, N III has become a real trace ion, and the (weak) line emission is formed in

⁵ A similar behavior is found for the N III triplet emission, for $T_{\text{eff}} \leq 40$ kK.

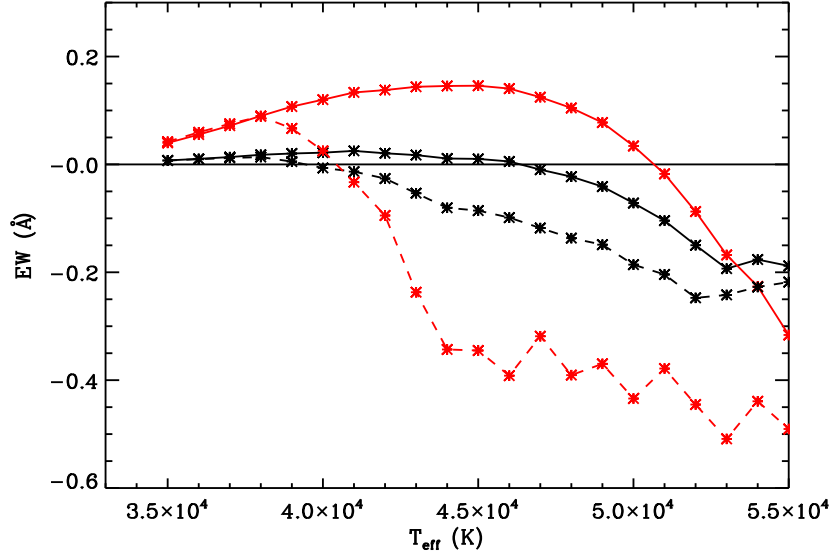


Figure 6.4: Equivalent width of N IV λ 4058 as a function of T_{eff} for models with $[\text{N}] = 7.78$ (black) and $[\text{N}] = 9.0$ (red). All models correspond to $\log g = 4.0$ and $Z = Z_{\odot}$, with mass-loss rates according to series ‘A’ (solid) and ‘E’ (dashed). See text.

quite deep layers, hardly affected by mass loss and velocity field (see also Fig. 4.10). In this case, the relative overpopulation is caused by recombination cascades and depopulation of the lower level by ‘two electron’ drain (particularly for low Z conditions), whilst dielectronic recombination remains unimportant.

6.3.3 N IV λ 4058 – dependence on nitrogen abundance

Figure 6.4 displays the reaction of N IV λ 4058 on variations of $[\text{N}]$ and $\log Q$ for MW models. As in Fig. 6.3, solid and dashed lines correspond to model series ‘A’ and ‘E’, respectively. We compare models with $[\text{N}] = 7.78$ (black) and highly enhanced nitrogen, $[\text{N}] = 9.0$ (red), selected to demonstrate extreme effects.

At first, we concentrate on the influence of $[\text{N}]$ for model series ‘E’ (supergiant mass-loss rates, dashed). These models behave as expected. As for the N III triplet (e.g., Fig. 6.2, lower panel), we obtain more emission when we increase the nitrogen content. This is mostly because the formation zone, due to the increased number of absorbers/emitters, is shifted outwards into the transition region photosphere/wind where the relative overpopulation becomes very large or even inverted (cf. Fig. 5.4). Small inaccuracies in the population ratio (e.g., due to inappropriate gridding) can lead to sizeable effects in line-strength when close to inversion, and this is the reason for the non-monotonicity in EW encountered for the high $[\text{N}]$ ‘E’-models.

Somewhat unexpectedly, however, we found the opposite reaction for low- \dot{M} models (solid). For large nitrogen content (red), we either obtain more absorption or less emission than solar- $[\text{N}]$ models (black), for almost the whole temperature range. Furthermore, the turning point from absorption to emission occurs at hotter T_{eff} (by 5 kK) than for the solar- $[\text{N}]$ models, whilst for the ‘E’ series this

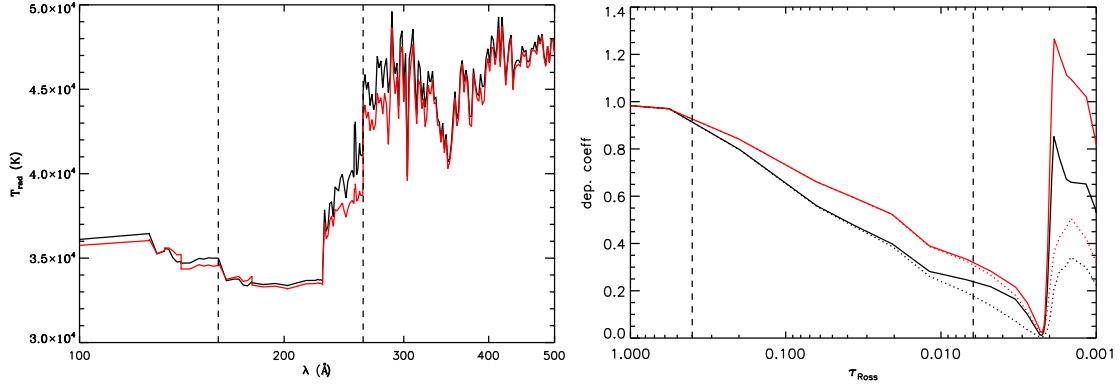


Figure 6.5: Radiation temperatures and NLTE departure coefficients for two MW-models at $T_{\text{eff}}=45$ kK, $\log g=4.0$, and a low density wind (series ‘A’), with solar (black) and strongly enhanced nitrogen ($[N]=9.0$, red). Left panel: Enhanced nitrogen leads to lower N IV (and N III) continuum-fluxes, here expressed as radiation temperatures. Corresponding edges at 160 \AA and 261 \AA indicated by vertical lines. Right panel: The lower fluxes give rise to less depopulated N IV ground- (solid) and $2p^2$ (dotted) states, where the latter are the lower levels of the important two-electron transitions draining N IV $3p$. Consequently, there is more absorption/less emission at N IV $\lambda 4058$ when $[N]$ becomes increased. Formation region of N IV $\lambda 4058$ indicated by dashed lines.

turning point remains rather unaffected by nitrogen content. The underlying mechanism is again related to a diminished drain of the lower level when $[N]$ becomes increased. Here, a higher $[N]$ is responsible for a lower N IV continuum-flux (Fig. 6.5, left), leading to less depopulated ground- and $2p^2$ states (Fig. 6.5, right), and thus to a higher population of $3p$, i.e., to more absorption/less emission at N IV $\lambda 4058$. Note that this process is similar to the effect produced by a higher Z (Sect. 6.3.2).

These findings imply an important consequence. According to our predictions, in a certain T_{eff} range N IV $\lambda 4058$ might switch, for growing $[N]$, from emission to absorption, provided the wind-strength is not too high! The other way round (and exploiting the results from the complete grid): If N IV $\lambda 4058$ is observed in absorption at $44 \text{ kK} \leq T_{\text{eff}} \leq 50 \text{ kK}$ (for Galactic stars), this would be an indication of strong nitrogen enrichment (and mass-loss rates below ‘D’ corresponding to $\log Q < -12.8$). The lower limit in T_{eff} corresponds to the absorption/emission turning point for ‘D’ models (at higher T_{eff} and similar or higher \dot{M} , only emission lines are predicted, independent of $[N]$), whilst the upper one refers to the same point for model series ‘A’.

6.4 Predictions on the N IV/N III emission line ratio

6.4.1 Overview

The complete Walborn et al. (2002) classification scheme proposed for ‘normal’ O-stars,⁶ which also covers the O4 type, is summarized in Table 6.2. Walborn et al. suggested to use the N IV/N III

⁶ Crowther & Walborn (2011) have updated the classification scheme for O2-3.5 If*/WN5-7 stars using the morphology of H_{β} .

Table 6.2: Classification scheme for spectral types O2-O4 using the emission line ratio $N\text{ IV}\lambda 4058/N\text{ III}\lambda 4640$ and the strength of $\text{He I}\lambda 4471$, as defined by Walborn et al. (2002). Luminosity classes defined as follows. Supergiants (I): $\text{He II}\lambda 4686$ in emission; giants (III): $\text{He II}\lambda 4686$ in weak absorption/P-Cygni profile; dwarfs (V): $\text{He II}\lambda 4686$ in strong absorption. Note that the f+ designation recently became obsolete since the Si IV emission at $\lambda\lambda 4089 - 4116$ has been established as a common feature in normal O-type spectra (Sota et al., 2011).

Spectral type	Criteria
Supergiants	
O2 If*	$N\text{ IV} \gg N\text{ III}$, no or very weak $\text{He I}\lambda 4471$
O3 If*	$N\text{ IV} > N\text{ III}$, very weak or no He I
O3.5 If*	$N\text{ IV} \sim N\text{ III}$, very weak He I
O4 If+	$N\text{ IV} < N\text{ III}$, weak He I
Giants	
O2 III(f*)	$N\text{ IV} \gg N\text{ III}$, no or very weak He I
O3 III(f*)	$N\text{ IV} > N\text{ III}$, very weak or no He I
O3.5 III(f*)	$N\text{ IV} \sim N\text{ III}$, very weak He I
O4 III(f+)	$N\text{ IV} < N\text{ III}$, weak He I
Dwarfs	
O2 V((f*))	$N\text{ IV} \gg N\text{ III}$, no He I
O3 V((f*))	$N\text{ IV} >$ or $\sim N\text{ III}$, very weak He I
O3.5 V((f+))	$N\text{ IV} < N\text{ III}$, very weak He I
O4 V((f+))	no $N\text{ IV}$, weak He I

emission line ratio as the primary classification criterion for the earliest spectral types, instead of the $\text{He I}/\text{He II}$ absorption line ratio. This scheme has been used in a variety of studies during the past years to classify spectra of early O-stars (e.g., Walborn et al. 2004, Massey et al. 2004, 2005, 2009, Evans et al. 2006, Sota et al. 2011), though there are still some controversial issues. (i) The classification criteria are not quantitative and involve secondary statements regarding the strength of $\text{He I}\lambda 4471$, see Table 6.2. (ii) Massey et al. (2005, hereafter Mas05) have criticized that relying on the strength of the nitrogen emission lines lacks a theoretical basis, i.e., it is not clear whether T_{eff} is the only parameter that differentiates the newly defined spectral types. Indeed, our previous and present work implies that the emission strength of $N\text{ IV}\lambda 4058$ (and also that of $N\text{ III}\lambda 4640$, at least until $T_{\text{eff}} \approx 46$ kK) crucially depends on \dot{M} . Based on their analysis of early LMC and SMC stars, Mas05 pointed out that for stars with similar T_{eff} and $\log g$ the $N\text{ IV}/N\text{ III}$ ratio could vary by the full range defined for the scheme (but see Sect. 6.6.5). Furthermore, they suggested that any spectroscopic classification should be able to constrain T_{eff} without knowledge of other important parameters such as $\log g$ or \dot{M} . (iii) Already Walborn et al. (2002) pointed out that even though there were no indications of any correlation between the newly defined spectral types and the corresponding host galaxy, effects of Z on the emission line ratio might need to be considered, accounting for the results from Crowther (2000) for WR-stars. Using synthetic WN models, Crowther had found that earlier spectral types are predicted at lower metallicity, following the Smith et al. (1996) classification scheme for WN stars. Since both nitrogen emission lines seem to react differently on variations of Z (Sect. 6.3.2), it is clear

that such a dependence cannot be ruled out.

In the following, we will address these and other problems, at first by means of theoretical predictions for the N IV/N III emission line ratio, and later on by a comparison with observed spectra.

6.4.2 Basic considerations

We took advantage of the large model-grid described in Sect. 6.2, and analyzed the influence of various parameters (Z , $\log Q$, $[N]$) by studying the iso-contours of specific emission line ratios in the $T_{\text{eff}}\text{-}\log g$ plane (Figs. 6.6 to 6.8). Here and in the following, we always used models with $Y_{\text{He}} = 0.1$.

To discriminate the specific spectral types by nitrogen lines alone, one has basically to account for five different, qualitatively defined ranges with respect to the line strengths of N IV $\lambda 4058$ vs. N III $\lambda 4640$ (see Table 6.2). Note that the ranges for luminosity classes I/III are somewhat shifted relative to class V. To allow for a quantitative description, we investigated the behavior of three extreme values, namely N IV/N III = 0.1 (lower limit for O4 I/III and O3.5 V), N IV/N III = 1 (O3.5 I/III and O3 V) and N IV/N III = 10 (representative for O2 I/III/V).

Before going into the details of our analysis, we compare in Fig. 6.6 the N IV/N III emission line ratios expressed in terms of EW (left) and line-strength (right, quantified in terms of emission peak height), to ensure that different definitions⁷ would not lead to different conclusions. Except for small subtleties, there is no significant change in the run of the iso-contours, regardless whether EWs or line-strengths are used to derive the line ratio. The encountered subtle differences are mostly caused by the considerable wind-strength (model series ‘E’) used in Fig. 6.6: Particularly for N IV $\lambda 4058$, enhanced EWs owing to extended wings are produced, whilst the peak heights remain unaffected. We have also convinced ourselves that a convolution of the theoretical spectra with typical rotational speeds, $v \sin i = 100 \text{ km s}^{-1}$, and/or a degrading to a resolving power of 6000 have a rather low impact (but see Markova et al. 2011): Generally, the iso-contours are shifted to somewhat lower T_{eff} , by roughly 500 to 1000 K in extreme cases of high wind-strength and high $[N]$. In the following we concentrate on the ratio of line-strengths alone, as originally defined by Walborn et al. (2002).

The inspection of the different iso-contours displayed in the $T_{\text{eff}}\text{-}\log g$ plane, Figs. 6.6 to 6.8, allows us to infer an important characteristics for the emission line ratio. As it is true for the He I/He II line ratio (e.g., Mas05), also the N IV/N III line ratio is a sensitive function of surface gravity. The hotter the temperature, the larger the $\log g$ -value necessary to preserve a specific ratio (ionization vs. recombination). This trend seems to have vanished for the cooler models ($T_{\text{eff}} \leq 40 \text{ kK}$) at high $\log g$ in Fig. 6.6, but here the influence of gravity is counteracted by the rather strong wind (see below).

Impact of background metallicity

Figure 6.6 shows the dependence of the line ratio on T_{eff} and $\log g$ for a fixed wind-strength, $\log Q = -12.45$, and $[N] = 7.78$, for iso-contours corresponding to N IV/N III = 0.1, 1 and 10. To study the influence of Z , we display the predicted behavior for MW (red), LMC (green), and SMC (blue) O-stars.

Even a first inspection indicates the potential of this line ratio as a temperature diagnostics. For a fixed surface gravity, e.g., $\log g = 4.0$, we find difference on the order of 3 kK (for MW models) to 8 kK (for SMC models) between iso-contours at N IV/N III = 0.1 and 1, roughly corresponding to O4 (lower limit) vs. O3.5 I/III or O3 V. For low- \dot{M} models this spread becomes somewhat smaller,

⁷ Note that line ratios for He I/He II are partly defined using EWs.

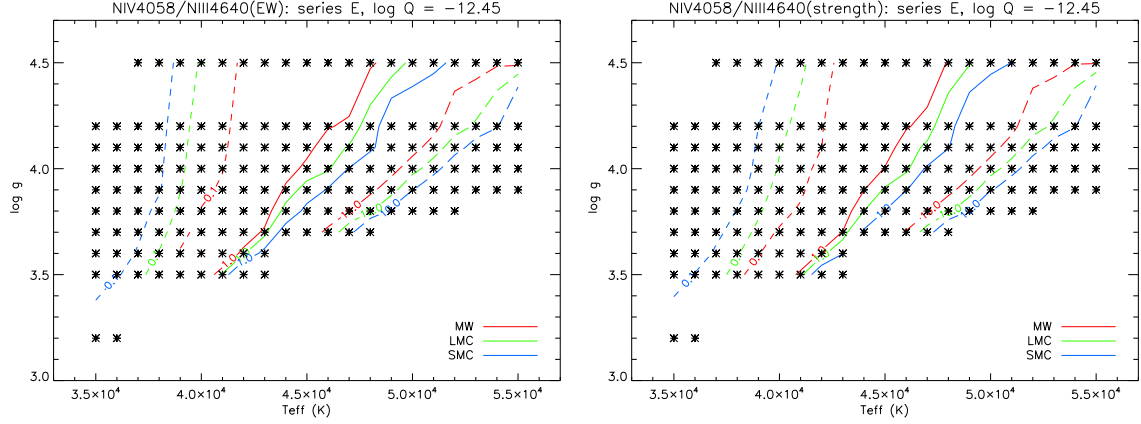


Figure 6.6: $N\text{IV}\lambda 4058/N\text{III}\lambda 4640$ for Galactic (red), LMC (green) and SMC (blue) O-stars. Displayed are iso-contours of the emission line ratio in the $T_{\text{eff}}\text{-log } g$ plane (model series ‘E’, $[N] = 7.78$), for values of $N\text{IV}/N\text{III} = 0.1$ (dashed), 1 (solid) and 10 (long-dashed). The asterisks indicate the position of the grid-models used. Left panel: emission line ratio calculated using EWs; right panel: emission line ratio calculated using line-strengths.

6 kK for SMC stars, whilst for Galactic objects the $N\text{IV}/N\text{III} = 0.1$ iso-contour is no longer present since $N\text{IV}$ turns into weak absorption (Fig. 6.3). The difference between the $N\text{IV}/N\text{III} = 1$ and 10 iso-contours (O3.5 I/III or O3 V vs. O2) is on the order of 4-5 kK for all metallicities, decreasing to 2.5-3 kK for low \dot{M} .

The specific differences of the emission line ratios as a function of Z can be easily explained in terms of our conclusions from Sect. 6.3.2 and by remembering the basic features displayed in Fig. 6.3. First, $N\text{III}\lambda 4640$ is strongly affected by Z (more emission at lower Z , irrespective of temperature), in contrast to $N\text{IV}\lambda 4058$. The latter line is increasing in strength over almost the complete range in T_{eff} , whilst the former is increasing until a certain maximum located at ≈ 40 kK, and decreasing thereafter. Taken together, this implies that *lower* T_{eff} are required to produce similar line ratios for low-metallicity objects at cooler temperatures, compared to Galactic objects (lower T_{eff} means less $N\text{III}$ emission, to compensate for the basically larger emission due to lower Z). Beyond 40 kK, on the other hand, *higher* T_{eff} are required instead to reduce the increased $N\text{III}$ emission. This explains why the SMC/LMC iso-contours at $N\text{IV}/N\text{III} = 0.1$ are located at cooler T_{eff} than their Galactic counterpart, whilst the corresponding $N\text{IV}/N\text{III} = 1$ and 10 iso-contours are on the hotter side. Because the Z effect is largest for SMC objects, also the T_{eff} differences between the $N\text{IV}/N\text{III} = 0.1$ and 1 levels are largest in this situation.

Finally, let us mention that the influence associated with Z (around 2-3 kK for a given line ratio) is comparable with the typical spread present in early spectral types, and thus in agreement with the non-detection of any correlation between the new spectral types and the host galaxy (see above).

Impact of wind-strength

To test the influence of $\log Q$ on the emission line ratio, in Fig. 6.7 we compare the iso-contours corresponding to $N\text{IV}/N\text{III} = 1$ (O3.5 I/III or O3 V) for different wind-strengths, from thin (series ‘A’) to dense winds (series ‘F’). All models have LMC background abundances and $[N] = 7.78$. Since lower

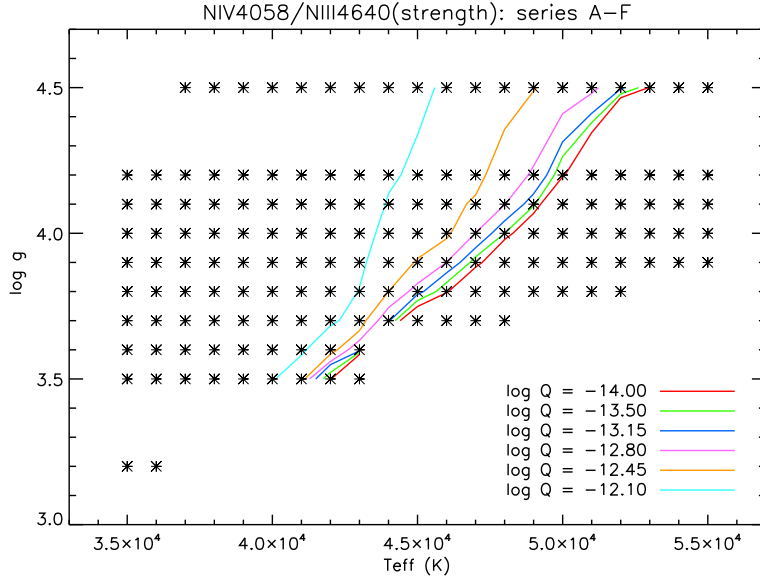


Figure 6.7: Dependence of $N\text{IV}\lambda 4058/N\text{III}\lambda 4640$ on wind-strength (series A-F), for LMC models with $[N] = 7.78$. The iso-contours correspond to a nitrogen emission line ratio of unity.

metallicities counteract the impact of wind-strength, corresponding iso-contours for SMC conditions vary to a lesser degree, whilst the variations are larger for Galactic conditions, in both cases by few hundreds of Kelvin.

Generally, the impact of wind-density on the $N\text{IV}/N\text{III}$ emission line ratio is quite strong, particularly for larger surface gravities. From Fig. 6.7 it is evident that for a fixed $\log g$, cooler T_{eff} are required to produce similar line ratios at higher wind densities. Basically, we can combine the reaction into three groups, namely ‘A’ to ‘C’ models, ‘D’ models, and models with winds stronger than ‘D’. The first group consists of low- \dot{M} models with line ratios which are almost insensitive to wind-strength. Models belonging to the ‘D’ series display a slight reaction, since the wind begins to affect the line emission (either from both lines or, for hotter stars, only from $N\text{IV}\lambda 4058$, see Fig. 6.3), and in a different way, so that the line ratio becomes modified. From the ‘E’ series on, we found larger differences, e.g., at $\log g = 4.0$, of roughly 2 and 4.5 kK for ‘E’ and ‘F’ models compared to low- \dot{M} ones.

In conclusion, objects with the same T_{eff} and $\log g$ but substantially different wind-strengths are predicted to display significantly different line ratios. Consequently, the assigned spectral types would be no longer monotonic in T_{eff} if there would be a large scatter in wind-strength. One has to note, however, that a certain $T_{\text{eff}}\text{-}\log g$ pair also implies a certain luminosity class, and that the wind densities per luminosity class are only mildly varying. Insofar, the monotonicity of a spectral type- T_{eff} relation might still be warranted for a *specified* luminosity class, as long as the corresponding luminosity class indicators (for the earliest O-stars, $\text{He II}\lambda 4686$) allow for a reliable classification (but see Sect. 6.8).

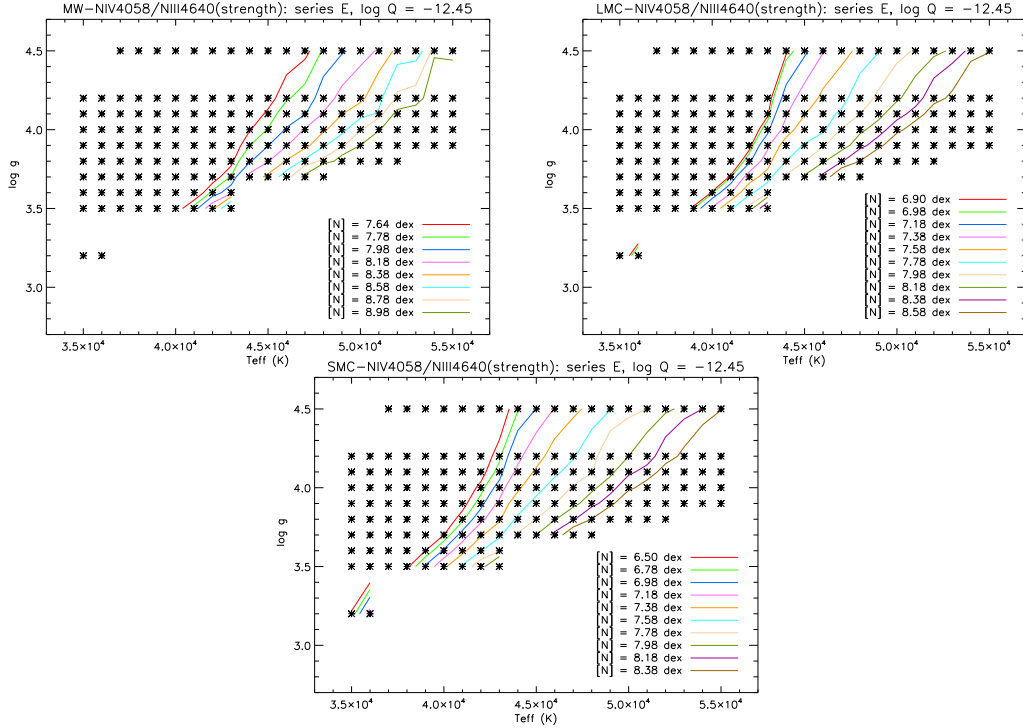


Figure 6.8: Dependence of $N\text{ IV}\lambda 4058/N\text{ III}\lambda 4640$ on nitrogen abundance, for three different background metallicities: Galactic (upper panel, left), LMC (upper panel, right), and SMC (lower panel). All models have $\log Q = -12.45$ (series ‘E’). The iso-contours correspond to a nitrogen emission line ratio of unity.

Impact of nitrogen abundance

After investigating the impact of background metallicity and wind-strength, we now concentrate on the influence of nitrogen content. At first glance, this is somewhat surprising. Abundance should have a marginal or only small effect on line *ratios*, since it should cancel out as long as the lines are not too strong and the ionization equilibrium is not disturbed. This statement, however, is only true if the lines form in a ‘typical’ way, i.e., are simple absorption lines (e.g., $\text{He I}\lambda 4471/\text{He II}\lambda 4541$ used for the classification of not too early O-stars). In the case considered here, however, the lines are formed by complex and *different* NLTE processes, and different abundances might have a different impact on the formation of both lines (see Sect. 6.3.3), so that the ratio might become affected. Moreover, the variation of $[N]$ in early type stars can be much larger than, e.g., the variation of Y_{He} , which amplifies the effect. Thus, it is mandatory to test for the impact of nitrogen content on the $N\text{ IV}/N\text{ III}$ emission line ratio.

For this purpose, we display in Fig. 6.8 the response of the line ratio on different nitrogen abundances as present in our model-grid, for each Z (Galactic, LMC, and SMC background abundances). To allow for a fair comparison, all models belong to series ‘E’. Again, we display only contours with $N\text{ IV}/N\text{ III} = 1$, as a representative value. Note that for each Z , the range of nitrogen content is different, from the corresponding baseline abundance to enrichments of roughly 1.3, 1.6, and 1.9 dex for

MW, LMC, and SMC objects, respectively (see legend and Table 6.1).

Generally, an enhancement of [N] at fixed $\log g$ shifts the iso-contours towards higher temperatures. We checked that this shift indeed is related to the different [N]-dependencies of the specific formation mechanisms of N IV λ 4058 and N III λ 4640 rather than to a modified ionization equilibrium, which remains quite unaffected from variations in [N]. Moreover, the shift is quite similar for all Z, producing an increase of roughly 1 kK for a change of +0.2 dex in nitrogen abundance (at $\log g = 4.0$; lower ΔT_{eff} are found at lower $\log g$). This is an interesting result because objects with considerable differences in [N] would display, for the same line ratio, i.e., spectral type, large differences in T_{eff} . If we, e.g., consider LMC models at $\log g = 4.0$, a line ratio of unity (corresponding to an O3 dwarf) would be obtained at temperatures differing by 6 kK if either [N] is at the baseline abundance (red, $T_{\text{eff}} \approx 42.5$ kK) or if [N] = 8.18 (dark green, $T_{\text{eff}} \approx 48.5$ kK), corresponding to a typical enrichment of LMC stars (Chapter 5)! Such a difference is much larger than the typical spread of temperature per spectral type, and we conclude that the present classification scheme for the earliest O-stars might be strongly biased by nitrogen abundance. Only if the nitrogen content/enrichment would be rather similar for a given position in the $T_{\text{eff}}\text{-}\log g$ plane,⁸ this bias would not contaminate a spectral-type- T_{eff} relation, similar to our argumentation regarding the bias by wind-strength from above.

6.5 Comparison with results from CMFGEN

In Chapter 4 we compared our results for N III lines with those from the alternative code CMFGEN, for a grid of models comprising dwarfs and supergiants in the T_{eff} range between 30 and 45 kK, and with ‘old’ solar abundances according to Grevesse & Sauval (1998). In the following, we check the consistency also with respect to N IV and N V, concentrating on the hotter models (d4v, d2v, s4a, s2a, see Table 6.3), but allowing for different nitrogen abundances to check the predictions from the previous sections.

CMFGEN models were computed with the a modified photospheric structure following the approach from Santolaya-Rey et al. (1997), smoothly connected to a beta velocity law. In our approach, the Rosseland mean from the original formulation was replaced by the more appropriate flux-weighted mean. Several comparisons using ‘exact’ photospheric structures from TLUSTY (Hubeny & Lanz, 1995) showed excellent agreement with our method (see also Najarro et al. 2011). A turbulent velocity of 10 km s^{-1} was assumed when computing both the level populations and line profiles. Our models account for the presence of H, He, C, N, O, Si, P, S, Fe, and Ni, totaling 3965 full levels (1319 super-levels) and $\approx 70,000$ lines.

At first, we examine the potential switch of N IV λ 4058 from emission to absorption when increasing the abundance. From Fig. 6.4, this effect should occur at lower wind-strengths and not too high T_{eff} , i.e., potentially for model d4v. Indeed, the predicted effect is clearly present in the corresponding CMFGEN models, where λ 4058 is in emission for [N] = 7.78 and 7.98, and in absorption for [N] = 8.38 and 8.78 (filled circles in Fig. 6.9). The total variation in equivalent width as a function of [N] compares very well to results from FASTWIND, which appear at somewhat higher $T_{\text{eff}} = 42.5$ kK, as shown by the solid lines (based on our FASTWIND grid for $\log g = 4.0$ and model series ‘D’). Thus we conclude that the predicted effect is more or less code independent.

In Fig. 6.10 we compare the influence of the nitrogen abundance on the emission line ratio N IV/N III (calculated from EWs), by means of model d2v. Again, CMFGEN (filled circles) predicts

⁸ If, e.g., nitrogen would be enriched by rotational mixing alone and the initial rotational speeds were similar.

Table 6.3: Stellar and wind parameters of models used to compare synthetic nitrogen line profiles from FASTWIND and CMFGEN. The grid is a subset of the grid presented by Lenorzer et al. (2004). For details, see Chapter 4. Even entries provide those parameters from our FASTWIND grid models which reproduce best the H/He spectra from CMFGEN. All models were calculated with $v_{\text{mic}} = 10 \text{ km s}^{-1}$, and with four different nitrogen abundances, $[\text{N}] = 7.78, 7.98, 8.38, 8.78$. Wind strength parameter, Q , calculated in units of $M_{\odot} \text{ yr}^{-1}$, R_{\odot} and km s^{-1} .

Model	code	T_{eff} (K)	R_* (R_{\odot})	$\log g$ (cgs)	$\log Q$
d2v	CMFGEN	46100	11.4	4.01	-12.43
E4740	FASTWIND	47000		4.00	-12.45
d4v	CMFGEN	41010	10.0	4.01	-12.75
D4140	FASTWIND	41000		4.00	-12.80
s2a	CMFGEN	44700	19.6	3.79	-11.99
F4540	FASTWIND	45000		3.80	-12.15
s4a	CMFGEN	38700	21.8	3.57	-12.15
F3935	FASTWIND	39000		3.50	-12.15

a similar effect as FASTWIND, i.e., the EW ratio increases with $[\text{N}]$. The actual values of these ratios, however, are quite different from those calculated by FASTWIND. Similar ratios are only reached at higher T_{eff} , because, as discussed below, FASTWIND predicts stronger N III and weaker N IV emission lines for hot objects. Nevertheless, the ‘ $[\text{N}]$ -effect’ is clearly visible in the CMFGEN models, not only for model d2v but also for the others. Thus, the position of a certain emission line ratio in the $T_{\text{eff}}\text{-}\log g$ plane depends on the actual nitrogen abundance. As already discussed, this can lead to an ambiguity of the spectral-type- T_{eff} relation. We come back to this problem in Sect. 6.7.

In Appendix B.2 we provide a detailed comparison of strategic H/He/N lines predicted by CMFGEN and FASTWIND, for all models from Table 6.3, and for different $[\text{N}]$. FASTWIND spectra have been taken from our grid, to show that the provided resolution in parameter space is sufficient in most cases.

Let us first concentrate on the H/He spectra (upper panels of Figs. B.15, B.18, B.19 and B.22), which turn out to remain unaffected by typical variations in $[\text{N}]$. In most cases, there is an excellent agreement between the H/He spectra from CMFGEN and the closest or almost closest FASTWIND grid-model, even for the He I singlet lines (but see Najarro et al. 2006). The Stark-wings of the Balmer lines are well reproduced at a similar gravity. The largest discrepancies occur for model d2v where He I $\lambda\lambda 4471, 4713$ result in a better fit at $T_{\text{eff}} = 47 \text{ kK}$ instead at the nominal value of 46 kK , and for model s4a where $\log g = 3.5$ produces better consistency than a model at $\log g = 3.6$ which would lie closer to the nominal value of $\log g = 3.57$. Finally, $\text{H}\alpha$ (FASTWIND) shows less emission for model s2a, mostly because the closest grid model has a lower wind-strength of $\log Q = -12.15$ than the nominal value, $\log Q = -11.99$. Figure B.15 illustrates how the H/He spectrum changes when T_{eff} is modified by $\pm 1000 \text{ K}$. In the considered temperature range, the major reaction occurs in He I, predominantly in the singlet lines ($\lambda\lambda 4387, 6678$).

The lower panels of Figs. B.15, B.18, B.19 and B.22 display important nitrogen lines for the four investigated models, at $[\text{N}] = 8.78$ (ten times solar), whilst Figs. B.16, B.17, B.20 and B.21 display

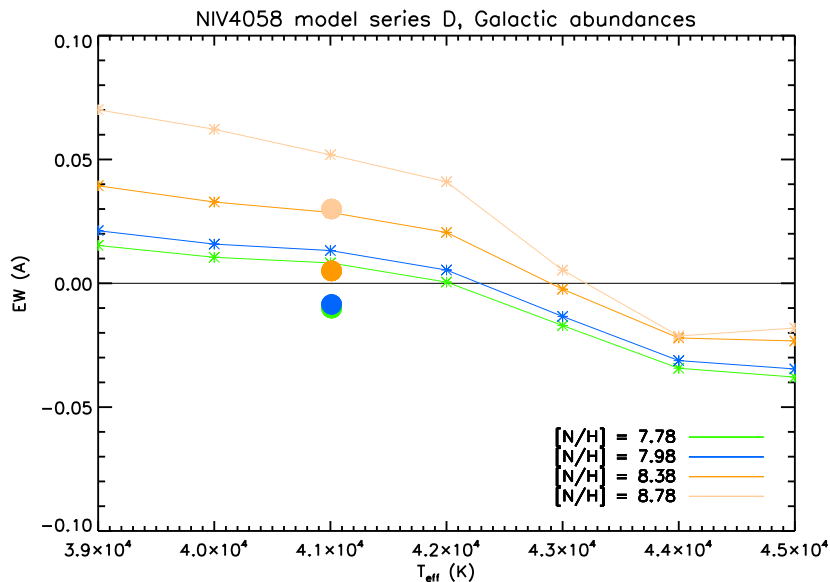


Figure 6.9: NIV λ 4058, switching from emission to absorption with increasing abundance. Model series ‘D’ ($\log Q = -12.8$), $\log g = 4.0$, compared to results from CMFGEN, model d4v (at $T_{\text{eff}} \approx 41$ kK, filled circles).

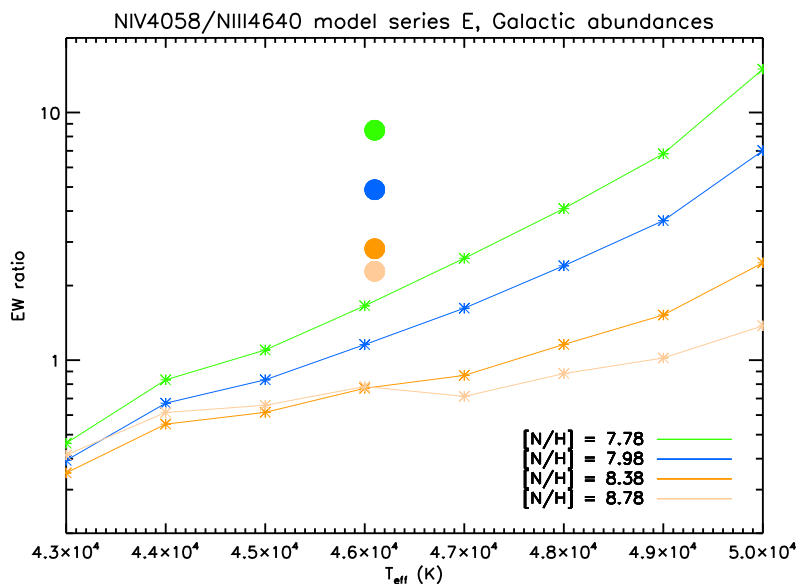


Figure 6.10: Equivalent width ratio NIV λ 4058/NIII λ 4640, as a function of nitrogen abundance. Model series ‘E’ ($\log Q = -12.45$), $\log g = 4.0$, compared to results from CMFGEN, model d2v (at $T_{\text{eff}} \approx 46$ kK, filled circles).

these lines for $[N] = 7.78$ (solar).

N III lines have been already compared in Chapter 4, for $[N] = 7.92$ (and $v_{\text{mic}} = 15 \text{ km s}^{-1}$), and these findings remain valid also at higher nitrogen abundance.

For the dwarf models d4v and d2v, the emission lines at $\lambda\lambda 4634\text{-}4640\text{-}4642$ are stronger than predicted by CMFGEN, and indeed stronger than displayed in Chapter 4, where the disagreement was less obvious. This discrepancy could be tracked down to a different value of v_{mic} used in the present models. A lower value (10 vs. 15 km s^{-1}) results in narrower resonance zones, and can lead to higher emission peaks.⁹ Moreover, differences in the occupation numbers - when close to inversion in certain regions - become more pronounced, due to less averaging. For models s4a and s2a we note similar discrepancies, though at a tolerable level.

As discussed in Chapter 4, the N III absorption line at $\lambda 4097$ is slightly stronger in FASTWIND models at hot temperatures. Note that for d2v the profiles become identical when comparing with a model that reproduces the CMFGEN He I lines, i.e., for $T_{\text{eff}} = 47 \text{ kK}$ instead of 46 kK .

The quartet lines¹⁰ at $\lambda\lambda 4510\text{-}4514\text{-}4518$ behave quite interestingly. Among the low $[N]$ models, these lines are in absorption only at d4v, whilst for the other models (higher T_{eff} and/or higher \dot{M}) they appear in emission. In a certain parameter range (models d2v and s4a) and in analogy to N IV $\lambda 4058$, these lines switch, for increasing $[N]$, from emission to absorption. Regarding these major trends, CMFGEN and FASTWIND behave similarly, and the lines agree quite well for the dwarf models. For the supergiant models, on the other hand, FASTWIND predicts more emission/less absorption than CMFGEN, in particular for s2a. Thus, and due to their complex behavior, the quartet lines need to be treated with care when analyzing *early* O-stars.

N III $\lambda 4003$ and $\lambda 4195$ (in the blue wing of He II $\lambda 4200$ and additionally blended by Si III at hotter temperatures) show a mostly reasonable agreement. N III $\lambda 4195$ matches almost perfectly when predicted to be in emission, and $[N]$ is low. The biggest discrepancy for $\lambda 4003$ is found in the low $[N]$ model of s4a, where CMFGEN predicts much more absorption.

N IV and N V lines have not been compared so far. N IV $\lambda 4058$ from FASTWIND shows always less emission than produced by CMFGEN, though for models s2a and for the low $[N]$ model s4a the agreement becomes satisfactory.

In combination with more emission from the N III triplet at hotter temperatures, this leads to a lower N IV/N III EW/line-strength ratio in FASTWIND (see Fig. 6.10), i.e., effective temperatures deduced from this line-ratio *alone* would be higher compared to CMFGEN results. This general trend is independent of abundance.

N IV $\lambda 3480$ is in good agreement for most models, except for d4v where FASTWIND predicts more absorption. In contrast, N IV $\lambda 6380$ shows considerable differences, and for almost all models (except for the high $[N]$ model of d4v) our grid predicts much more absorption. Since this line provided no difficulties when comparing with observations (neither in Chapter 5 nor in the present investigation), we suggest that it might suffer from certain problems in CMFGEN. We are currently working on this problem, which we think is connected to the desaturation of the N IV resonance line around 247 \AA at the base of the wind.

Finally, the N V doublet $\lambda\lambda 4603\text{-}4619$ compares very well in most cases, and only for the low $[N]$ models of s2a and s4a we find more absorption by FASTWIND.

⁹ A similar influence of v_{turb} has been seen, e.g., in synthetic spectra of Br α when in emission due to *photospheric* processes (Najarro et al., 2011).

¹⁰ Preferentially used by Martins et al. (2011a) to derive nitrogen abundances in magnetic O-stars of late and intermediate spectral type.

Summarizing the major discrepancies, we note that in the early O-type domain FASTWIND produces more emission in the N III triplet, less emission at N IV λ 4058, and mostly much more absorption at N IV λ 6380, compared to CMFGEN. We now ask how such discrepancies might affect an abundance/ T_{eff} analysis, and how one might proceed to diminish the impact of corresponding uncertainties.

Since the H/He lines are in very good agreement, the stellar parameters should be constrained quite well, as long as He I remains visible. For the hottest stars with no or negligible He I, the situation might become more difficult, since T_{eff} needs to be constrained mostly from the nitrogen lines, and we would deduce lower T_{eff} from CMFGEN if concentrating on the N III triplet and N IV λ 4058 alone (see above). In turn, this would lead to rather different abundances. Fortunately, however, there is also N V which is very sensitive on T_{eff} (see below and Figs. B.15, B.17 and B.18), and seems to be quite code-independent¹¹. In conclusion, T_{eff} for ‘cooler’ objects should be mostly determined from the He I/He II ionization balance. Potential discrepancies regarding N III λ 4634-4640-4642 and N IV λ 4058 because of ‘erroneous’ predictions can be easily identified then. For the hottest objects, on the other hand, N V should obtain a strong weight when determining T_{eff} . As long as either N IV λ 6380 or N IV λ 3480 are observed, these lines might be used as abundance indicators, whilst any inconsistency of N IV λ 4058 will tell about the quality of that line.

In Fig. 6.11 we now ‘analyze’ synthetic spectra from CMFGEN by means of our FASTWIND grid, to check the overall consistency when accounting for *all* important lines. This is done for the high [N] model of d4v, which is a prototypical case, and by means of EW iso-contours in the T_{eff} -[N] plane (for the appropriate model series ‘D’ with $\log Q = -12.8$, and a gravity of $\log g = 4.0$). Equivalent width for all analyzed lines have been measured from the CMFGEN spectra. These EWs are displayed as iso-contours with respect to our FASTWIND grid and should cross, in the ideal case of a perfect consistency between both codes, at one point corresponding to the model parameters, i.e., $T_{\text{eff}} = 41$ kK and [N] = 8.78. Because of the various discrepancies discussed above, this is not the case, but at least almost all iso-contours are close to each other in quite a confined region, roughly centered at the actual parameter set and marked by a black box. In particular, five out of eight lines cross around the point $T_{\text{eff}} = 41.5$ kK/[N] = 8.55. At the original (CMFGEN) values, $T_{\text{eff}} = 41$ kK and [N] = 8.78, on the other hand, there is only N V λ 4603 and N III λ 4003. Thus, a FASTWIND analysis of this model spectrum would yield lower nitrogen abundances, by roughly 0.2 dex (more on this below).

The figure displays a number of interesting aspects. Most iso-contours have a parabola-like shape with a minimum at low [N], where the ‘left’ branch with negative slope relates to increasing ionization fractions (the same EW at higher T_{eff} implies a lower abundance), and the ‘right’ branch with positive slope to decreasing fractions. Because the right branch applies for lines from lower ionization stages (N III), and the left branch for lines from higher ones (N IV, N V), these different slopes allow to constrain the actual parameter region quite well, even though both codes produce different line-strengths when compared at the same location in parameter space.

The only feature which is quite outside the enclosed region is the N III triplet, which is *significantly* different in both codes (and stronger in FASTWIND, thus formed at lower T_{eff} when compared to the CMFGEN EWs).

At the comparatively ‘cool’ temperature of model d4v, N V λ 4603-4619 becomes almost independent of abundance (almost vertical left branch), and thus a very sensitive temperature indicator. Indeed, it perfectly fits at the actual T_{eff} (which is also true for the He I/He II lines, see Fig. B.15). In-

¹¹ And not affected by X-rays from wind embedded shocks under typical conditions, see Chapter 5.

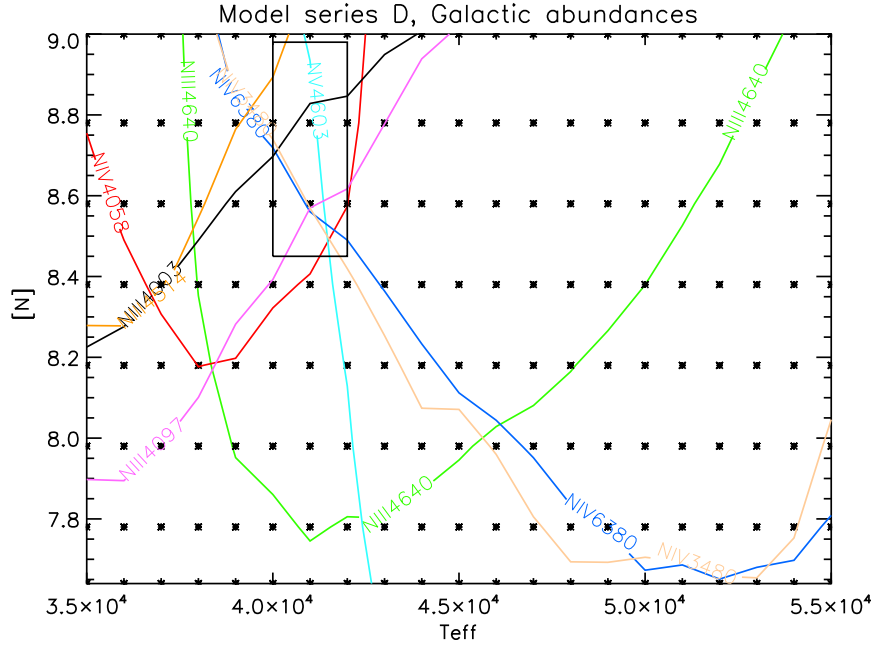


Figure 6.11: Nitrogen abundance ‘analysis’ of CMFGEN model d4v with $[N] = 8.78$. EW iso-contours for important nitrogen lines are displayed in the $T_{\text{eff}}-[N]$ plane of our FASTWIND model grid (series ‘D’, $\log Q = -12.8$, $\log g = 4.0$). The displayed iso-contours refer to EWs measured from the CMFGEN spectra of model d4v. In the ideal case, i.e., if CMFGEN and FASTWIND produce identical results, all iso-contours would cross at a single point located at $T_{\text{eff}} = 41\text{kK}$ and $[N] = 8.78$. The black box marks the smallest region in parameter space where almost all lines (except for N III $\lambda 4640$) are predicted at the measured value. In particular, five out of eight lines cross around the point $T_{\text{eff}} = 41.5\text{ kK}/[N] = 8.55$, i.e., at a lower abundance (by roughly 0.2 dex) than present in the original CMFGEN model.

Interestingly as well, the iso-contours for N IV $\lambda 6380$ and N IV $\lambda 3480$ occupy an almost identical region, i.e., give very similar results, though being members of different spin systems (singlet and triplet system, respectively). Insofar, the information provided by both lines is similar, and the observation/analysis of either of these lines should be sufficient, which is fortunate since the 3500 Å region is scarcely observed.

Overall, when ‘analyzing’ $[N]$ from the CMFGEN spectrum and accounting for the rather fixed T_{eff} and $\log g$ values from H/He and N V, we would derive a lower or roughly similar nitrogen abundance from most lines, compared to the actual value used by CMFGEN, except for the N III quartet lines which would imply a somewhat higher abundance. These results are also valid for the other models from Table 6.3. We thus conclude that in those cases where T_{eff} can be additionally constrained, FASTWIND analyzes of early O-type stars will yield mostly lower nitrogen abundances than analyzes performed by means of CMFGEN.¹²

¹²At the present stage of knowledge, we do not know which code does a ‘better’ job in reproducing reality.

6.6 Analysis of a sample of LMC/SMC early-type O-stars

So far, we mainly provided theoretical predictions on the N IV/ N III emission line ratio as used by Walborn et al. (2002) to classify the earliest O-stars, and concentrated on the impact of various parameters. For testing our predictions, we need to confront these results with the analysis of a significant stellar sample. The LMC sample analyzed in Chapter 5 contained only a few early-type objects (BI237, BI253, N11-026, N11-031, and N11-060). These stars, biased towards O2, did not cover all spectral types and luminosity classes within the classification scheme. To allow for a larger sample, we added the earliest stars from the analyzes of LMC/SMC objects by Massey et al. (2004, 2005, 2009, hereafter Mas04, Mas05, and Mas09).

6.6.1 The stellar sample

In particular, we selected objects with spectral types earlier than O5. Table 6.4 gives a complete list of all early O-type stars considered in the following, along with their spectral type and galaxy membership. The final sample consists of seventeen stars, fourteen from the LMC and three from the SMC. Thirteen objects have been drawn from Mas04 and Mas05, plus one object from Mas09 (the only early-type star of that sample). Two of the objects analyzed in Chapter 5 (BI237 and BI253) were also studied by Mas05. For these objects, as well as for the remaining sample members (N11-026, N11-031, and N11-060), we refer to our analysis from Chapter 5.

From the original subsample of early-type stars studied by Mas04 and Mas05, we selected representative objects. Owing to various reasons, eight stars have been discarded. (i) Three dwarfs (R136-033, R136-040 and R136-055) did not show any trace of either N III λ 4634-4640-4642 or N IV λ 4058 in their spectra, and Massey and co-workers could not classify them according to the Walborn et al. (2002) scheme. Therefore, we analyzed only one prototypical example for these stars, R136-040. (ii) From the four early giants compiled in Mas05, we discarded two of them, R136-047 (O2 III(f*)) and LH 64-16 (O2N III(f*)). The FOS data used for the R136 stars, see Sect. 6.6.2, suffered from an intermittent behavior of some of the FOS diodes (Massey & Hunter, 1998), which could result in the appearance of spurious features contaminating the spectra. Owing to a rather bad quality of the spectra, we were not able to obtain a satisfactory fit for R136-047, and we decided to discard it from the analysis. This problem was not met for the remaining R136 stars used within this work (R136-018 and R136-040). The other giant discarded, LH 64-16, shows similar severe discrepancies as we had found in Chapter 5 for another star of this class, N11-031. Owing to extreme difficulties to fit either N III/N IV or N IV/N V lines, we excluded it from the present analysis. (iii) Regarding supergiants, we selected three out of seven stars. For typical conditions ($\dot{M} \geq 10^{-5} M_{\odot} \text{yr}^{-1}$, $v_{\infty} \sim 3000 \text{ km s}^{-1}$, and $R_* \sim 15 R_{\odot}$), the corresponding wind-strength, $\log Q \geq -12$, is well outside of our model-grid (Table 6.1), and we concentrated on representative objects since analyzing all of them would have been extremely time-consuming, even with a fast code such as FASTWIND.

In summary, our sample comprises 9 dwarfs, 5 giants, and 3 supergiants. The source of the corresponding spectral types for each object is listed in Table 6.4.

6.6.2 Observational data

Spectra for the 12 early O-stars from Massey et al. were taken in three ranges, the UV, the blue and the red visual band. Only optical data were used within this work.

Table 6.4: Sample stars used within this study, along with galaxy membership and spectral type. The horizontal line separates stars analyzed within this work (drawn from Mas04/05/09) from stars previously analyzed in Chapter 5. Identifications are as follows: "AV" from Azzopardi & Vigneau (1982); "BAT" from Breysacher et al. (1999); "BI" from Brunet et al. (1975); "LH" from Lucke (1972) except "LH10-3058" that is from Walborn et al. (2002, 2004); "N11" from Evans et al. (2006); "NGC" from Massey et al. (1989); "P" from Parker et al. (1992); "R136" from Massey & Hunter (1998); "R136a" from Malumuth & Heap (1994); "Sk" from Sanduleak (1970).

Star	Cross-IDs	Galaxy	Spectral Type
AV 177	-	SMC	O4 V((f)) ^a
AV 435	-	SMC	O3 V((f*)) ^a
NGC 346-355	NGC 346 W3	SMC	ON2 III(f*) ^b
LH 81:W28-5	-	LMC	O4 V((f+)) ^a
LH 81:W28-23	-	LMC	O3.5 V((f+)) ^a
LH 90:ST 2-22	-	LMC	O3.5 III(f+) ^a
LH 101:W3-24	ST 5-27	LMC	O3.5 V((f+)) ^a
LH 101:W3-19	ST 5-31	LMC	O2 If* ^a
R136-018	-	LMC	O3 III(f*) ^a
R136-040	R136a-535	LMC	O2-3.5 V ^a
Sk-65° 47	LH 43-18	LMC	O4 If ^a
Sk-67° 22	BAT 99-12	LMC	O2 If*/WN5 ^c
BI237	-	LMC	O2 V((f*)) ^d
BI253	-	LMC	O2 V((f*)) ^d
N11-026	-	LMC	O2 III(f*) ^d
N11-031	P3061/LH10-3061	LMC	ON2 III(f*) ^d
N11-060	P3058/LH10-3058	LMC	O3 V((f*)) ^d

^aMas05

^bWalborn et al. (2004)

^cCrowther & Walborn (2011)

^dMokiem et al. (2007a) and references therein

(i) For the bulk of the stars, these data were obtained at the Cerro Tololo Inter-American Observatory (CTIO) 4m Blanco telescope with the RC spectrograph, during January 1999 (P.I. P. Massey). The blue and red spectra cover the ranges 3750-4900 Å and 5400-7800 Å, respectively. The spectral resolution was 1.4 Å for the blue and 2.8 Å for the red band, with a S/N between 200 to 560 per resolution element, corresponding to about 4 pixels, in the blue (measured at 4500 Å), and a typical S/N of about 150 per resolution element in the red.

For LH 101:W3-24, additional spectra for the H α region were taken by means of the Hubble Space Telescope (HST) using STIS/CCD (as part of programme GO-9412, P.I. P. Massey), to amend the ground-based observations which were heavily contaminated by strong nebulosity. These data cover 6300-6850 Å, with a spectral resolution of 0.84 Å and S/N of 50.

(ii) For the R136 stars, we used two different data sets obtained with the HST. One was taken

with the G400 FOS/RD configuration under GO-6417 (P.I. P. Massey), with a resulting wavelength coverage from 3250 to 4820 Å, 3 Å resolution and a S/N of 60 at 4400 Å. Additional observations were taken with STIS/CCD under GO-7739 (P.I. P. Massey). Blue observations covered the wavelength range 4310-4590 Å, at a S/N of 100 for a spectral resolution of 0.4 Å. Observations centered around H_{α} were made with the same setup as for LH 101:W3-24 described above. Since the STIS spectra have better S/N and resolution, we used them preferentially for our analysis. Because of their limited wavelength coverage, excluding the spectral region that comprises the most important nitrogen lines, we nevertheless had to consider the FOS data, see Figs. C.23 and C.27.

(iii) Spectra for NGC 346-355 were collected with the Clay 6.5m (Magellan II) telescope at the Las Campanas Observatory, using the Boller & Chivens Spectrograph (P.I. P. Massey). The coverage was 3410-5040 Å with a S/N of 600 at 4500 Å in the blue, and from 5315 to 6950 Å in the red, achieving a S/N of 400 at 6500 Å. For both ranges, the spectral resolution was 2.4 Å.

All spectra were reduced with IRAF,¹³ and we performed additional re-normalizations for different wavelength ranges within this work.

As outlined in Sect. 6.6.1, our present sample includes two objects (BI237 and BI253) which have been studied both in Chapter 5 and by Mas05. The UVES spectra used in the former analysis have a considerably higher resolving power, 40,000, compared to a resolving power of 3,000 as provided by the RC spectrograph used by Mas05. After comparing both data sets amongst each other and with our fits from Chapter 5, it turned out that the nitrogen lines are quite similar, whilst the cores of the hydrogen (except for H_{α}) and He II lines are somewhat deeper in the UVES data, more than expected from the higher resolution. Because of the high quality of the UVES data, we kept the parameters as derived in Chapter 5, though a re-analysis based on the Mas05 data would have provided rather similar values.

6.6.3 Analysis

Stellar and wind parameters were derived following the methodology outlined in Chapter 5, and are listed in Table 6.5. Comments on individual objects and corresponding H/He/N line fits are provided in Sect. 6.6.4 and Appendix C.2, respectively.

In brief, we proceeded as follows. In accordance with Chapter 5 and the analyzes by Massey and collaborators, we assumed unclumped mass-loss throughout the analysis.¹⁴ First, we determined $v \sin i$ for each object using the Fourier method (Gray, 1976).¹⁵ Subsequently, we roughly constrained the stellar/wind parameters as well as the helium and nitrogen abundances by means of our model-grids for LMC and SMC background metallicities. For deriving T_{eff} , we used both the helium and nitrogen ionization balance when possible, i.e., when nitrogen lines from at least two ionization stages were visible (see Table 6.5 for the particular diagnostics applied). For the cooler objects of our sample ($T_{\text{eff}} \leq 44$ kK), we mainly relied on the helium ionization balance, and used nitrogen as a consistency check. For hotter objects, where He II $\lambda 4541$ begins to lose its sensitivity to T_{eff} , we gave larger weight to the nitrogen balance, as long as a reasonable fit to the He I/He II lines could be maintained. Note that any $T_{\text{eff}}/[N]$ degeneracy (as present, e.g., for the line-strength *ratio* of N IV/N III) is broken by the absolute strengths of the lines, and the fact that we have usually more than two lines at our

¹³IRAF is distributed by the National Optical Astronomy Observatories, which are operated by the Association of Universities for Research in Astronomy, Inc., under cooperative agreement with the National Science Foundation.

¹⁴Regarding the impact of clumping on the synthetic nitrogen spectra, see Chapter 5.

¹⁵As implemented and tested in the OB-star range by Simón-Díaz et al. (2006) and Simón-Díaz & Herrero (2007).

Table 6.5: Fundamental parameters for the early O-star sample, assuming unclumped mass-loss. For each star, the additional (or even primary) T_{eff} diagnostics used in parallel with the He I/He II ionization equilibrium is indicated. For four stars, two parameter sets are provided, see text.

Star	Spectral type	Nitrogen T_{eff} diag.	T_{eff} (kK)	$\log g$ (cgs)	$\log g_{\text{true}}$ (cgs)	R_* (R_{\odot})	$\log L_*$ (L_{\odot})	\dot{M}^c	$\log Q$	β	v_{∞} (km s^{-1})	$v \sin i$ (km s^{-1})	v_{mac} (km s^{-1})	Y_{He}	[N]
Dwarfs															
BI253 ^a	O2 V((f*))	N IV/N V	54.8	4.18	4.20	10.7	5.97	1.53	-12.61	1.21	3180	230	-	0.08	7.90
BI237 ^a	O2 V((f*))	N IV/N V	53.2	4.11	4.12	9.7	5.83	0.62	-12.98	1.26	3400	140	-	0.09	7.38
R136-040	O2-3.5 V	-	>51.0	4.01	4.02	10.3	5.81	1.93	-12.53	0.80	3400	120	-	0.08	6.90
N11-060 ^a	O3 V((f*))	N III/N IV/N V	48.0	3.97	3.97	9.5	5.63	0.51	-12.92	1.26	2740	68	40	0.12	8.20
		N IV/N V	51.0	4.10	4.10	9.2	5.71	0.48	-12.92						8.15
AV 435 ^b	O3 V((f*))	N III/N IV	46.0	3.90	3.91	13.8	5.88	0.21	-13.15	0.80	1500	110	-	0.10	7.58
LH 81:W28-23	O3.5 V((f+))	N III/N IV/N V	47.0	3.80	3.82	10.0	5.65	1.57	-12.53	1.00	3050	146	-	0.25	8.40
LH 101:W3-24	O3.5 V((f+))	-	47.0	4.00	4.01	8.1	5.46	0.27	-13.00	0.80	2400	120	-	0.10	7.78
LH 81:W28-5	O4 V((f+))	N III/N IV/N V	44.0	3.80	3.81	9.8	5.51	1.08	-12.60	0.80	2700	120	80	0.15	8.38
AV 177 ^b	O4 V((f))	-	44.0	3.80	3.85	8.8	5.42	0.23	-13.19	0.80	2650	220	-	0.15	7.78
Giants															
N11-031 ^a	ON2 III(f*)	N III/N IV	47.8	3.95	3.95	13.4	5.92	2.02	-12.64	1.08	3200	71	60	0.11	7.83
		N IV/N V	56.0	4.00	4.00	12.2	6.12	2.20	-12.54						8.30
NGC 346-355 ^b	ON2 III(f*)	N IV/N V	55.0	4.00	4.01	12.0	6.08	2.50	-12.39	0.80	2800	140	-	0.10	8.10
		N III/N IV	51.0	4.00		12.5	5.98	2.00	-12.51						7.98
N11-026 ^a	O2 III(f*)	N III/N IV/N V	49.0	4.00	4.00	11.3	5.82	1.56	-12.63	1.08	3120	72	60	0.10	7.80
		N IV/N V	52.0	4.10	4.10	11.0	5.89	1.49	-12.63						7.75
R136-018	O3 III(f*)	N III/N IV/N V	47.0	3.90	3.92	14.2	5.95	1.68	-12.76	0.80	3200	180	-	0.10	8.18
LH 90:ST 2-22	O3.5 III(f+)	N III/N IV/N V	44.0	3.70	3.71	18.8	6.08	4.56	-12.36	0.80	2560	120	80	0.15	8.58
Supergiants															
Sk-67° 22	O2 If*/WN5	N III/N IV/N V	46.0	3.70	3.74	12.4	5.80	15.00	-11.60	0.80	2650	200	-	0.30	8.78
LH 101:W3-19	O2 If*	N III/N IV/N V	44.0	3.90	3.91	25.3	6.34	20.86	-11.97	0.80	2850	180	-	0.10	8.18
Sk-65° 47	O4 If	N III/N IV	40.5	3.60	3.62	19.8	5.98	11.00	-11.89	0.80	2100	160	-	0.12	7.78

^aStellar/wind parameters derived in Chapter 5; ^bSMC star; ^cin units of $10^{-6} M_{\odot} \text{yr}^{-1}$

disposal, which react quite differently on changes in T_{eff} and $[\text{N}]$ (cf. Fig. 6.11). Thus, as long as lines from at least two nitrogen ionization stages are available, T_{eff} and $[\text{N}]$ can be determined in parallel from fitting these lines (as long as the other stellar/wind parameters can be inferred from independent diagnostics). If nitrogen lines were not available (too weak), we either relied on He I/He II alone (LH 101:W3-24 and AV 177), or, when even He I was no longer visible, we settled for a lower limit on T_{eff} (R136-040). We refer to Sect. 6.6.4 for a detailed discussion on the specific diagnostics used (see also Table 6.5), and on particular problems for individual stars.

Gravities were inferred from the wings of the Balmer lines, and $\log Q$ from fitting $\text{H}\alpha$ and He II $\lambda 4686$, with nitrogen lines serving as a consistency check for both quantities. Because of the rather low resolution and the mostly high $v \sin i$ values, we were able to constrain the ‘macro-turbulence’, v_{mac} , for only two objects (LH 81:W28-5 and LH 90:ST 2-22). For the remaining ones, our fits were acceptable without any need for extra-broadening.

At this point, we adopted terminal velocities as derived by Massey et al. from UV lines, updating \dot{M} to preserve Q if necessary. For the bulk of the stars, we kept the velocity field exponent used within our model-grid, $\beta = 0.8$, because of reasons of consistency, since also Massey et al. used this value. Only for LH 81:W28-23 we adopted $\beta = 1.0$, to better reproduce He II $\lambda 4686$ (see Fig. C.24). For those objects with $\text{H}\alpha$ and He II $\lambda 4686$ in emission (LH 101:W3-19, Sk-67° 22, and Sk-65° 47), it would have been also possible to derive β from the profile shape. Because of the quite good fit-quality for both lines already with $\beta = 0.8$ (see Figs. C.29, C.30, and C.31), we had no real reason to change this value though.

Final parameters were derived from a grid of much higher resolution around the initial constraints. Stellar radii were calculated from M_V as provided by Mas04/05/09 and synthetic fluxes, with a corresponding final update of \dot{M} . Following our experience for the earliest O-stars from Chapter 5, we used a micro-turbulent velocity, $v_{\text{mic}} = 10 \text{ km s}^{-1}$, for all objects considered here.

Errors on stellar/wind parameters are adopted following Chapter 5. In brief, we estimate an uncertainty of $\pm 1 \text{ kK}$ in T_{eff} (for those objects with a unique solution, see Table 6.5), $\pm 0.1 \text{ dex}$ in $\log g$, and $\pm 0.05 \text{ dex}$ in $\log R_*$, adopting a typical error of $\pm 0.25 \text{ mag}$ in M_V (see Eq. 8 in Repolust et al. 2004). Together with the errors for T_{eff} , this adds up to an uncertainty of $\pm 0.11 \text{ dex}$ for $\log L/L_\odot$. Larger errors, plus/minus a factor of two, are present for \dot{M} , when $\text{H}\alpha$ is in absorption.¹⁶ For objects with mass-loss indicators in emission, the error is somewhat lower. Errors on v_∞ are on the order of $\pm 100 \text{ km s}^{-1}$, taken from Massey et al., and we estimate the errors on $v \sin i$ and v_{mac} as ± 10 to 20 km s^{-1} . A rough estimate on the error of Y_{He} is ± 0.01 to 0.02 . Regarding $[\text{N}]$, we adopt a conservative value of ± 0.15 to 0.20 dex to account for the dependence on stellar and wind parameters.

6.6.4 Comments on the individual objects

In the following, we give specific comments on the individual objects, regarding peculiarities and problems found during our analysis. We separate between galaxy membership, and sort by luminosity class and spectral type. Line fits are displayed in Figs. C.23 to C.34, for important H/He/N lines: $\text{H}\alpha$, $\text{H}\beta$, $\text{H}\gamma$, $\text{H}\delta$, $\text{H}\epsilon$, He I $\lambda\lambda$ 4387, 4471, 4713, He II (+He I) λ 4026, He II $\lambda\lambda$ 4200, 4541, 4686, 6406, 6527, 6683, N III $\lambda\lambda$ 4003, 4097, 4195, 4379, $\lambda\lambda$ 4634-4640-4642, and $\lambda\lambda$ 4510-4514-4518, N IV $\lambda\lambda$ 4058, 6380, and N V $\lambda\lambda$ 4603/4619. All spectra were corrected for radial velocity shifts. If not explicitly stated, any comparison made in the following text refers to the results from Mas05.

¹⁶In this case, one is unable to derive β from line-fitting, and the uncertainty in β reflects in quite a large error for \dot{M} (Markova et al. 2004)

LMC stars

R136-040 – O2-3.5 V (Fig. C.23). This star could not be classified by Mas05 using the scheme by Walborn et al. (2002), because neither N III $\lambda\lambda$ 4634-4640-4642 nor N IV λ 4058 were visible in the spectra. As outlined in Sect. 6.6.2, for the R136 stars we have spectra from both STIS and FOS available. Taking advantage of the better quality of the STIS data and using H α , H γ , and He II λ 4541, we derived a similar lower limit (no He I and no nitrogen lines)! on T_{eff} as Mas04, but a substantially larger (by 0.2 dex) gravity, which agrees better with its dwarf designation. Our analysis also resulted in a low helium content, $Y_{\text{He}} = 0.08$ (Mas04: $Y_{\text{He}} = 0.1$). Note the discrepancy in the cores of H δ , H ϵ , and He II $\lambda\lambda$ 4026, 4200 when comparing with the FOS data. Such a discrepancy was also found for the remaining H/He II lines in the FOS data, when used instead of the STIS spectra.

The missing nitrogen lines imply an upper limit for the nitrogen content corresponding to the LMC baseline abundance $[\text{N}] = 6.90$, which also agrees quite well with the low He content.

LH 81:W28-23 – O3.5 V((f+)) (Fig. C.24). The modeling of this star was straightforward, and we obtained similar results as Mas05. However, we considered a larger $\beta = 1.0$ to better reproduce the marginal P-Cygni profile at He II λ 4686, which might indicate a luminosity class III object (see Walborn et al. 2002). To preserve the fit of H α , we needed to reduce \dot{M} . All nitrogen lines are consistent with the temperature derived from the helium ionization equilibrium. The quite large nitrogen abundance ($[\text{N}] = 8.40$) agrees well with the helium abundance $Y_{\text{He}} = 0.25$, indicating an evolved nature of this object.

LH 101:W3-24 – O3.5 V((f+)) (Fig. C.25). We derived a somewhat cooler T_{eff} (by 1 kK) together with a lower helium content, $Y_{\text{He}} = 0.10$, which was consistent for all helium lines. Nitrogen lines are barely visible, because the spectrum of this star displays more noise than the bulk of our sample stars, caused by the use of a narrow extraction aperture to reduce effects from nebular emission for the ground-based observations (cf. Sect 6.6.2). Due to the noisy spectrum, we were only able to infer an upper limit for the nitrogen abundance, $[\text{N}] \leq 7.78$.

LH 81:W28-5 – O4 V((f+)) (Fig. C.26). This is one of the standards used by Walborn et al. (2002) for defining the O4 V((f+)) class. A consistent analysis of the helium and nitrogen ionization equilibrium yielded a cooler temperature, $T_{\text{eff}} = 44$ kK, which required a helium abundance of $Y_{\text{He}} = 0.15$ to reproduce He I λ 4471. An excellent fit to most nitrogen lines from all three ionization stages was achieved for this star, indicating a significant enrichment, $[\text{N}] = 8.38$.

R136-018 – O3 III(f*) (Fig. C.27). Also for this O3 giant we have used data from both STIS and FOS. A consistent analysis of the H/He lines from STIS and nitrogen lines (mostly from FOS) suggested a hotter T_{eff} , by 2 kK, as well as a higher surface gravity, by ~ 0.1 dex. Again, we found discrepancies in the cores of the H/He II lines from the FOS spectra, except for He II λ 4686. An acceptable fit for N III/N IV/N V using $[\text{N}] = 8.18$ was possible, where only N IV λ 4058 was slightly underpredicted. Even though the nitrogen lines contained in the STIS dataset, N III $\lambda\lambda$ 4510-4514-4518 and N IV λ 6380, are diluted in the continuum, they support our analysis.

LH 90:ST 2-22 – O3.5 III(f+) (Fig. C.28). An unproblematic analysis provided the same results as obtained by Mas05, except that we opted for a lower helium abundance, $Y_{\text{He}} = 0.15$. Again, a remarkable fit to the nitrogen lines was possible, at $[\text{N}] = 8.58$, indicating an extreme enrichment.

Sk-67° 22 – O2 If*/WN5 (Fig. C.29). This star was re-classified¹⁷ as O2 If*/WN 5 by Crowther & Walborn (2011) using their updated classification scheme, because of the H_{β} P-Cygni profile. Using lines from N III/N IV/N V, we inferred $T_{\text{eff}} = 46$ kK which is hotter than the lower limit (from very weak He I $\lambda 4471$) quoted by Mas05. Our fit seems to slightly overpredict the emission in N IV $\lambda 4058$ and to underpredict the N V doublet. An extreme nitrogen abundance, $[\text{N}] = 8.78$, was required, the largest one found in our sample. Such an abundance would be certainly too large when comparing even with strongly nitrogen-enhanced O-stars, and also with predictions from evolutionary calculations tailored for the LMC (Brott et al. 2011b and Chapter 5), thus supporting a rather evolved nature of this object and its ‘slash-star’ designation. This star was also analyzed by Doran & Crowther (2011) using N IV/N V lines (without discussion of He I and N III), only providing a $T_{\text{eff}} = 49.3$ kK for this object. Such hotter temperature would improve our fits for N IV $\lambda 4058$ and the N V doublet, but is inconsistent with the observed strength of N III.

LH 101:W3-19 – O2 If* (Fig. C.30). For this supergiant, a consistent He/N analysis allowed us to derive $T_{\text{eff}} = 44$ kK, hotter than the lower limit (marginal He I $\lambda 4471$) assigned by Mas05. Using N III/N IV/N V in parallel, we achieved an almost excellent fit for the nitrogen lines at $[\text{N}] = 8.18$.

Sk-65° 47 – O4 If (Fig. C.31). The parameter set derived for this star using H/He/N lines is quite similar to the results from Mas05, with somewhat larger $Y_{\text{He}} = 0.12$. A potential discrepancy provides N IV $\lambda 4058$, where we might slightly overpredict the observed emission.

SMC stars

AV 435 – O3 V(f*) (Fig. C.32). The only discrepancies found during our analysis correspond to an overprediction of He II $\lambda \lambda 6406, 6527, 6683$. Both the He I/He II and the N III/N IV ionization equilibrium suggest a hotter temperature than quoted by Mas05, $T_{\text{eff}} = 46$ kK. This temperature seems to be somewhat cool for its spectral type O3 V assigned by Mas05 because of N IV $\lambda 4058 \lesssim$ N III $\lambda 4640$, but quite consistent with our predictions for the derived wind-strength and nitrogen content, $[\text{N}] = 7.58$ (cf. Figs. 6.7 and 6.8).

AV 177 – O4 V(f) (Fig. C.33). The H/He analysis of this star produced similar parameters as found by Mas05. Owing to a high rotation, $v \sin i = 220 \text{ km s}^{-1}$, nitrogen lines are barely visible in the spectrum. Weak traces of emission at N III $\lambda \lambda 4634-4640-4642$ and N III $\lambda \lambda 4510-4514-4518$ together with weak absorption at N IV $\lambda 6380$ are fitted consistently at $[\text{N}] = 7.78$.

NGC 346-355 – ON2 III(f*) (Fig. C.34). This star was considered as a standard for the O2 III(f*) category by Walborn et al. (2002), and later on updated to ON2 III(f*) by Walborn et al. (2004). As for N11-031 (same type!) analyzed in Chapter 5, we found problems to fit all N III/N IV/N V lines in parallel, but to a lesser extent. The basic difference is related to He I $\lambda 4471$, which is not as clearly

¹⁷Mas05: O2 If*

visible as for N11-031. During our analysis, we considered two possible parameter sets: a cooler solution with $T_{\text{eff}} = 51$ kK (red) and a hotter one with $T_{\text{eff}} = 55$ kK (black), using either the N III/N IV or the N IV/N V ionization equilibrium. By inspection of He I $\lambda 4471$, we note that both temperatures might be consistent with the very weak observed feature. For a similar nitrogen abundance, $[\text{N}] = 7.98$, we were able to fit either N III $\lambda \lambda 4634\text{-}4640\text{-}4642$, N III $\lambda \lambda 4510\text{-}4514\text{-}4518$ and N IV $\lambda 6380$ for the cooler solution, or N IV $\lambda 6380$ and N V $\lambda \lambda 4603\text{-}4619$ for the hotter one.

Mas09, restricted to He I $\lambda 4471$ as a primary temperature indicator, derived $T_{\text{eff}} = 49.5$ kK and $\log g = 3.9$, which would agree with our cool solution, but is insufficient for the N IV/N V lines. The hotter solution is in better agreement with results from Bouret et al. (2003) and Walborn et al. (2004), who found $T_{\text{eff}} = 52.5$ kK and $\log g = 4.0$ fitting the N IV/N V lines by means of CMFGEN. In particular, we achieved a similar fit quality as Bouret et al. (2003), for a similar nitrogen content. Bouret et al. stated that at $T_{\text{eff}} \sim 55$ kK (identical with our hotter solution) their fit for He II $\lambda 4686$ would improve. Such an increase in temperature would also improve their fit of N V, which we are able to fit accurately. The same stellar parameters as determined by Bouret et al. (2003) and Walborn et al. (2004) were derived by Heap et al. (2006) using TLUSTY, mostly based on lines from highly ionized species, in particular N V and N IV. Unfortunately, they did not comment on He I and N III, but reassuringly they derived a nitrogen abundance very similar to ours, $[\text{N}] = 7.92$.

6.6.5 Comparison with results from Massey et al.

In the following, we briefly discuss overall differences between the stellar/wind parameters derived within this work and by Massey et al. for overlapping objects, also regarding BI237 and BI253 which were already analyzed in Chapter 5. For details, see Sect. 6.6.4 and Appendix C.2.

For the majority of objects, where we still could use the He I/He II balance as a primary temperature indicator (but also accounting for nitrogen, see Sect. 6.6.3), we derived slightly cooler T_{eff} , on the order of 0.5 to 1 kK. This is not too disturbing, however, as one often finds systematic differences of this order when different elements are used to derive T_{eff} for hot stars, as, e.g., in the case of using Si vs. He for early B-/late O-type stars (e.g., Hunter et al. 2007). The maximum difference amounts to $\Delta T_{\text{eff}} = -2$ kK for LH 81:W28-23, on the margin of the adopted errors.

For a few objects (BI237, BI253, NGC 346-355, R136-018, and Sk-67° 22) where we needed to exploit the nitrogen ionization balance to break the helium degeneracy, we inferred considerably hotter temperatures ($\Delta T_{\text{eff}} \sim 2\text{-}7$ kK). Admittedly, and owing to the restricted quality of the data for some of the earliest objects with weak N III triplet emission and very weak He I $\lambda 4471$, the effective temperatures derived might be affected by uncertainties due to noise and continuum placement. Nevertheless, the fact that also here the differences are systematic suggests that the solution to this problem may not be purely observational.

We also derived quite similar values for $\log g$, except for the five objects explicitly mentioned above, which indicated higher gravities (mostly because of the higher T_{eff}), with a maximum difference of roughly 0.25 dex for BI253. Our \dot{M} values are systematically lower, mostly because of the lower T_{eff} . For those stars with increased T_{eff} , the reduction is caused by lower R_* and/or higher β , where the latter effect is particularly strong for BI253 which displays the largest difference, $\Delta \log \dot{M} = -0.51$ dex. Helium abundances agree quite well except for those few stars with a larger change in T_{eff} , where we had to adapt Y_{He} to preserve the fit quality of the helium lines. The largest difference found amounts to about 0.05 in Y_{He} for LH 90:ST 2-22. Finally, most of our $v \sin i$ are in good agreement with the Massey et al. values, and only three objects displayed substantial differences,

with the largest one of about 30 km s^{-1} for BI253.

One of the major implications of our re-analysis of the earliest O-stars as considered by Massey et al. can be stated already now: We do not find the pronounced degeneracy of the N IV/N III emission line ratio as claimed by Mas05 (for details, see Sect. 6.7.3). For instance, these authors questioned the monotonicity of the classification scheme with respect to T_{eff} , because, among other problems, they inferred similar T_{eff} for two dwarfs, LH 101:W3-24 (O3.5) and BI237 (O2), which on the other hand displayed considerable differences in their N IV/N III emission line ratios. These T_{eff} were derived by a pure H/He analysis. By exploiting the nitrogen ionization balance, we are now able to break this degeneracy, since, e.g., we find a considerably hotter temperature for BI237 (see table 6.5), similar to the temperature derived for BI253, the other O2 dwarf from the sample.

6.7 Discussion

6.7.1 Nitrogen abundances

Though not the major topic of our present work, let us briefly comment on the nitrogen abundances derived within this analysis. Globally, these are consistent with our results from Chapter 5. The bulk of the LMC stars displays a considerable enrichment, stronger than expected from tailored evolutionary calculations (Brott et al., 2011b), and supporting the idea of an efficient mixing during very early phases of O-star evolution. We confirm the tight correlation between the derived helium and nitrogen content.

Only three dwarfs (note that only one prototypical case of nitrogen-weak objects, R136-040, has been analyzed) seem to be unenriched, visible already in the absence of nitrogen lines in their spectra. The star with the highest enrichment within the sample is Sk-67° 22 (O2 I^{*}/WN5), and the derived [N] lies roughly 1.9 dex above the LMC baseline abundance, larger than any of the values found in Chapter 5. In analogy, also its helium content is extreme, and both findings support the evolved nature indicated by its ‘slash’ designation.

Although the nitrogen content (in absolute numbers) of the few SMC sample members lies below that of most of our LMC stars, all of them are strongly enriched, by more than one dex above the SMC nitrogen baseline abundance¹⁸. The largest enrichment (by ~ 1.6 dex) was found for NGC 346-355, in agreement with its ‘ON’ designation. A very similar abundance, [N] = 7.92, together with similar stellar parameters, has been previously derived by both Bouret et al. (2003) and Heap et al. (2006) for this star, see Sect. 6.6.4.

6.7.2 Effective temperatures vs. spectral types

In Fig. 6.12, we display the derived effective temperatures as a function of spectral type for our present stellar sample (Table 6.4), augmented by all (LMC-) stars later than O4 from Chapter 5 to extend the sampling toward cooler types analyzed in a uniform way.

Because it was not possible to assign a specific spectral type to R136-040 (see above), this star is not contained in Fig. 6.12. We also discarded N11-031 (ON2 III(f*)) from this diagram, owing to severe problems in the determination of its T_{eff} . In Chapter 5 we were not able to derive a unique effective temperature from He I and all three nitrogen ionization stages in parallel, whilst using either He I/N III/N IV or N IV/N V resulted in a difference of $\Delta T_{\text{eff}} = 8 \text{ kK}$, which is too large to allow for

¹⁸According to Hunter et al. (2007), [N]_{baseline} = 6.5

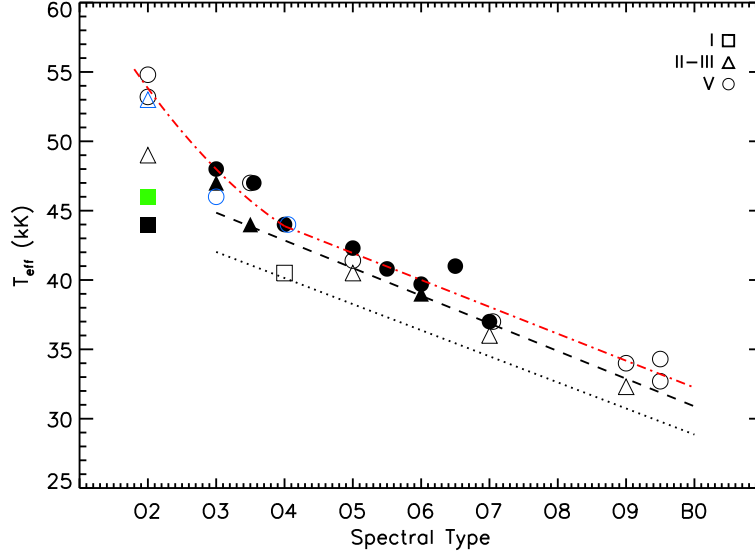


Figure 6.12: Effective temperatures as a function of spectral type, for LMC and SMC O-stars analyzed within this work and Chapter 5 (N11-031 and R136-040 discarded, see text). For NGC 346-355 (ON2 III(f^*), SMC), T_{eff} according to our ‘average’ solution, see text. Black symbols: LMC objects; blue symbols: SMC objects; green symbol: Sk-67° 22 (O2 If*/WN5, LMC). Squares refer to supergiants, triangles to (bright) giants, and circles to dwarfs. Filled symbols correspond to objects with $[N] \geq 8.0$, and open ones to objects with $[N] < 8.0$. The dashed-dotted (red) line displays a least square linear and quadratic fit to all dwarfs, according to Eq. 6.1. The T_{eff} calibration from Martins et al. (2005a) for Galactic O-dwarfs (dashed) and supergiants (dotted) is displayed for comparison. For clarity, some objects have been slightly shifted horizontally.

further conclusions. Nevertheless, our sample contains another ON2 giant, NGC 346-355 from the SMC. Also for this object, we were only able to obtain a hotter (based on N IV/N V) and a cooler (based on N III/N IV) solution, but the difference is much smaller, $\Delta T_{\text{eff}} = 4$ kK. In Fig. 6.12 we assigned a mean value, $T_{\text{eff}} = 53$ kK (accounting for larger errors than typical, on the order of 3 kK), to remain unbiased from a somewhat subjective view, but note that both the hot and the mean temperature are considerably higher than what we would have derived using just the He II/He I lines alone. Further comments on the ON2 stars are given at the end of this section.

To check the impact of $[N]$ on the T_{eff} estimates for a given spectral type, in Fig. 6.12 we denote objects with nitrogen abundances above and below $[N] = 8.0$ by filled and open symbols, respectively. This threshold has been chosen according to our findings from Chapter 5, roughly separating LMC objects with mild or typical enrichment from those with unexpectedly strong enrichment. We note that this value would be too high for SMC objects if one would be interested in displaying the actual enrichment,¹⁹ but for our purpose of testing and comparing the impact of $[N]$, only the absolute value

¹⁹Indeed, all SMC objects in Fig. 6.12 appear with open symbols, despite their strong enrichment. Because of the lower baseline abundance, a threshold of $[N] = 8.0$ corresponds to an enrichment of 1.5 dex, which is very unlikely to occur except for extreme objects such as NGC 346-355 located close to this value.

and not the enrichment is decisive (see Sect. 6.4.2).

The complete LMC sample considered in Fig. 6.12 covers 26 stars spread over (almost) the full range of spectral subtypes, comprising 16 dwarfs, 7 (bright) giants, and 3 supergiants. On the other hand, only three early SMC objects (two dwarfs and one giant) have been analyzed, preventing firm conclusions.

Before we concentrate on the earliest types, we highlight some general trends. From a first glance, and even though the number of supergiants and (bright) giants within our sample is lower than the number of dwarfs, it is obvious that T_{eff} increases with luminosity class for all spectral types, similar to Galactic conditions (e.g., Repolust et al. 2004; Martins et al. 2005a). At least for types later than O3.5, giants and supergiants are about 1 kK and 4 kK cooler than dwarfs, respectively. The latter difference is similar to what has been found in previous studies, e.g., by Mas05, Mokiem et al. (2007a), and Mas09. For the earliest types, on the other hand, this difference becomes much larger, about 10 kK at O2.

We can also clearly distinguish different behaviors of the spectral-type- T_{eff} relation. For luminosity classes V and II-III, later types follow a linear trend, whilst the increase in T_{eff} is much steeper for the earliest ones. On the other hand, the few early supergiants of our sample seem to follow a linear trend with a slope similar to cooler objects.

At least for the dwarfs, we are able to provide a *typical* relation, when ignoring any differences in Z and $[N]$. Using a linear and a quadratic least-square fit for the objects later/including and earlier than O4, respectively, we find

$$T_{\text{eff}} = \begin{cases} 51.64 - 1.94 \times ST & \text{if } ST \geq 4 \\ 70.87 - 10.29 \times ST + 0.88 \times ST^2 & \text{if } 2 \leq ST < 4, \end{cases} \quad (6.1)$$

where ST is the spectral type for O-dwarfs and T_{eff} is expressed in kK. At the present state of knowledge, this relation might be applied to LMC stars only, since the low number of analyzed SMC-dwarfs as well as other arguments (see Sect. 6.7.5) prohibit an application for stars from the SMC.

For comparison, we show in Fig.6.12 the observed spectral-type- T_{eff} relation for Galactic dwarfs (dashed) and supergiants (dotted) from Martins et al. (2005a). For the dwarfs, there is a typical offset of roughly 1 kK, whereas the (cooler) O2 and O4-supergiant seem to follow the Galactic calibration.

A similar comparison between their LMC sample and Galactic dwarfs was provided by Mokiem et al. (2007a), who found a somewhat larger offset by ~ 2 kK. This difference is caused by lower T_{eff} as resulting from the updated version of FASTWIND for later spectral types (see Chapter 5).

Reassuringly, the scatter in the spectral-type- T_{eff} relation for objects later than O4 is small (~ 1 kK), since the spectral types (as well as our primary T_{eff} indicator) rely on the He I/He II line strength (or EW) ratio, which is a rather monotonic function of T_{eff} for a given luminosity class (controlling gravity and wind-strength) and background abundance.²⁰ The only outlier is N11-065, an O6.5 dwarf. The analysis of this star was quite difficult, and for the determination of T_{eff} (and other parameters) we used also the N III/N IV ionization balance, in parallel with He I/He II. Nevertheless, we found considerable problems in fitting the emission at N III $\lambda\lambda 4634-4640-4642$ together with the pronounced absorption at N IV $\lambda 4058$ and the remaining nitrogen lines. Even though this problem became somewhat relaxed by allowing for wind-clumping, it seems that there was indeed a problem in the analysis of this star, and that it might be cooler.

Our sample includes two O4 dwarfs, one from the LMC (LH 81:W28-5) and the other from the SMC (AV 177). For these stars we derive similar T_{eff} and $\log g$, see Table 6.5, though the SMC star

²⁰All our cool objects are LMC stars.

(because of lower Z and weaker winds) should be hotter (e.g., Bouret et al. 2003; Heap et al. 2006, Mas04/05, Mokiem et al. 2006). Mas04/05, who came to the same general conclusion, found from a pure H/He analysis the same T_{eff} for AV177 (SMC), whilst they derived an even higher T_{eff} for LH 81:W28-5 (LMC). We note that the present spectrum of LH 81:W28-5 shows weak emission in N IV λ 4058 (Fig. C.26), so that the star might be alternatively classified as O3.5. Since also the derived gravities are quite low for lc V stars, the situation for both objects remains somewhat unclear, even though the derived parameters are fully consistent with the observed N IV and N III lines.

We concentrate now on the impact of different parameters such as $[N]$, Z , and \dot{M} , on the spectral-type- T_{eff} relation for the earliest O-types (O2-O3.5), for which the spectral classification depends majorly on the N IV/N III emission lines, whilst our T_{eff} diagnostics includes additional lines from those ions as well as from N V when visible. To allow for an easy understanding of the following, we summarize the results from our parameter study in Sect. 6.4: For a given emission line ratio (i.e., spectral type), the derived T_{eff} should increase with $[N]$ and $\log g$, and decrease with Z (at least for higher T_{eff} , see Fig. 6.6) and \dot{M} (more precisely, $\log Q$).

Thus, the general T_{eff} -difference between dwarfs, (bright) giants, and supergiants can be easily attributed to differences in $\log g$ and $\log Q$, which increase and decrease for increasing luminosity class, respectively. In this way, both effects add up, leading to $T_{\text{eff}}(\text{lc V}) > T_{\text{eff}}(\text{lc III}) > T_{\text{eff}}(\text{lc I})$, at least for comparable $[N]$ and Z . Regarding this general trend, a classification in terms of nitrogen (early O-types) and helium (late O-types) provides similar effects.

- For the two LMC O3.5 dwarfs (LH 81:W28-23 and LH 101:W3-24), we find the same T_{eff} , though $\log g$ differs by 0.2 dex. The effect produced by the larger $[N]$ of LH 81:W28-23 ($\Delta[N] \approx 0.6$ dex compared to LH 101:W3-24, implying a shift towards higher T_{eff}) is counteracted by both its denser wind and a lower $\log g$. Anyway, it is not clear whether LH 81:W28-23 is correctly designated as a dwarf. Indications of a giant nature are its low surface gravity ($\log g = 3.8$), the wind-strength, and the trace of a P-Cygni profile at He II λ 4686 (Fig C.24). If this would be the case, the inferred T_{eff} might be too high for this luminosity class when compared to the ‘other’ O3.5 giant, LH 90:ST 2-22.
- The two O3 dwarfs, N11-060 from the LMC and AV 435 from the SMC, show different T_{eff} . Astonishingly, the LMC star is hotter than the SMC one, by 3 kK, contrary to what might be expected. Here, the $[N]$ effect outweighs the corresponding one associated to Z ,²¹ whilst differences in $\log g$ and wind-strength compensate each other. We will come back to this finding and probable consequences in Sect. 6.7.5.
- The largest T_{eff} spread seen in our analysis occurs for the O2 stars, with T_{eff} ranging from 44 to 55 kK when accounting for all luminosity classes. Again, the more enriched of the two dwarfs (BI253 vs. BI237) is the hotter one, since the $[N]$ effect dominates over the larger wind-strength. For the two supergiants (Sk-67° 22 and LH 101:W3-19), we find a similar T_{eff} difference, consistent with our predictions for a combination of $[N]$ and $\log Q$. Interestingly, the effect from a lower $\log g$ (3.70 vs. 3.90), as seen for the O3 dwarfs, becomes inhibited by the extreme mass-loss. In Fig. 6.7, we noted that the N IV/N III emission line ratio begins to lose its sensitivity on $\log g$ at the ‘F’-series of our model-grid. The wind-densities of the two supergiants are even higher (roughly corresponding to ‘G’), and in this situation the surface

²¹In cooler stars, the He I/He II ionization balance used for classification is almost only affected by background abundance (less Z , less EUV line-blocking), see Repolust et al. (2004).

gravity does not play any role for determining the line ratio. Finally, the difference between two O2 giants (N11-026 from the LMC and NGC 346-355 from the SMC), $\Delta T_{\text{eff}} = 3$ kK with respect to the ‘average’ solution for NGC 346-355, is larger than expected, since all other parameters except for Z are quite similar, and the Z effect alone should amount to 1 kK (see Fig. 6.6). Note, however, that the errors in T_{eff} for both objects are larger than typical (≥ 3 kK), related to the problems we encountered for ON2 (III) stars.

The ON2 (III) stars. Let us point out already here that there seems to be a general, severe problem with the ON2 III class, as indicated from our results for N11-031 and NGC 346-355, and the inspection of LH 64-16 (see Sect. 6.6.1). This problem must relate to some unknown physical process allowing for the presence of strong N III, N IV and N V lines in combination with weak, but still visible He I. Having explored hundreds of models (both from our grid and additional, fine-tuned ones), varying the N abundances as well as other parameters, it turned out that these lines could not be synthesized in parallel. Moreover, we explored a variety of potential sources also from the CMFGEN side, manipulating the photosphere-wind transition zone, including wind-clumping with a variety of clumping laws, and near-photospheric X-rays,²² etc., and found that none of these would solve the problem. Insofar, we can be also sure that the problem is neither related to FASTWIND nor to our present nitrogen model atom.

Also the mass-discrepancy found for these objects underpins their problematic nature. Using the hotter solutions for N11-031 and NGC 346-355, we derived spectroscopic masses of 60 and 53 M_{\odot} , respectively. Evolutionary masses from non-rotating tracks by Charbonnel et al. (1993) and Schaerer et al. (1993)²³ yield 90-95 M_{\odot} for both stars. Note however that also for a cooler solution for NGC 346-355, at $T_{\text{eff}} = 49.5$ kK, already Mas05 stated quite a mass discrepancy, in this case 50 (spectroscopic) vs. 75 M_{\odot} (evolutionary). For another LMC ON2 III star, LH 64-16, not analyzed during the present work, Mas05 found an even larger discrepancy, 26 vs. 76 M_{\odot} . The authors suggested that the latter star might be the result of binary evolution, since it shows highly processed material at the surface, and since this star appeared to be located to the left of the ZAMS. This seems also to be the case for N11-031 (at least for the hot solution), but not for NGC 346-355. A similar problem was also found for some of the close binaries in the R136 cluster (Massey et al., 2002), supporting the idea that these stars suffered from binary interactions. An alternative to binarity might be quasi-homogeneous evolution, but the low $v \sin i$ values measured for our objects (on the order of 100 km s⁻¹) render this possibility as unlikely.

6.7.3 N IV/N III emission line ratio

To further test the significance of the Walborn et al. (2002) classification scheme, we investigated the relation between the N IV/N III emission line ratio and T_{eff} for our O2-O4 sample stars in a quantitative way, similar to previous work by Mas05, but using our updated parameters (see Sect. 6.6.5). Unlike Mas05 who used EW ratios, we employed the line-strength ratios to be consistent with the classification scheme. Later on, we also consider an alternative line ratio, N V λ 4603/N IV λ 6380 (hereafter N V/N IV), to check its potential for classification purposes, and to test whether this ratio might break potential degeneracies inherent to N IV/N III.

²²Which do not help because of the destruction of N III and He I, see Chapter 5

²³For the hottest stars, the inclusion of rotation has only a modest effect, resulting in ~ 10 % lower masses, e.g., Mas05, as long as the initial rotation is not high enough to induce quasi-homogeneous evolution.

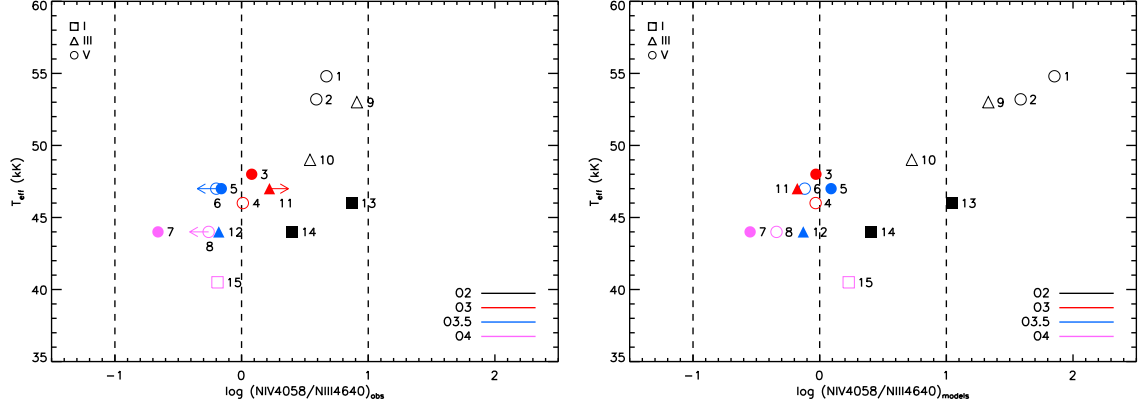


Figure 6.13: Effective temperatures as a function of $\log N\text{ IV}/N\text{ III}$, for O2-O4 sample stars. Spectral types distinguished according to legend. Left panel: observed emission line ratios, limits indicated by arrows; right panel: emission line ratios predicted from the (globally) best-fitting models. Objects numbered according to Table 6.6. Filling and symbols as in Fig. 6.12. Dashed vertical lines (at $\log N\text{ IV}/N\text{ III} = -1, 0, 1$) correspond to the limits used in Fig. 6.6. For object #9 (NGC 346-355), T_{eff} and theoretical line ratio according to our ‘average’ solution. Stars #4, #8, and #9 are SMC stars.

Table 6.6 lists the line ratios for our targets, as derived both from the observations and from the synthetic models associated to our best-fitting solutions. Again, we discarded N11-031 and R136-040 (see Sect. 6.7.2). Note that at the lower and upper end of the scheme the errors on the observed line ratios can become significant, due to noise and/or absence of $N\text{ IV}\lambda 4058$ or $N\text{ III}\lambda 4640$. In those cases, we provide corresponding lower or upper limits and their uncertainties. Typical errors are on the order of 0.1 to 0.2 dex.

Figure 6.13 displays the derived effective temperatures as a function of the observed (left panel) and ‘model’ (right panel) $N\text{ IV}/N\text{ III}$ line ratios, expressed logarithmically. Number designations for each object refer to Table 6.6. Different colors are used for each spectral type: O2 (black), O3 (red), O3.5 (blue), and O4 (purple). Symbols referring to luminosity classes and filling referring to [N] are as in Fig. 6.12.

If we examine the *observed* emission line ratio, we find quite a monotonic behavior, confirming its T_{eff} sensitivity, and similar trends as in the previous section. On the one hand, dwarfs and giants behave rather similar (though the giants seem to be a little cooler), except for the O2 types where the spread is larger. On the other, the observed relation for supergiants lies in parallel to the relation for dwarfs, but at considerably lower T_{eff} . As already pointed out, this is caused by the different gravities and wind-strengths. E.g., from Table 6.5 we find $\log Q$ values in the ranges $[-13.00, -12.53]$ for the LMC dwarfs, around -13.2 for the SMC dwarfs, $[-12.76, -12.36]$ for the giants, partly overlapping with the dwarfs, and $[-11.97, -11.60]$ for the supergiants.

The various spectral subtypes are located in quite different ranges (by definition, consistent with the Walborn et al. 2002 scheme): All O2 stars are located at $\log N\text{ IV}/N\text{ III} \geq 0.4$, and O3 dwarfs and O3.5 giants around $\log N\text{ IV}/N\text{ III} \sim 0$ ($N\text{ IV} \sim N\text{ III}$). Finally, one of the O4 dwarfs is located at $\log N\text{ IV}/N\text{ III} \approx -0.7$, for the other one (#8) we are only able to provide an upper limit, $\log N\text{ IV}/N\text{ III} \lesssim -0.3$, whilst the O4 supergiant (#15) lies close to the O3.5 border.

We see small [N] effects²⁴ on the line ratio, where a larger abundance tends to increase (but not necessarily) the emission line ratio within a given spectral subtype, in particular for the following pairs of stars: O3.5 dwarfs – LH 101:W3-24 (#6, upper limit) and LH 81:W28-23 (#5); O3 dwarfs – AV435 (#4, SMC) and N11-060 (#3); O2 dwarfs – BI237 (#2) and BI253 (#1); O2 supergiants – LH 101:W3-19 (#14) and Sk-67° 22 (#13). This effect seems to be absent in the pair of O4 dwarfs – AV177 (#8) and LH 81:W28-5 (#7), but note the quite large uncertainty in the the observed line ratio for the former object. Since, on the other hand, the emission line ratio should decrease for enhanced [N] when keeping all other parameters fixed, a consistent solution requires these objects to have a higher T_{eff} . For the pair of O4 dwarfs – AV177 (#8, SMC) and LH 81:W28-5 (#7), we note that the star with the higher abundance (#7) seems to have a lower emission line ratio,²⁵ but this is consistent with the *similar* T_{eff} of these stars.

Indeed, there are not only [N] effects, but also mass-loss effects on the emission line ratio. For all pairs considered above, the object with higher [N] has also a higher wind strength, $\log Q$ (cf. Table 6.5), which potentially counteracts the [N] effect. Comparing the differences in [N] with the differences in $\log Q$, it turns out that the [N] effect should dominate in all cases though.

Taken together, our findings explain the almost monotonic increase of T_{eff} with N IV/N III also within the individual spectral subtypes, and is consistent with the derived scatter of T_{eff} per subtype. Differences in background metallicity and wind-strength seem to play a secondary role, compared with the larger impact of [N].

If we now inspect the line ratios *predicted* by our best-fitting models (right panel), we mostly find quite similar values and trends. For the bulk of the stars there are only small shifts due to minor problems in properly fitting the lines (see Table 6.6 for particular comments on each star). However, more severe differences are present for BI237 (#1), BI253 (#2), and NGC 346-355 (#9, SMC). For the former O2 dwarfs, we predict too weak N III emission, thus overestimating the line ratio, but note that the *observed* emission is also rather weak for these stars. For NGC 346-355, the problem is different since we are not able to reproduce both lines using the ‘average’ solution (see Fig.C.34) displayed here.

We conclude that, for a given luminosity class, the effective temperatures are a rather monotonic function of $\log \text{N IV/N III}$, that the scatter within a spectral subtype is mostly due to abundance effects, and that our models are in fair agreement with the observed line-ratios, except for the hottest objects where we underestimate the observed (low) N III emission strength.

6.7.4 N V/N IV line ratio

Since both N IV λ 6380 and N V λ 4603 are absorption lines (i.e, less affected by complex formation processes), since they turned out to be quite reliable during our analyzes, and since N V λ 4603 is very T_{eff} sensitive (Sect. 6.5), we checked the corresponding line ratio as a potential diagnostic tool, which might be even used for future classification purposes.

From Fig. 6.14, we see that the relation T_{eff} vs. $\log \text{N V/N IV}$ is remarkably monotonic. By inspection of the *observed* line ratios (left panel), we find again two different trends, one for dwarfs and (bright) giants and another one for supergiants. The objects are basically grouped together within three regions: O2 stars with $\log (\text{N V/N IV})_{\text{obs}} > 0$, O3/O3.5 dwarfs and giants around $\log (\text{N V/N IV})_{\text{obs}} \approx -0.3 \dots 0$, and the O4 stars with $\log (\text{N V/N IV})_{\text{obs}} \lesssim -0.4$. The only discrepant object seems to be the

²⁴Slightly contaminated by mass-loss effects, see below.

²⁵But note also the quite large uncertainty for object #8.

Table 6.6: Observed and predicted line-strength ratios for N IV/N III and N V/N IV, for the O2-O4 stars analyzed within this work. Observed ratios (or limits) inclusive errors. Numbers refer to Figs. 6.13 and 6.14. Errors in brackets provide uncertainties of lower or upper limits. Predicted line ratios ('model') drawn from best-fitting synthetic spectra. N11-031 and R136-040 discarded, see text.

Star	#	ST	T_{eff} (kK)	$\log(\frac{\text{NIV}}{\text{NIII}})$ obs	$\log(\frac{\text{NIV}}{\text{NIII}})$ model	$\log(\frac{\text{NV}}{\text{NIV}})$ obs	$\log(\frac{\text{NV}}{\text{NIV}})$ model	Comments
BI253	1	O2 V((f*))	54.8	0.67 \pm 0.15	1.85	0.53 \pm 0.23	0.43	N III λ 4640 and N IV λ 4058 underpredicted ^a
BI237	2	O2 V((f*))	53.2	0.59 \pm 0.14	1.58	0.36 \pm 0.14	0.21	N III λ 4640 underpredicted ^a
N11-060	3	O3 V((f*))	48.0	0.08 \pm 0.02	-0.03	-0.07 \pm 0.03	-0.30	N IV λ 4058 and N V λ 4603 underpredicted ^{a,b}
AV 435	4	O3 V((f*))	46.0	0.01 \pm 0.18	-0.03	< -0.30 (+0.10)	-0.46	N V λ 4603 diluted in noise
LH 81:W28-23	5	O3.5 V((f+))	47.0	-0.16 \pm 0.04	0.09	-0.01 \pm 0.05	-0.18	N III λ 4640 underpredicted
LH 101:W3-24	6	O3.5 V((f+))	47.0	< -0.20 (+0.12)	-0.12	< -0.28 (+0.14)	-0.38	N III λ 4640 underpredicted
LH 81:W28-5	7	O4 V((f+))	44.0	-0.66 \pm 0.10	-0.55	-0.53 \pm 0.13	-0.60	Satisfactory fits
AV 177	8	O4 V((f))	44.0	< -0.26 (+0.13)	-0.34	< -0.36 (+0.09)	-0.57	Only N III λ 4640 and N IV λ 6380 visible
NGC 346-355	9	ON2 III(f*)	53.0	0.91 \pm 0.09	1.33	0.19 \pm 0.04	0.21	N III λ 4640, N IV λ 4058, N V λ 4603 underpred. ^c
N11-026	10	O2 III(f*)	49.0	0.54 \pm 0.06	0.73	0.14 \pm 0.02	-0.08	N III λ 4640, N IV λ 4058, N V λ 4603 underpred. ^{a,b}
R136-018	11	O3 III(f*)	47.0	> +0.22 (-0.21)	-0.18	> -0.20 (-0.13)	-0.32	N III λ 4640 and N IV λ 4058 underpredicted
LH 90:ST 2-22	12	O3.5 III(f+)	44.0	-0.18 \pm 0.06	-0.13	-0.20 \pm 0.04	-0.39	Satisfactory fits
Sk-67° 22	13	O2 If*/WN5	46.0	0.87 \pm 0.14	1.04	0.35 \pm 0.03	0.31	N V λ 4603 under, N IV λ 4058 overpredicted
LH 101:W3-19	14	O2 If*	44.0	0.40 \pm 0.07	0.41	0.05 \pm 0.14	0.00	N V λ 4603 overpredicted
Sk-65° 47	15	O4 If	40.5	-0.19 \pm 0.12	0.23	< -0.38 (+0.08)	-0.52	N IV λ 4058 overpredicted

^aFor fits, see Chapter 5 and Appendix C.1; ^bCompromise solution, see Chapter 5; ^c'Average' solution.

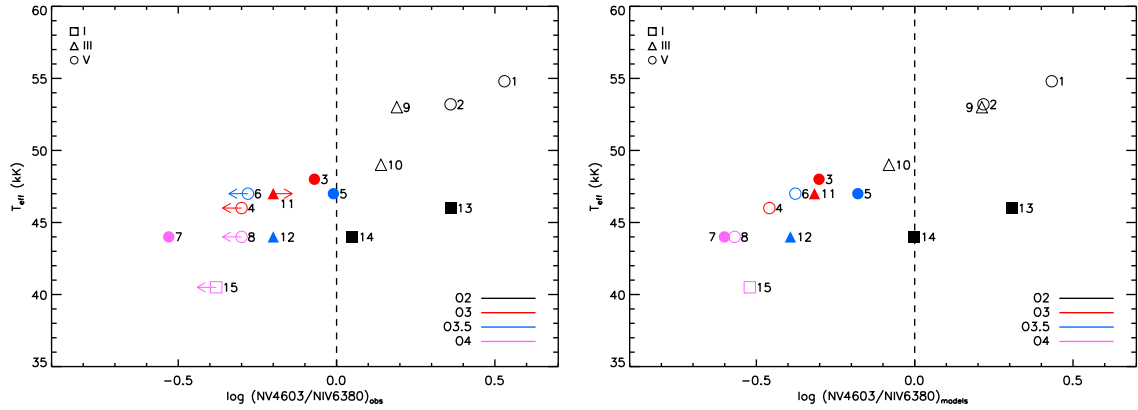


Figure 6.14: As Fig. 6.13, but for the $N\text{v}\lambda 4603/N\text{IV}\lambda 6380$ line ratio.

SMC O3-dwarf AV 435 (#4), which appears at the edge of the O4-region. However, this ‘erroneous’ position could be tracked down to a considerable error in the measured line ratio, because of very weak N v lines diluted in the continuum (Fig. C.32).

Compared to the N IV/N III emission line ratio, there seems to be a clearer separation between the different subtypes, e.g., Sk-65° 47 (#15) is located closer to the remaining O4 objects, whilst regarding N IV/N III it is closer to the O3 V/O3.5 III group. Moreover, there is a clear separation between the two O2 dwarfs (#1,2) and the ON2 giant (#9, SMC) because of weaker N IV $\lambda 6380$.

Comparing now with the *predicted* line ratios (right panel), we see that predicted and observed ones agree quite well *over the complete range*. Still, there are certain shifts because of a non-perfect representation by our synthetic lines (Table 6.6), but interestingly we do no longer find the extreme differences for BI237, BI253, and NGC 346-355 as present in the N IV/N III diagram, which indicates that we are able to obtain a satisfactory representation of the N IV/N V ionization balance. So far, we cannot comment on any [N] related bias, since we did not perform corresponding theoretical studies. In case the N V/N IV line ratio might be used in future classification schemes, this will become certainly necessary.

The monotonic behavior of the N V/N IV line ratio illuminates its promising potential, particularly for the hottest objects (O2), simply because there is more N v than N III present at these temperatures. We suggest to investigate this possibility when larger samples become available.

6.7.5 Caveats for low-metallicity stars

Summarizing our findings, we conclude that already the present Walborn et al. (2002) classification scheme allows for a reasonable relation between spectral type and effective temperature, *as long as it is possible to discriminate the luminosity class*. The only significant bias in the scheme might be produced by nitrogen abundance effects (or *extreme* variations in wind strength). E.g., if the nitrogen abundance is not the same in an O3 III and an O3.5 III star, then the O3 III star is not necessarily hotter than the O3.5 III.

However, there are also important caveats regarding low-metallicity (e.g., SMC) stars. As it is well-known, effective temperatures increase with decreasing Z for a given spectral type if the classification is based on the helium ionization balance, i.e., the He I/He II line-strength ratio (O4-O9.7 stars,

e.g., Bouret et al. 2003, Mas04/05, Heap et al. 2006, Mokiem et al. 2006, 2007b). According to our predictions, this no longer needs to be true for the earliest O-stars classified by means of nitrogen.

- (i) *O2/O3 stars.* Though for similar [N] a lower metallicity implies a higher T_{eff} (at least for spectral types O3(dwarfs)/O3.5(giants and supergiants) and earlier, see Fig. 6.6), this effect might be counteracted by a different nitrogen content if we assume typical (maximum) enrichments, of roughly +0.6, +0.9, and +1.0 dex above the corresponding MW, LMC, and SMC baseline abundance, as predicted by Brott et al. (2011a) for a $40 M_{\odot}$ star at an initial rotation of 270 km s^{-1} . As visible from Fig. 6.8, for an O3 dwarf with $\log g = 4.0$ dex, our predictions indicate $T_{\text{eff}} \approx 47\text{--}48 \text{ kK}$ for the Galaxy and $T_{\text{eff}} \approx 46 \text{ kK}$ for the LMC/SMC.²⁶ Such cooler or at least similar T_{eff} for stars in a lower Z environment should be present only for typical nitrogen abundances; objects with a considerably different enrichment will contribute to enlarging the spread.
- (ii) *O3.5/O4 stars.* In view of the results from Sect. 6.4.2, there might be an additional problem around O3.5/O4. From Fig. 6.6, SMC stars should be *cooler* than corresponding LMC ones, even at a similar [N], for a line ratio around $\text{N IV}/\text{N III} = 0.1$ (which represents a lower limit for O3.5 V and O4 I/III). Since the SpT- T_{eff} relation is rather monotonic for LMC stars at *all* spectral types, derived either by helium or nitrogen (see Fig. 6.12), the corresponding relation for SMC stars might be not monotonically connected between these two regime: Even though there seems to be a monotonic relation between $\text{N IV}/\text{N III}$ and T_{eff} on the hot side, the potential ‘jump’ would be caused by the fact that the SMC SpT- T_{eff} relation on the cooler side (based on He I/He II) lies above the LMC relation.

To confirm or disprove these predictions and caveats, a thorough analysis of a large sample of SMC stars is certainly required, given the few SMC objects investigated so far.

6.7.6 SMC Of-stars

The luminosity criteria for O-type stars are based primarily on their ‘Of’ characteristics; i.e., the strength of the N III triplet and the He II $\lambda 4686$ emission.²⁷ As already emphasized by Mas04/05/09, this can lead to significant problems with luminosity classification of O-stars found in low metallicity environments, such as the SMC.

The problem is that the emission strengths of the Of features are tied to mass-loss rates (both for He II and N III), which in turn scale with metallicity, and to (average) nitrogen abundances (for N III).²⁸ One thus expects a star in the SMC to show weaker Of-characteristics for the same physical properties than would a similar star in the Milky Way. As demonstrated in Sect. 6.3.1, in particular the N III emission strength of the SMC star should be lower, unless the nitrogen abundances of the two objects were similar, which would mean the rare case of an *extreme* enrichment of the SMC star.

Throughout their studies of Magellanic Cloud O-type stars, and particularly those in the SMC, Mas04/05/09 found numerous examples where the Of-type properties indeed were weaker than would be expected given the absolute magnitude of those stars²⁹. We can demonstrate the weakness of Of-

²⁶See also Fig. 6.12, where the SMC O3 dwarf AV 435 indeed is cooler than the corresponding LMC objects.

²⁷These emission features were linked with luminosity for Galactic stars (see, for example, Walborn 1972), a refinement over the luminosity criteria proposed by Conti & Alschuler (1971) based primarily on the Si IV $\lambda 4089$ to He I $\lambda 4143$ ratio.

²⁸Counteracting the increase of N III emission because of less blocking in a low Z environment.

²⁹The alternative explanation that all such discrepant stars were too bright owing to their being binaries was contradicted by the excellent fits obtained to the spectral features; this would require both components of a binary to be of identical spectral subtype and brightness.

features statistically as follows. If we restrict ourselves to the SMC O-type stars with spectral subtypes determined from slit spectroscopy (Table 6 of Massey 2002) we find 74 stars, only 5 (7%) have ‘f’ type designations. Similarly, of the 83 O-type stars listed by Evans & Howarth (2008), only 7 (8%) have any ‘f’ designation, and all of these are either ‘(f)’ or ‘((f))’ indicating that He II λ 4686 is weakly in emission or in absorption. In contrast, Of-characteristics abound among O-type stars in the Milky Way. Of the 378 Galactic O-type stars catalogued by Maíz-Apellániz et al. (2004), 160 (42%) display Of-characteristics. Since Of-type stars are brighter than non-Of stars (at least in the Milky Way), this may overestimate the true percentage. If we instead restrict ourselves just to the sample of 24 O-type stars with well-established distances by HIPPARCOS (Maíz-Apellániz et al. 2004 Table 7) we find that 7 (29%) have Of-characteristics.

Thus we conclude that there are strong indications for a significantly lower percentage of SMC Of-stars, compared to Galactic ones, which we attribute to the effects outlined in Sect. 6.3.1. Remember, however, that a lower wind-strength alone is not sufficient to explain this finding (Fig. 6.2, upper panel), but that a lower average nitrogen content needs to be present as well.

6.8 Summary and conclusions

We investigated open questions raised by our previous studies on the formation of N III λ 4640 and N IV λ 4058. We provided first theoretical predictions for the N IV/N III emission line ratio, and confronted these predictions with observational findings, concentrating on a sample of early-type O-stars. The results of this work can be summarized as follows.

1. The emission strength of the N III triplet from objects with similar T_{eff} and $\log g$ depends on their metallicity, associated mass-loss, and nitrogen content. Whilst even under SMC conditions lower mass-loss rates alone are not able to compensate the increase in emission for decreasing Z , a lower [N], coupled to a significantly lower base-line abundance, can easily outweigh the Z effect and lead to overall lower emission strengths. This might explain the relatively low number of SMC ‘Of’ stars.
2. Our models predict an only weak Z -dependence of N IV λ 4058 (contrasted to the N III triplet). SMC-abundance models with $T_{\text{eff}} \leq 45$ kK display slightly more emission than their Galactic counterparts, and vice versa for hotter temperatures. Much stronger is the impact of wind-strength though.
3. It turned out that N IV λ 4058 behaves quite unexpectedly when [N] is increased in low- \dot{M} models. For almost the whole temperature range, we either obtain more absorption or less emission, compared to models with a lower nitrogen content. For a specific temperature range, N IV λ 4058 can even switch from emission to absorption when increasing [N]. For Galactic stars at $44 \text{ kK} \leq T_{\text{eff}} \leq 50 \text{ kK}$ and comparatively low \dot{M} , our models imply that if N IV λ 4058 is observed in absorption, this would indicate a strong nitrogen enrichment.
4. We provided first theoretical predictions on the N IV/N III emission line ratio, as a function of Z , $\log Q$, and [N], by studying line-ratio iso-contours in the $T_{\text{eff}}\text{-}\log g$ plane. For an emission line ratio of unity (i.e., a spectral type of O3.5 I/III or O3 V), the corresponding T_{eff} increases with [N] (~ 1 kK per increment of 0.2 dex in [N]) and $\log g$ (~ 1 kK per increment of 0.1 dex in $\log g$). In addition, it should decrease with Z , at least for higher T_{eff} ($\sim 2\text{-}3$ kK difference between SMC and MW objects), and $\log Q$ ($\sim 2\text{-}4.5$ kK between low- and high- \dot{M} models).

5. We performed a comparison with results from the alternative model atmosphere code CMFGEN, for a small grid of early O-type dwarfs and supergiants. Our basic predictions regarding the impact of [N] on (i) N IV λ 4058 for low- \dot{M} models (see item 3), and (ii) on the N IV/N III emission line ratio (see item 4) were confirmed by corresponding CMFGEN results.

Regarding specific line predictions, we found a mostly satisfactory agreement, except for some systematic deviations: For early O-stars, FASTWIND produces more emission at the N III triplet, less emission at N IV λ 4058, and mostly much more absorption at N IV λ 6380. This would lead to lower T_{eff} and quite different [N] in analyses performed by means of CMFGEN, if concentrating on the N III triplet and N IV λ 4058 alone. Fortunately, the remarkably good agreement of the H/He lines in both codes enables an identification of potential problems regarding the nitrogen lines, as long as the helium ionization balance is used to constrain T_{eff} . In the hot O-star domain, the latter approach is no longer feasible because of vanishing He I. Nevertheless, potential problems should become obvious also here when relying on the N v λ 4603-4619 doublet, which turned out to be very sensitive on T_{eff} as well as code-independent.

6. We confronted our theoretical predictions with results from an analysis of a medium-size sample of LMC/SMC O-stars, drawn from studies by Massey et al. (early types), and from Chapter 5. The basic difference to the Massey et al. analyses is found in the procedure for deriving T_{eff} , where we used the nitrogen ionization balance in the hotter T_{eff} regime instead of the helium one, to avoid any degeneracy. For the cooler objects of our sample ($T_{\text{eff}} \leq 44$ kK) we mainly relied, when possible, on helium, using nitrogen as a consistency check. For these stars we found similar or slightly cooler T_{eff} compared to Massey et al.. Considerably hotter T_{eff} , on the other hand, were inferred for the earliest O-stars, by means of the nitrogen diagnostics. Nevertheless, in most cases the corresponding synthetic He II/He I lines were still consistent with the observations, or indicated only slightly lower temperatures. Notable exceptions are the ON2 III stars (see below). The nitrogen abundances derived within our analysis are consistent with our results from Chapter 5: again, the bulk of the stars displays a considerable enrichment.
7. By inspecting the inferred effective temperatures, we saw that T_{eff} increases with luminosity class for all spectral types, consistent with earlier results. For spectral types later than O3.5 (down to O9.5), LMC giants are cooler by ~ 1 kK, and supergiants are cooler by ~ 4 kK, compared to dwarfs. For types earlier than O3.5, this difference (and also the scatter) becomes larger, amounting to ~ 10 kK at O2 when comparing supergiants and dwarfs. For LMC dwarfs and giants later than O3.5, and for all LMC supergiants, we found linear relations between T_{eff} and spectral type, again consistent with previous work. The earliest dwarfs and giants, on the other hand, display a much steeper increase in T_{eff} . The dominating effect responsible for the scatter in the SpT- T_{eff} relation at earliest types was attributed to difference in [N], where for a given spectral type more enriched objects are typically hotter.
8. The relation between the observed N IV/N III emission line ratio and T_{eff} turned out to be quite monotonic, if discriminating for luminosity class. Because of the high T_{eff} derived for the earliest stars by means of the nitrogen ionization balance, we did not find the pronounced degeneracy of the N IV/N III emission line ratio as claimed by Mas05. The scatter found within a spectral subtype is, again, primarily produced by abundance effects. Our model predictions are in fair agreement with the observed line-ratios, except for the hottest objects where we underestimate the observed (low) N III emission-strength.

9. We provided first insights into the relation between T_{eff} and the $\text{N V } \lambda 4603\text{-}4619/\text{N IV } \lambda 6380$ absorption line ratio, which is remarkably monotonic, particularly for the hottest objects in our sample, and we highlighted the promising potential of this line ratio for future classification schemes.

Both our theoretical predictions and our observational analysis suggest that the Walborn et al. (2002) classification scheme is able to provide a meaningful relation between spectral type and effective temperature. In particular, and as one might have expected, the $\text{N IV}/\text{N III}$ emission line ratio changes with effective temperature, all other factors being equal. However, this ratio is also sensitive to surface gravity, mass-loss rate, and to nitrogen abundance, which are expected to vary among a sample of stars. Thus, the significance of the classification scheme (within the uncertainties caused by nitrogen abundance) might be only warranted as long as it is possible to fairly discriminate the luminosity class (as a proxy to gravity), and as long as there is a strong correlation between spectral type/luminosity class and wind-strength. If, e.g., there would be weak-winded stars (Marcolino et al. 2009; Najarro et al. 2011 and references therein) also in the early O-type regime and not only at later spectral types, the monotonicity with respect to T_{eff} might become severely disturbed.

A clear identification of early O-type luminosity classes from spectral morphology alone becomes difficult in low- Z environments such as the SMC. We emphasize the same point as made by Mas04/05/09, that the standard luminosity classification criterion, primarily based on the morphology of $\text{He II } \lambda 4686$, is significantly biased on mass-loss rates. Owing to lower wind-strengths for SMC conditions, $\text{He II } \lambda 4686$ is typically in absorption not only for Ic V , but also for lower gravity objects which under Galactic conditions would correspond to Ic I/III . Thus, there are O-type stars in the SMC whose physical properties (visual luminosities and surface gravities) might be in accord with them being giants or supergiants whereas their spectroscopically determined luminosity classes may be dwarfs or giants, respectively. To circumvent this caveat, other information, such as the absolute visual magnitude of the system, may have to be appealed to. Without such additional information, an appropriate classification may rest on a more precise determination of the surface gravity, e.g., using a visual inspection of the wings of H_γ . Another possibility is to extend the classification scheme by including the strength of H_α (which needs to be carefully calibrated, since also this wind-line remains in absorption).

Our study also implies important consequences which need to be validated or investigated in future work:

- (i) The $\text{SpT-}T_{\text{eff}}$ scale constrained from our LMC sample turned out to be, for a given luminosity class, more or less monotonic. However, the majority of the analyzed objects displayed a considerable nitrogen enrichment. To quantify the actual impact of nitrogen abundance would require the analysis of a significant number of un- or mildly enriched earliest MW/LMC objects³⁰ that according to our predictions should be cooler than the enriched ones.
- (ii) Typical SMC stars of earliest spectral types might have effective temperatures below corresponding LMC objects, and the overall $\text{SpT-}T_{\text{eff}}$ relation for SMC stars might be non-monotonic around O3.5/O4.

³⁰For SMC objects, the nitrogen baseline abundance is too low to allow for a clear-cut classification and spectroscopic analysis by nitrogen lines, at least in the optical. This was already a problem for unenriched LMC stars, e.g., R136-040, and the similar objects R136-033 and R136-055.

- (iii) Our predictions suggest that there should be (enriched) Galactic O4 dwarfs with emission at $\text{N III}\lambda 4640$ and absorption at $\text{N IV}\lambda 4058$ (item 3 from above). So far, the Walborn et al. (2002) classification scheme only states that $\text{N IV}\lambda 4058$ should be absent for such objects. A quick inspection of the IACOB database of Galactic OB stars (Simón-Díaz et al., 2011) allowed us to find a first indication of this effect, for HD 46223 (O4 V((f))), and we were able to reproduce its strong emission at $\text{N III}\lambda 4640$ together with a pronounced absorption at $\text{N IV}\lambda 4058$, for a considerable nitrogen enrichment.
- (iv) As became apparent throughout this work (first indications were already found in Chapter 5), we encountered severe problems for ON2 III stars. For these objects, we were not able to find a simultaneous fit of the pronounced $\text{N III}/\text{N IV}/\text{N V}$ lines and the weak, but still clearly present $\text{He I}\lambda 4471$, independent whether we used FASTWIND or CMFGEN. Though we were able to derive a cooler (fitting $\text{N III}/\text{N IV}$ and He I) and a hotter solution (fitting $\text{N IV}/\text{N V}$), we were not able to favor one of those. In some cases, the T_{eff} difference between the hotter and the cooler solution is extreme, e.g., for N11-031 analyzed in Chapter 5. Because of the restricted quality of our present dataset, new observations with higher S/N and higher resolution would be extremely valuable to verify our results using the nitrogen ionization balance and/or the pure $\text{He II}/\text{He I}$ results from Massey et al. when He I (and N III) become extremely weak.

Future work is certainly needed to address the aforementioned issues. Upcoming analyses of extensive O-star samples, e.g., from the VLT-FLAMES Tarantula survey and the IACOB data base, will be fundamental for trying to explain these open questions.

Chapter 7

Summary and outlook

7.1 Summary

The main long-term goal of the project started with this thesis is aimed at improving our knowledge about O-stars, and, in particular, about their earliest spectral types. This topic has received particular interest during the past years from research focused on deriving empirical upper limits for stellar masses. This has become clear from the variety of press releases related to the investigations by Crowther et al. (2010), who claimed an ‘universal’ upper mass cut-off around $300 M_{\odot}$, exceeding the widely accepted $150 M_{\odot}$ limit (e.g., Oey & Clarke 2005; Figer 2005).

In this respect, nitrogen is a key element. First, this element is the best tracer for testing the implementation and effects of rotational mixing in massive stellar models, allowing us to further constrain the stellar evolution of massive stars. Next, nitrogen presents a promising potential for deriving effective temperatures in the very *early* O-star regime. Finally, emission lines of high-ionization stages of nitrogen have been used for spectroscopically discriminating the earliest O-stars. To provide more insight into this matter, we started a project with the objective to enable *quantitative nitrogen spectroscopy* in O-type stars.

After developing an accurate nitrogen model atom, well-suited to perform an extensive analysis regarding the formation mechanism of emission in strategic nitrogen lines such as N III λ 4634-4640-4642 and N IV λ 4058, we were able to better constrain observed stellar properties in the early O-star regime, in particular the effective temperatures. In addition, we were able to increase the so far scarce number of nitrogen abundance determinations for O-stars. Finally, we confirmed the potential of nitrogen spectroscopy as a tool for constraining massive star evolution, in particular with respect to rotational mixing.

In the following, we summarize our most important results and conclusions achieved within this study.

Implementation of a nitrogen model atom into FASTWIND

We developed a new nitrogen model atom (partly based on older work), comprising the ionization stages N II to N V. In order to synthesize the corresponding spectra, we implemented this model atom into the atmospheric code FASTWIND. Moreover, we incorporated the dielectronic recombination mechanism into FASTWIND, which was previously unable to deal with this process. Two different

ways to treat dielectronic recombination were successfully tested, showing a fair agreement when consistent atomic data were used.

Line formation mechanism of strategic nitrogen emission lines

An investigation regarding the line-formation process of strategic nitrogen emission lines such as N III λ 4634-4640-4642 and N IV λ 4058 was performed during this study.

- **N III λ 4634-4640-4642**

We suggested a (basic) mechanism for the formation of the N III emission lines in O-star spectra when a more realistic physical scenario is considered than present in the seminal work by Mihalas & Hummer (1973), i.e., a complete treatment of line blocking/blanketing and the consideration of the presence of a wind. Unlike the results from Mihalas & Hummer, it turned out that, under Galactic conditions, dielectronic recombination plays only a secondary role, both for O-stars with ‘compact’ and with ‘extended’ atmospheres. The key aspect is now played by the stellar wind (Swings mechanism), as long as the wind-strength is large enough to enable a significantly accelerating velocity field already in the photospheric formation region of the resonance line connected to the upper level of the involved transition. Actually, the strength of the emission might be also affected by an additional O III resonance line overlapping with the N III resonance line.

Our study implied that the efficiency of the ‘two electron’ drain - which depopulates the lower level of the N III triplet transition(s) - is strongly dependent on the EUV line-blocking, i.e., on Z . Consequently, the emission might become enhanced in metal-poor environments, due to less EUV line-blocking. On the other hand, for low- Z environments also the wind-strengths and the base-line nitrogen abundance become lower, counteracting the Z effect. It turned out that under SMC conditions lower mass-loss rates alone are not able to compensate the increase in emission for decreasing Z . Instead, a lower nitrogen abundance can outweigh the Z effect and lead to overall lower emission strengths. We suggested this effect as the explanation for the relatively low number of SMC ‘Of’ stars.

- **N IV λ 4058**

A rather similar mechanism has been suggested for the formation of emission at N IV λ 4058. The dominating process is the strong depopulation of the lower level by the ‘two-electron’ transitions, taking (mostly) place in photospheric regions. This drain increases as a function of \dot{M} because of increasing ionizing fluxes, via the coupled ground state. Contrasted to the N III triplet emission, resonance lines do not usually play a role for typical O-star mass-loss rates and below. However, at higher T_{eff} and \dot{M} , the resonance line connected with the lower level of N IV λ 4058 leaves detailed balance and the level becomes pumped instead of being depopulated. This effect is stronger at low Z , owing to higher EUV-fluxes. Thus, less emission is produced compared to Galactic conditions.

Comparison against the alternative atmospheric code CMFGEN

In order to check our new nitrogen model atom and the predictive power of FASTWIND, we performed first comparisons with results from the atmospheric code CMFGEN, for a small grid of O-type dwarfs

and supergiants. For this objective we used a set of important nitrogen lines in the blue part of the visual spectrum. The overall agreement between both codes is mostly satisfactory.

Within the range of $30,000 \text{ K} \leq T_{\text{eff}} \leq 35,000 \text{ K}$, however, some major discrepancies have been found regarding the behavior of N III $\lambda\lambda 4634\text{-}4640\text{-}4642$ in both codes. CMFGEN triggers the emission at N III $\lambda\lambda 4634\text{-}4640\text{-}4642$ at cooler temperatures than (present) predictions from FASTWIND. This effect could be traced down to the overlap of the N III resonance line with a resonance line from O III. Thus, not only the N III resonance line itself is responsible for the triplet emission, but also an overlapping O III resonance line, at least at later O-types. We have shown that the impact of the oxygen abundance on the strength of the emission at N III $\lambda\lambda 4634\text{-}4640\text{-}4642$ remains rather unimportant. Fortunately, the contamination of the other optical nitrogen lines by this process remains weak, so that these lines can be used already now, and the nitrogen abundance determination by FASTWIND is not hindered.

In addition to this discrepancy, FASTWIND produces more emission at the N III triplet and less emission at N IV $\lambda 4058$ than CMFGEN in *early* O-star models. Therefore, CMFGEN analyses using these strategic nitrogen lines alone would lead to lower T_{eff} and quite different nitrogen abundances. Fortunately, the remarkably good agreement of the H/He lines in both codes enables an identification of potential problems regarding the nitrogen lines, as long as the helium ionization balance is used to constrain T_{eff} . In the hot O-star domain, the latter approach is no longer feasible because of vanishing He I. Nevertheless, the N V $\lambda\lambda 4603\text{-}4619$ doublet, which turned out to be very sensitive on T_{eff} as well as code-independent, might be helpful to spot potential problems with both the N III triplet and N IV $\lambda 4058$.

Surface nitrogen abundances for O-stars in the Large Magellanic Cloud

We determined the nitrogen abundances of a sample of 25 LMC O- and early B-stars, which had been previously analyzed by Mokiem et al. (2007b) by means of H/He spectroscopy alone. In addition, we performed a first comparison with corresponding predictions from stellar evolution including rotational mixing.

- **Nitrogen spectroscopy of a sample of LMC stars**

We re-determined the stellar and wind parameters of the sample stars, exploiting the He and the N ionization balance in parallel, to avoid any possible degeneracy. Besides, we also derived the projected rotational velocities, $v \sin i$, in a first, separate step. In addition to systematically lower $v \sin i$, we also inferred mostly lower T_{eff} , but the differences to Mokiem et al. were generally small except for few objects, provided that the fits to He I/He II were still consistent. Overall, we found no problems in fitting the nitrogen lines, reproducing the 'f' features quite well. Only for some of the hotter objects, where lines from all three stages, N III, N IV and N V, are visible, we needed to aim at a compromise solution. Only for one star, we found considerable problems to reproduce the nitrogen lines. We provide further comments on this and other ON2 III stars in Sect. 7.2.

The majority of the O-stars analyzed were found to be strongly enriched. Five objects indicated an extreme enrichment, up to $[\text{N}] = 8.5$, whilst only three objects showed almost no enrichment. Moreover, we found a fairly good correlation between the derived nitrogen and helium surface abundances.

- **Comparison with results from stellar population synthesis**

We compared the derived nitrogen abundances as a function of $v \sin i$ with results from stellar population synthesis. We found a significant number of highly enriched, low $v \sin i$ objects, which should not exist according to population synthesis. The detection of strong nitrogen enrichment in the bulk of O-stars might indicate that efficient mixing takes place already during the very early phases of stellar evolution of LMC O-stars.

The earliest O-stars

We provided first theoretical predictions on the N IV/N III emission line ratio, which has been used during the past years in a variety of studies to spectroscopically classify early O-type stars. We confronted our theoretical predictions with results from an analysis of a sample of LMC/SMC O-stars.

- **Theoretical predictions on the N IV/N III emission line ratio**

We presented first theoretical predictions on the N IV/N III emission line ratio, as a function of different parameters, such as metallicity, wind-strength, and nitrogen abundance. Though it turned out that there is indeed a monotonic relationship between the N IV/N III emission line ratio and the effective temperature, all other parameters being equal, our predictions indicate additional dependencies on other stellar parameters, most notably, the nitrogen abundance. Therefore, our results suggest that the Walborn et al. (2002) classification scheme might be mainly biased by nitrogen content, provided that there is an almost unique relation between spectral type/luminosity class and wind-density. In addition, we found that for a given line ratio (i.e., spectral type), more enriched objects should typically have hotter T_{eff} . These basic predictions were confirmed by results from the atmospheric code CMFGEN.

- **Analysis of a sample of LMC/SMC early-type O-stars**

We confronted our theoretical predictions with results from the analysis of a medium-size sample of LMC/SMC O-stars, drawn from studies by Massey et al. (2004, 2005, 2009), and from our previous analyses of a LMC sample. The basic difference to the original Massey et al. analyses is rooted in our procedure for deriving T_{eff} , where we used the nitrogen ionization balance in the hotter T_{eff} regime instead of the helium one, to avoid any degeneracy. In comparison to the results by Massey et al., the additional nitrogen diagnostics allowed us to infer considerably hotter T_{eff} for the earliest O-stars. Nevertheless, in most cases the corresponding synthetic He II/He I lines were still consistent with the observations, or indicated only slightly lower temperatures.

The nitrogen abundances derived within our analysis were consistent with our previous results, displaying a considerable enrichment for the bulk of the analyzed stars, stronger than expected from tailored evolutionary calculations.

Consistent with earlier results from H/He analyses, the derived effective temperatures increase from supergiants to dwarfs for all spectral types in the LMC. The relation between the *observed* N IV/N III emission line ratio and the effective temperature, for a given luminosity class, turned out to be quite monotonic for our stellar sample, and to be fairly consistent with our model predictions. We found that the scatter within a spectral sub-type is mainly produced by abundance effects.

In addition, we provided first insights into the relation between T_{eff} and the $\text{N V } \lambda\lambda 4603\text{-}4619/\text{N IV } \lambda 6380$ absorption line ratio, which turned out to be remarkably monotonic, particularly for the hottest objects in our sample, and we highlighted the promising potential of this line ratio for future classification schemes.

Following both our theoretical predictions and our observational analysis, we suggest that the Walborn et al. (2002) classification scheme is indeed able to provide a meaningful relation between spectral type and effective temperature. In particular, we have shown that the $\text{N IV}/\text{N III}$ emission line ratio increases monotonically with effective temperature, all other parameters being equal. However, it turned out that this ratio is also rather sensitive to other important stellar parameters, such as the surface gravity, mass-loss rate, and *especially* to nitrogen abundance. Thus, the significance of the classification scheme might be only warranted as long as the classified stars do not show extreme variations in $[\text{N}]$ and it is possible to discriminate their luminosity class (as a proxy for gravity and an indicator of mass-loss). In terms of spectral morphology, this might be difficult to achieve in low- Z environments such as the SMC.

7.2 Outlook

According to the results achieved within this thesis, nitrogen has shown its promising potential for performing quantitative spectroscopy of O-type stars. Indeed, Herrero et al. (2012) have used the present version of FASTWIND together with the newly developed nitrogen model atom to analyze an O-star located in the low- Z galaxy IC 1613. This analysis has (among other results) provided the first nitrogen abundance measurement for an O-star beyond the Milky Way and the Magellanic Clouds.

The results accomplished during this thesis will probably turn out as a major milestone regarding the nitrogen spectroscopy in O-stars. However, future work is certainly needed to address different open issues, both on the theoretical and the observational side.

For instance, we have shown that the observed emission at the N III triplet lines is of photospheric origin and depends on the actual wind-strength, mostly via the N III resonance line. However, the strength of the emission is also strongly controlled by an O III resonance line, at least in the range of $30,000 \text{ K} \leq T_{\text{eff}} \leq 35,000 \text{ K}$. To cope with this additional effect, and if we aim at deriving nitrogen abundances at cooler temperatures from the triplet lines alone, which often are the only nitrogen features in O-star spectra, we need to incorporate this process into FASTWIND. So far, FASTWIND does not incorporate a complete oxygen model atom,¹ and future work into this direction is certainly needed.

Another interesting topic where our results on the N III triplet line formation could be of major impact regards the so-called ‘weak-winded’ stars. These objects have rather weak winds for their luminosity, being a factor of up to 100 times thinner than predicted/observed for the winds of ‘normal’ O-stars. Thus, it might be suspected that weak-winded stars should display much less triplet emission than stars with ‘normal’ winds of similar type.² The comparison of a significant sample of ‘normal’ and weak-winded O-stars will shed more light on the nature of these peculiar objects.

In addition to nitrogen, there are many other elements that display optical line emission in the hot star regime, most notably, carbon, oxygen, and silicon. We suspect that similar formation processes

¹ Corresponding ions suited for the spectroscopic studies of B-stars, i.e., O I and O II, are already available.

² Provided that there are weak-winded stars also at intermediate O-types. So far, most weak-winded stars have been found only at later O-types where N III $\lambda\lambda 4634\text{-}4640\text{-}4642$ is already in absorption.

might be invoked because of similar electronic configurations/transitions. In particular, modeling the emission at C III $\lambda\lambda$ 4647-4650-4652 could be of major interest. Walborn et al. (2010) introduced a new category of O-stars, the "Ofc" stars. This category consists of O-stars with 'normal' spectra but with C III $\lambda\lambda$ 4647-4650-4652 emission lines of comparable strength as the N III triplet lines. The appearance of the former features is strongly peaked at spectral type O5, at all luminosity classes. Since optical lines from high ionization stages of carbon are scarce, a theoretical investigation and modeling of these emission features needs to be performed if in future studies we aim at deriving carbon abundances.

Let us now comment on the most important caveats found during our analysis of the sample stars. As became apparent in Chapters 5 and 6, we encountered severe problems for ON2 III stars. This problem must relate to some unknown physical process allowing for the presence of strong N III/N IV/N V lines and weak, but still clearly visible He I. For these objects, we were not able to find a simultaneous fit to all of these features, independent from the atmospheric code used. Different processes were inspected (wind-clumping, near-photospheric X-rays, etc.), but none could solve the problem. Moreover, the extreme mass-discrepancies found for these peculiar objects underpinned their problematic nature. Binary interactions have been invoked to explain these extreme mass-discrepancies (Massey et al. 2002), as well as quasi-homogenous evolution. We considered the latter possibility as unlikely, owing to the low $v \sin i$ values measured for our analyzed objects. Further work on the nature of these objects is certainly needed.

Another important consequence drawn from this work is related to the detection of strong nitrogen enrichment in the bulk of the analyzed LMC O-star. From an inspection of the so-called 'Hunter-plot' ([N] vs. $v \sin i$), we found that two thirds of the objects display slow rotation and high enrichment, a fraction which is much too large in terms of (single-star!) population synthesis. A similar group of objects (though with a lower fraction) had been also found in the B-star sample analyzed within the FLAMES-I survey. Since the discrepancies in the O-star group are (much) more severe, this might be an indication that efficient mixing takes place already during very early phases of the O-star evolution. Nevertheless, since the number of investigated objects is still low, results from a detailed statistical analysis involving much larger samples are needed to draw firm conclusions. Upcoming results from the VLT-FLAMES Tarantula survey will help to unveil these problems.

Additional processes, such as binarity and/or magnetic fields, rather than rotational mixing, have been invoked for explaining these unpredicted nitrogen enrichments (see Chapter 1). Recently, Martins et al. (2011a) have provided preliminary observational constraints regarding the role of magnetic fields. These authors have investigated the surface nitrogen content of the six magnetic O-stars known to date, comparing these abundances to predictions of evolutionary models in order to isolate the effects of magnetic field on the transport of elements in the stellar interior. They found that the presence of a magnetic field in O-stars appears to separate the stars analyzed in two groups: either normally rotating non-enriched stars (one object) or slowly rotating enriched stars (five objects). The star belonging to the former group, which is also the object with the weakest magnetic field of the sample, displayed a surface nitrogen content lower than the predictions of evolutionary models, implying that the presence of a magnetic field probably extinguished the transport of chemical elements. They suggested that solid body rotation might explain the properties of the non-enriched star, but its rather normal $v \sin i$, might exclude this assumption. On the other hand, regarding the N enriched stars, they displayed a nitrogen content that corresponded to that observed in non-magnetic O-stars with initial $v \sin i$ of 300 km s^{-1} , while the initial rotational velocity of these stars were more likely of a few tenths of km s^{-1} at most. The authors suggested that this extra-enrichment is most likely originated by

dipolar, fossil fields, which might tend to lead to extra mixing in the interior of O-stars in their early evolution. Unfortunately, so far, evolutionary calculations including fossil fields are not available. Future work is certainly needed in order to test the latter hypothesis.

Of course, observations may be also over-interpreted, in particular when the full set of information is not accounted for. In our case, our conclusions regarding stellar evolution rely on one indicator alone, namely the nitrogen abundance. To confirm these conclusions, in particular regarding the efficiency of very early mixing in O-stars, the determination of both carbon and oxygen abundances will be of major importance. Evolutionary models for massive stars predict very tight relations for the changes in the surface N/C and N/O abundance ratios and for the build-up of helium, as a consequence of mixing with CNO-cycle processed material (see Chapter 1). For instance, Przybilla et al. (2010) have recently undertaken a large effort to investigate these predicted relations in the B-star regime. They compiled CNO abundances for Galactic stars from their previous studies, for B-types up to $25 M_{\odot}$. The behaviour of these abundances displayed a clear trend in their whole sample, confirming the predicted N/C and N/O abundance ratios.³ Moreover, the authors showed that the tight observational constraints that are required for a thorough test of evolutionary models are within reach. A similar study in the O-star regime for larger samples in the Milky Way and other galaxies may finally provide the empirical basis to further test stellar evolution also in this domain. Then, it might become feasible to disentangle the effects of metallicity, rotation, magnetic fields, and binarity on massive stellar evolution. As outlined above, this will be only possible when consistent model atoms for oxygen and carbon, well-suited for analyzing O-stars, will become available, and will have been carefully tested by quantitative spectroscopy of significant O-star samples.

Also our study of the *earliest* O-stars implies consequences which need to be validated in future work. First, the SpT- T_{eff} scale constrained from our LMC sample turned out to be, for a given luminosity class, more or less monotonic. However, this result is somewhat preliminary, since the majority of the sample stars showed a considerable nitrogen enrichment, and the analysis of a significant number of un- or mildly enriched early-type O-stars will be required to quantify the actual bias due to nitrogen abundance. Second, the earliest SMC O-stars might have effective temperatures below corresponding LMC ones, implying that the overall SpT- T_{eff} relation for SMC stars might be non-monotonic around spectral types O3.5/O4. Finally, our theoretical predictions indicated that there should be enriched Galactic O4 dwarfs with emission at N III λ 4640 and absorption at N IV λ 4058. So far, the Walborn et al. (2002) classification scheme only states that there should be no traces of N IV λ 4058 in O4 dwarfs. First observational evidence for the presence of such an absorption feature suggests that a revision of the original Walborn et al. (2002) classification scheme might be needed.

Upcoming results from larger stellar samples, most notably, the VLT-FLAMES Tarantula survey, will enable a more complete view of the nature of O-stars. In particular, the determination of O-star CNO abundances will place very tight constraints on the early evolutionary phases of O-stars and, finally, on the complete massive star evolution theory.

³ This does not explain the ‘peculiar’ B-stars from the FLAMES-I survey.

Appendix A

Testing the N II model ion

To test our somewhat simple N II model ion,¹ we compared synthetic line profiles with corresponding ones from TLUSTY and DETAIL/SURFACE (Giddings, 1981; Butler & Giddings, 1985), the latter based on the newly developed N II model by Przybilla et al.

A summary of the various tests is provided in Table A.1. We started by comparing with line profiles from the BSTAR2006 model grid (Lanz & Hubeny, 2007). This grid has been calculated using the model atmosphere code TLUSTY, a code that assumes plane-parallel geometry, hydrostatic and radiative equilibrium, and calculates line-blanketed NLTE model atmospheres and corresponding synthetic profiles. Owing to its restrictions, only objects with negligible winds can be analyzed.

We used this grid of models as reference because it covers the parameter range at which N II/N III are the dominant ionization stages, and the N II lines are clearly visible in the synthetic spectra. In addition, the BSTAR2006 grid has been used in numerous studies aiming at the determination of stellar abundances and parameters in B-stars (e.g., Lanz et al., 2008).

We calculated a grid of FASTWIND model, covering the temperature range $20 \text{ kK} \leq T_{\text{eff}} \leq 30 \text{ kK}$, using a typical step size of 2.5 kK, and gravities representative for dwarfs and giants. Because TLUSTY does not account for the presence of a wind, we used negligible mass-loss rates, $\dot{M} = 10^{-9} \dots 10^{-10} M_{\odot} \text{yr}^{-1}$. Because FASTWIND allows for employing external photospheric structures, we created a second grid using the TLUSTY photospheric structure, smoothly connected to the wind structure as calculated by FASTWIND, with the usual β velocity law. For consistency with the TLUSTY grid, all models were calculated with the ‘older’ solar nitrogen abundance, $[\text{N}] = 7.92$ (Grevesse & Sauval, 1998). Note that all tests were performed with the complete nitrogen model atom involving the ions N II to N V as described in Chapter 3.

We found substantial differences between the synthetic N II line profiles calculated by TLUSTY (TL) and FASTWIND (FW), even though the hydrogen/helium lines agree very well (except for the forbidden component of He I which is stronger in FW-models). The latter code predicts stronger N II profiles, which is also true for the FASTWIND results based on the TLUSTY photospheric structure (FW2, see Figs. A.2 to A.7).

For dwarfs, there are almost no differences between the profiles from the FW and FW2 models. This is readily understood, since the photospheric stratification of electron temperature, T_e , and electron density, n_e , are essentially the same (see Fig. A.1, panel 1, 3, 5), i.e., FASTWIND and TLUSTY predict the same structures.

¹ Important, e.g., for our comparison with B-star nitrogen abundances from alternative analyses, see Sect. 5.6.2

Table A.1: N II test series.

Series	Atomic model	Photospheric stratification	NLTE/line formation
FW	see Sect. 3.2	FASTWIND	FASTWIND
FW2	see Sect. 3.2	TLUSTY	FASTWIND
TL	TLUSTY	TLUSTY	TLUSTY
Prz	Przybilla et al.	KURUCZ	DETAIL/SURFACE

On the other hand, models for giants at higher T_{eff} display (mostly) weak differences. At $T_{\text{eff}} = 27.5$ kK and $\log g = 3.0$, e.g., there is a small disagreement of the electron densities in photospheric regions ($\tau_{\text{Ross}} \leq 10^{-5}$), even though the temperatures agree quite well (Fig. A.1, panel 6). In particular, the TLUSTY and thus the FW2 structure shows a lower electron density at optical depths where the photospheric lines are formed, because of a higher photospheric radiative line pressure in this model.

Because of the lower electron density, the lower recombination rates (at $T_{\text{eff}} = 27.5$ kK, N III is the dominant ion) lead to somewhat weaker N II profiles in the FW2 models compared to the FW ones, see Fig. A.7. Nevertheless, differences to the profiles as predicted by TL itself are still considerable, and we conclude that the photospheric structure is not the origin of the discrepancies.

As an independent check, we compared our results with spectra calculated by N. Przybilla (priv. comm.) for two of our grid models, denoted by Prz in the following. These spectra are based on the NLTE/line formation code DETAIL/SURFACE, and the N II model ion recently developed by Przybilla et al.. We consider this atomic model as the superior one in the present context, because the atomic data were successfully improved and tested, and the corresponding synthetic spectra perfectly match high-resolution/high-signal-to-noise observations from various B-stars (Przybilla et al., 2008).

Figures A.2 and A.4 show that the FW and Prz profiles agree excellently, which leaves us with the conclusion that there might be problems in the N II atomic data used in the BSTAR2006 grid. Important studies using TLUSTY have been carried out during the past years (e.g., Dufton et al. 2006; Trundle et al. 2007; Hunter et al. 2009b), including the determination of N II abundances in LMC and SMC B-stars. These studies utilized a different model atom, developed by Allende Prieto et al. (2003), which has been tested by N. Przybilla at our request, with a positive outcome. Therefore these analyses should be free from uncertainties related to a potentially insufficient atomic model.

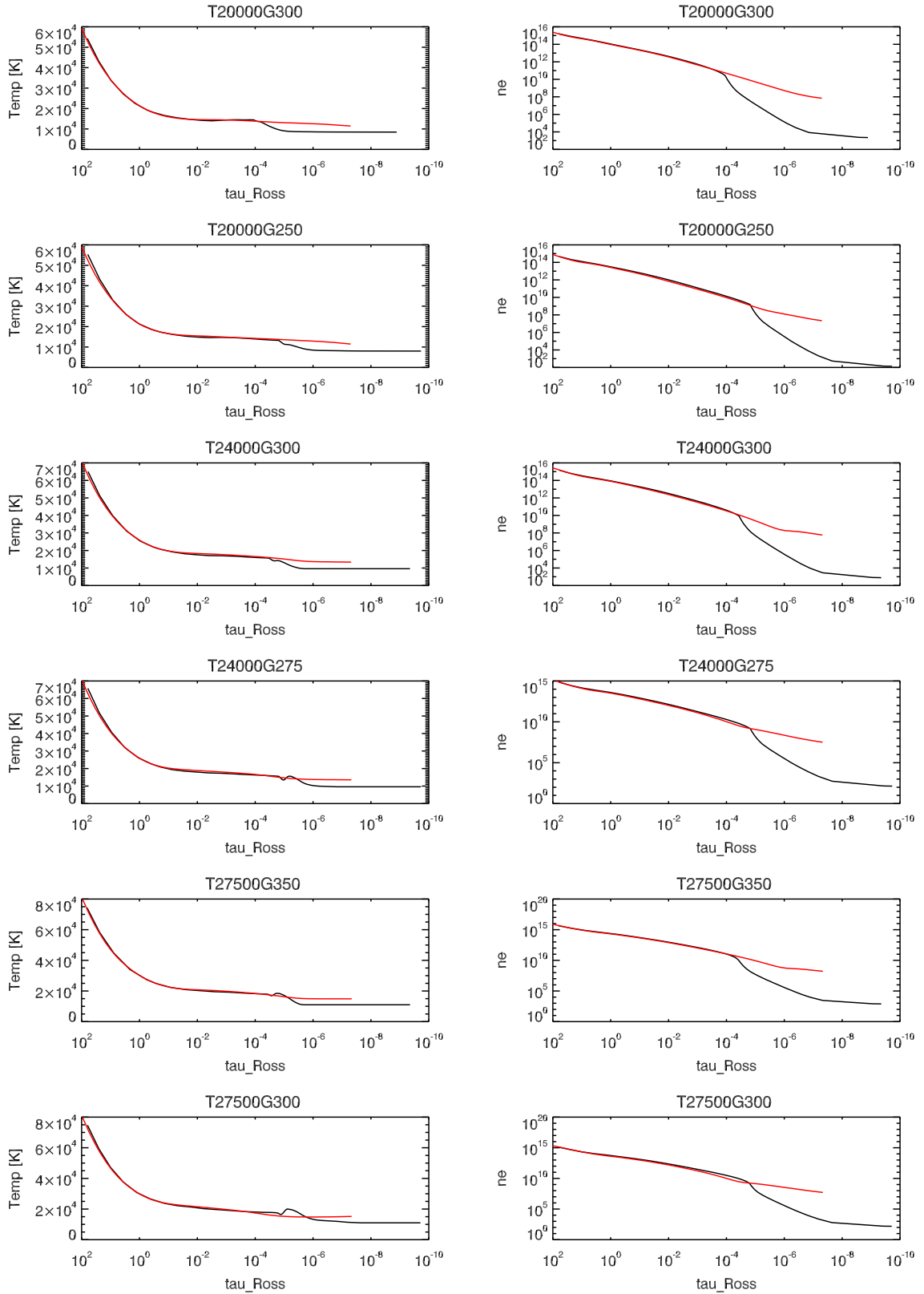


Figure A.1: FASTWIND (black) vs. TLUSTY (red): comparison of electron temperature and electron density as a function of Rosseland optical depth for the six models corresponding to Figs. A.2 to A.7.

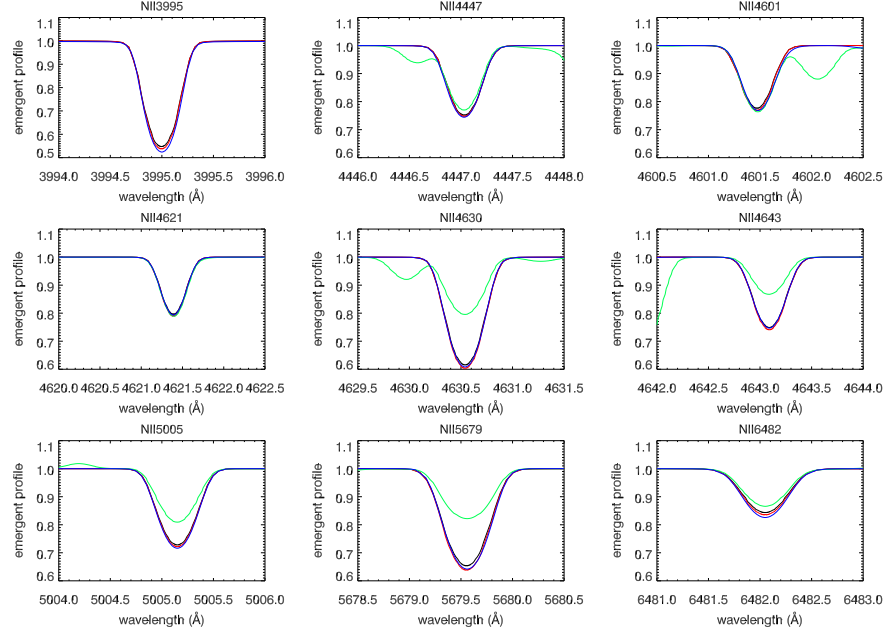


Figure A.2: Comparison of important optical N II line profiles for a model with $T_{\text{eff}} = 20$ kK and $\log g = 3.0$, for models – see Table A.1 – FW (black), FW2 (red), TL (green) and Prz (blue). Note that N II λ 3995 is not present in the BSTAR2006 grid.

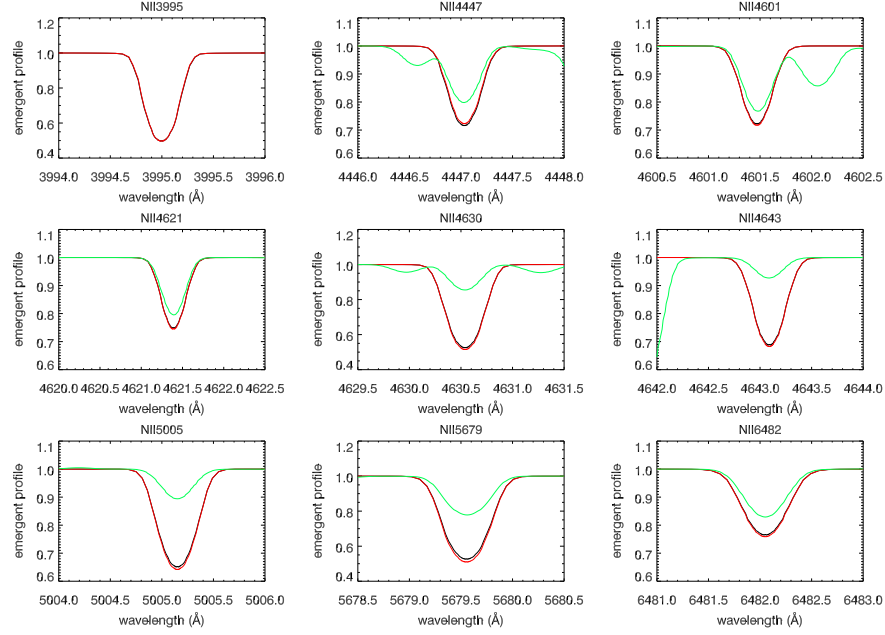


Figure A.3: As Fig. A.2, but for $T_{\text{eff}} = 20$ kK and $\log g = 2.5$.

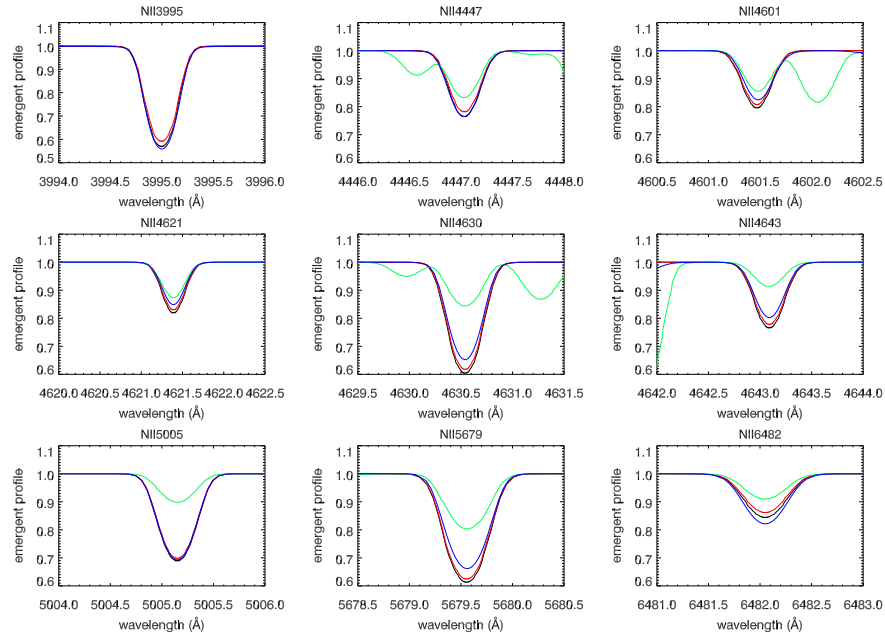


Figure A.4: As Fig. A.2, but for $T_{\text{eff}} = 24$ kK and $\log g = 3.0$.

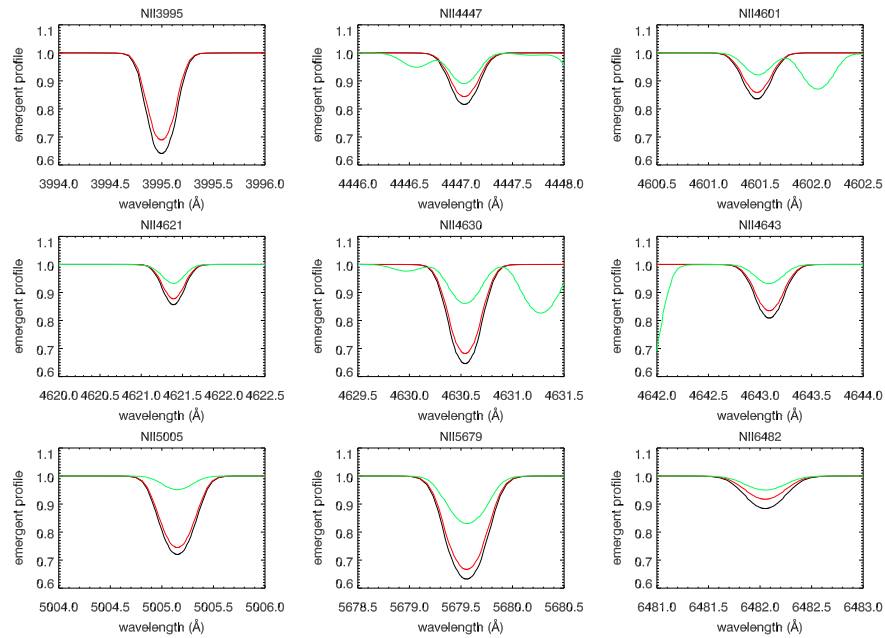


Figure A.5: As Fig. A.3, but for $T_{\text{eff}} = 24$ kK and $\log g = 2.75$.

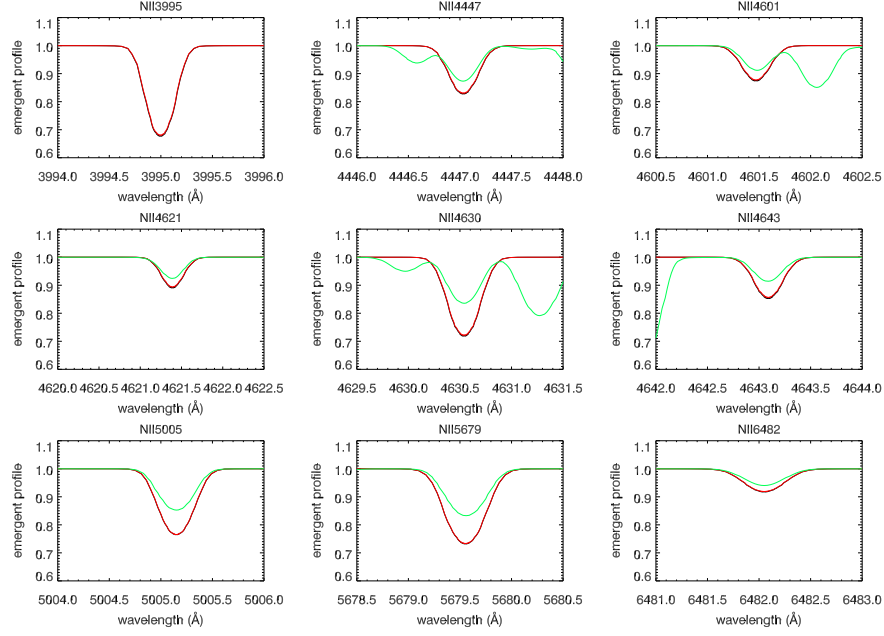


Figure A.6: As Fig. A.3, but for $T_{\text{eff}} = 27.5$ kK and $\log g = 3.5$.

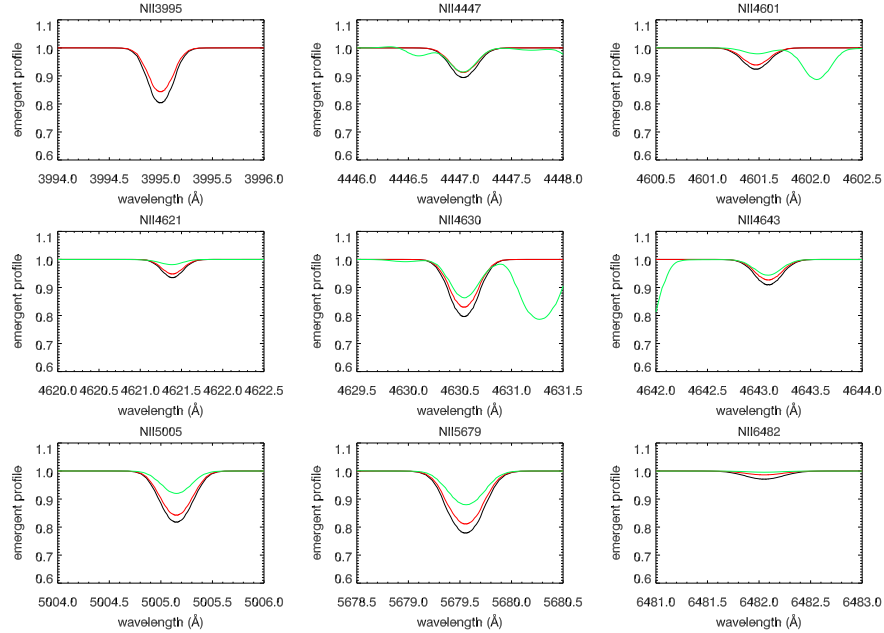


Figure A.7: As Fig. A.3, but for $T_{\text{eff}} = 27.5$ kK and $\log g = 3.0$.

Appendix B

Comparison of line profiles with results from CMFGEN

B.1 Comparison of N II/N III line profiles

In this appendix, we display a comparison of N III (and partly N II) line profiles from FASTWIND (black) and CMFGEN (green), for all models from the grid presented in Table 4.3. For a discussion, see Sect. 4.5.

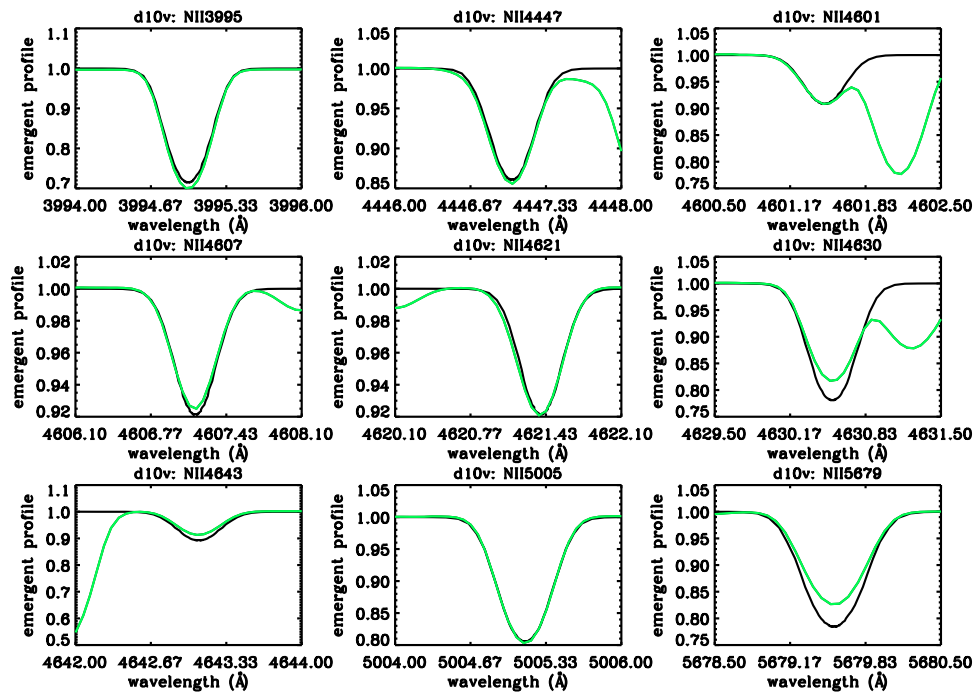


Figure B.1: Comparison of N II line profiles from present work (black) and CMFGEN (green), for model d10v (for parameters, see Table 4.3).

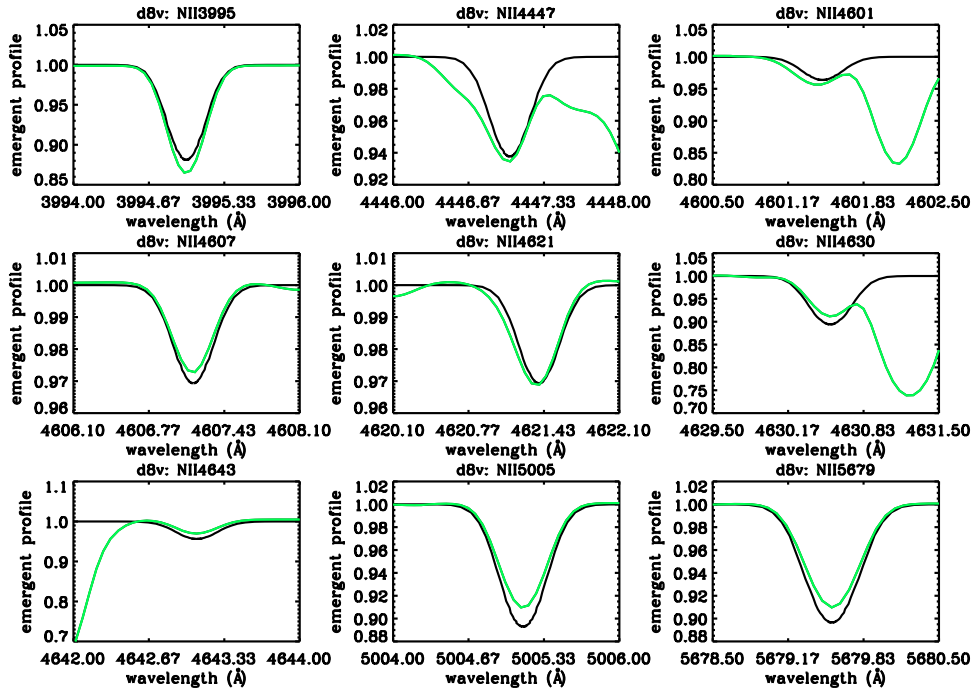


Figure B.2: As Fig. B.1, but for model d8v.

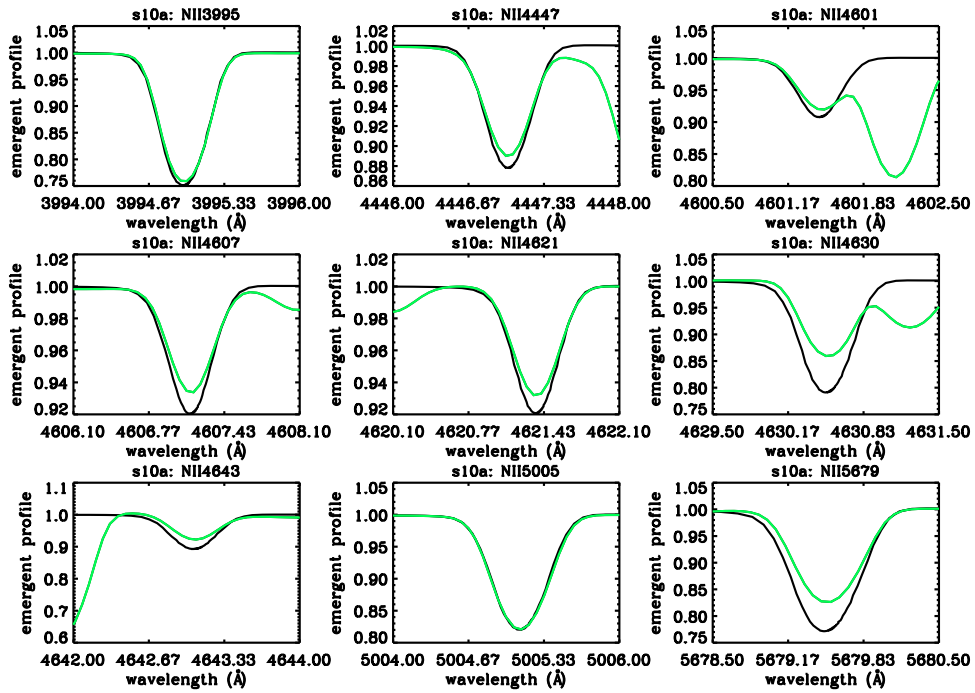


Figure B.3: As Fig. B.1, but for model s10a.

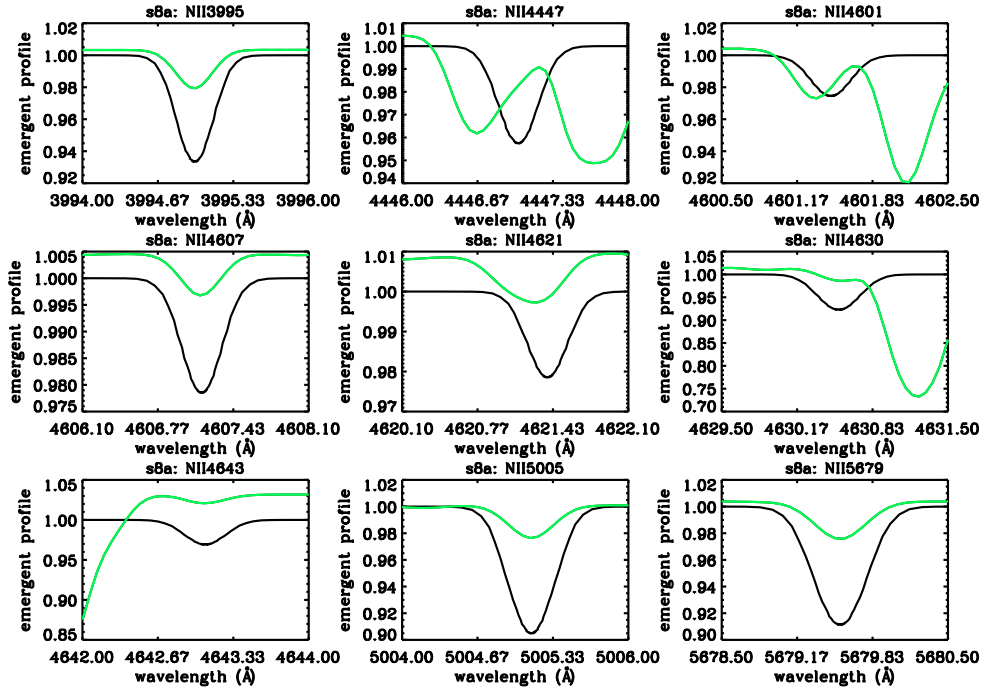


Figure B.4: As Fig. B.1, but for model s8a.

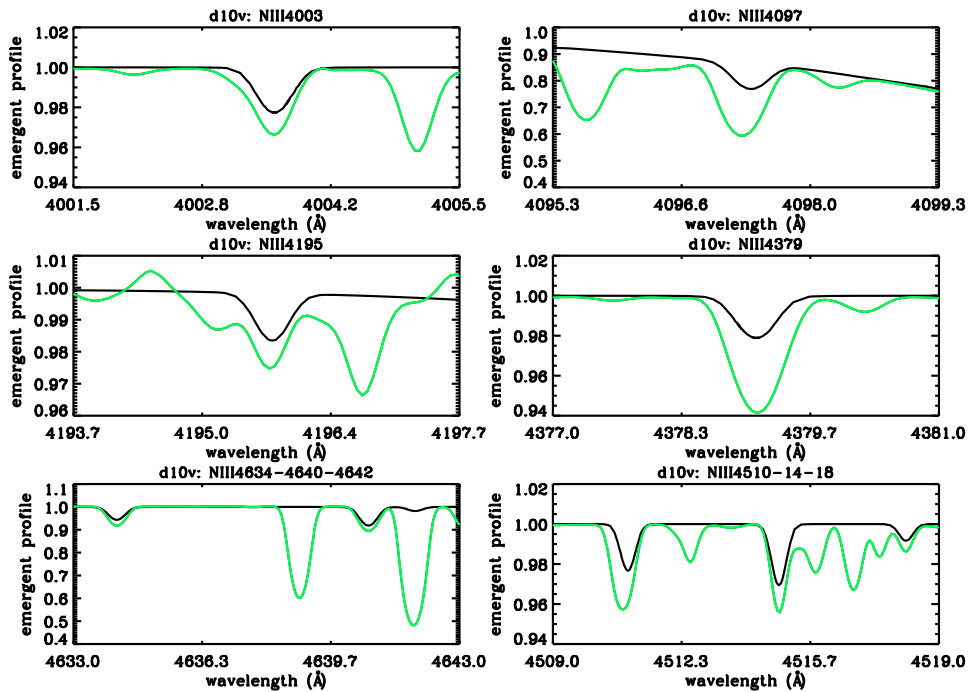


Figure B.5: Comparison of N III line profiles from present work (black) and CMFGEN (green), for model d10v.

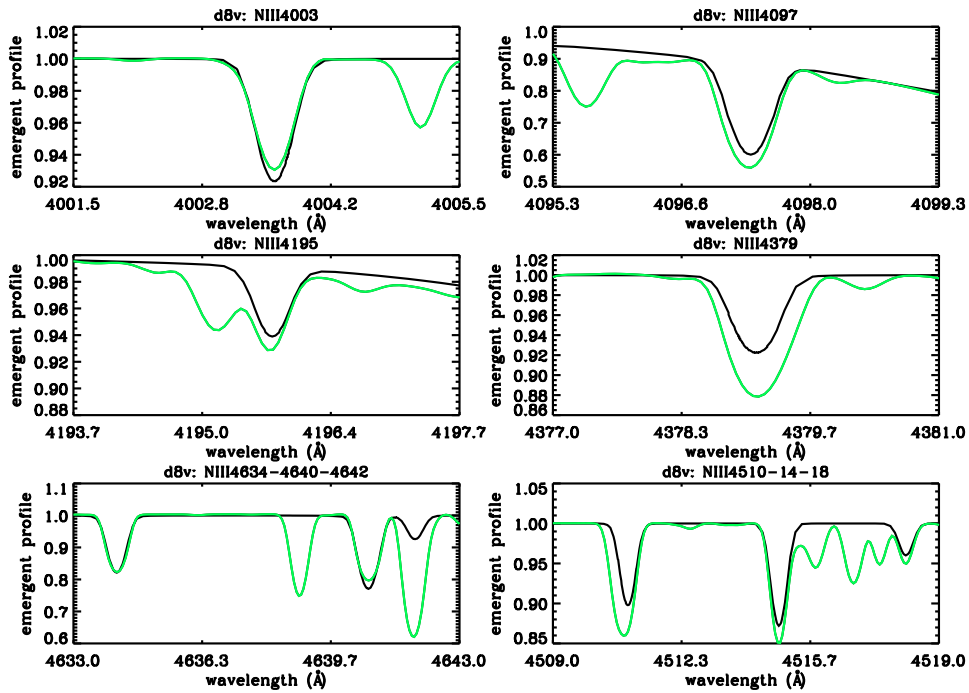


Figure B.6: As Fig. B.5, but for model d8v.

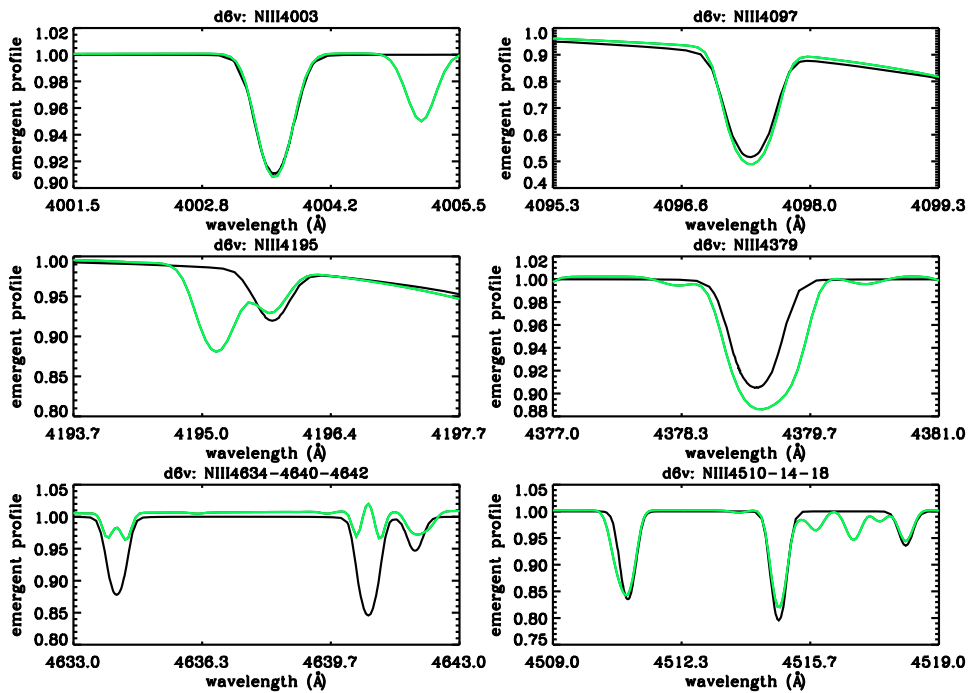


Figure B.7: As Fig. B.5, but for model d6v.

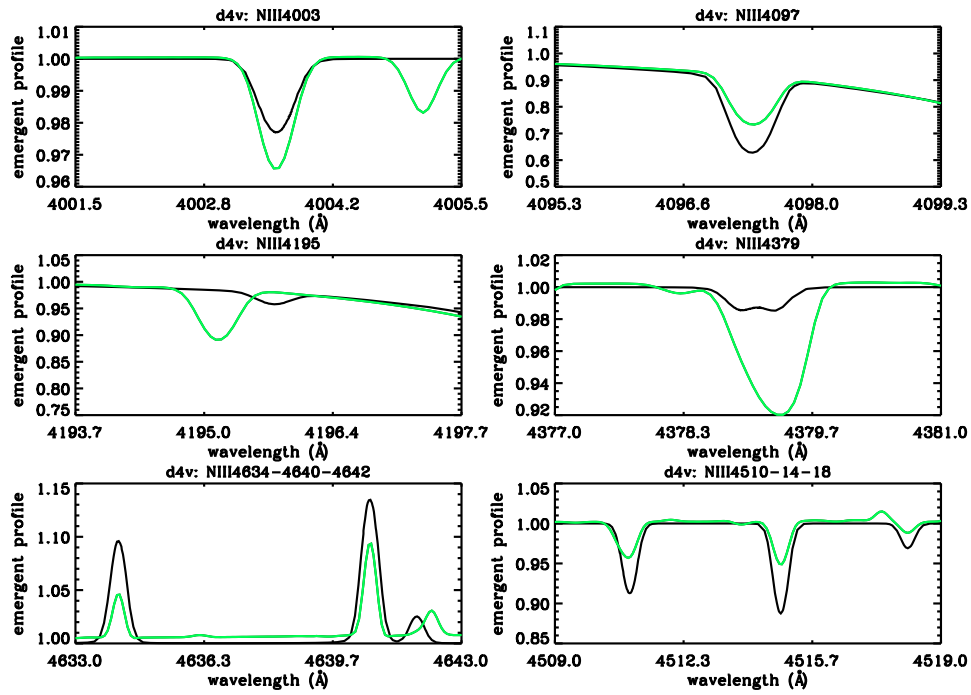


Figure B.8: As Fig. B.5, but for model d4v.

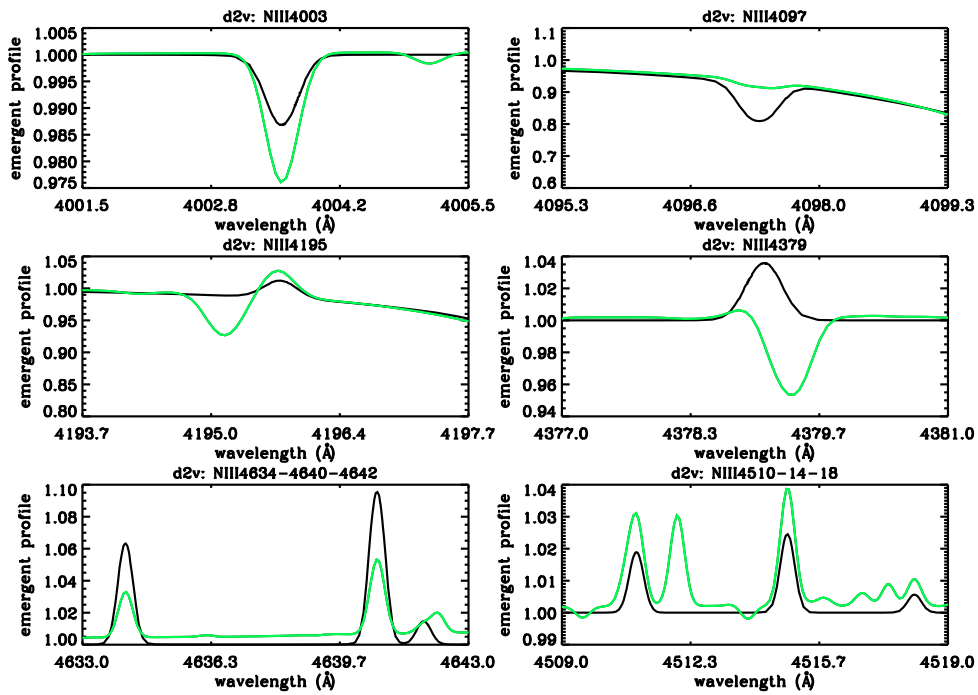


Figure B.9: As Fig. B.5, but for model d2v.

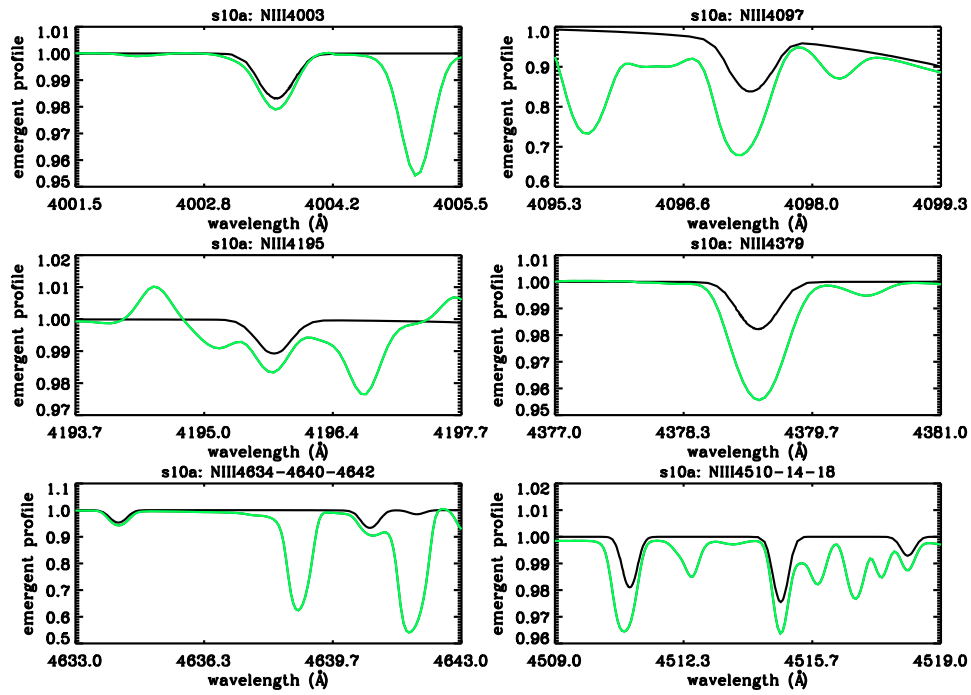


Figure B.10: As Fig. B.5, but for model s10a.

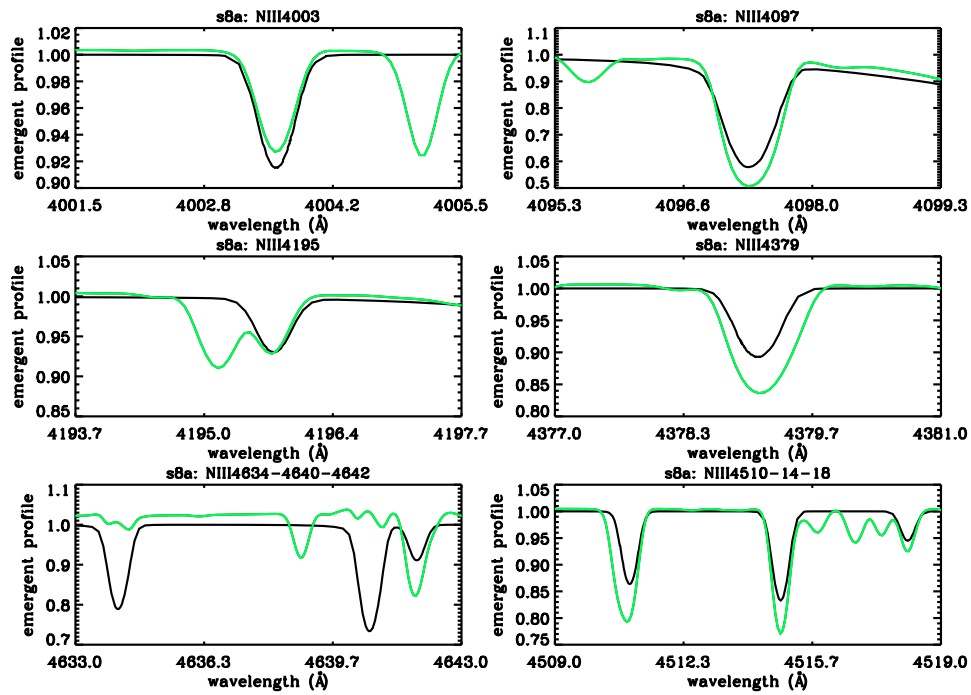


Figure B.11: As Fig. B.5, but for model s8a.

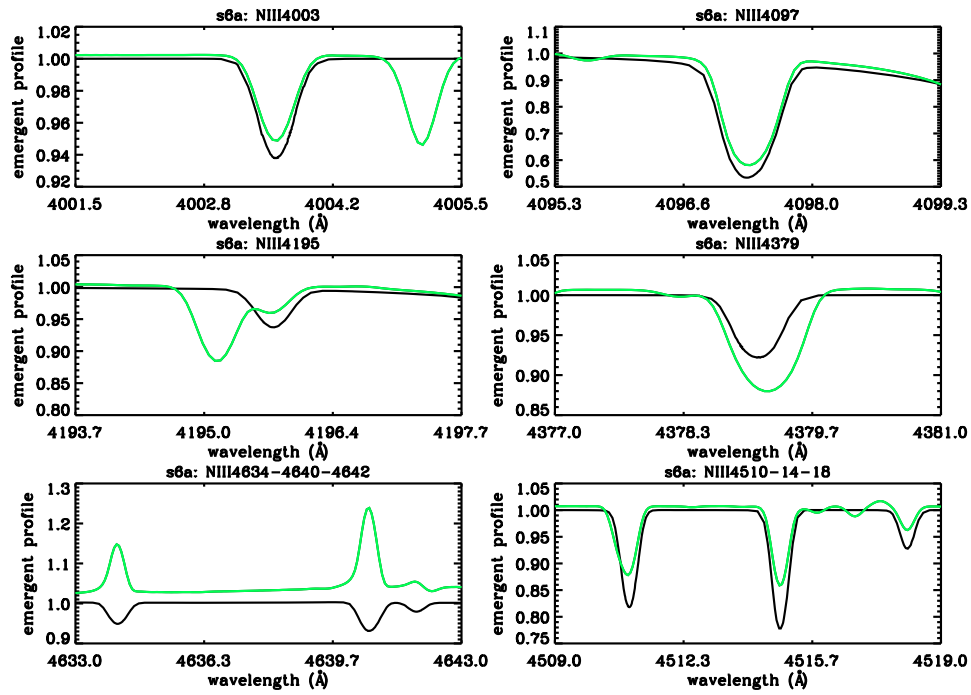


Figure B.12: As Fig. B.5, but for model s6a.

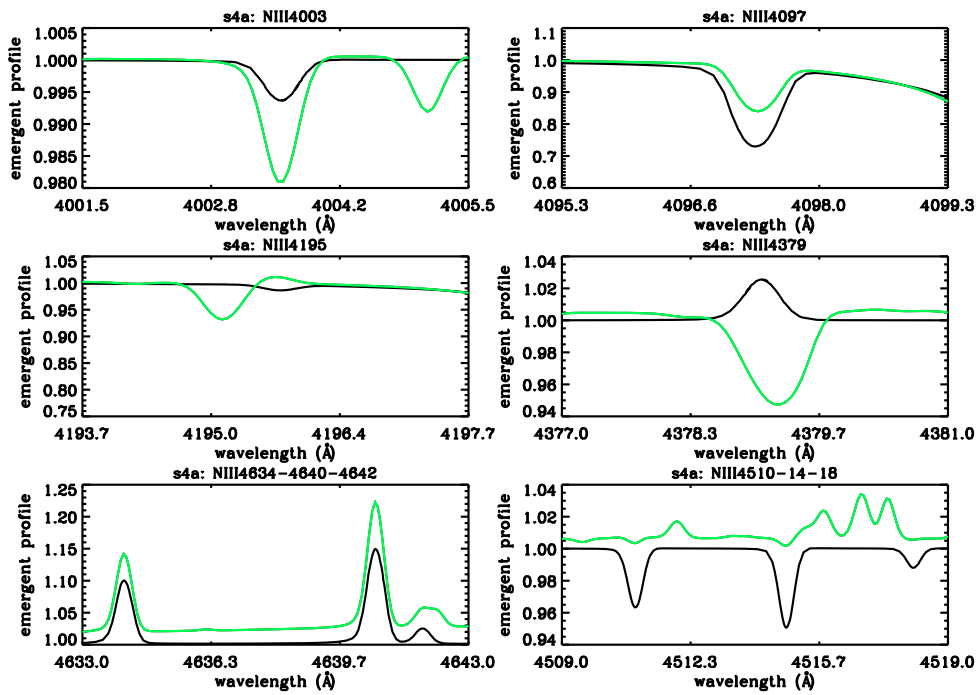
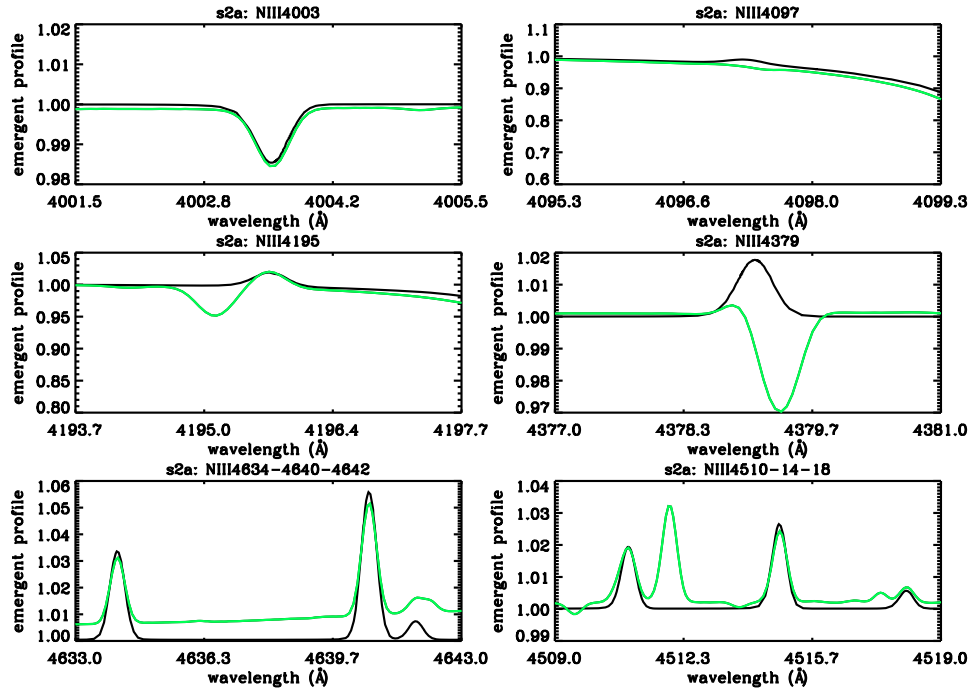


Figure B.13: As Fig. B.5, but for model s4a.

Figure B.14: As Fig. B.5, but for model *s2a*.

B.2 Comparison of H/He/N line profiles for models with different nitrogen abundances

Figures B.15 to B.22 provide a detailed comparison between H/He and N III/N IV/N V CMFGEN spectra for models *d2v*, *d4v*, *s2a*, and *s4a* (see Table 6.3), and corresponding FASTWIND profiles from closest or almost closest grid models, for a nitrogen abundance of $[N] = 8.78$ and $[N] = 7.78$. If not explicitly stated else, no convolution has been applied to the spectra. For details, see Sect. 6.5.

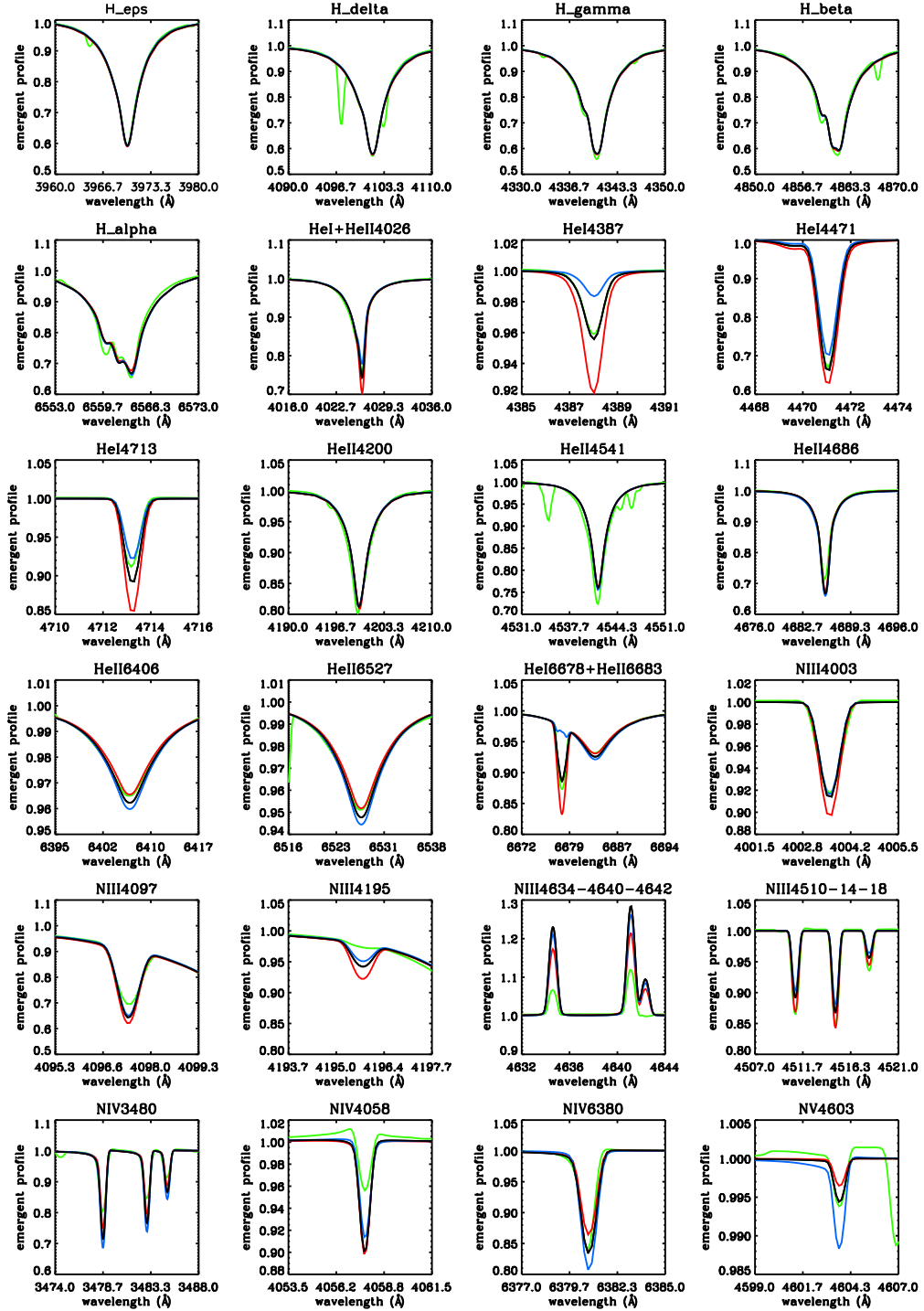


Figure B.15: Model d4v at $[N] = 8.78$. Comparison of H/He/N spectra from CMFGEN (green) and FASTWIND, at the closest grid-model (black: $T_{\text{eff}} = 41$ kK, $\log g = 4.0$, $\log Q = -12.8$, $[N] = 8.78$) and at neighboring grid models with $T_{\text{eff}} = 40$ kK (red) and $T_{\text{eff}} = 42$ kK (blue). To allow for an easier comparison, all profiles have been convolved with $v \sin i = 30 \text{ km s}^{-1}$.

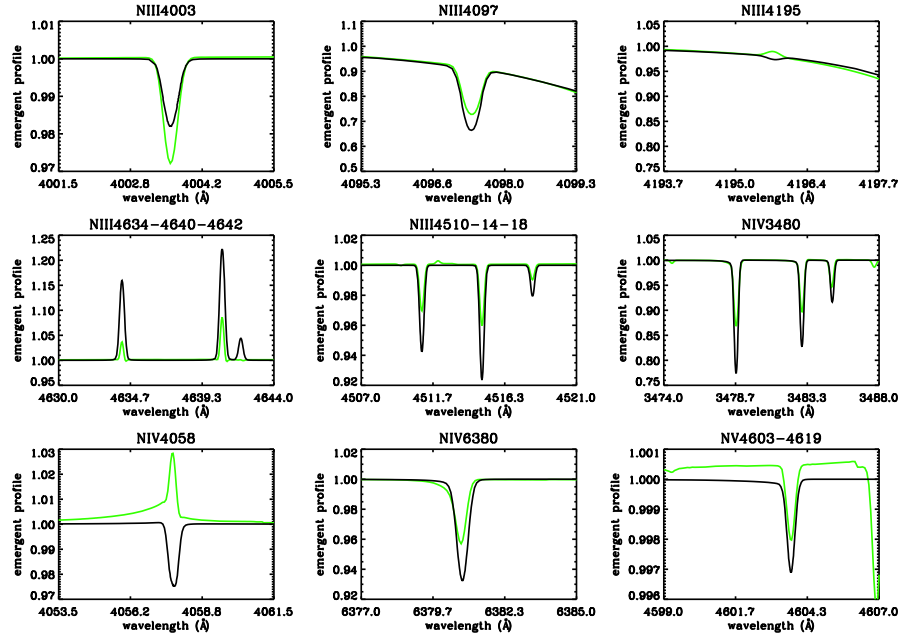


Figure B.16: Model d4v at $[N] = 7.78$ (solar). Comparison of N spectra from CMFGEN (green) and FASTWIND, at the closest grid-model. (black: $T_{\text{eff}} = 41$ kK, $\log g = 4.0$, $\log Q = -12.8$, $[N] = 7.78$). The H/He spectra remain as in Fig. B.15. No convolution applied.

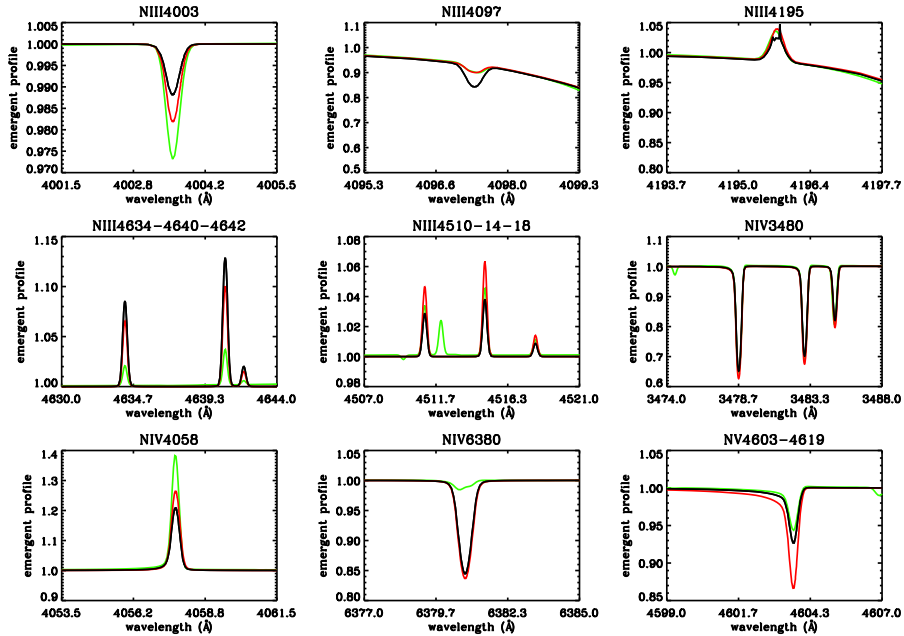


Figure B.17: Model d2v at $[N] = 7.78$ (solar). Comparison of N spectra from CMFGEN (green) and FASTWIND, at the closest grid-model (black: $T_{\text{eff}} = 46$ kK, $\log g = 4.0$, $\log Q = -12.45$, $[N] = 7.78$), and at the neighboring grid model with $T_{\text{eff}} = 47$ kK (red). The H/He spectra remain as in Fig. B.18.

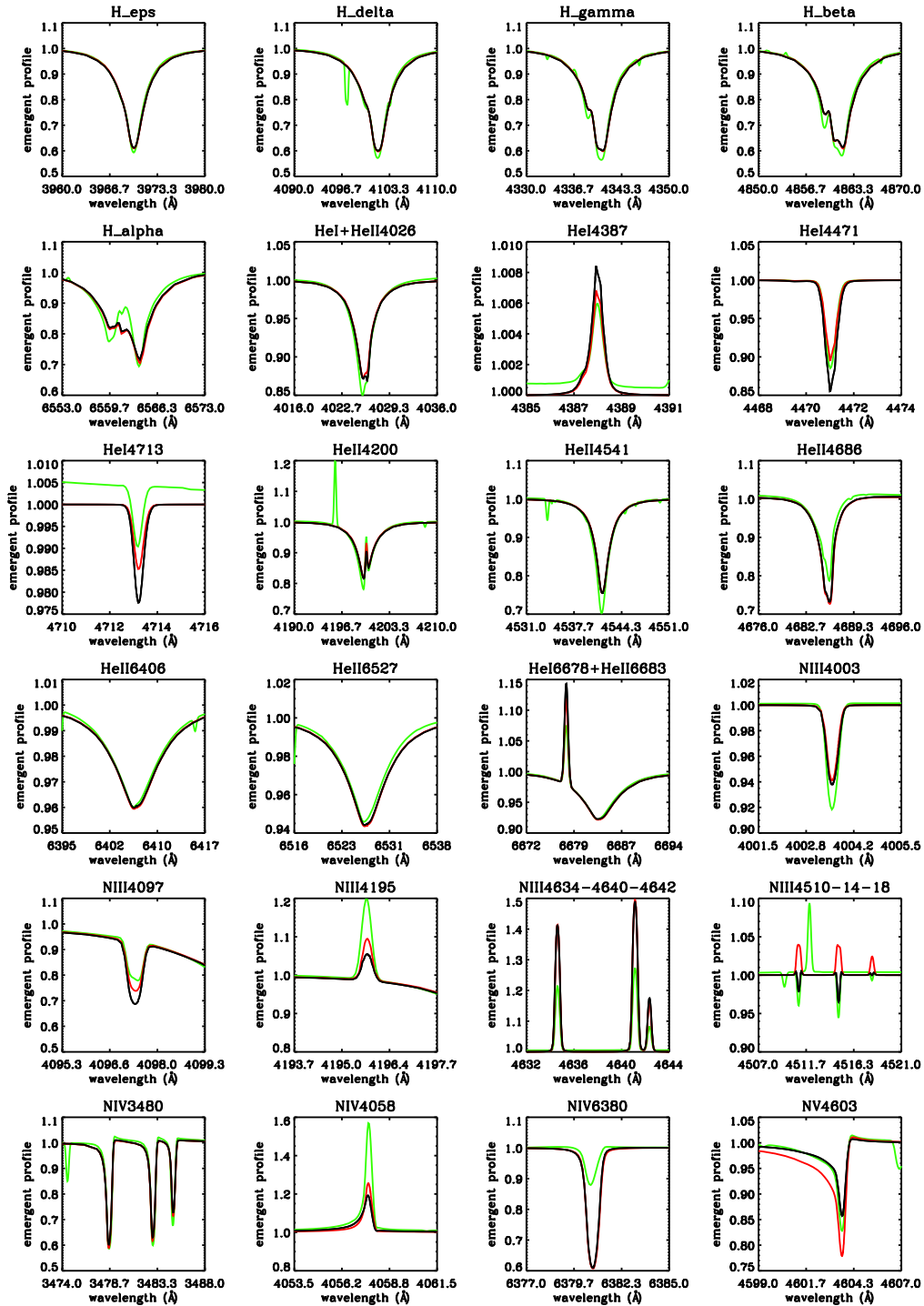


Figure B.18: Model d2v at $[N] = 8.78$. Comparison of H/He/N spectra from CMFGEN (green) and FASTWIND, at the closest grid-model (black: $T_{\text{eff}} = 46$ kK, $\log g = 4.0$, $\log Q = -12.45$, $[N] = 8.78$) and at neighboring grid model with $T_{\text{eff}} = 47$ kK (red). No convolution has been applied.

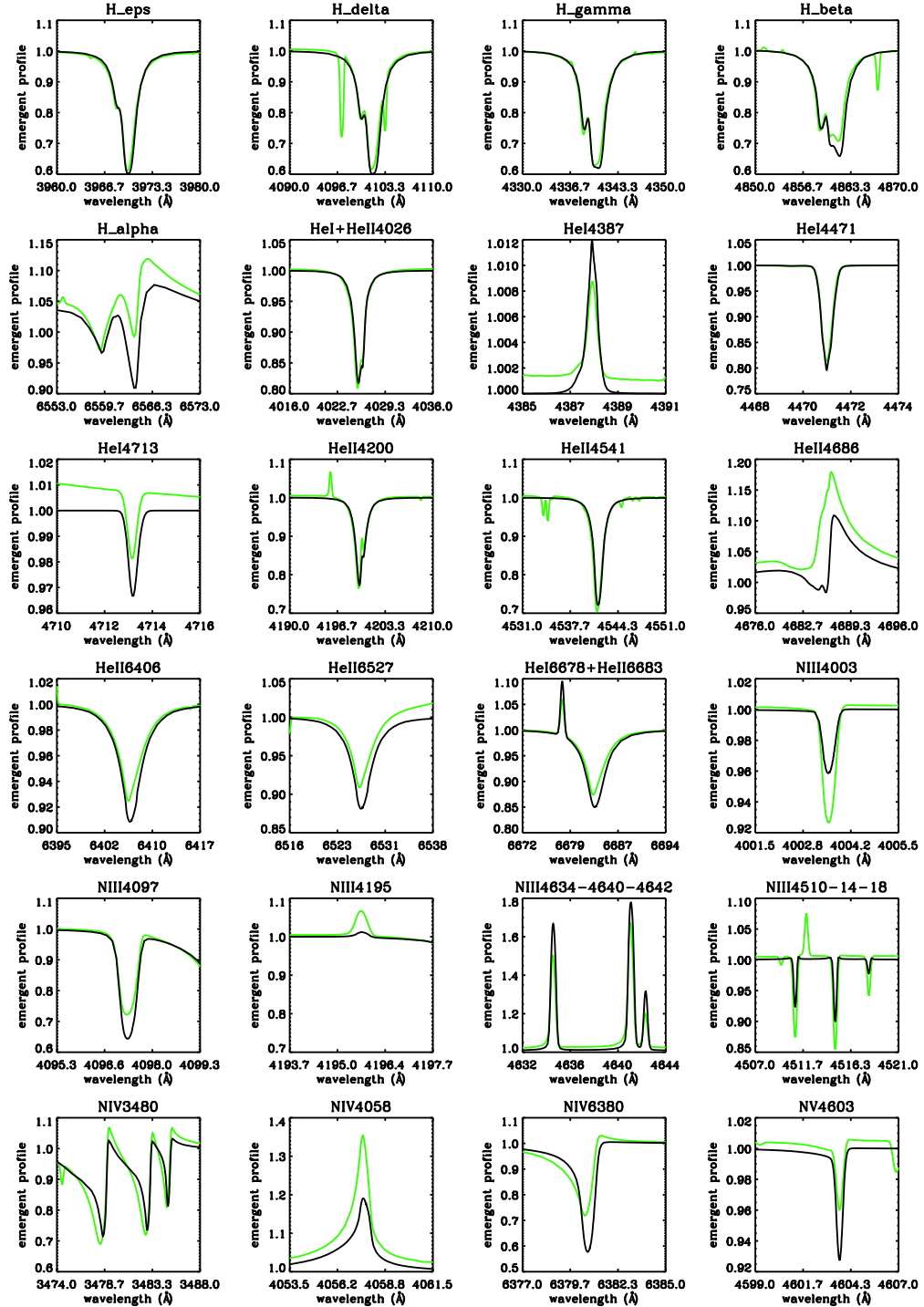


Figure B.19: Model $s4a$ at $[N] = 8.78$. Comparison of H/He/N spectra from CMFGEN (green) and FASTWIND, at the closest grid-model (black: $T_{\text{eff}} = 39$ kK, $\log g = 3.5$, $\log Q = -12.10$, $[N] = 8.78$).

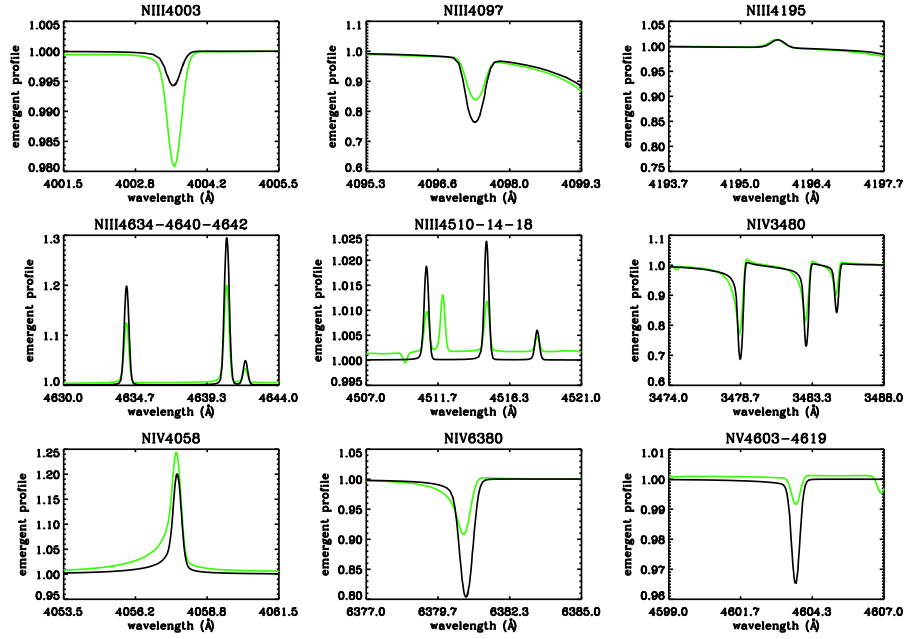


Figure B.20: Model $s4a$ at $[N] = 7.78$ (solar). Comparison of N spectra from CMFGEN (green) and FASTWIND, at the closest grid-model (black: $T_{\text{eff}} = 39$ kK, $\log g = 3.5$, $\log Q = -12.10$, $[N] = 7.78$). The H/He spectra remain as in Fig. B.19.

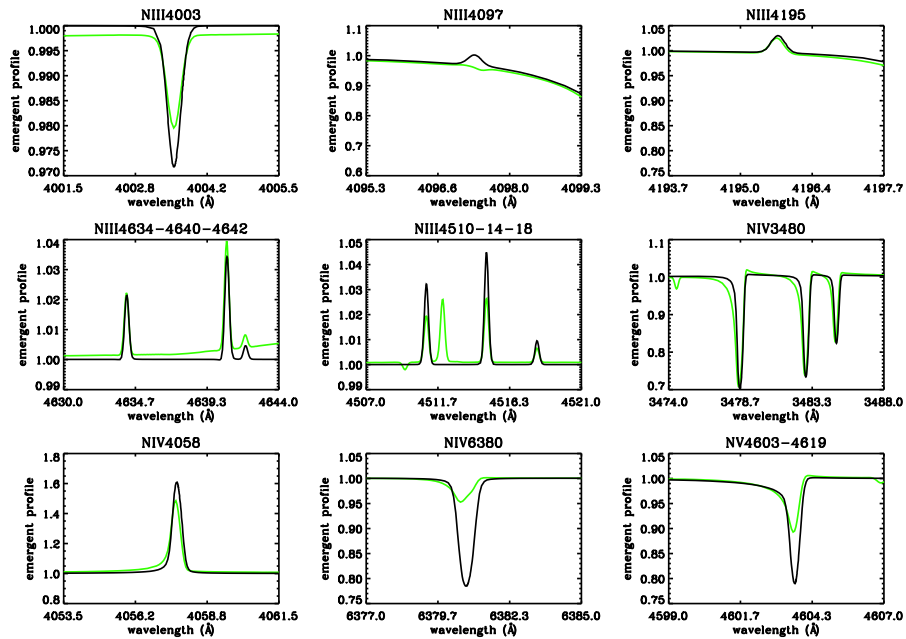


Figure B.21: Model $s2a$ at $[N] = 7.78$ (solar). Comparison of N spectra from CMFGEN (green) and FASTWIND, at the (almost) closest grid-model (black: $T_{\text{eff}} = 46$ kK, $\log g = 3.8$, $\log Q = -12.10$, $[N] = 7.78$). The H/He spectra remain as in Fig. B.22.

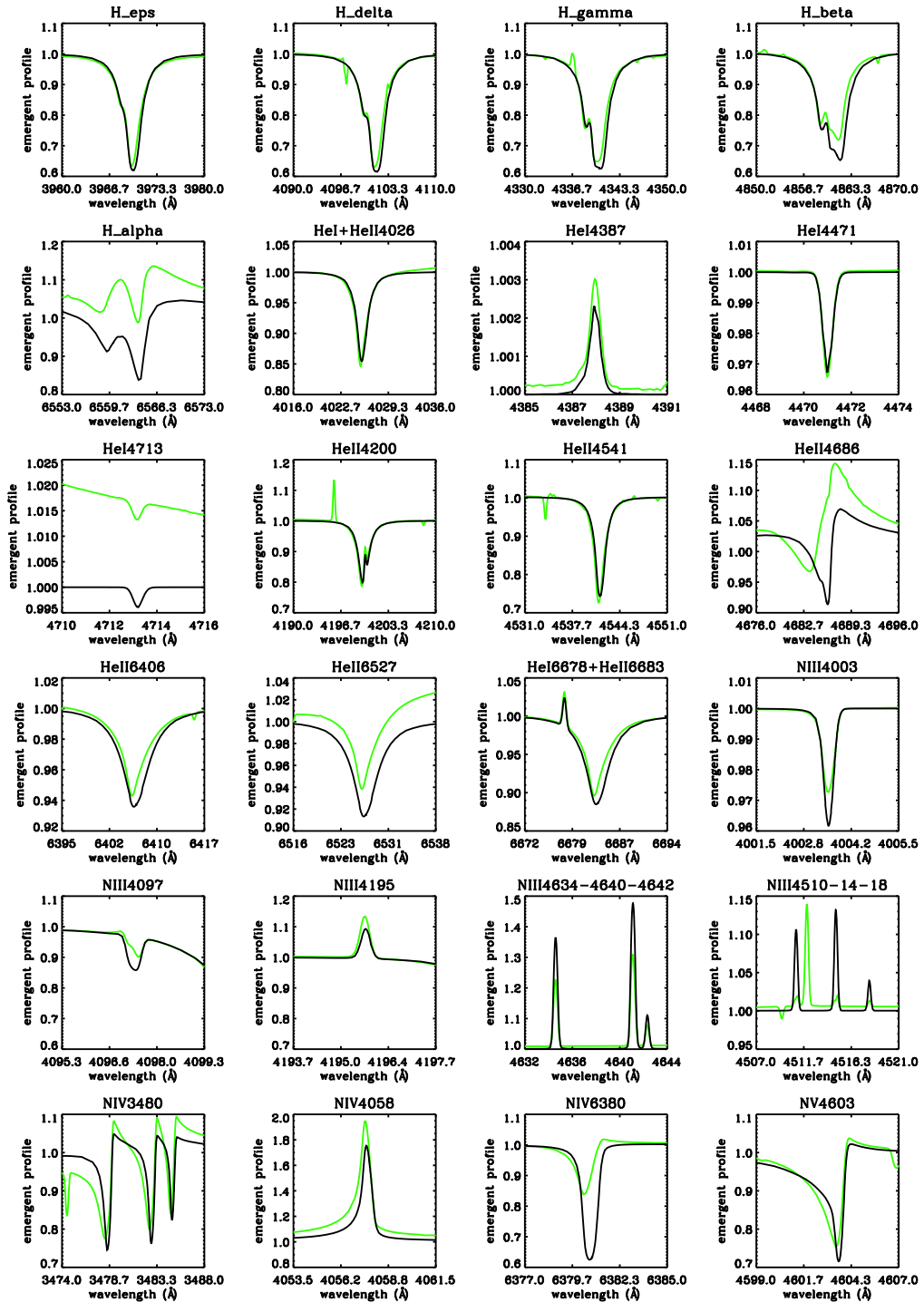


Figure B.22: Model $s2a$ at $[N] = 8.78$. Comparison of H/He/N spectra from CMFGEN (green) and FASTWIND, at the (almost) closest grid-model (black: $T_{\text{eff}} = 46$ kK, $\log g = 3.8$, $\log Q = -12.10$, $[N] = 8.78$).

Appendix C

Line fits for individual objects

C.1 Line fits for the LMC sample

Figures C.1 to C.22 display the observed (green) and best-fitting optical nitrogen spectra (black) for all objects analyzed in Chapter 5, except for N11-072, N11-032, and BI237, which are contained in Sect. 5.5. Blue and red spectra show corresponding synthetic line profiles with $[N]$ at the lower and upper limit, respectively. For N11-031 (Fig. C.7), we show the fits corresponding to the two alternative solutions for this star (see Sect. 5.5). For details on the line fits, see Sect. 5.5, and for adopted stellar parameters and derived nitrogen abundances inspect Table 5.2 and Table 5.4, respectively. All fits are based on unclumped winds except when explicitly stated.

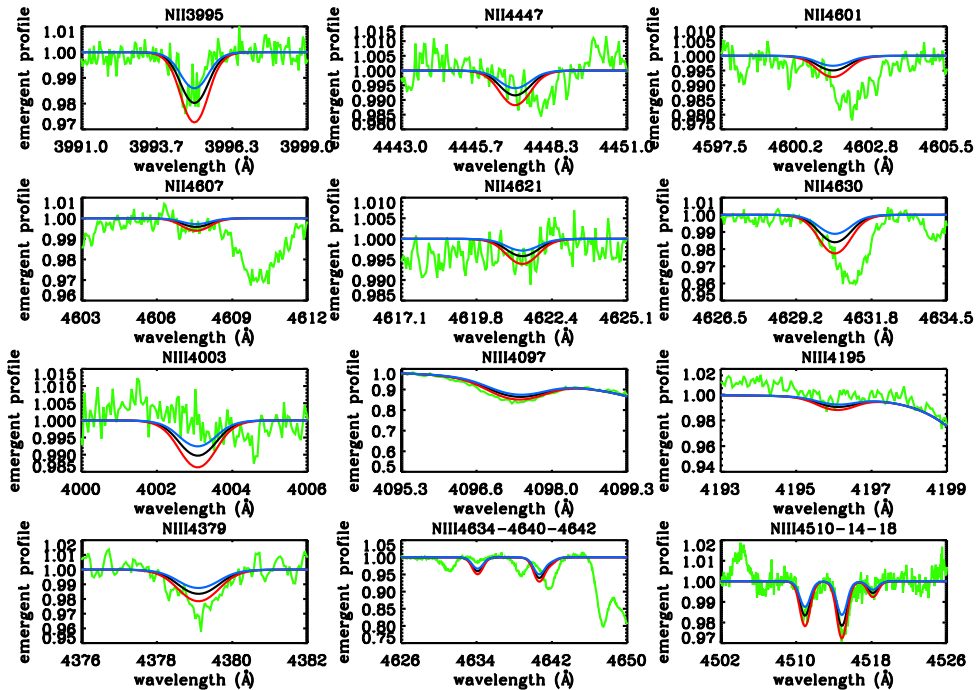


Figure C.1: N11-029 – O9.7 Ib.

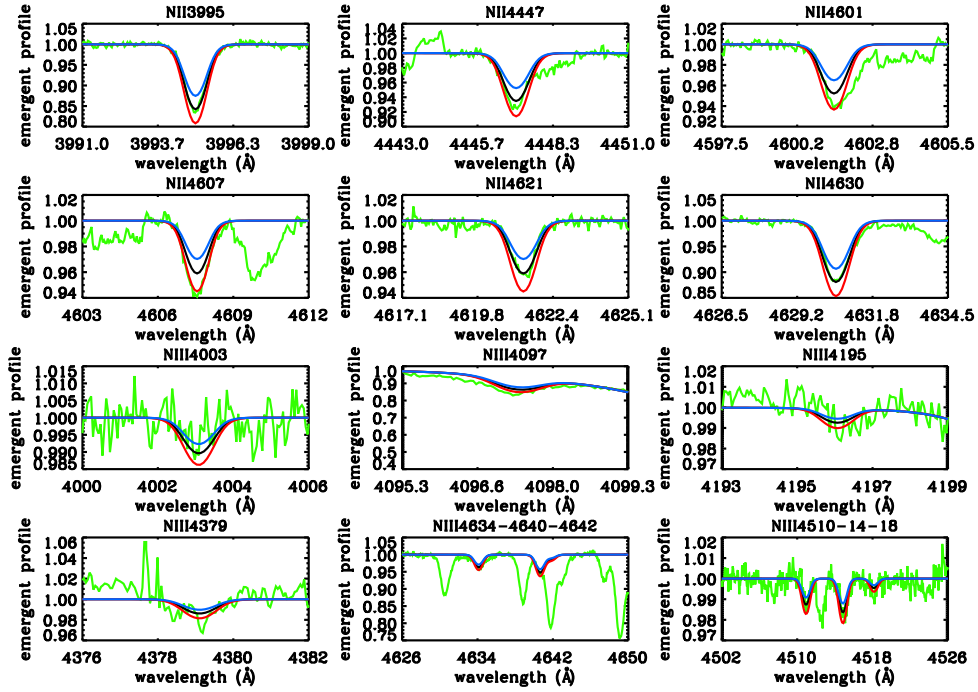


Figure C.2: N11-036 – B0.5 Ib.

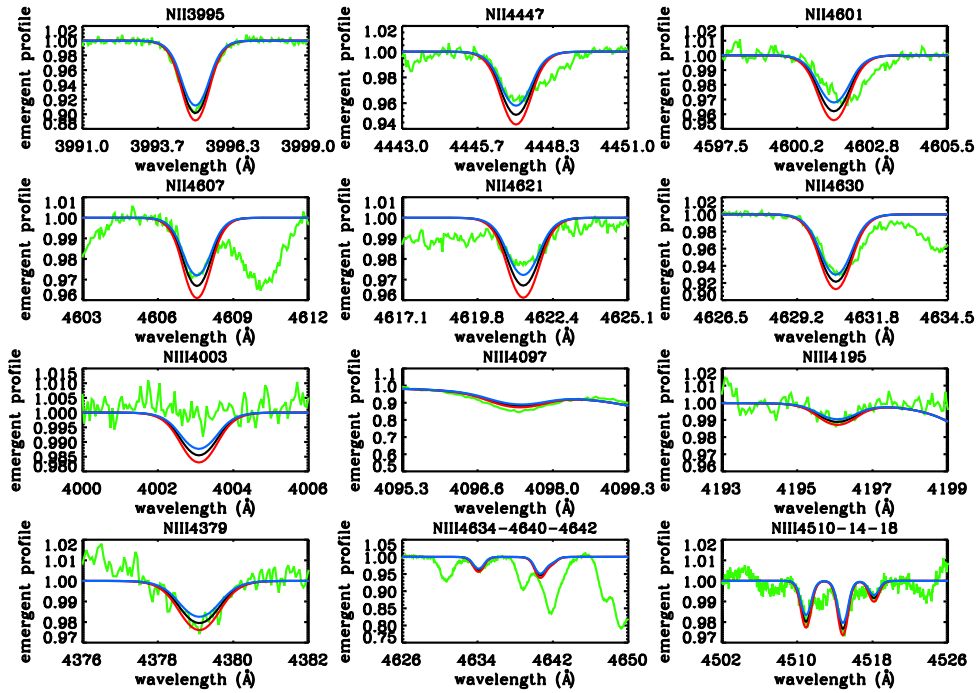


Figure C.3: N11-008 – B0.7 Ia.

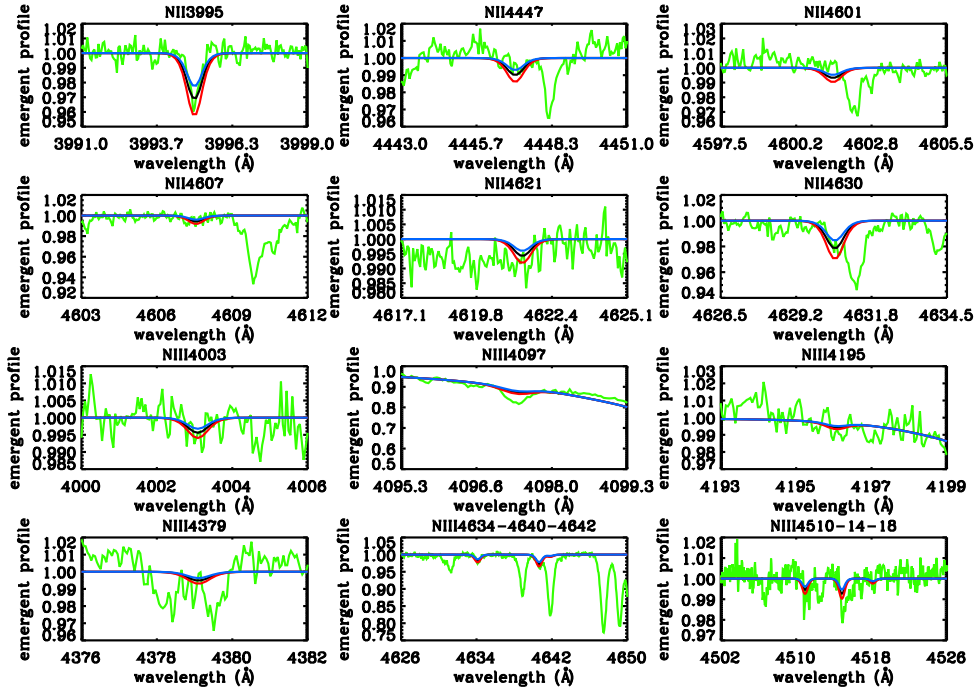


Figure C.4: N11-042 – B0 III.

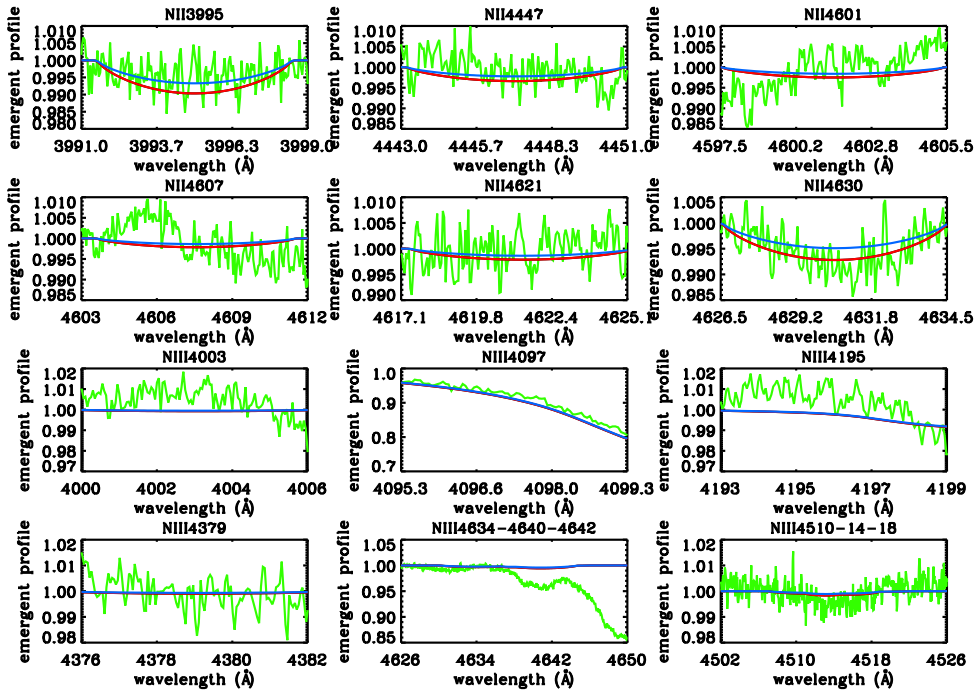
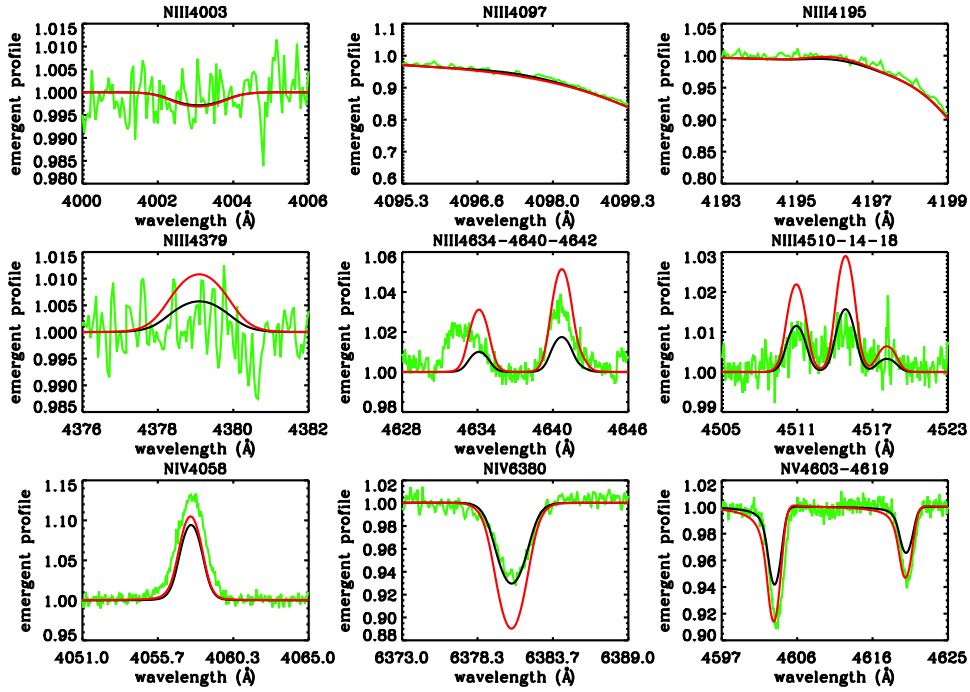
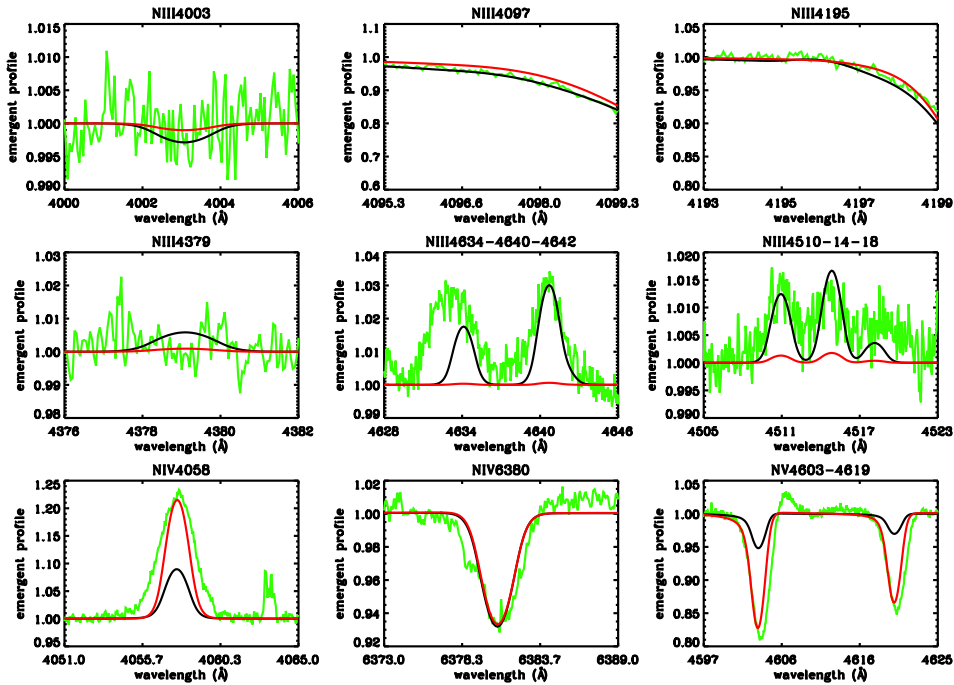


Figure C.5: N11-033 – B0 III_n.

Figure C.6: N11-026 – O2 III(f^*).Figure C.7: N11-031 – ON2 III(f^*). Black: cooler solution, supported by He I λ 4471, N III and N IV λ 6380. Red: hotter solution, supported by the N IV/N V lines (see Sect. 5.5).

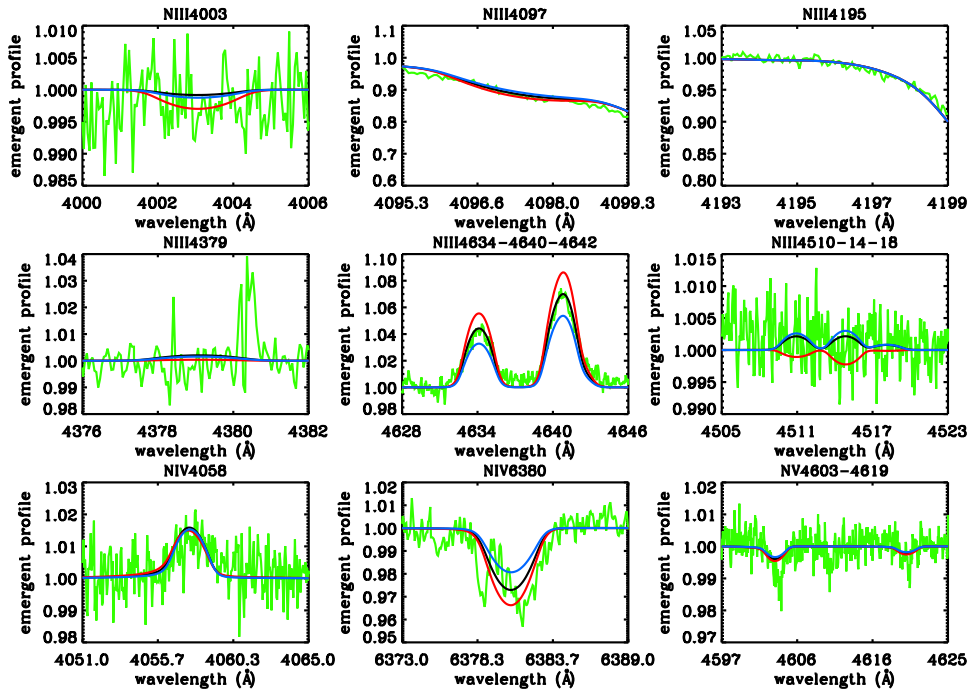


Figure C.8: N11-038 – O5 II(f⁺).

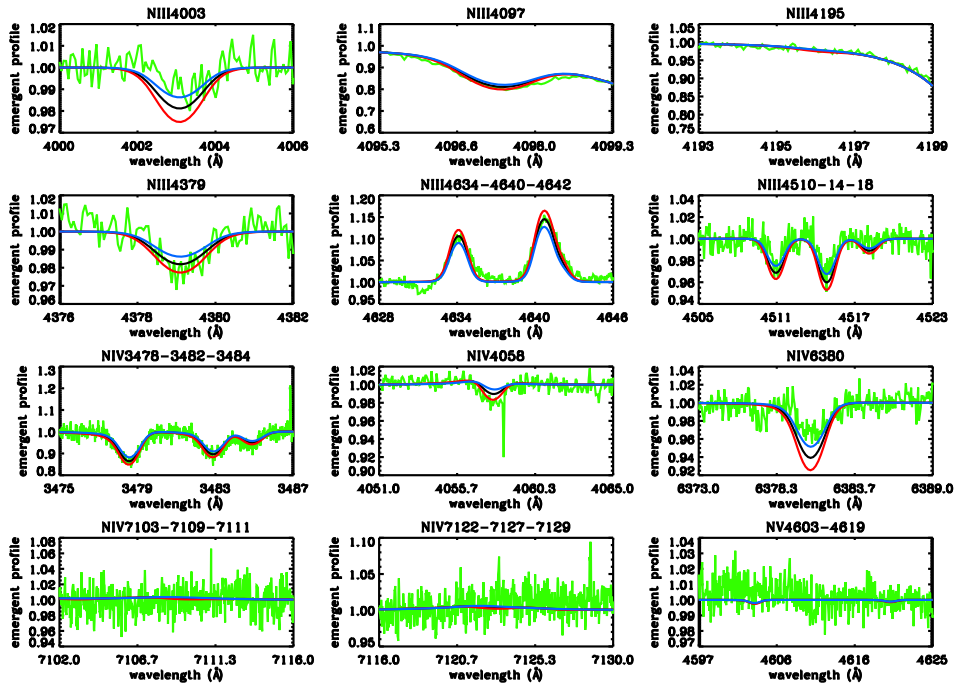


Figure C.9: Sk-66° 100 – O6 II(f).

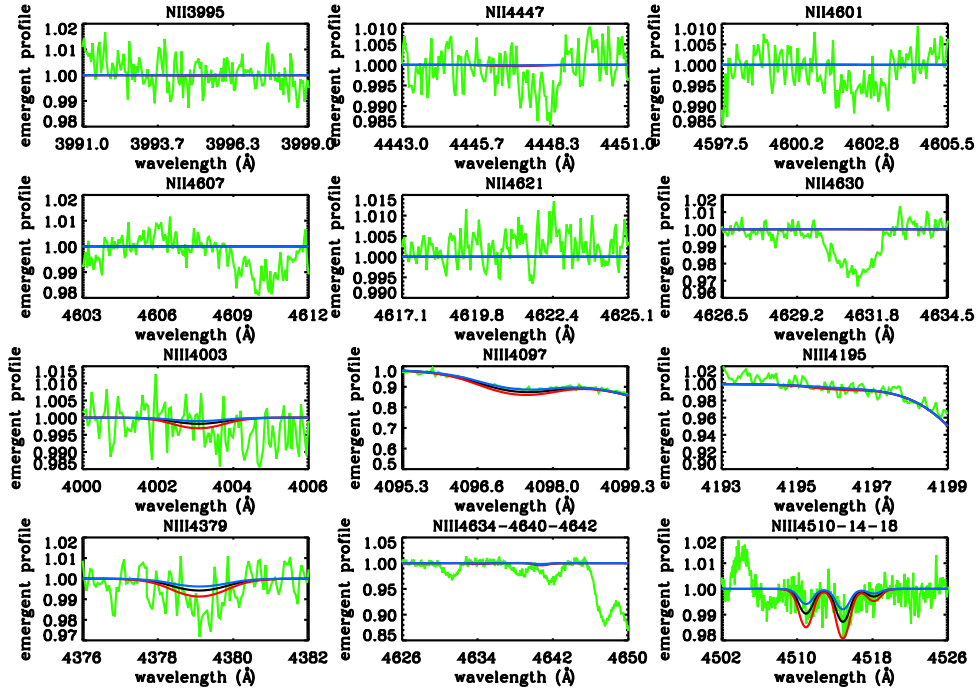


Figure C.10: N11-045 – O9 III.

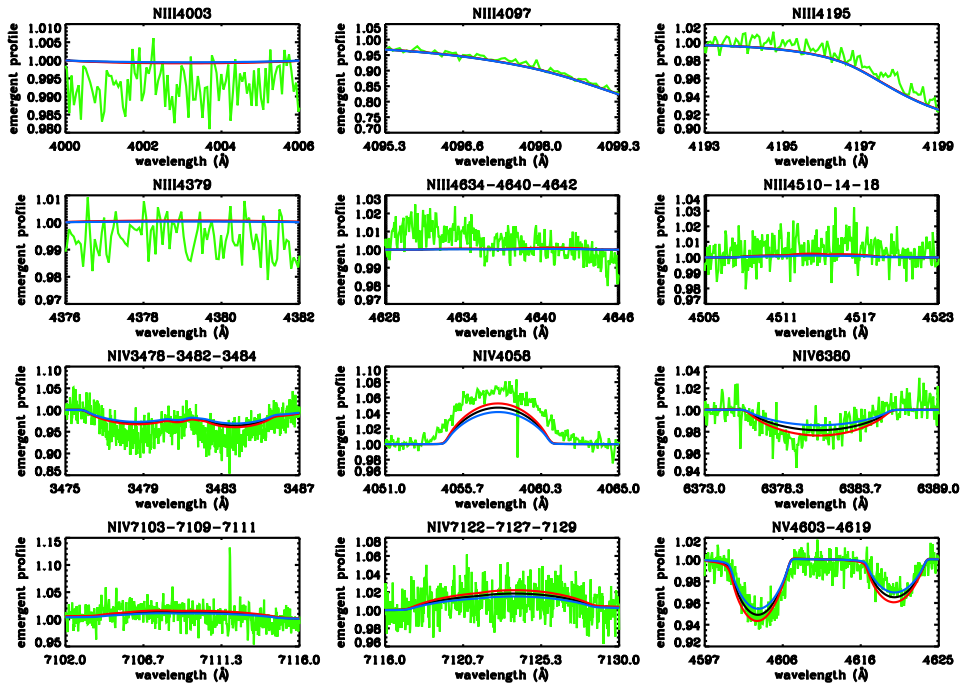


Figure C.11: BI253 – O2 V((f*)).

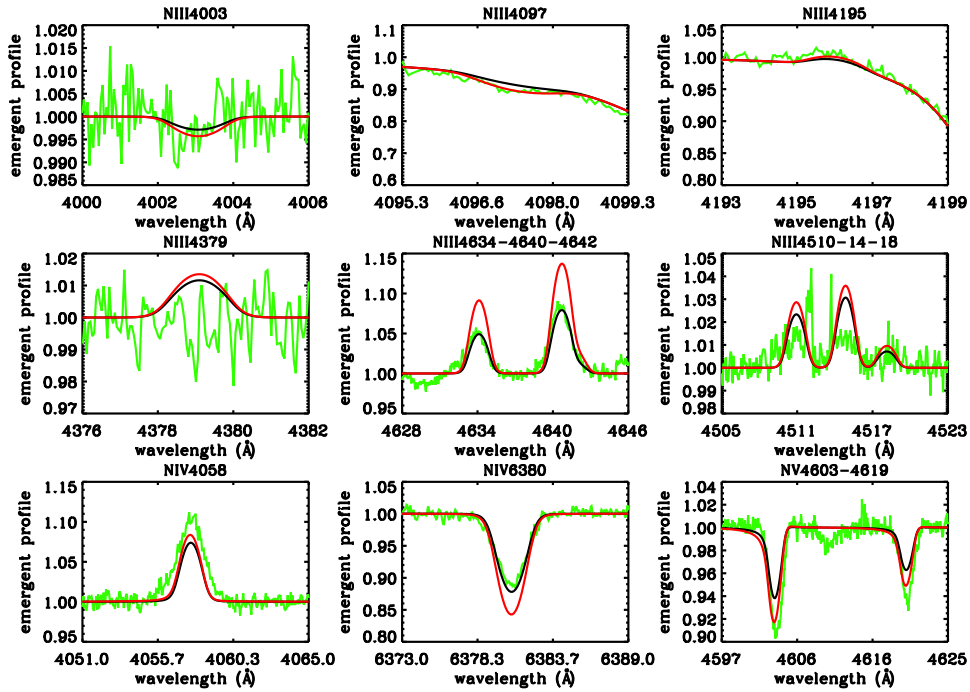


Figure C.12: N11-060 – O3 V((f*)).

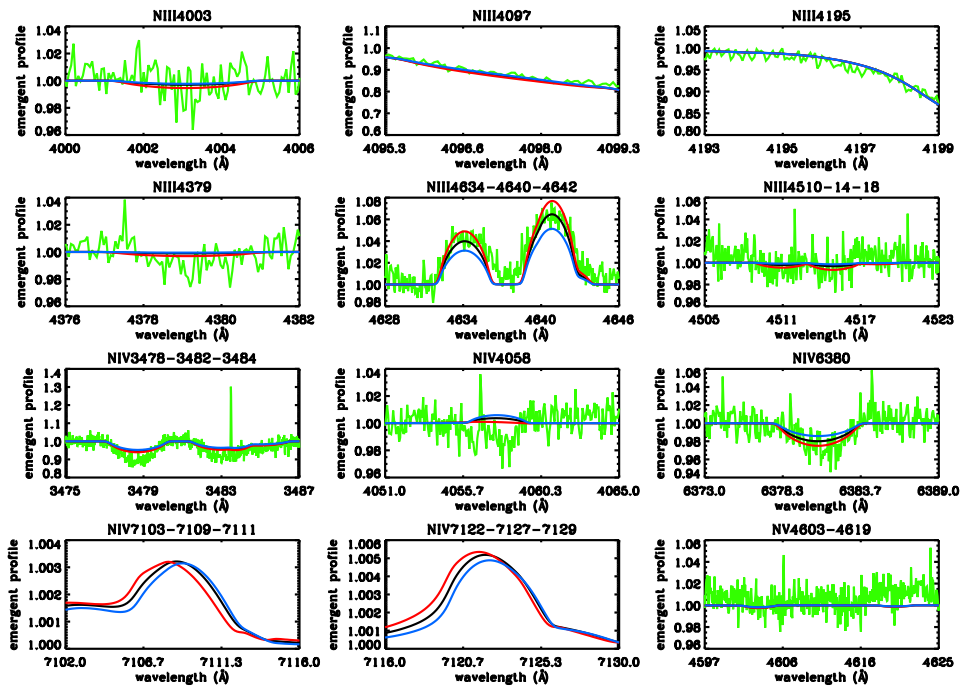


Figure C.13: Sk-70° 69 – O5 V((f)). For this star, the NIV multiplet at 7103-7129 Å has not been observed.

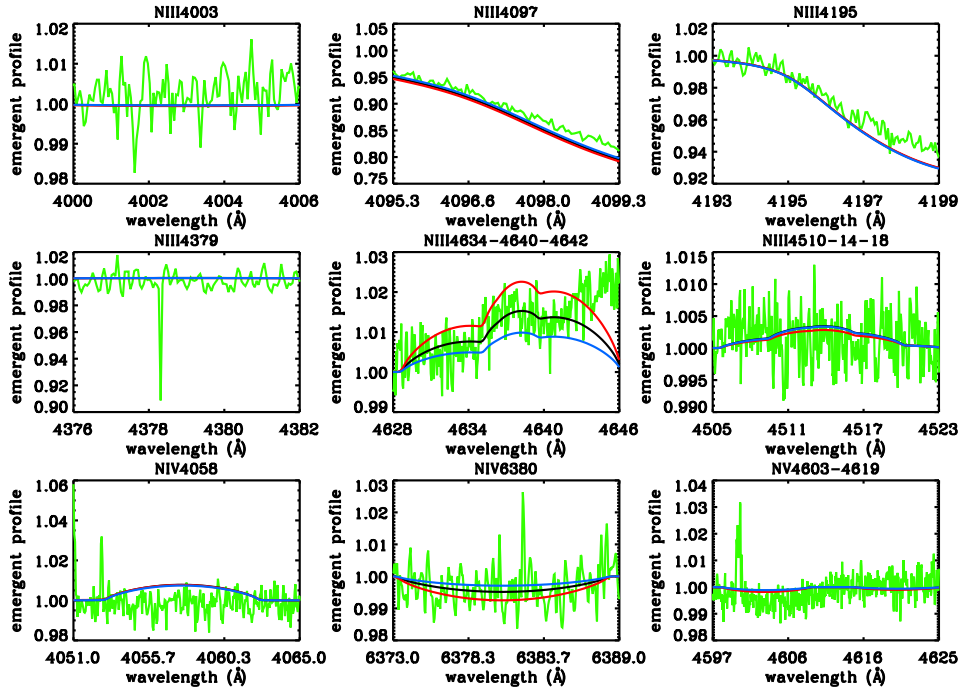


Figure C.14: N11-051– O5 Vn(f).

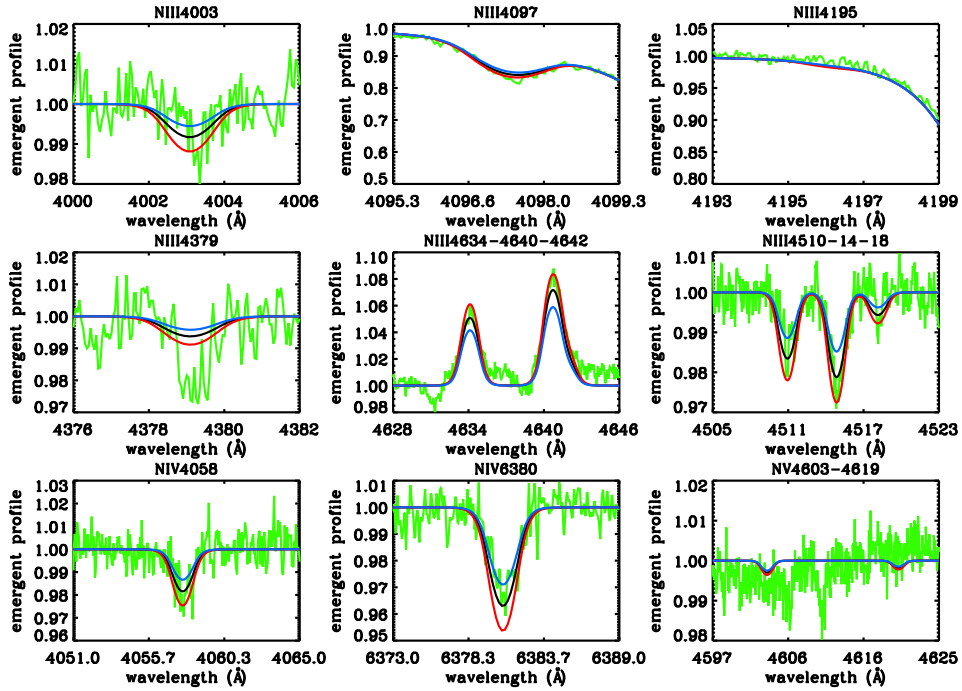


Figure C.15: N11-058 – O5.5 V(f).

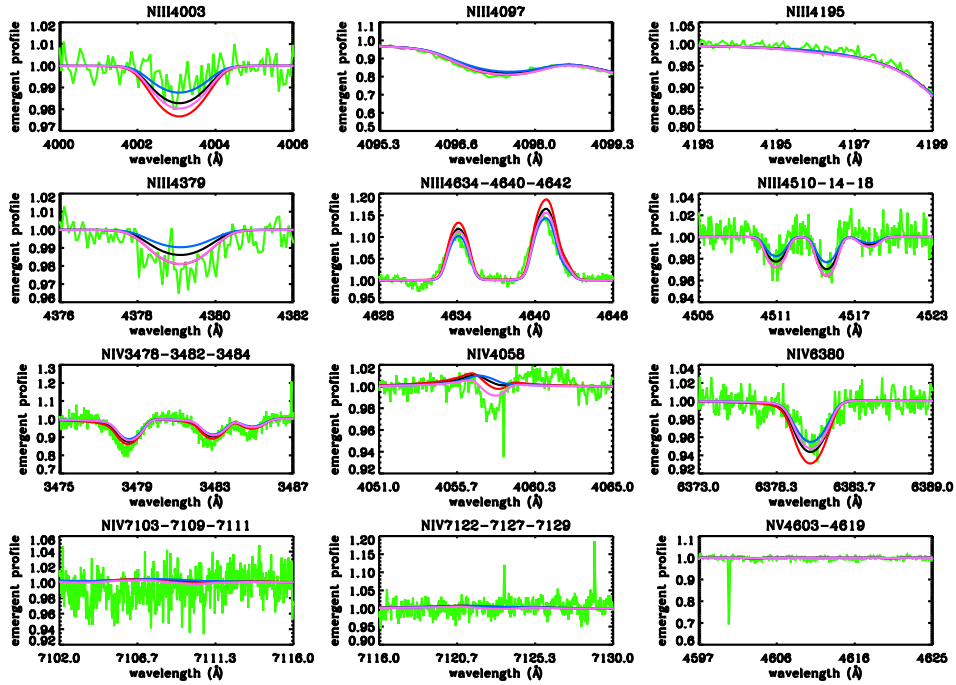


Figure C.16: Sk-66° 18 – O6 V((f)). Magenta spectra correspond to a weakly clumped model. For details, see Sect. 5.5.

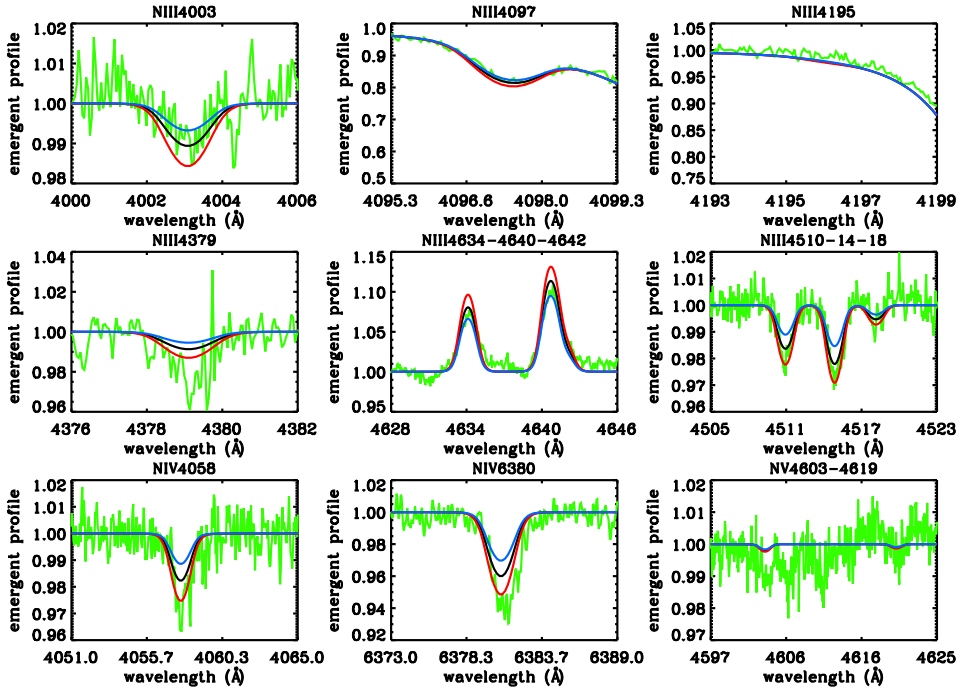


Figure C.17: N11-065 – O6.5 V((f)).

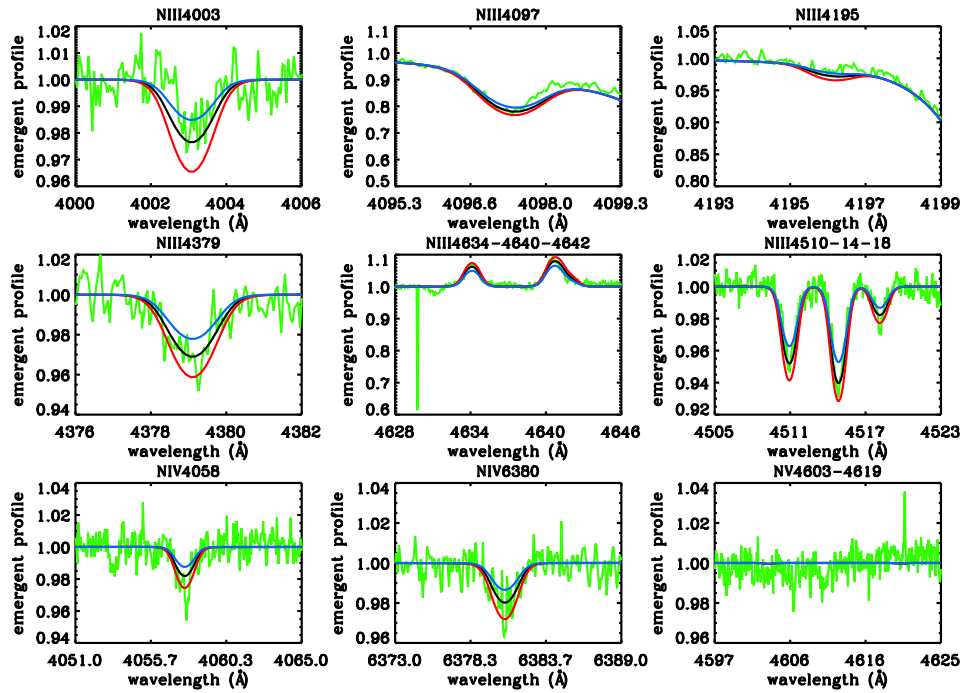


Figure C.18: N11-066 – O7 V((f)).

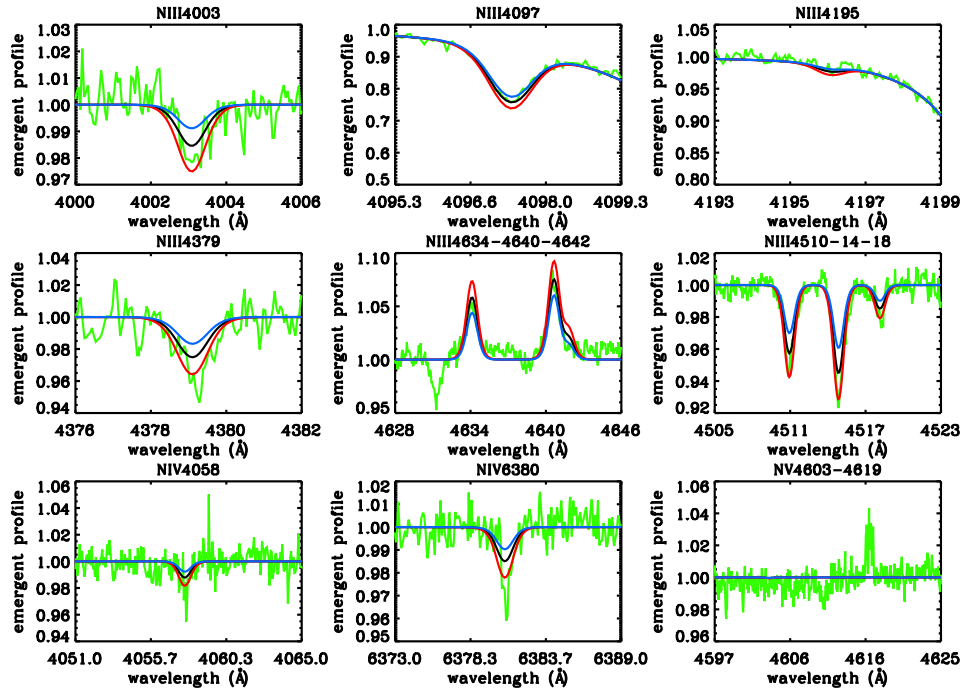


Figure C.19: N11-068 – O7 V((f)).

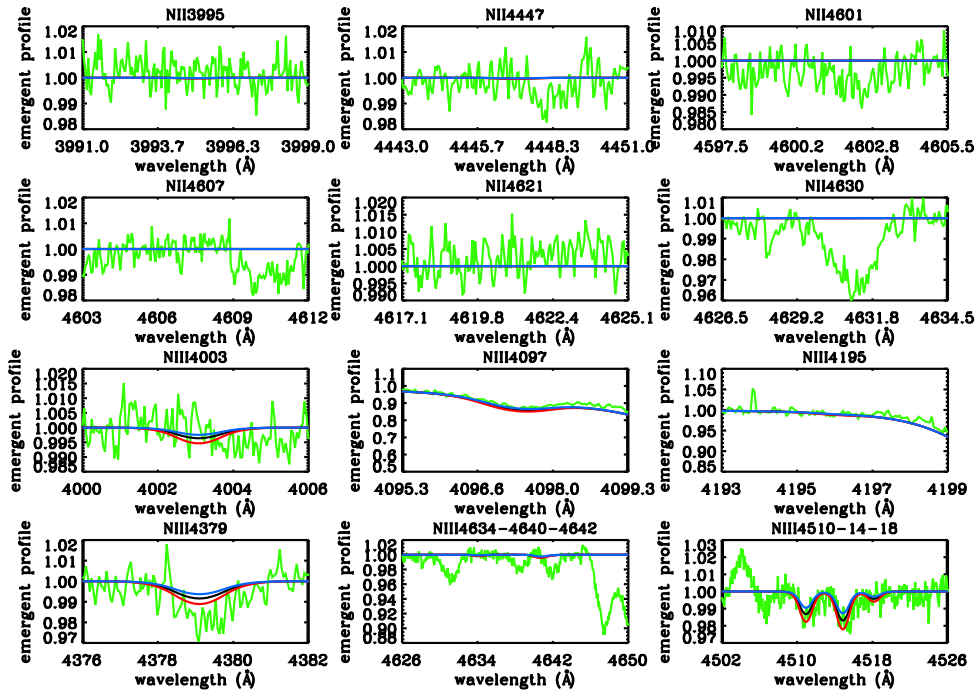


Figure C.20: N11-061 – O9 V.

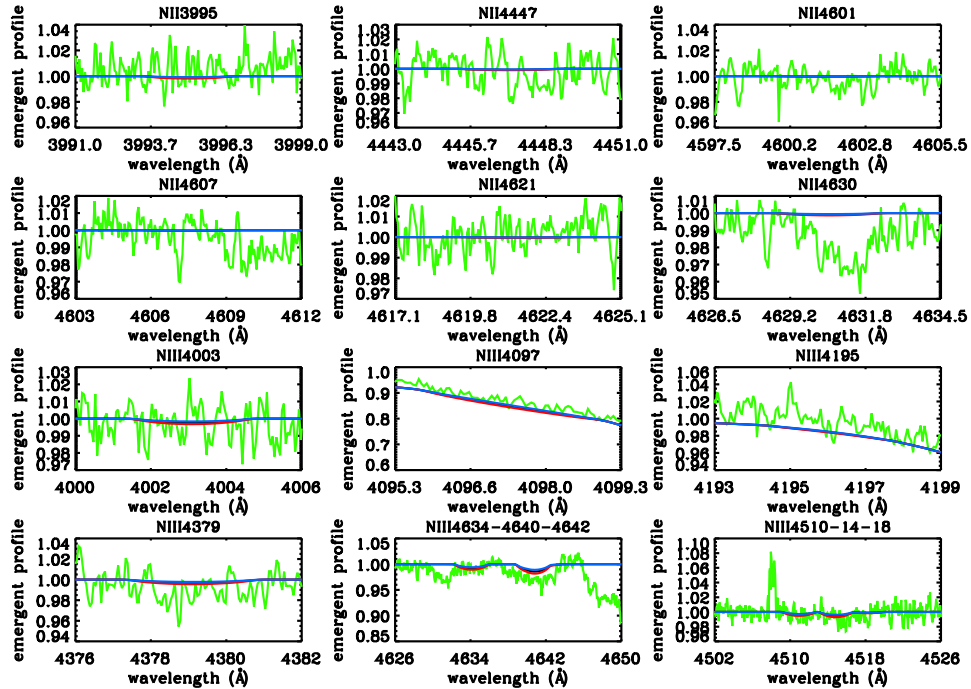


Figure C.21: N11-123 – O9.5 V.

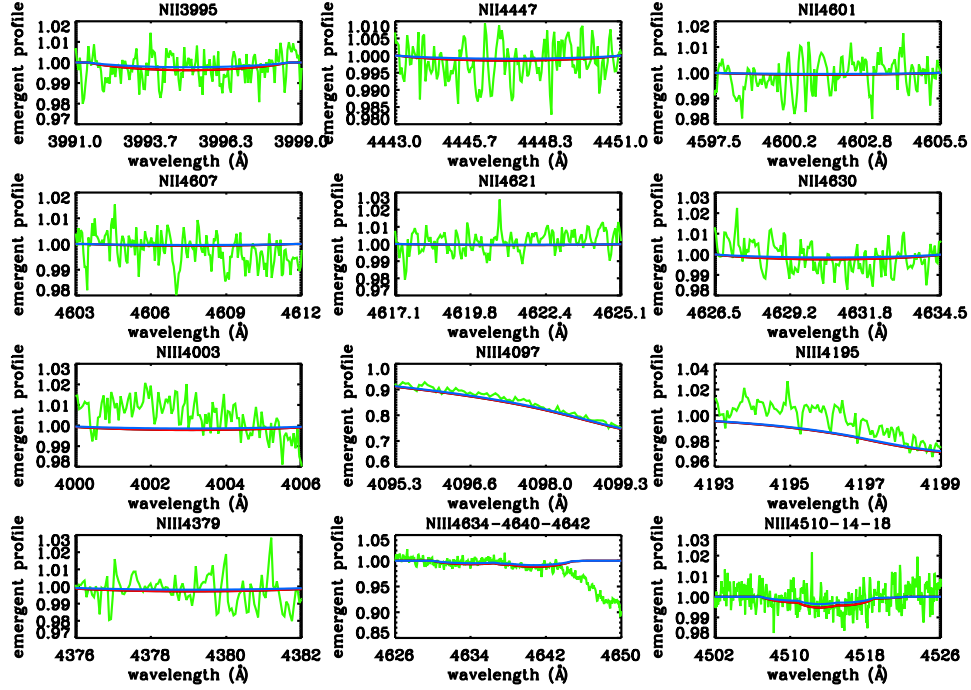


Figure C.22: N11-087 – O9.5 Vn.

C.2 Line fits for the LMC/SMC early O-star sample

In the following, we display the observed (green) and best-fitting optical H/He/N spectra (black) for all objects analyzed in Chapter 6 (Figs. C.23 to C.34). For NGC 346-355 (Fig. C.34), we show the fits corresponding to the two alternative solutions for this star and an 'average' solution as well (see Sect. 6.6.4). For details on the line fits, see Sect. 6.6.4, and for adopted stellar parameters and derived nitrogen abundances inspect Table 6.5.

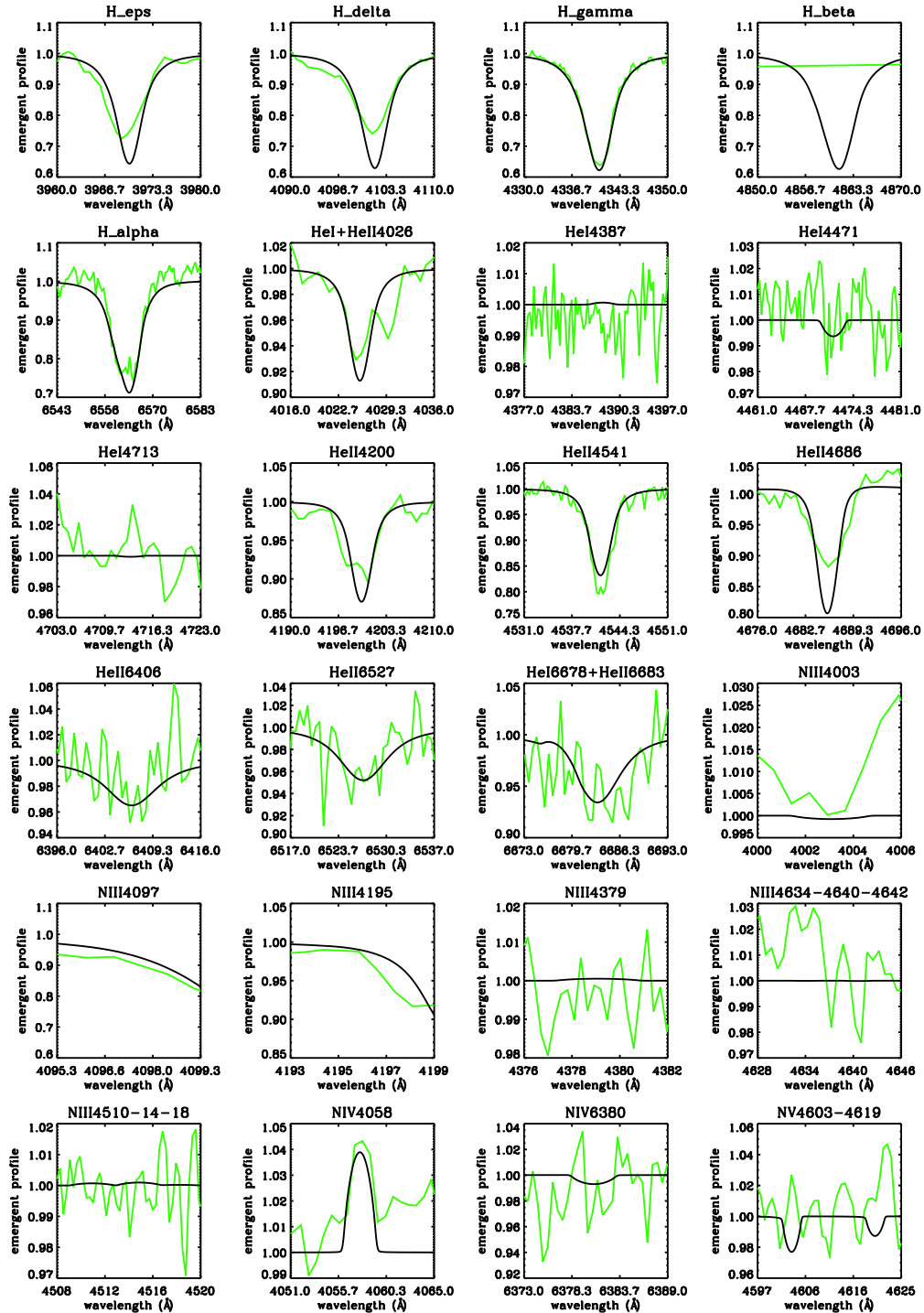


Figure C.23: R136-040 - O2-3.5 V. For the R136 O-stars, observed spectra for H_α , H_γ , $He\ I\ \lambda\lambda 4387$, 4471, 6678, $He\ II\ \lambda\lambda 4541$, 6406, 6527, 6683, $N\ III\ \lambda\lambda 4510$ -4514-4518, and $N\ IV\ \lambda 6380$ taken from the STIS/CCD dataset. Remaining, lower quality spectra collected by FOS. H_β was not observed for this star.

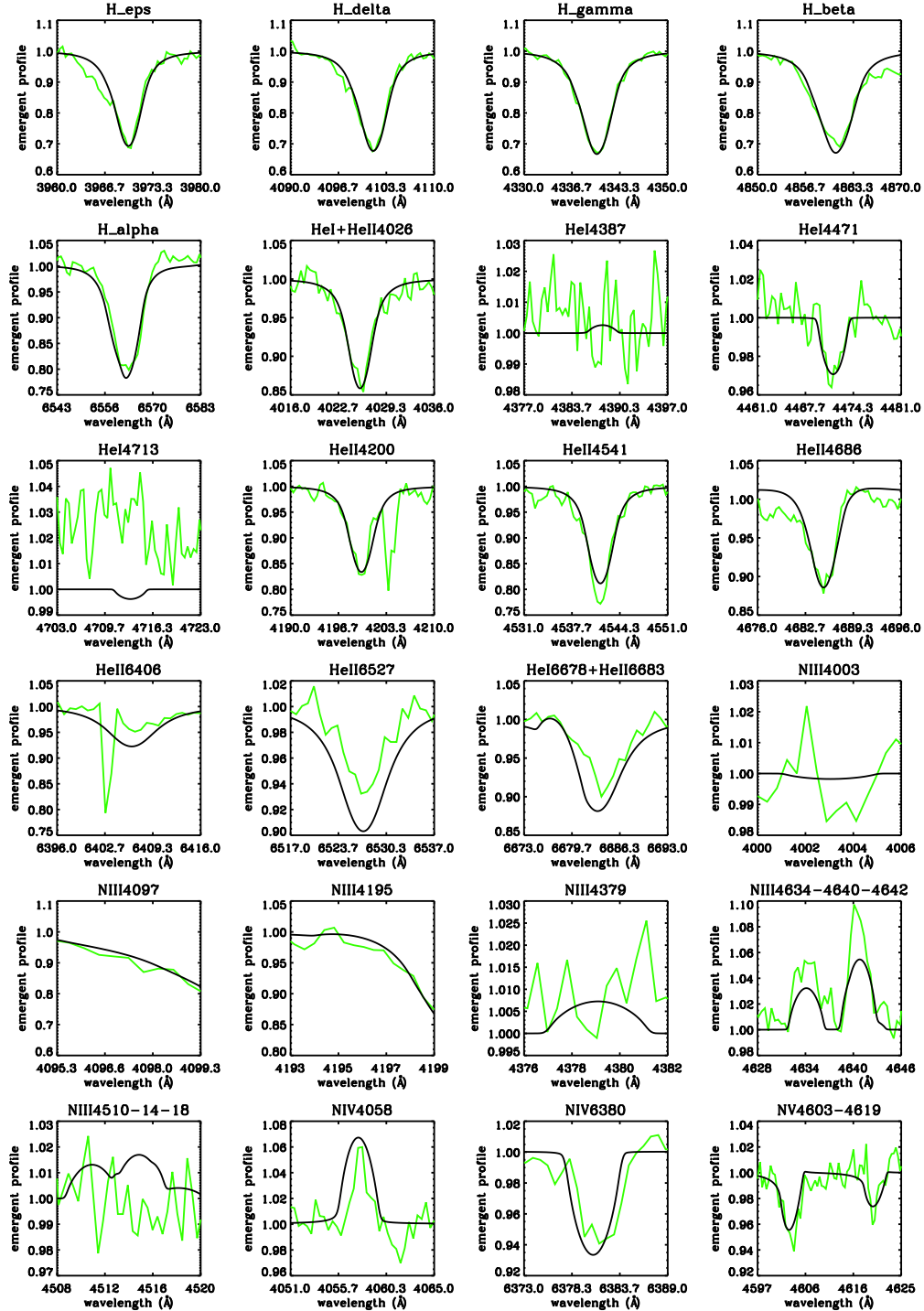


Figure C.24: LH 81:W28-23 - O3.5 V(f+).

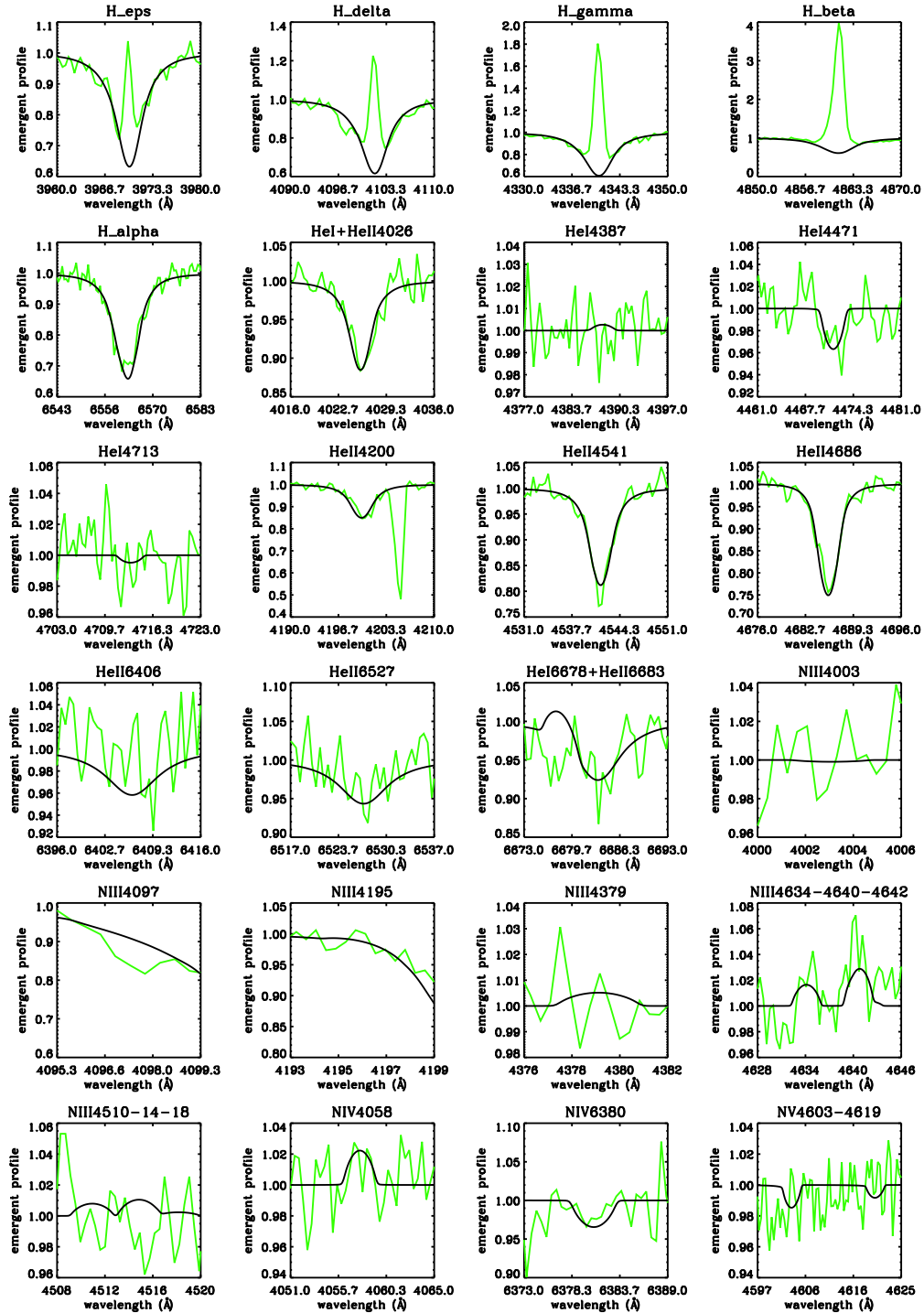


Figure C.25: LH 101:W3-24 - O3.5 V(f+).

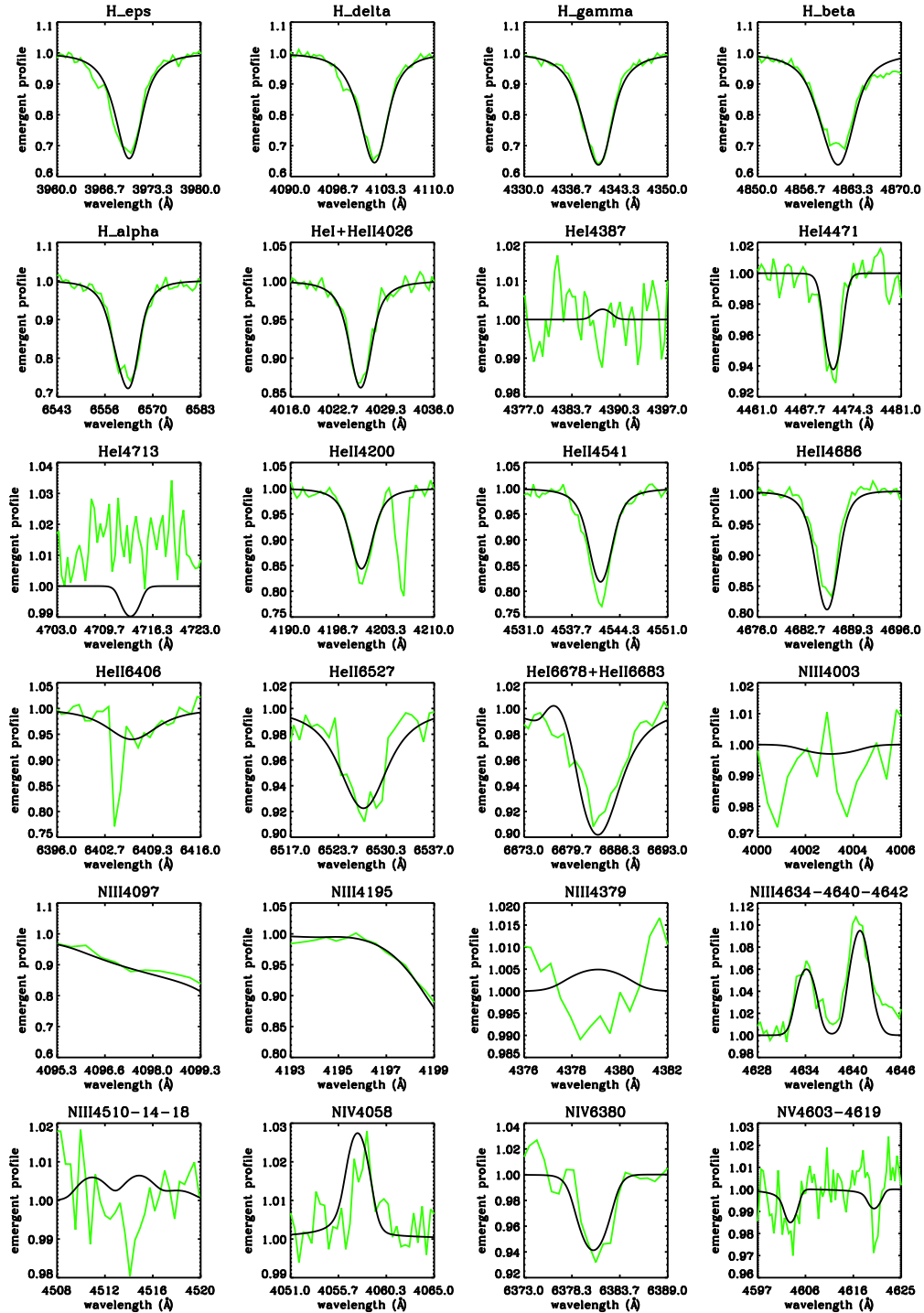
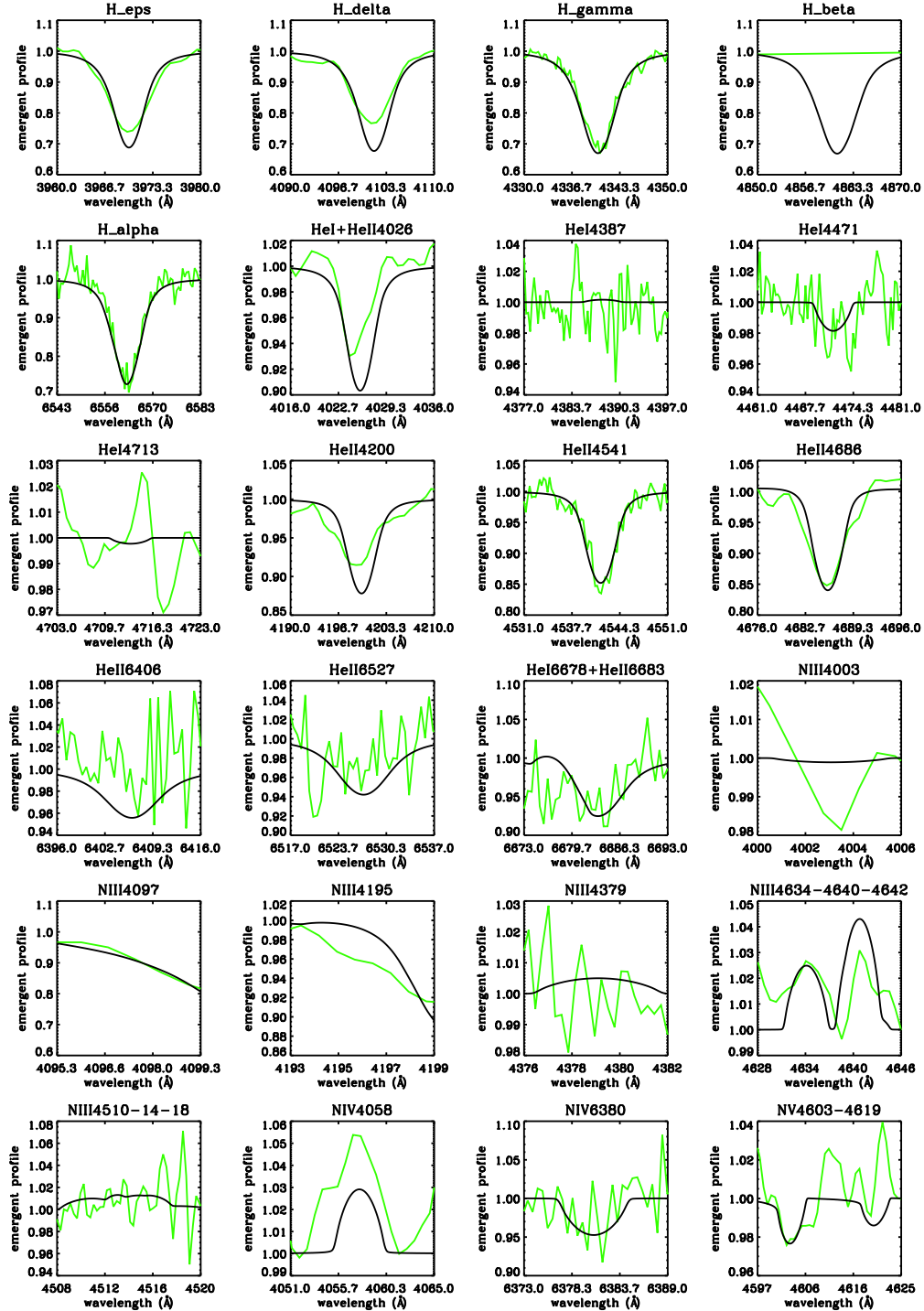


Figure C.26: LH 81:W28-5 - O4 V((f+)).

Figure C.27: R136-018 - O3 III(f^{*}). Observations as for R136-040 (Fig. C.23).

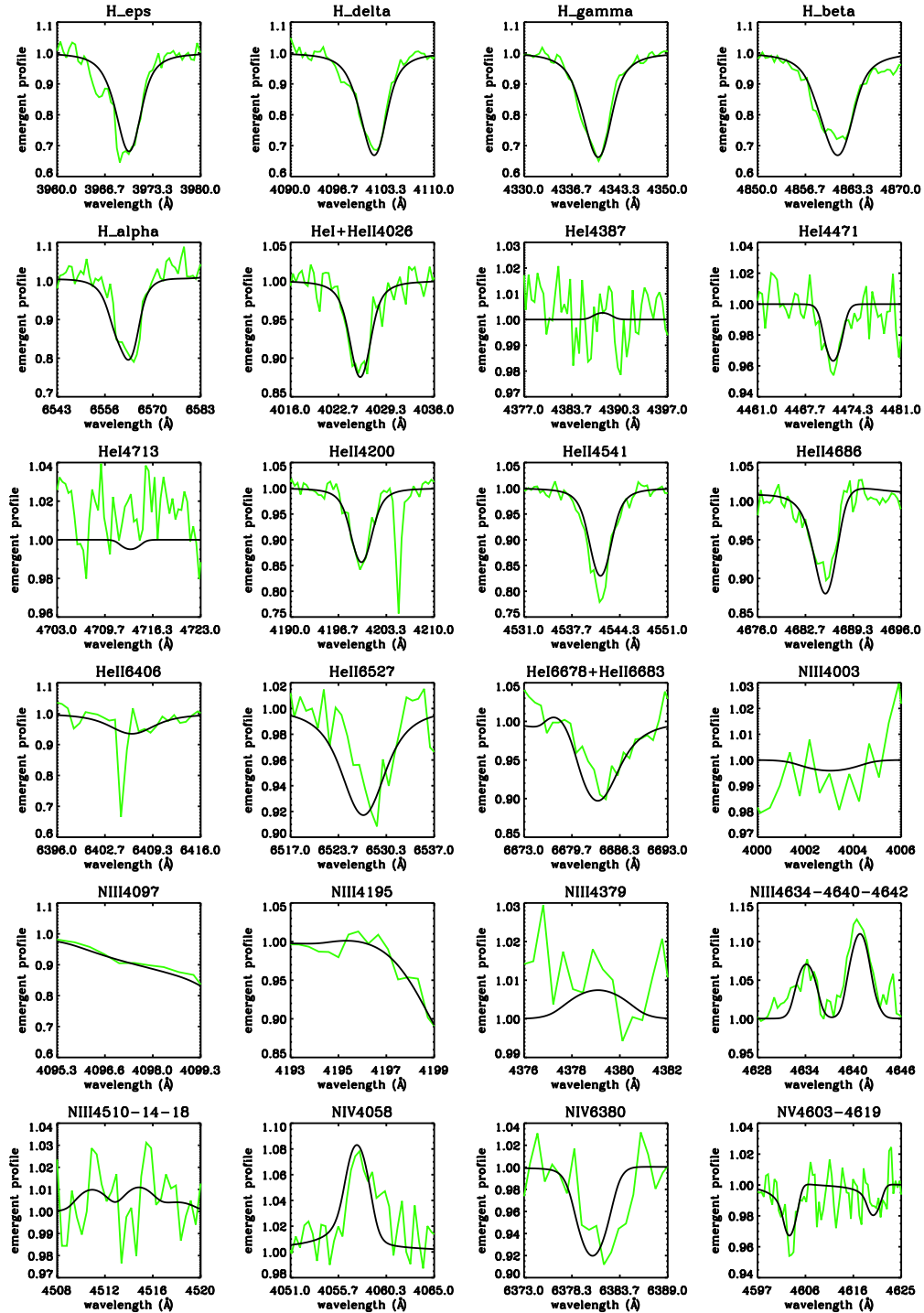


Figure C.28: LH 90:ST 2-22 - O3.5 III(f+).

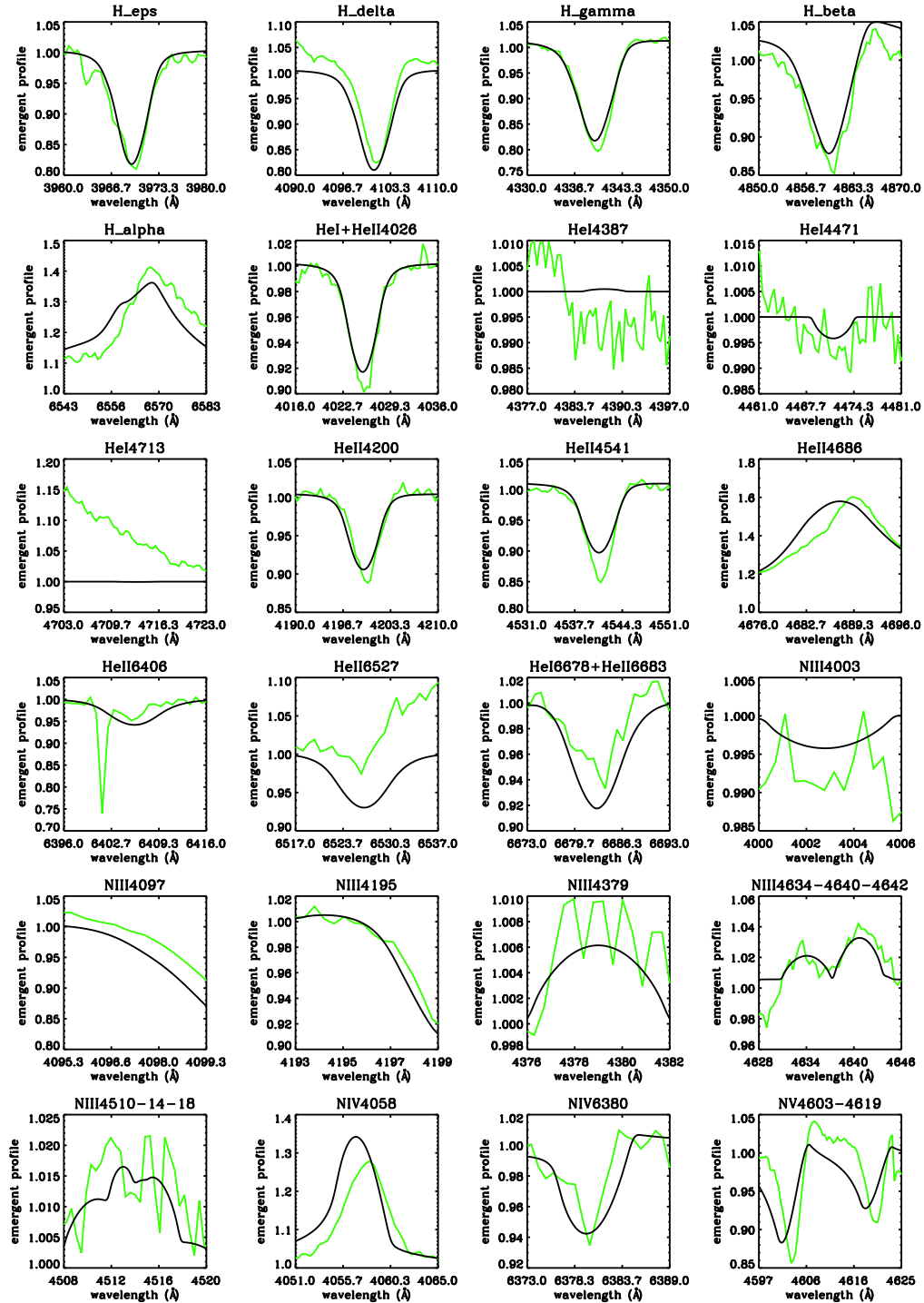


Figure C.29: Sk-67° 22 - O2 I^{*}/WN5.

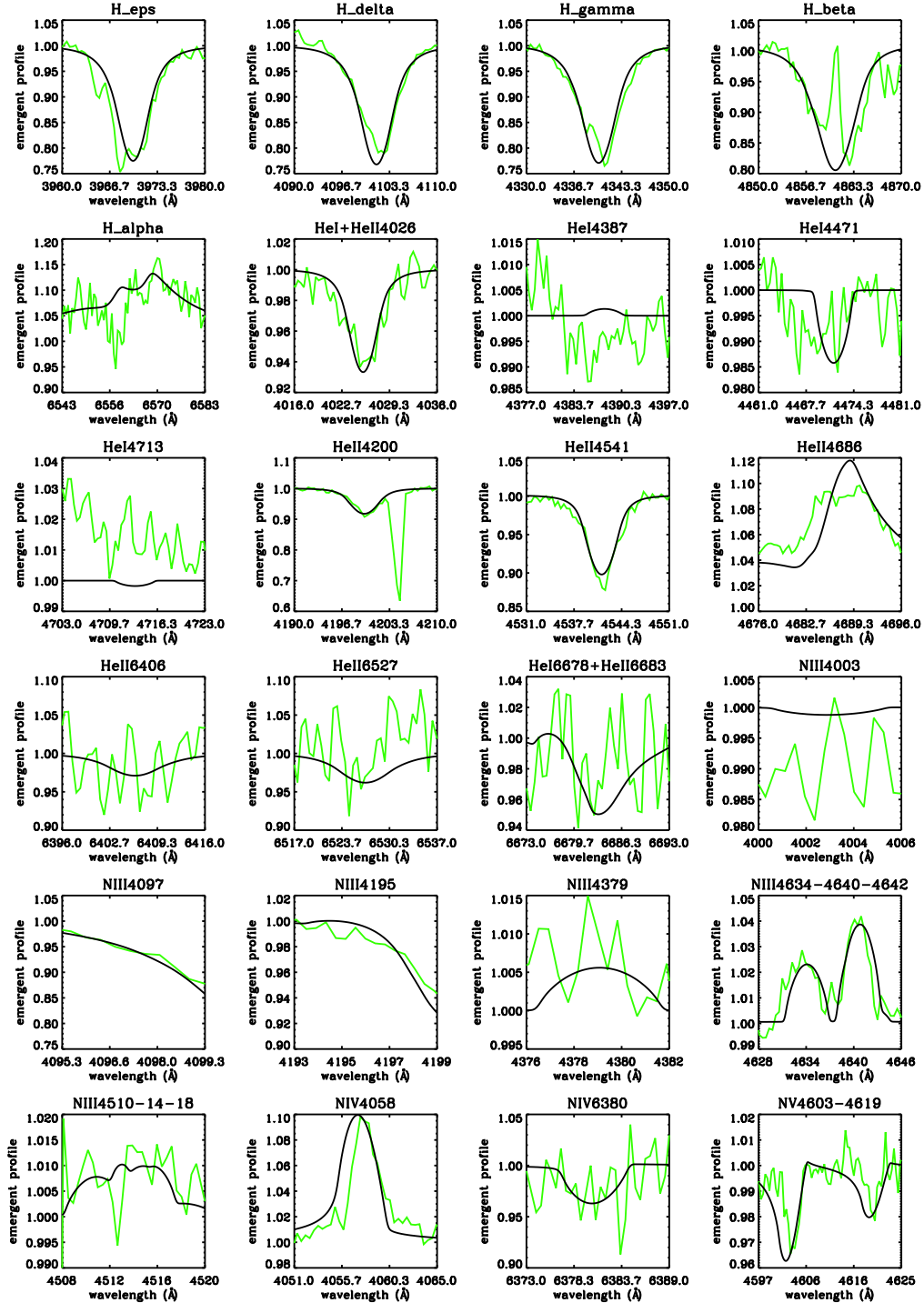


Figure C.30: LH 101:W3-19 - O2 If*.

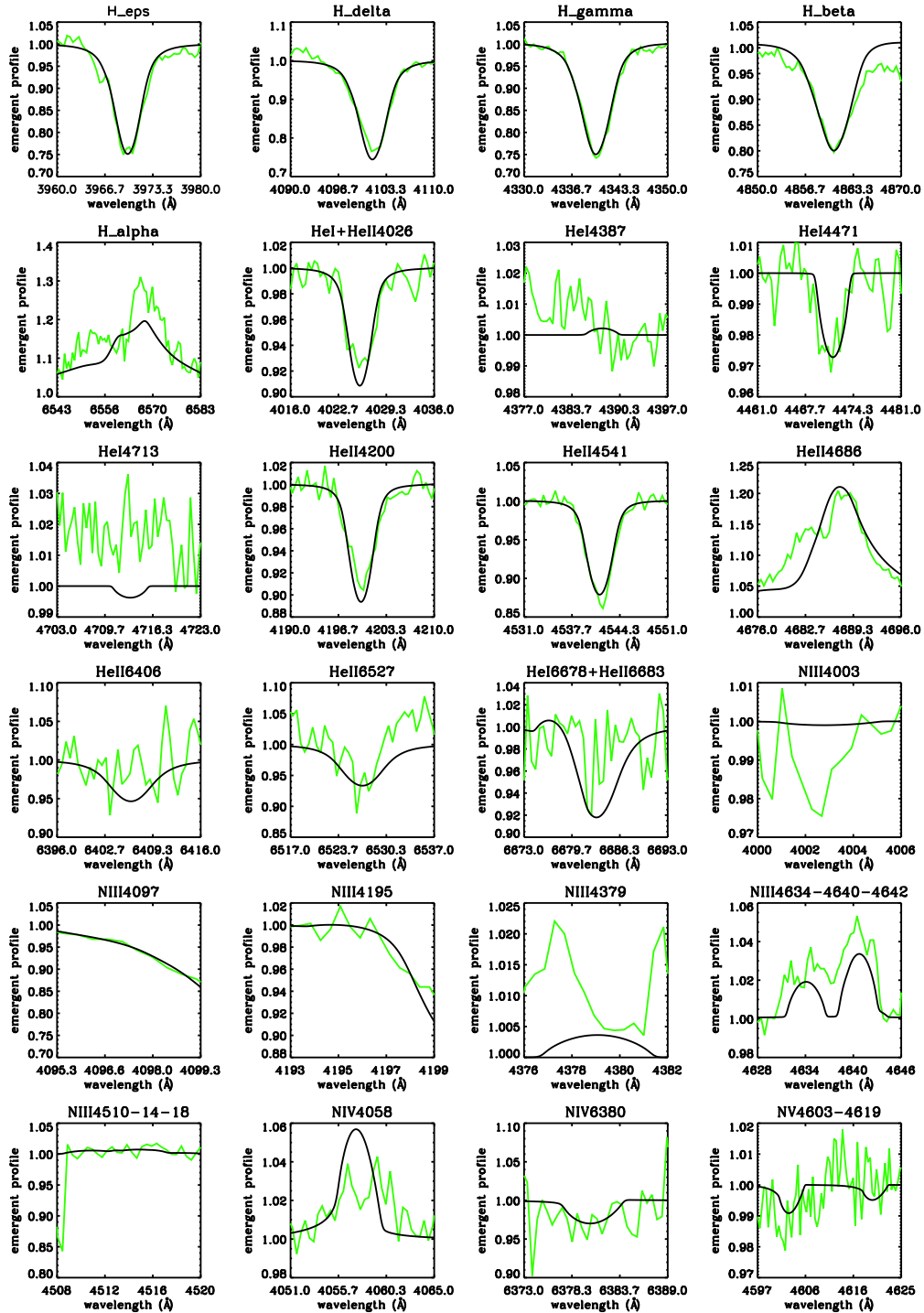


Figure C.31: Sk-65° 47 - O4 If.

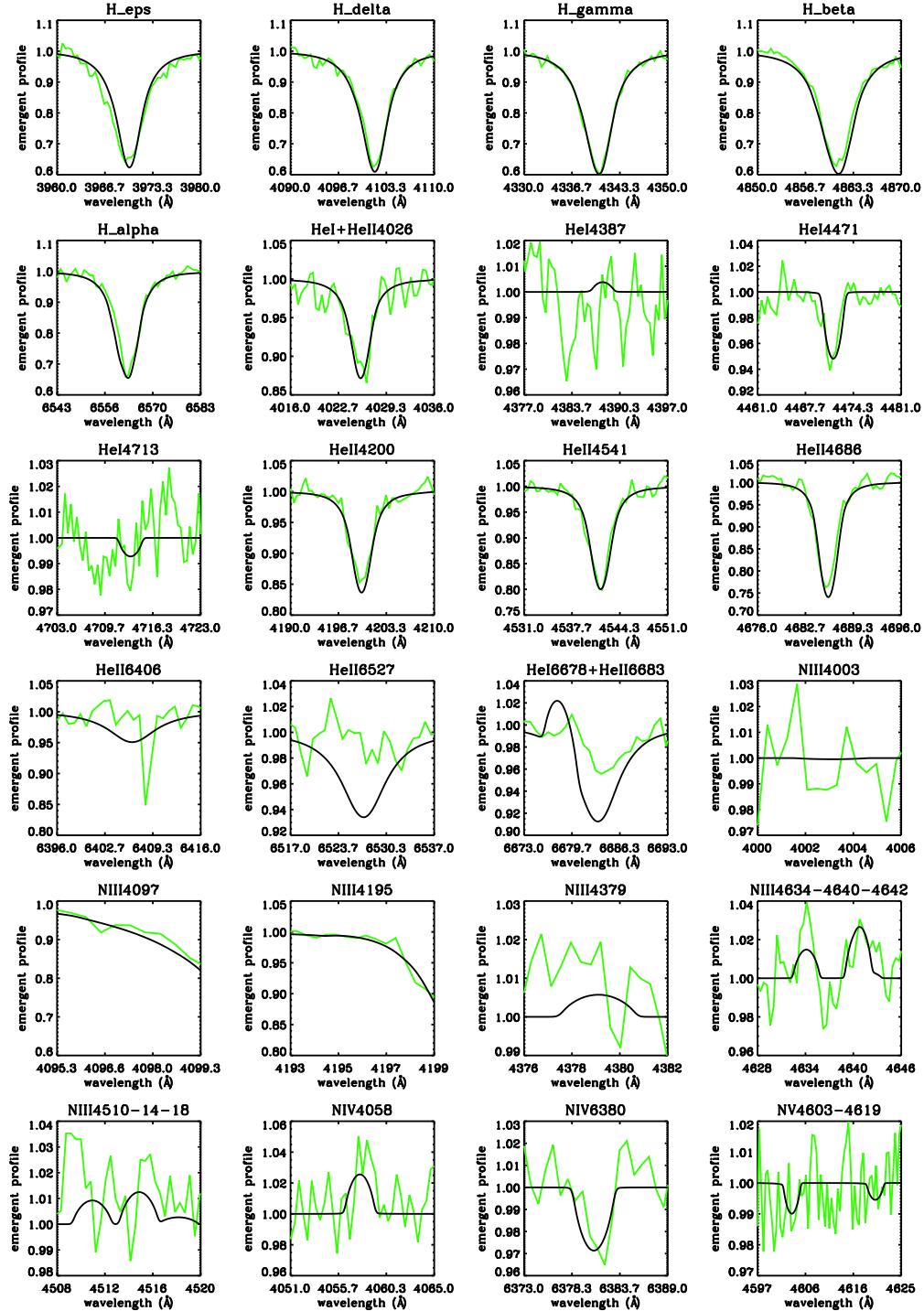


Figure C.32: AV 435 - O3 V((f*)).

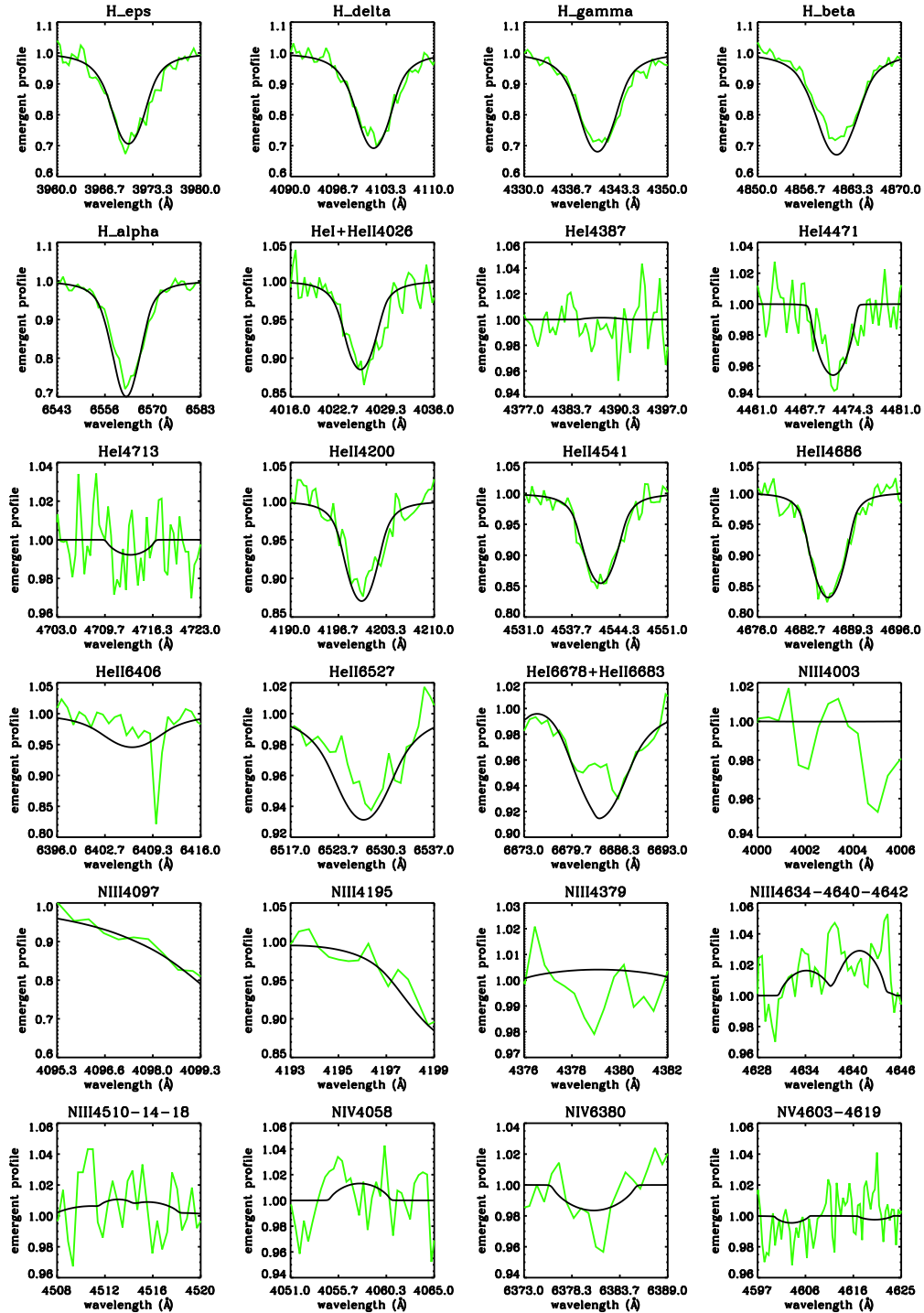


Figure C.33: AV 177 - O4 V(f).

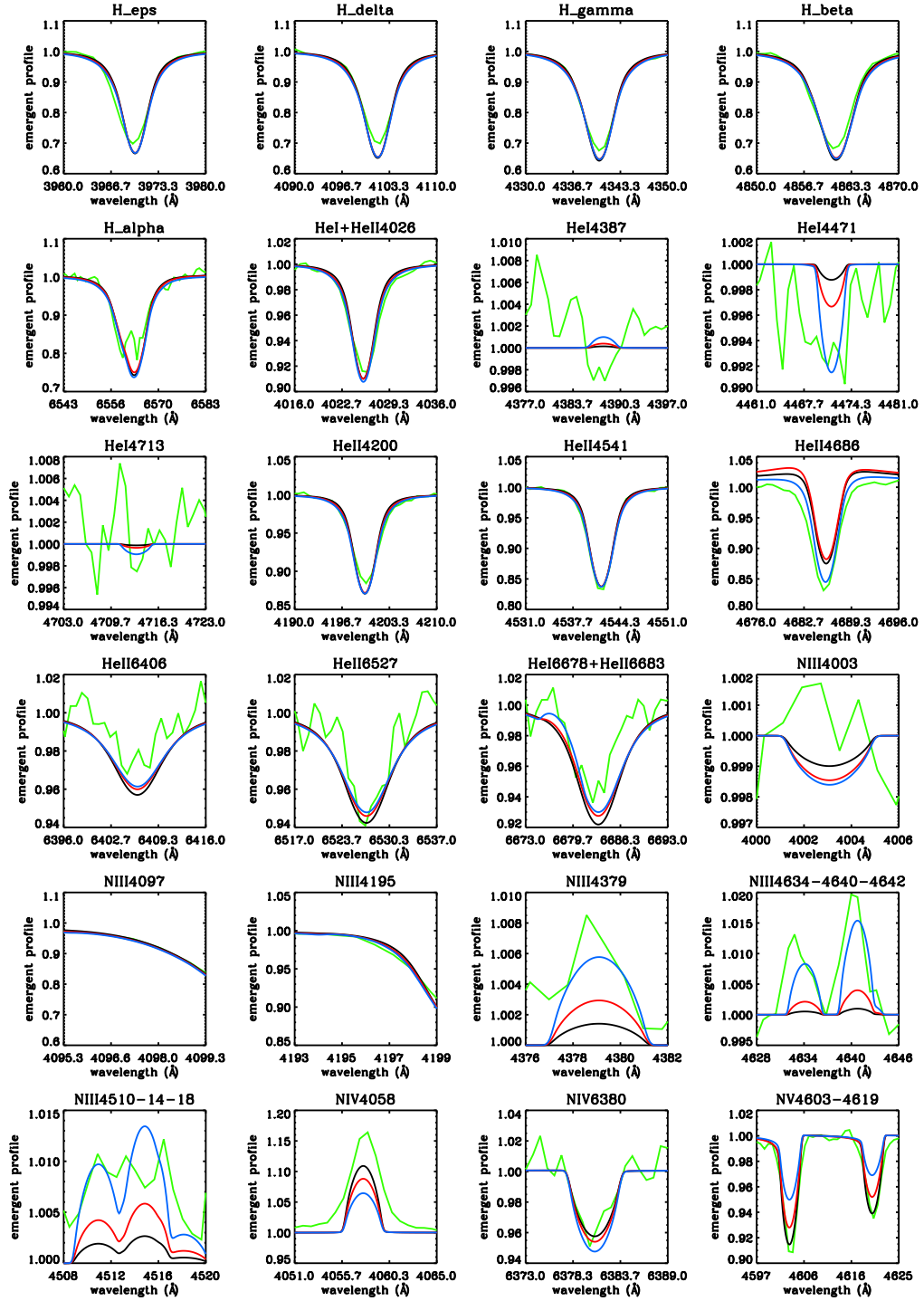


Figure C.34: NGC 346-355 - ON2 III(f^*). Black: hotter solution ($T_{\text{eff}} = 55$ kK), supported by N IV/N V lines. Blue: cooler solution ($T_{\text{eff}} = 51$ kK), mostly supported by N III (together with N IV λ 6380). Red: 'average' solution ($T_{\text{eff}} = 53$ kK) used in Sect. 6.7.

Bibliography

- Aerts, C., Puls, J., Godart, M., & Dupret, M.-A. 2009: *Collective pulsational velocity broadening due to gravity modes as a physical explanation for macroturbulence in hot massive stars*, A&A, 508, 409
- Allen, C. W. 1973, *Astrophysical quantities* (London: University of London, Athlone Press, 1973, 3rd ed.)
- Allende Prieto, C., Lambert, D. L., Hubeny, I., & Lanz, T. 2003: *Non-LTE Model Atmospheres for Late-Type Stars. I. A Collection of Data for Light Neutral and Singly Ionized Atoms*, ApJS, 147, 363
- Alongi, M., Bertelli, G., Bressan, A., Chiosi, C., Fagotto, F., Greggio, L., & Nasi, E. 1993: *Evolutionary sequences of stellar models with semiconvection and convective overshoot. I - $Z = 0.008$* , A&AS, 97, 851
- Asplund, M., Grevesse, N., & Sauval, A. J. 2005: *The Solar Chemical Composition*, in *Astronomical Society of the Pacific Conference Series*, Vol. 336, *Cosmic Abundances as Records of Stellar Evolution and Nucleosynthesis*, ed. T. G. Barnes III & F. N. Bash, 25
- Asplund, M., Grevesse, N., Sauval, A. J., & Scott, P. 2009: *The Chemical Composition of the Sun*, arXiv, 47, 481
- Azzopardi, M. & Vigneau, J. 1982: *Catalogue of the Small Magellanic Cloud star members*, A&AS, 50, 291
- Barbá, R. H., Gamen, R., Arias, J. I., Morrell, N., Maíz Apellániz, J., Alfaro, E., Walborn, N., & Sota, A. 2010: *Spectroscopic survey of galactic O and WN stars. OWN Survey: new binaries and trapezium-like systems*, in *Revista Mexicana de Astronomía y Astrofísica*, vol. 27, Vol. 38, *Revista Mexicana de Astronomía y Astrofísica Conference Series*, 30–32
- Bautista, M. A., Romano, P., & Pradhan, A. K. 1998: *Resonance-averaged Photoionization Cross Sections for Astrophysical Models*, ApJS, 118, 259
- Becker, S. R. & Butler, K. 1989: *Non-LTE line formation in early B and late O stars. IV - Singly ionized nitrogen*, A&A, 209, 244
- Bell, K. L., Hibbert, A., Stafford, R. P., & Brage, T. 1995: *Transition probabilities for some spectral lines of N III*, MNRAS, 272, 909

- Berrington, K. A., Burke, P. G., Butler, K., Seaton, M. J., Storey, P. J., Taylor, K. T., & Yan, Y. 1987: *Atomic data for opacity calculations. II. Computational methods*, Journal of Physics B Atomic Molecular Physics, 20, 6379
- Bosch, G., Terlevich, E., & Terlevich, R. 2009: *Gemini/GMOS Search for Massive Binaries in the Ionizing Cluster of 30 Dor*, AJ, 137, 3437
- Bouret, J.-C., Lanz, T., Hillier, D. J., Heap, S. R., Hubeny, I., Lennon, D. J., Smith, L. J., & Evans, C. J. 2003: *Quantitative Spectroscopy of O Stars at Low Metallicity: O Dwarfs in NGC 346*, ApJ, 595, 1182
- Bowen, I. S. 1935: *The Spectrum and Composition of the Gaseous Nebulae*, ApJ, 81, 1
- Bressan, A., Fagotto, F., Bertelli, G., & Chiosi, C. 1993: *Evolutionary sequences of stellar models with new radiative opacities. II - $Z = 0.02$* , A&AS, 100, 647
- Breysacher, J., Azzopardi, M., & Testor, G. 1999: *The fourth catalogue of Population I Wolf-Rayet stars in the Large Magellanic Cloud*, A&AS, 137, 117
- Briceño, C. 2009: *OB Associations: new insights from large scale surveys*, in Revista Mexicana de Astronomía y Astrofísica Conference Series, Vol. 35, Revista Mexicana de Astronomía y Astrofísica Conference Series, 27–32
- Bromm, V., Kudritzki, R. P., & Loeb, A. 2001: *Generic Spectrum and Ionization Efficiency of a Heavy Initial Mass Function for the First Stars*, ApJ, 552, 464
- Bromm, V. & Larson, R. B. 2004: *The First Stars*, ARA&A, 42, 79
- Bromm, V., Yoshida, N., Hernquist, L., & McKee, C. F. 2009: *The formation of the first stars and galaxies*, Nat, 459, 49
- Brott, I., de Mink, S. E., Cantiello, M., Langer, N., de Koter, A., Evans, C. J., Hunter, I., Trundle, C., & Vink, J. S. 2011a: *Rotating massive main-sequence stars. I. Grids of evolutionary models and isochrones*, A&A, 530, A115
- Brott, I., Evans, C. J., Hunter, I., de Koter, A., Langer, N., Dufton, P. L., Cantiello, M., Trundle, C., Lennon, D. J., de Mink, S. E., Yoon, S.-C., et al. 2011b: *Rotating massive main-sequence stars. II. Simulating a population of LMC early B-type stars as a test of rotational mixing*, A&A, 530, A116
- Bruccato, R. J. & Mihalas, D. 1971: *On the excitation mechanism of M emission in the Of stars*, MNRAS, 154, 491
- Brunet, J. P., Imbert, M., Martin, N., Mianes, P., Prévot, L., Rebeirot, E., & Rousseau, J. 1975: *Studies of the LMC stellar content. I. A catalogue of 272 new O-B2 stars.*, A&AS, 21, 109
- Butler, K. & Giddings, J. R. 1985: *notitle*, Newsl. Anal. Astron. Spectra, 9
- Cantiello, M., Langer, N., Brott, I., de Koter, A., Shore, S. N., Vink, J. S., Voegler, A., Lennon, D. J., & Yoon, S.-C. 2009: *Sub-surface convection zones in hot massive stars and their observable consequences*, A&A, 499, 279

- Charbonnel, C., Meynet, G., Maeder, A., Schaller, G., & Schaerer, D. 1993: *Grids of Stellar Models - Part Three - from 0.8 to 120-SOLAR-MASSSES at Z=0.004*, A&AS, 101, 415
- Conti, P. S. & Alschuler, W. R. 1971: *Spectroscopic Studies of O-Type Stars. I. Classification and Absolute Magnitudes*, ApJ, 170, 325
- Cowley, C. R. 1971: *An approximate Stark broadening formula for use in spectrum synthesis*, The Observatory, 91, 139
- Cranmer, S. R. & Owocki, S. P. 1995: *The effect of oblateness and gravity darkening on the radiation driving in winds from rapidly rotating B stars*, ApJ, 440, 308
- Crowther, P. 2007: *Physical properties of Wolf-Rayet stars*, ARA&A, 45, 177
- Crowther, P. A. 2000: *Wind properties of Wolf-Rayet stars at low metallicity: Sk 41 (SMC)*, A&A, 356, 191
- Crowther, P. A., Hillier, D. J., Evans, C. J., Fullerton, A. W., De Marco, O., & Willis, A. J. 2002: *Revised Stellar Temperatures for Magellanic Cloud O Supergiants from Far Ultraviolet Spectroscopic Explorer and Very Large Telescope UV-Visual Echelle Spectrograph Spectroscopy*, ApJ, 579, 774
- Crowther, P. A., Schnurr, O., Hirschi, R., Yusof, N., Parker, R. J., Goodwin, S. P., & Kassim, H. A. 2010: *The R136 star cluster hosts several stars whose individual masses greatly exceed the accepted $150M_{\text{solar}}$ stellar mass limit*, MNRAS, 408, 731
- Crowther, P. A. & Walborn, N. R. 2011: *Spectral classification of O2-3.5 If*/WN5-7 stars*, MNRAS, 416, 1311
- Cunto, W. & Mendoza, C. 1992: *The Opacity Project - the Topbase Atomic Database*, Revista Mexicana de Astronomia y Astrofisica, vol. 23, 23, 107
- Daflon, S., Cunha, K., & Butler, K. 2004: *Chemical Abundances for a Sample of Southern OB Stars*, ApJ, 604, 362
- de Mink, S. E., Pols, O. R., & Hilditch, R. W. 2007: *Efficiency of mass transfer in massive close binaries. Tests from double-lined eclipsing binaries in the SMC*, A&A, 467, 1181
- de Mink, S. E., Pols, O. R., Langer, N., & Izzard, R. G. 2009: *Massive binaries as the source of abundance anomalies in globular clusters*, A&A, 507, L1
- Doran, E. I. & Crowther, P. A. 2011: *A VLT/UVES spectroscopy study of O2 stars in the LMC*, Bulletin de la Societe Royale des Sciences de Liege, 80, 129
- Dufour, R. J. 1984: *The composition of H II regions in the Magellanic Clouds*, in IAU Symposium, Vol. 108, Structure and Evolution of the Magellanic Clouds, ed. S. van den Bergh & K. S. D. de Boer, 353
- Dufton, P. L., Smartt, S. J., Lee, J. K., Ryans, R. S. I., Hunter, I., Evans, C. J., Herrero, A., Trundle, C., Lennon, D. J., Irwin, M. J., & Kaufer, A. 2006: *The VLT-FLAMES survey of massive stars: stellar parameters and rotational velocities in NGC 3293, NGC 4755 and NGC 6611*, A&A, 457, 265

- Eissner, W. 1991: *Superstructure - an atomic structure code*, J. Phys. IV (France), 1, C1
- Eissner, W. & Nussbaumer, H. 1969, in *Premiere Reunion de l'Association Europeene de Spectroscopie Atomique* No. No. 42 (Paris-Orsay: Faculte des Sciences)
- Evans, C. J., Bastian, N., Beletsky, Y., Brott, I., Cantiello, M., Clark, J. S., Crowther, P. A., de Koter, A., de Mink, S. E., Dufton, P. L., Dunstall, P., et al. 2010: *The VLT-FLAMES Tarantula Survey*, in *IAU Symposium*, Vol. 266, IAU Symposium, ed. R. de Grijs & J. R. D. Lépine, 35–40
- Evans, C. J., Crowther, P. A., Fullerton, A. W., & Hillier, D. J. 2004: *Quantitative Studies of the Far-Ultraviolet, Ultraviolet, and Optical Spectra of Late O- and Early B-Type Supergiants in the Magellanic Clouds*, *ApJ*, 610, 1021
- Evans, C. J. & Howarth, I. D. 2008: *Kinematics of massive stars in the Small Magellanic Cloud*, *MNRAS*, 386, 826
- Evans, C. J., Hunter, I., Smartt, S. J., Lennon, D. J., de Koter, A., Mokiem, M. R., Trundle, C., Dufton, P. L., Ryans, R. S. I., Puls, J., Vink, J. S., et al. 2008: *The VLT-FLAMES Survey of Massive Stars*, *ArXiv e-prints*, 803
- Evans, C. J., Lennon, D. J., Smartt, S. J., & Trundle, C. 2006: *The VLT-FLAMES survey of massive stars: observations centered on the Magellanic Cloud clusters NGC 330, NGC 346, NGC 2004, and the N11 region*, *A&A*, 456, 623
- Evans, C. J., Smartt, S. J., Lee, J.-K., & and 23 coauthors. 2005: *The VLT-FLAMES survey of massive stars: Observations in the Galactic clusters NGC 3293, NGC 4755 and NGC 6611*, *A&A*, 437, 467
- Evans, C. J., Taylor, W. D., Hénault-Brunet, V., Sana, H., de Koter, A., Simón-Díaz, S., Carraro, G., Bagnoli, T., Bastian, N., Bestenlehner, J. M., Bonanos, A. Z., et al. 2011: *The VLT-FLAMES Tarantula Survey. I. Introduction and observational overview*, *A&A*, 530, A108
- Fagotto, F., Bressan, A., Bertelli, G., & Chiosi, C. 1994a: *Evolutionary sequences of stellar models with new radiative opacities. III. $Z=0.0004$ and $Z=0.05$* , *A&AS*, 104, 365
- Fagotto, F., Bressan, A., Bertelli, G., & Chiosi, C. 1994b: *Evolutionary sequences of stellar models with new radiative opacities. IV. $Z=0.004$ and $Z=0.008$* , *A&AS*, 105, 29
- Fagotto, F., Bressan, A., Bertelli, G., & Chiosi, C. 1994c: *Evolutionary sequences of stellar models with very high metallicity. V. $Z=0.1$* , *A&AS*, 105, 39
- Fernley, J. A., Hibbert, A., Kingston, A. E., & Seaton, M. J. 1999: *Atomic data for opacity calculations: XXIV. The boron-like sequence*, *Journal of Physics B Atomic Molecular Physics*, 32, 5507
- Figer, D. F. 2005: *An upper limit to the masses of stars*, *Nat*, 434, 192
- Gabler, R., Gabler, A., Kudritzki, R. P., Puls, J., & Pauldrach, A. 1989: *Unified NLTE model atmospheres including spherical extension and stellar winds - Method and first results*, *A&A*, 226, 162

- Getman, K. V., Feigelson, E. D., Luhman, K. L., Sicilia-Aguilar, A., Wang, J., & Garmire, G. P. 2009: *Protoplanetary Disk Evolution Around the Triggered Star-Forming Region Cepheus B*, ApJ, 699, 1454
- Giddings, J. R. 1981 PhD thesis, , University of London, (1981)
- Gies, D. R. & Lambert, D. L. 1992: *Carbon, nitrogen, and oxygen abundances in early B-type stars*, ApJ, 387, 673
- Girardi, L., Bressan, A., Chiosi, C., Bertelli, G., & Nasi, E. 1996: *Evolutionary sequences of stellar models with new radiative opacities. VI. $Z=0.0001$.*, A&AS, 117, 113
- Gray, D. F. 1976, The observation and analysis of stellar photospheres (Research supported by the National Research Council of Canada. New York, Wiley-Interscience, 1976. 484 p.)
- Grevesse, N. & Sauval, A. J. 1998: *Standard Solar Composition*, Space Science Reviews, 85, 161
- Gritschneider, M., Naab, T., Walch, S., Burkert, A., & Heitsch, F. 2009: *Driving Turbulence and Triggering Star Formation by Ionizing Radiation*, ApJ, 694, L26
- Groenewegen, M. A. T., Lamers, H. J. G. L. M., & Pauldrach, A. W. A. 1989: *The winds of O-stars. II - The terminal velocities of stellar winds of O-type stars*, A&A, 221, 78
- Haser, S. M., Pauldrach, A. W. A., Lennon, D. J., Kudritzki, R.-P., Lennon, M., Puls, J., & Voels, S. A. 1998: *Quantitative UV spectroscopy of early O stars in the Magellanic Clouds. The determination of the stellar metallicities*, A&A, 330, 285
- Heap, S. R., Lanz, T., & Hubeny, I. 2006: *Fundamental Properties of O-Type Stars*, ApJ, 638, 409
- Heger, A. & Langer, N. 2000: *Presupernova Evolution of Rotating Massive Stars. II. Evolution of the Surface Properties*, ApJ, 544, 1016
- Heger, A., Langer, N., & Woosley, S. E. 2000: *Presupernova Evolution of Rotating Massive Stars. I. Numerical Method and Evolution of the Internal Stellar Structure*, ApJ, 528, 368
- Herbig, G. H. 1975: *The diffuse interstellar bands. IV - The region 4400-6850 Å*, ApJ, 196, 129
- Herrero, A. 2003: *CNO in OB Main Sequence Stars (invited review)*, in Astronomical Society of the Pacific Conference Series, Vol. 304, Astronomical Society of the Pacific Conference Series, ed. C. Charbonnel, D. Schaerer, & G. Meynet, 10
- Herrero, A., Garcia, M., Puls, J., Uytterhoeven, K., Najarro, F., Lennon, D. J., & Rivero-Gonzalez, J. G. 2012: *A peculiar Of star in the Local Group galaxy IC 1613*, ArXiv e-prints
- Herrero, A., Kudritzki, R. P., Vilchez, J. M., Kunze, D., Butler, K., & Haser, S. 1992: *Intrinsic parameters of galactic luminous OB stars*, A&A, 261, 209
- Herrero, A. & Lennon, D. J. 2004: *Abundance Anomalies and Rotation in Main Sequence OB Stars (Invited Review)*, in IAU Symposium, Vol. 215, Stellar Rotation, ed. A. Maeder & P. Eenens, 209
- Herrero, A., Puls, J., & Villamariz, M. R. 2000: *Fundamental parameters of Galactic luminous OB stars. IV. The upper HR diagram*, A&A, 354, 193

- Hertzprung, E. 1911: *Ueber die Verwendung photographischer effektiver Wellenlaengen zur Bestimmung von Farbaequivalenten*, Publikationen des Astrophysikalischen Observatoriums zu Potsdam, 63
- Hillier, D. J., Lanz, T., Heap, S. R., Hubeny, I., Smith, L. J., Evans, C. J., Lennon, D. J., & Bouret, J. C. 2003: *A Tale of Two Stars: The Extreme O7 Iaf+ Supergiant AV 83 and the OC7.5 III((f)) star AV 69*, ApJ, 588, 1039
- Hillier, D. J. & Miller, D. L. 1998: *The Treatment of Non-LTE Line Blanketing in Spherically Expanding Outflows*, ApJ, 496, 407
- Hillier, D. J. & Miller, D. L. 1999: *Constraints on the Evolution of Massive Stars through Spectral Analysis. I. The WC5 Star HD 165763*, ApJ, 519, 354
- Howarth, I. D., Siebert, K. W., Hussain, G. A. J., & Prinja, R. K. 1997: *Cross-correlation characteristics of OB stars from IUE spectroscopy*, MNRAS, 284, 265
- Hubeny, I. 1988: *A computer program for calculating non-LTE model stellar atmospheres*, Computer Physics Communications, 52, 103
- Hubeny, I. 1992: *Accelerated Lambda iteration (review)*, in Lecture Notes in Physics, Berlin Springer Verlag, Vol. 401, The Atmospheres of Early-Type Stars, ed. U. Heber & C. S. Jeffery, 377
- Hubeny, I. 1998: *Non-LTE line-blanketed model atmospheres of hot stars*, in Astronomical Society of the Pacific Conference Series, Vol. 138, 1997 Pacific Rim Conference on Stellar Astrophysics, ed. K. L. Chan, K. S. Cheng, & H. P. Singh, 139
- Hubeny, I. & Lanz, T. 1995: *Non-LTE line-blanketed model atmospheres of hot stars. 1: Hybrid complete linearization/accelerated lambda iteration method*, ApJ, 439, 875
- Hummer, D. G., Berrington, K. A., Eissner, W., Pradhan, A. K., Saraph, H. E., & Tully, J. A. 1993: *Atomic data from the IRON Project. 1: Goals and methods*, A&A, 279, 298
- Humphreys, R. M. & Davidson, K. 1979: *Studies of luminous stars in nearby galaxies. III - Comments on the evolution of the most massive stars in the Milky Way and the Large Magellanic Cloud*, ApJ, 232, 409
- Hunter, I., Brott, I., Langer, N., Lennon, D. J., Dufton, P. L., Howarth, I. D., Ryans, R. S. I., Trundle, C., Evans, C. J., de Koter, A., & Smartt, S. J. 2009a: *The VLT-FLAMES survey of massive stars: constraints on stellar evolution from the chemical compositions of rapidly rotating Galactic and Magellanic Cloud B-type stars*, A&A, 496, 841
- Hunter, I., Brott, I., Lennon, D. J., Langer, N., Dufton, P. L., Trundle, C., Smartt, S. J., de Koter, A., Evans, C. J., & Ryans, R. S. I. 2008a: *The VLT FLAMES Survey of Massive Stars: Rotation and Nitrogen Enrichment as the Key to Understanding Massive Star Evolution*, ApJ, 676, L29
- Hunter, I., Dufton, P. L., Smartt, S. J., Ryans, R. S. I., Evans, C. J., Lennon, D. J., Trundle, C., Hubeny, I., & Lanz, T. 2007: *The VLT-FLAMES survey of massive stars: surface chemical compositions of B-type stars in the Magellanic Clouds*, A&A, 466, 277

- Hunter, I., Lennon, D. J., Dufton, P. L., Trundle, C., Simón-Díaz, S., Smartt, S. J., Ryans, R. S. I., & Evans, C. J. 2008b: *The VLT-FLAMES survey of massive stars: atmospheric parameters and rotational velocity distributions for B-type stars in the Magellanic Clouds*, A&A, 479, 541
- Hunter, I., Lennon, D. J., Dufton, P. L., Trundle, C., Simón-Díaz, S., Smartt, S. J., Ryans, R. S. I., & Evans, C. J. 2009b: *The VLT-FLAMES survey of massive stars: atmospheric parameters and rotational velocity distributions for B-type stars in the Magellanic Clouds*, A&A, 504, 211
- Johnson, J. L., Greif, T. H., & Bromm, V. 2008: *The First Stars*, in IAU 250 Massive Stars as Cosmic Engines, ed. P. C. F. Bresolin & J. Puls
- Kelleher, D. E., Mohr, P. J., Martin, W. C., Wiese, W. L., Sugar, J., Fuhr, J. R., Olsen, K., Musgrove, A., Reader, J., Sansonetti, C. J., & Dalton, G. R. 1999: *New NIST Atomic Spectra Database*, in Society of Photo-Optical Instrumentation Engineers (SPIE) Conference Series, Vol. 3818, Society of Photo-Optical Instrumentation Engineers (SPIE) Conference Series, ed. G. R. Carruthers & K. F. Dymond, 170
- Kilian, J., Becker, S. R., Gehren, T., & Nissen, P. E. 1991: *Chemical abundances in early B-type stars. III - NLTE temperature and gravity determination*, A&A, 244, 419
- Kippenhahn, R. & Weigert, A. 1990: *Book-Review - Stellar Structure and Evolution*, 80, 504
- Krelowski, J., Sneden, C., & Hiltgen, D. 1995: *A survey of weak diffuse interstellar bands in selected ranges between 5600 and 7000 Å*, planss, 43, 1195
- Kudritzki, R.-P. 1980: *Non-LTE analysis of the O 3-star HD 93250*, A&A, 85, 174
- Kudritzki, R.-P. & Puls, J. 2000: *Winds from Hot Stars*, araa, 38, 613
- Kudritzki, R.-P., Urbaneja, M. A., Bresolin, F., & Przybilla, N. 2008: *Extragalactic Stellar Astronomy with the Brightest Stars in the Universe*, in IAU Symposium, Vol. 250, Massive Stars as Cosmic Engines, ed. F. Bresolin, P. A. Crowther, & J. Puls
- Kurucz, R. L. 1979: *Model atmospheres for G, F, A, B, and O stars*, ApJS, 40, 1
- Lajoie, C.-P. & Sills, A. 2011: *Mass Transfer in Binary Stars Using Smoothed Particle Hydrodynamics. II. Eccentric Binaries*, ApJ, 726, 67
- Lamers, H. J. G. L. M., Vink, J. S., de Koter, A., & Cassinelli, J. P. 1999: *Disks formed by Rotation Induced Bi-Stability*, in Lecture Notes in Physics, Berlin Springer Verlag, Vol. 523, IAU Colloq. 169: Variable and Non-spherical Stellar Winds in Luminous Hot Stars, ed. B. Wolf, O. Stahl, & A. W. Fullerton, 159
- Langer, N. 1998: *Coupled mass and angular momentum loss of massive main sequence stars*, A&A, 329, 551
- Langer, N., Cantiello, M., Yoon, S.-C., Hunter, I., Brott, I., Lennon, D., de Mink, S., & Verheijdt, M. 2008: *Rotation and Massive Close Binary Evolution*, in IAU Symposium, Vol. 250, IAU Symposium, ed. F. Bresolin, P. A. Crowther, & J. Puls, 167–178

- Lanz, T., Cunha, K., Holtzman, J., & Hubeny, I. 2008: *Argon Abundances in the Solar Neighborhood: Non-LTE Analysis of Orion Association B-Type Stars*, ApJ, 678, 1342
- Lanz, T. & Hubeny, I. 2003: *A Grid of Non-LTE Line-blanketed Model Atmospheres of O-Type Stars*, ApJS, 146, 417
- Lanz, T. & Hubeny, I. 2007: *A Grid of NLTE Line-blanketed Model Atmospheres of Early B-Type Stars*, ApJS, 169, 83
- Lefever, K., Puls, J., & Aerts, C. 2007: *Statistical properties of a sample of periodically variable B-type supergiants. Evidence for opacity-driven gravity-mode oscillations*, A&A, 463, 1093
- Leitherer, C., Robert, C., & Drissen, L. 1992: *Deposition of mass, momentum, and energy by massive stars into the interstellar medium*, ApJ, 401, 596
- Lenorzer, A., Mokiem, M. R., de Koter, A., & Puls, J. 2004: *Modeling the near-infrared lines of O-type stars*, A&A, 422, 275
- Levesque, E. M. 2010: *The Physical Properties of Red Supergiants*, in Astronomical Society of the Pacific Conference Series, Vol. 425, Hot and Cool: Bridging Gaps in Massive Star Evolution, ed. C. Leitherer, P. D. Bennett, P. W. Morris, & J. T. Van Loon, 103
- Lucke, P. B. 1972: *The OB Stellar Associations in the Large Magellanic Cloud*, PhD thesis, UNIVERSITY OF WASHINGTON.
- MacGregor, K. B. & Cassinelli, J. P. 2003: *Magnetic Fields in Massive Stars. II. The Buoyant Rise of Magnetic Flux Tubes through the Radiative Interior*, ApJ, 586, 480
- Maeder, A. 1997: *Stellar evolution with rotation. II. A new approach for shear mixing.*, A&A, 321, 134
- Maeder, A. 1999a: *Comparisons of young clusters in the Galaxy, LMC, and SMC: the way to new stellar models.*, in Revista Mexicana de Astronomia y Astrofisica, vol. 27, Vol. 8, Revista Mexicana de Astronomia y Astrofisica Conference Series, ed. N. I. Morrell, V. S. Niemela, & R. H. Barbá, 83–88
- Maeder, A. 1999b: *Stellar evolution with rotation IV: von Zeipel's theorem and anisotropic losses of mass and angular momentum*, A&A, 347, 185
- Maeder, A. 2009, *Physics, Formation and Evolution of Rotating Stars*, ed. Maeder, A.
- Maeder, A. & Mermilliod, J. C. 1981: *The extent of mixing in stellar interiors - Evolutionary models and tests based on the HR diagrams of 34 open clusters*, A&A, 93, 136
- Maeder, A. & Meynet, G. 1989: *Grids of evolutionary models from 0.85 to 120 solar masses - Observational tests and the mass limits*, A&A, 210, 155
- Maeder, A. & Meynet, G. 1994: *New models of Wolf-Rayet stars and comparison with data in galaxies*, A&A, 287, 803
- Maeder, A. & Meynet, G. 2000: *The Evolution of Rotating Stars*, araa, 38, 143

- Maeder, A. & Meynet, G. 2001a: *Stellar evolution with rotation. VII. . Low metallicity models and the blue to red supergiant ratio in the SMC*, A&A, 373, 555
- Maeder, A. & Meynet, G. 2001b: *Stellar evolution with rotation. VII. . Low metallicity models and the blue to red supergiant ratio in the SMC*, A&A, 373, 555
- Maeder, A. & Meynet, G. 2003: *Stellar evolution with rotation and magnetic fields. I. The relative importance of rotational and magnetic effects*, A&A, 411, 543
- Maeder, A. & Meynet, G. 2004: *Stellar evolution with rotation and magnetic fields. II. General equations for the transport by Tayler-Spruit dynamo*, A&A, 422, 225
- Maeder, A. & Meynet, G. 2005: *Stellar evolution with rotation and magnetic fields. III. The interplay of circulation and dynamo*, A&A, 440, 1041
- Maeder, A. & Meynet, G. 2010: *Evolution of massive stars with mass loss and rotation*, NewAR, 54, 32
- Maeder, A., Meynet, G., Georgy, C., & Ekström, S. 2009: *The basic role of magnetic fields in stellar evolution*, in IAU Symposium, Vol. 259, IAU Symposium, 311–322
- Maeder, A. & Zahn, J.-P. 1998: *Stellar evolution with rotation. III. Meridional circulation with MU -gradients and non-stationarity*, A&A, 334, 1000
- Maíz-Apellániz, J., Walborn, N. R., Galué, H. Á., & Wei, L. H. 2004: *A Galactic O Star Catalog*, ApJS, 151, 103
- Malumuth, E. M. & Heap, S. R. 1994: *UBV stellar photometry of the 30 Doradus region of the large Magellanic Cloud with the Hubble Space Telescope*, AJ, 107, 1054
- Marcolino, W. L. F., Bouret, J., Martins, F., Hillier, D. J., Lanz, T., & Escolano, C. 2009: *Analysis of Galactic late-type O dwarfs: more constraints on the weak wind problem*, A&A, 498, 837
- Markova, N. & Puls, J. 2008: *Bright OB stars in the Galaxy. IV. Stellar and wind parameters of early to late B supergiants*, A&A, 478, 823
- Markova, N., Puls, J., Repolust, T., & Markov, H. 2004: *Bright OB stars in the Galaxy. I. Mass-loss and wind-momentum rates of O-type stars: A pure $H\alpha$ analysis accounting for line-blanketing*, A&A, 413, 693
- Markova, N., Puls, J., Scuderi, S., Simón-Díaz, S., & Herrero, A. 2011: *Spectroscopic and physical parameters of Galactic O-type stars. I. Effects of rotation and spectral resolving power in the spectral classification of dwarfs and giants*, A&A, 530, A11
- Marquez-Lugo, R. A. & Phillips, J. P. 2010: *Imaging of four Galactic supernova remnants in the mid-infrared, and their interaction with the interstellar medium*, MNRAS, 407, 94
- Martins, F., Escolano, C., Wade, G. A., Donati, J.-F., Bouret, J.-C., & the MiMeS collaboration. 2011a: *Observational effects of magnetism in O stars: surface nitrogen abundances*, ArXiv e-prints

- Martins, F., Mahy, L., Rauw, G., & Hillier, D. J. 2011b: *A quantitative study of O stars in NGC2244 and the Mon OB2 association*, ArXiv e-prints
- Martins, F., Schaerer, D., & Hillier, D. J. 2005a: *A new calibration of stellar parameters of Galactic O stars*, A&A, 436, 1049
- Martins, F., Schaerer, D., Hillier, D. J., Meynadier, F., Heydari-Malayeri, M., & Walborn, N. R. 2005b: *O stars with weak winds: the Galactic case*, A&A, 441, 735
- Mason, B. D., Hartkopf, W. I., Gies, D. R., Henry, T. J., & Helsel, J. W. 2009: *The High Angular Resolution Multiplicity of Massive Stars*, AJ, 137, 3358
- Massa, D., Fullerton, A. W., Sonneborn, G., & Hutchings, J. B. 2003: *Constraints on the Ionization Balance of Hot-Star Winds from FUSE Observations of O Stars in the Large Magellanic Cloud*, ApJ, 586, 996
- Massey, P. 2002: *A UBVR CCD Survey of the Magellanic Clouds*, ApJS, 141, 81
- Massey, P., Bresolin, F., Kudritzki, R. P., Puls, J., & Pauldrach, A. W. A. 2004: *The Physical Properties and Effective Temperature Scale of O-Type Stars as a Function of Metallicity. I. A Sample of 20 Stars in the Magellanic Clouds*, ApJ, 608, 1001
- Massey, P. & Hunter, D. A. 1998: *Star Formation in R136: A Cluster of O3 Stars Revealed by Hubble Space Telescope Spectroscopy*, ApJ, 493, 180
- Massey, P., Lang, C. C., Degioia-Eastwood, K., & Garmany, C. D. 1995: *Massive stars in the field and associations of the magellanic clouds: The upper mass limit, the initial mass function, and a critical test of main-sequence stellar evolutionary theory*, ApJ, 438, 188
- Massey, P., Meyer, M., & Murdin, P. 2001, *Stellar Masses*, ed. Murdin, P.
- Massey, P., Parker, J. W., & Garmany, C. D. 1989: *The stellar content of NGC 346 - A plethora of O stars in the SMC*, AJ, 98, 1305
- Massey, P., Penny, L. R., & Vukovich, J. 2002: *Orbits of Four Very Massive Binaries in the R136 Cluster*, ApJ, 565, 982
- Massey, P., Puls, J., Pauldrach, A. W. A., Bresolin, F., Kudritzki, R. P., & Simon, T. 2005: *The Physical Properties and Effective Temperature Scale of O-Type Stars as a Function of Metallicity. II. Analysis of 20 More Magellanic Cloud Stars and Results from the Complete Sample*, ApJ, 627, 477
- Massey, P., Zangari, A. M., Morrell, N. I., Puls, J., DeGioia-Eastwood, K., Bresolin, F., & Kudritzki, R.-P. 2009: *The Physical Properties and Effective Temperature Scale of O-Type Stars as a Function of Metallicity. III. More Results From the Magellanic Clouds*, ApJ, 692, 618
- Matteucci, F. & Calura, F. 2005: *Early chemical enrichment of the universe and the role of very massive population III stars*, MNRAS, 360, 447
- Meynet, G., Eggenberger, P., & Maeder, A. 2011: *Massive star models with magnetic braking*, A&A, 525, L11

- Meynet, G. & Maeder, A. 1997: *Stellar evolution with rotation. I. The computational method and the inhibiting effect of the μ -gradient.*, A&A, 321, 465
- Meynet, G. & Maeder, A. 2000: *Stellar evolution with rotation. V. Changes in all the outputs of massive star models*, A&A, 361, 101
- Meynet, G., Maeder, A., Schaller, G., Schaerer, D., & Charbonnel, C. 1994: *Grids of massive stars with high mass loss rates. V. From 12 to 120 Msun at Z=0.001, 0.004, 0.008, 0.020 and 0.040*, A&AS, 103, 97
- Mihalas, D. 1971: *A Comment on the Interpretation of the Broad Component of N III $\lambda\lambda$ 4634-4640 Emission in of Stars*, ApJ, 170, 541
- Mihalas, D. 1978, *Stellar atmospheres* (2nd edition) (San Francisco: W. H. Freeman and Co., 1978)
- Mihalas, D. & Hummer, D. G. 1973: *Analyses of light-ion spectra in stellar atmospheres.*, ApJ, 179, 827
- Mihalas, D., Kunasz, P. B., & Hummer, D. G. 1975: *Solution of the comoving frame equation of transfer in spherically symmetric flows. I - Computational method for equivalent-two-level-atom source functions*, ApJ, 202, 465
- Mihalas, D., Kunasz, P. B., & Hummer, D. G. 1976: *Solution of the Comoving-Frame Equation of Transfer in Spherically Symmetric Flows. III. Effect of Aberration and Advection Terms*, ApJ, 206, 515
- Mokiem, M. R., de Koter, A., Evans, C. J., Puls, J., Smartt, S. J., Crowther, P. A., Herrero, A., Langer, N., Lennon, D. J., Najarro, F., Villamariz, M. R., et al. 2007a: *The VLT-FLAMES survey of massive stars: wind properties and evolution of hot massive stars in the Large Magellanic Cloud*, A&A, 465, 1003
- Mokiem, M. R., de Koter, A., Evans, C. J., Puls, J., Smartt, S. J., Crowther, P. A., Herrero, A., Langer, N., Lennon, D. J., Najarro, F., Villamariz, M. R., et al. 2006: *The VLT-FLAMES survey of massive stars: mass loss and rotation of early-type stars in the SMC*, A&A, 456, 1131
- Mokiem, M. R., de Koter, A., Puls, J., Herrero, A., Najarro, F., & Villamariz, M. R. 2005: *Spectral analysis of early-type stars using a genetic algorithm based fitting method*, A&A, 441, 711
- Mokiem, M. R., de Koter, A., Vink, J. S., Puls, J., Evans, C. J., Smartt, S. J., Crowther, P. A., Herrero, A., Langer, N., Lennon, D. J., Najarro, F., et al. 2007b: *The empirical metallicity dependence of the mass-loss rate of O- and early B-type stars*, A&A, 473, 603
- Moore, C. E. 1971, *Selected tables of atomic spectra - A: Atomic energy levels - Second edition - B: Multiplet tables; N IV, N V, N VI, N VII. Data derived from the analyses of optical spectra (NSRDS-NBS (National Standard Reference Series - National Bureau of Standards, Washington, DC: U.S. Department of Commerce, National Bureau of Standards, 1971)*
- Moore, C. E. 1975, *Selected tables of atomic spectra - A: Atomic energy levels - Second edition - B: Multiplet table; N I, N II, N III. Data derived from the analyses of optical spectra (NSRDS-NBS (National Standard Reference Series - National Bureau of Standards, Washington, DC: U.S. Department of Commerce, National Bureau of Standards, 1975)*

- Morales, M. F. & Wyithe, J. S. B. 2010: *Reionization and Cosmology with 21-cm Fluctuations*, ARA&A, 48, 127
- Morel, T. 2009: *Abundances of massive stars: some recent developments*, Communications in Asteroseismology, 158, 122
- Morel, T., Butler, K., Aerts, C., Neiner, C., & Briquet, M. 2006: *Abundance analysis of prime B-type targets for asteroseismology. I. Nitrogen excess in slowly-rotating β Cephei stars*, A&A, 457, 651
- Morel, T., Hubrig, S., & Briquet, M. 2008: *Nitrogen enrichment, boron depletion and magnetic fields in slowly-rotating B-type dwarfs*, A&A, 481, 453
- Najarro, F., Hanson, M. M., & Puls, J. 2011: *L-band spectroscopy of Galactic OB-stars*, A&A, 535, A32
- Najarro, F., Hillier, D. J., Puls, J., Lanz, T., & Martins, F. 2006: *On the sensitivity of He I singlet lines to the Fe IV model atom in O stars*, A&A, 456, 659
- Najarro, F., Kudritzki, R. P., Cassinelli, J. P., Stahl, O., & Hillier, D. J. 1996: *Stellar winds and the EUV continuum excess of early B-giants.*, A&A, 306, 892
- Neguereuela, I. & Clark, J. S. 2005: *Further Wolf-Rayet stars in the starburst cluster γ -ASTROBJ/Westerlund 1/ASTROBJ*, A&A, 436, 541
- Nelan, E. P., Walborn, N. R., Wallace, D. J., Moffat, A. F. J., Makidon, R. B., Gies, D. R., & Panagia, N. 2004: *Resolving OB Systems in the Carina Nebula with the Hubble Space Telescope Fine Guidance Sensor*, AJ, 128, 323
- Neugent, K. F., Massey, P., Skiff, B., Drout, M. R., Meynet, G., & Olsen, K. A. G. 2010: *Yellow Supergiants in the Small Magellanic Cloud: Putting Current Evolutionary Theory to the Test*, ApJ, 719, 1784
- Nikitin, A. A. & Yakubovskii, O. A. 1963: *The Investigation of the N III Recombination Spectrum in Stellar Envelopes and Nebulae. VI. The Equations of Statistical Equilibrium for the Lower Excited Levels of C II, N III, and O. IV*, Soviet Astronomy, 7, 189
- Nugis, T. & Lamers, H. J. G. L. M. 2000: *Mass-loss rates of Wolf-Rayet stars as a function of stellar parameters*, A&A, 360, 227
- Nussbaumer, H. & Storey, P. J. 1983: *Dielectronic recombination at low temperatures*, A&A, 126, 75
- Oey, M. S. 2006: *The Local Group as an astrophysical laboratory for massive star feedback*, in The Local Group as an Astrophysical Laboratory, ed. M. Livio & T. M. Brown, 72–85
- Oey, M. S. & Clarke, C. J. 2005: *Statistical Confirmation of a Stellar Upper Mass Limit*, ApJ, 620, L43
- Oey, M. S. & Kennicutt, Jr., R. C. 1997: *Comparison of H II region luminosities with observed stellar ionizing sources in the Large Magellanic Cloud*, MNRAS, 291, 827
- Oke, J. B. 1954: *A Study of the Atmospheres of Early O and of Stars.*, ApJ, 120, 22

- Parker, J. W., Garmany, C. D., Massey, P., & Walborn, N. R. 1992: *The stellar content of LH 9 and 10 (N11) in the LMC - A case for sequential star formation*, AJ, 103, 1205
- Pauldrach, A. W. A., Hoffmann, T. L., & Lennon, M. 2001: *Radiation-driven winds of hot luminous stars. XIII. A description of NLTE line blocking and blanketing towards realistic models for expanding atmospheres*, A&A, 375, 161
- Pauldrach, A. W. A., Kudritzki, R. P., Puls, J., Butler, K., & Hunsinger, J. 1994: *Radiation-driven winds of hot luminous stars. 12: A first step towards detailed UV-line diagnostics of O-stars*, A&A, 283, 525
- Pauldrach, A. W. A., Lennon, M., Hoffmann, T. L., Sellmaier, F., Kudritzki, R.-P., & Puls, J. 1998: *Realistic Models for Expanding Atmospheres*, in *Astronomical Society of the Pacific Conference Series*, Vol. 131, *Properties of Hot Luminous Stars*, ed. I. Howarth, 258
- Pauldrach, A. W. A. & Puls, J. 1990: *Radiation-driven winds of hot stars. VIII - The bistable wind of the luminous blue variable P Cygni (B1 Ia/+)*, A&A, 237, 409
- Peimbert, A. 2003: *The Chemical Composition of the 30 Doradus Nebula Derived from Very Large Telescope Echelle Spectrophotometry*, ApJ, 584, 735
- Pellerin, A., Maíz Apellániz, J., Simón-Díaz, S., & Barbá, R. H. 2012: *NoMaDS: The Northern Massive Dim Stars Survey*, in *American Astronomical Society Meeting Abstracts*, Vol. 219, *American Astronomical Society Meeting Abstracts*, 224
- Petrenz, P. & Puls, J. 2000: *2-D non-LTE models of radiation driven winds from rotating early-type stars. I. Winds with an optically thin continuum*, A&A, 358, 956
- Petrovic, J., Langer, N., & van der Hucht, K. A. 2005: *Constraining the mass transfer in massive binaries through progenitor evolution models of Wolf-Rayet+O binaries*, A&A, 435, 1013
- Przybilla, N. 2010: *Non-LTE Model Atom Construction*, in *EAS Publications Series*, Vol. 43, *EAS Publications Series*, ed. R. Monier, B. Smalley, G. Wahlgren, & P. Stee, 115–133
- Przybilla, N. & Butler, K. 2001: *Non-LTE line formation for N: Abundances and stellar parameters. Model atom and first results on BA-type stars*, A&A, 379, 955
- Przybilla, N., Firnstein, M., Nieva, M. F., Meynet, G., & Maeder, A. 2010: *Mixing of CNO-cycled matter in massive stars*, A&A, 517, A38
- Przybilla, N., Nieva, M., & Butler, K. 2008: *A Cosmic Abundance Standard: Chemical Homogeneity of the Solar Neighborhood and the ISM Dust-Phase Composition*, ApJ, 688, L103
- Puls, J. 2008: *Physical and Wind Properties of OB-Stars*, in *IAU Symposium*, Vol. 250, *Massive Stars as Cosmic Engines*, ed. F. Bresolin, P. A. Crowther, & J. Puls
- Puls, J. 2009: *Modeling the atmospheres of massive stars*, *Communications in Asteroseismology*, 158, 113

- Puls, J., Kudritzki, R.-P., Herrero, A., Pauldrach, A. W. A., Haser, S. M., Lennon, D. J., Gabler, R., Voels, S. A., Vilchez, J. M., Wachter, S., & Feldmeier, A. 1996: *O-star mass-loss and wind momentum rates in the Galaxy and the Magellanic Clouds Observations and theoretical predictions.*, A&A, 305, 171
- Puls, J., Markova, N., Scuderi, S., Stanghellini, C., Taranova, O. G., Burnley, A. W., & Howarth, I. D. 2006: *Bright OB stars in the Galaxy. III. Constraints on the radial stratification of the clumping factor in hot star winds from a combined $H\alpha$, IR and radio analysis*, A&A, 454, 625
- Puls, J., Sundqvist, J. O., & Rivero González, J. G. 2010: *OB-stars as extreme condition test beds*, ArXiv e-prints
- Puls, J., Urbaneja, M. A., Venero, R., Repolust, T., Springmann, U., Jokuthy, A., & Mokiem, M. R. 2005: *Atmospheric NLTE-models for the spectroscopic analysis of blue stars with winds. II. Line-blanketed models*, A&A, 435, 669
- Puls, J., Vink, J. S., & Najarro, F. 2008: *Mass loss from hot massive stars*, A&ARv, 16, 209
- Ramsbottom, C. A., Berrington, K. A., Hibbert, A., & Bell, K. L. 1994: *Electron impact excitation rates for transitions involving the $n = 2$ and $n = 3$ levels of beryllium-like N IV*, Phys. Scr., 50, 246
- Repolust, T., Puls, J., Hanson, M. M., Kudritzki, R.-P., & Mokiem, M. R. 2005: *Quantitative H and K band spectroscopy of Galactic OB-stars at medium resolution*, A&A, 440, 261
- Repolust, T., Puls, J., & Herrero, A. 2004: *Stellar and wind parameters of Galactic O-stars. The influence of line-blocking/blanketing*, A&A, 415, 349
- Rivero Gonzalez, J. G., Puls, J., Massey, P., & Najarro, F. 2012: *Nitrogen line spectroscopy in O-stars – III. The earliest O-stars*, ArXiv e-prints
- Rivero González, J. G., Puls, J., & Najarro, F. 2011: *Nitrogen line spectroscopy of O-stars. I. Nitrogen III emission line formation revisited*, A&A, 536, A58
- Rivero González, J. G., Puls, J., Najarro, F., & Brott, I. 2012: *Nitrogen line spectroscopy of O-stars. II. Surface nitrogen abundances for O-stars in the Large Magellanic Cloud*, A&A, 537, A79
- Russell, H. N. 1913: *"Giant" and "dwarf" stars*, The Observatory, 36, 324
- Russell, S. C. & Dopita, M. A. 1990: *Abundances of the heavy elements in the Magellanic Clouds. II - H II regions and supernova remnants*, ApJS, 74, 93
- Sana, H., Gosset, E., & Evans, C. J. 2009: *The massive star binary fraction in young open clusters - II. NGC6611 (Eagle Nebula)*, MNRAS, 400, 1479
- Sana, H., Gosset, E., Nazé, Y., Rauw, G., & Linder, N. 2008: *The massive star binary fraction in young open clusters - I. NGC 6231 revisited*, MNRAS, 386, 447
- Sana, H., James, G., & Gosset, E. 2011: *The massive star binary fraction in young open clusters - III. IC 2944 and the Cen OB2 association*, MNRAS, 416, 817

- Sanduleak, N. 1970: *A deep objective-prism survey for Large Magellanic Cloud members*, Contributions from the Cerro Tololo Inter-American Observatory, 89
- Santolaya-Rey, A. E., Puls, J., & Herrero, A. 1997: *Atmospheric NLTE-models for the spectroscopic analysis of luminous blue stars with winds.*, A&A, 323, 488
- Schaerer, D., Meynet, G., Maeder, A., & Schaller, G. 1993: *Grids of stellar models. II - From 0.8 to 120 solar masses at $Z = 0.008$* , A&AS, 98, 523
- Schaller, G., Schaerer, D., Meynet, G., & Maeder, A. 1992: *New grids of stellar models from 0.8 to 120 solar masses at $Z = 0.020$ and $Z = 0.001$* , A&AS, 96, 269
- Schuster, M. T., Humphreys, R. M., & Marengo, M. 2006: *The Circumstellar Environments of NML Cygni and the Cool Hypergiants*, AJ, 131, 603
- Seaton, M. J. 1953: *Electron Excitation of Forbidden Lines Occurring in Gaseous Nebulae*, Royal Society of London Proceedings Series A, 218, 400
- Seaton, M. J. 1958: *The Quantum Defect Method*, MNRAS, 118, 504
- Seaton, M. J. 1962: *The Theory of Excitation and Ionization by Electron Impact*, in Atomic and Molecular Processes, ed. D. R. Bates (New York, Academic Press), 375
- Seaton, M. J. 1987: *Atomic data for opacity calculations. I - General description*, Journal of Physics B Atomic Molecular Physics, 20, 6363
- Seaton, M. J., Yan, Y., Mihalas, D., & Pradhan, A. K. 1994: *Opacities for Stellar Envelopes*, MNRAS, 266, 805
- Sepinsky, J. F., Willems, B., Kalogera, V., & Rasio, F. A. 2009: *Interacting Binaries with Eccentric Orbits. II. Secular Orbital Evolution due to Non-conservative Mass Transfer*, ApJ, 702, 1387
- Sigut, T. A. A. & Lester, J. B. 1996: *Infrared Rydberg Emission Lines in Early-Type Stars. I. MG II*, ApJ, 461, 972
- Simon, K. P., Kudritzki, R. P., Jonas, G., & Rahe, J. 1983: *Non-LTE analysis of massive O stars. III - The O3 stars HD 93128, HD 93129A, and HDE 303308*, A&A, 125, 34
- Simón-Díaz, S., Castro, N., Garcia, M., & Herrero, A. 2011: *The IACOB spectroscopic database of galactic OB stars*, in IAU Symposium, Vol. 272, IAU Symposium, ed. C. Neiner, G. Wade, G. Meynet, & G. Peters, 310–312
- Simón-Díaz, S. & Herrero, A. 2007: *Fourier method of determining the rotational velocities in OB stars*, A&A, 468, 1063
- Simón-Díaz, S., Herrero, A., Esteban, C., & Najarro, F. 2006: *Detailed spectroscopic analysis of the Trapezium cluster stars inside the Orion nebula. Rotational velocities, stellar parameters, and oxygen abundances*, A&A, 448, 351
- Simón-Díaz, S. & Stasińska, G. 2008: *The ionizing radiation from massive stars and its impact on HII regions: results from modern model atmospheres*, MNRAS, 389, 1009

- Simón-Díaz, S., Uytterhoeven, K., Herrero, A., Castro, N., & Puls, J. 2010: *Is macroturbulent broadening in OB Supergiants related to pulsations?*, *Astronomische Nachrichten*, 331, 1069
- Smith, L. F., Shara, M. M., & Moffat, A. F. J. 1996: *A three-dimensional classification for WN stars*, *MNRAS*, 281, 163
- Sobolev, V. V. 1960, *Moving envelopes of stars* (Cambridge: Harvard University Press, 1960)
- Sota, A., Maíz Apellániz, J., Walborn, N. R., Alfaro, E. J., Barbá, R. H., Morrell, N. I., Gamen, R. C., & Arias, J. I. 2011: *The Galactic O-Star Spectroscopic Survey. I. Classification System and Bright Northern Stars in the Blue-violet at $R \sim 2500$* , *ApJS*, 193, 24
- Stafford, R. P., Bell, K. L., & Hibbert, A. 1994: *Electron impact excitation of N III - Fine-structure collision strengths and Maxwellian-averaged rate coefficients*, *MNRAS*, 266, 715
- Sundqvist, J. O., Puls, J., Feldmeier, A., & Owocki, S. P. 2011: *Mass loss from inhomogeneous hot star winds. II. Constraints from a combined optical/UV study*, *A&A*, 528, A64
- Swings, P. 1948: *Anomalies in the earliest spectral types*, *Annales d'Astrophysique*, 11, 228
- Swings, P. & Struve, O. 1940: *Spectrographic Observations of Peculiar Stars.*, *ApJ*, 91, 546
- Talon, S. & Zahn, J.-P. 1997: *Anisotropic diffusion and shear instabilities.*, *A&A*, 317, 749
- Taresch, G., Kudritzki, R. P., Hurwitz, M., Bowyer, S., Pauldrach, A. W. A., Puls, J., Butler, K., Lennon, D. J., & Haser, S. M. 1997: *Quantitative analysis of the FUV, UV and optical spectrum of the O3 star HD 93129A.*, *A&A*, 321, 531
- Townsend, R. H. D., Oksala, M. E., Cohen, D. H., Owocki, S. P., & ud-Doula, A. 2010: *Discovery of Rotational Braking in the Magnetic Helium-strong Star Sigma Orionis E*, *ApJ*, 714, L318
- Trundle, C., Dufton, P. L., Hunter, I., Evans, C. J., Lennon, D. J., Smartt, S. J., & Ryans, R. S. I. 2007: *The VLT-FLAMES survey of massive stars: evolution of surface N abundances and effective temperature scales in the Galaxy and Magellanic Clouds*, *A&A*, 471, 625
- Tsamis, Y. G., Barlow, M. J., Liu, X.-W., Danziger, I. J., & Storey, P. J. 2003: *Heavy elements in Galactic and Magellanic Cloud HII regions: recombination-line versus forbidden-line abundances*, *MNRAS*, 338, 687
- Tully, J. A., Seaton, M. J., & Berrington, K. A. 1990: *Atomic data for opacity calculations. XIV - The beryllium sequence*, *Journal of Physics B Atomic Molecular Physics*, 23, 3811
- Urbaneja, M. 2004: *B Supergiants in the Milky Way and Nearby Galaxies: Models and Quantitative Spectroscopy*, PhD thesis, Universidad de la Laguna, La Laguna, Spain
- van Regemorter, H. 1962: *Rate of Collisional Excitation in Stellar Atmospheres.*, *ApJ*, 136, 906
- Vanbeveren, D., De Loore, C., & Van Rensbergen, W. 1998: *Massive stars*, *A&ARv*, 9, 63
- Venn, K. A. & Przybilla, N. 2003: *New Nitrogen and Carbon in AF-supergiants (invited review)*, in *Astronomical Society of the Pacific Conference Series*, Vol. 304, Astronomical Society of the Pacific Conference Series, ed. C. Charbonnel, D. Schaerer, & G. Meynet, 20

- Vermeij, R. & van der Hulst, J. M. 2002: *The physical structure of Magellanic Cloud H II regions. II. Elemental abundances*, A&A, 391, 1081
- Vink, J. S. 2009: *Eta Carinae and the Luminous Blue Variables*, in *Eta Carinae and the supernova imposters*, ed. R. Humphreys & K. Davidson
- Vink, J. S., Brott, I., Gräfener, G., Langer, N., de Koter, A., & Lennon, D. J. 2010: *The nature of B supergiants: clues from a steep drop in rotation rates at 22 000 K. The possibility of Bi-stability braking*, A&A, 512, L7
- Vink, J. S., de Koter, A., & Lamers, H. J. G. L. M. 2000: *New theoretical mass-loss rates of O and B stars*, A&A, 362, 295
- Vink, J. S., de Koter, A., & Lamers, H. J. G. L. M. 2001: *Mass-loss predictions for O and B stars as a function of metallicity*, A&A, 369, 574
- Walborn, N. R. 1971a: *Some Extremely Early O Stars Near Eta Carinae*, ApJ, 167, L31
- Walborn, N. R. 1971b: *Some Spectroscopic Characteristics of the OB Stars: an Investigation of the Space Distribution of Certain OB Stars and the Reference Frame of the Classification*, ApJS, 23, 257
- Walborn, N. R. 1972: *Spectral classification of OB stars in both hemispheres and the absolute-magnitude calibration.*, AJ, 77, 312
- Walborn, N. R., Howarth, I. D., Lennon, D. J., Massey, P., Oey, M. S., Moffat, A. F. J., Skalkowski, G., Morrell, N. I., Drissen, L., & Parker, J. W. 2002: *A New Spectral Classification System for the Earliest O Stars: Definition of Type O2*, AJ, 123, 2754
- Walborn, N. R., Lennon, D. J., Haser, S. M., Kudritzki, R.-P., & Voels, S. A. 1995: *The physics of massive OB stars in different parent galaxies. 1: Ultraviolet and optical spectral morphology in the Magellanic Clouds*, pasp, 107, 104
- Walborn, N. R., Morrell, N. I., Howarth, I. D., Crowther, P. A., Lennon, D. J., Massey, P., & Arias, J. I. 2004: *A CNO Dichotomy among O2 Giant Spectra in the Magellanic Clouds*, ApJ, 608, 1028
- Walborn, N. R., Sota, A., Maíz Apellániz, J., Alfaro, E. J., Morrell, N. I., Barbá, R. H., Arias, J. I., & Gamen, R. C. 2010: *Early Results from the Galactic O-Star Spectroscopic Survey: C III Emission Lines in Of Spectra*, ApJ, 711, L143
- Yan, Y. & Seaton, M. J. 1987: *Atomic data for opacity calculations. IV. Photoionisation cross sections for C II*, Journal of Physics B Atomic Molecular Physics, 20, 6409
- Yoon, S.-C., Langer, N., & Norman, C. 2006: *Single star progenitors of long gamma-ray bursts. I. Model grids and redshift dependent GRB rate*, A&A, 460, 199
- Zahn, J.-P. 1992: *Circulation and turbulence in rotating stars*, A&A, 265, 115

Acknowledgements

Every time I thought about how to acknowledge the people who has helped me over the past years, it always came to my mind the same idea: since I have no music skills, this is going to be the closer I am going to get for being a rock star. It is going to be like writing a music album's acknowledgements that I always enjoy to read and try to decode all the hidden messages contained on them. Hence, likewise, some of them are going to be a bit cryptic but I hope the people at whom each message is aimed will understand it.

Many people have contributed over the last years to the success of this work. Even more helped me over my whole life to get to this point. There are many people to thank, more than I can name here, so I apologize beforehand if I forget to mention someone.

First, I am deeply grateful to my thesis supervisor Joachim Puls for his great support during my PhD. I like to thank him for both his guidance and his honesty. For his guidance because everything was always very well planned (always small but solid steps) and he never hesitated for offering his help whenever I needed it. These qualities are, alas, rarely found in most supervisors. I am also thankful for his honesty. I believe teaching/learning is best achieved through this quality. He never had any problem to either tell me whenever I was doing something really wrong or congratulate me whenever I was working properly and things were going well. And for me this is the most effective and best way to learn about anything. Finally, I am grateful for his (almost) endless patience over these four years, not only in topics related to science. Sometimes, it was difficult, at least for me, but I know, at the end, we got along fine and learned how to work together. I hope we still get in touch in one way or another in the future.

I gratefully acknowledge a grant from the German DFG, under grant 418 SPA 112/1/08 (agreement between the DFG and the Instituto de Astrofísica de Canarias), and from the LMU Graduate Center (Completion grant).

It has also been a privilege to meet and work with a number of excellent astronomers. Especially, I wish to express my gratitude and thanks to Francisco Najarro, Philip Massey and Ines Brott, without their contribution, the work achieved within this thesis would not have been possible. Thanks also to Artemio Herrero for invite me to spend some time at the IAC, where I had a fruitful experience and enjoy very helpful discussions; to Adalbert Pauldrach for providing me with the WM-basic atomic database; to Keith Butler for his helpful discussions on atomic physics; and to Jon Sundqvist for his help on many different topics. I also would like to express my gratitude to Miguel Urbaneja, Sergio Simón Díaz, Miriam García, Norberto Castro, Paul Crowther, Nolan Walborn and Hugues Sana.

I would like to thank my family now, therefore, I change the language from English to Spanish for that.

Primeramente me gustaría darles las gracias a mis padres, especialmente por su apoyo en las decisiones que he tomado y que me han llevado hasta aquí. Gracias por siempre preocuparse por mi

y por mirar por mi porvenir como dice mi madre. Tambien por acompañarme muchas noches desde la distancia. Aunque a veces no lo parezca porque soy un poco dejado para estas cosas, todas esas conversaciones por Skype a las tantas de la noche han hecho que no me sienta tan lejos de casa. Gracias madre y padre. También a mis hermanos, Manolo y Javi, sin su apoyo y ejemplo no hubiera sido la persona que soy ahora. Gracias al resto de mi familia y tambien al nuevo miembro, mi sobrino Nestor, al que tengo muchas ganas de conocer. Quería mandar también un recuerdo especial a mi abuela que falleció recientemente.

I switch back to English to thank all the wonderful people I met in Munich over these years. It is difficult to summarize my gratitude in a few words but I'll try my best.

Mayte and Sebas, I will always appreciate the way you welcomed me when I arrived in Munich. Mayte, thanks for always count me in for every trip, party, dinner, etc that you organized. We had great times in the Australian pub celebrating all Barcelona's victories, *vamos equipo!* Sebas what a delicious Paellas you cooked and what a funny *remontadas* we made over these years, especially, when Spain won the World Cup! Michi and Fede, when I met you guys, it felt like I knew you for a long time. And I like when these things happen. It was nice to have people around always eager to try different things, like watching the Star Wars' trilogies in a row. Where most people failed, you succeeded! Fede, I had a great time when you started working at the observatory. Michi, I had a lot fun making the GalileoMobile's documentary with you and Eva and I hope that we make the short film someday. Eva and Jose, my Munich's grandparents! I am kidding. Seriously, it was very nice to meet you guys. You are very special people, don't ever change! I wish you the best for your new adventure in Paris. Pati, together with Eva, you were my "mothers" in Munich. *Obrigadinho* for taking care of me even though I always foolishly chose to make the opposite of what you told me.

Rhea, seeing your smile when I arrived at the office every morning comforted me a lot during the past four years. I also finally forgive you for putting a snow ball down my t-shirt. All the best for you and Alfredo. Cornelius, I'll always remember you for the story behind "Salud y capullo". Wolfgang and Judith, it was also nice to share the office with you. Chucho, always a smile on his face. That's the first thing everyone notice when they meet him. Don't loose it! Thanks for giving me shelter when I had no place to go a couple of summers ago. Alex, I hope someday I'll be the proud owner of a pocket watch like yours. And also big thanks to everyone who has helped me from the USM.

I am deeply grateful to the original team members of GalileoMobile: Fede, Michi, Eva, Pati, Faabiooo deeel Sooordooo, Silvia, Pilar, Nuno, Chucho, María, Victor, and Phil. Thank you for letting me be part of this dream. And also a big northern thank you to the children and wonderful people we met in our journey.

Friday's night in Munich always meant volleyball+dinner. Andrea, Marcella, Mattia, Feli, Alessandro, Giorgio, Manolis, Rasmus, Stefania, Luis, Emmanuel, Pati, Nuno, Dado, Ilaria, Piero, Carlos, Silvia, Raúl, etc. Thanks guys!

I would also like to mention my friends from La Laguna: Ángel, Jorge, Elisa, Miguel, Sara, Rut and Marimar. If I am here right now is because of your help. And also to the rest of the people I met there. And María, you are cool too.

And thanks to: Yau, Carla and Ro; Tere for our endless nights talking over the internet about la Rusa, la bohemia, la escocesa, la italiana among other funny things; Jose Manuel, aka Nene, and all people from "Donde el rio hierve"; David and Elena; the ePOD people; Marc and Javi; Andy, Elaine, and Sigurd; Gemma for all the funny stories you told me; Nuria, Hector and Andreu; and all the people who has ever helped me and I forgot their names.

This is the end, my beautiful friends, the end. See you on the road!

Curriculum Vitae

Personal information

Name: Jorge Gustavo Rivero González

Date of birth: July 21, 1984

Place of birth: Las Palmas de Gran Canaria, Spain

Civil Status: Single

Nationality: Spanish

D.N.I.: 78517074L

Address: Scheinerstr. 1, Bogenhausen, 81679, Munich, Germany

Education

October 2002 - July 2008 Physics Degree - Specialty Astrophysics, Faculty of Physics -
Universidad de La Laguna, Spain

June 2010 Diploma in Physics Faculty of Physics - Ludwig-Maximilians-
Universität München. Thesis title: "Nitrogen line synthesis
in atmospheric models of hot massive stars Implementation
and first tests"

October 2008 - July 2012 PhD in Astrophysics, Faculty of Physics - Ludwig-
Maximilians-Universität München. Thesis title: "Nitrogen line
spectroscopy of O-stars"

Publications

Refereed

Rivero Gonzalez, J.G.; Puls, J.; Massey, P.; Najarro, F.

Nitrogen line spectroscopy of O-stars - III. The earliest O-stars

Accepted for publication in *Astronomy & Astrophysics*. Pre-print available at arXiv:1205.4444

Rivero Gonzalez, J.G.; Puls, J.; Najarro, F.; Brott I.

Nitrogen line spectroscopy of O-stars - II. Surface nitrogen abundances for O-stars in the Large Magellanic Cloud

Astronomy & Astrophysics, 2012, 537, A79

Rivero Gonzalez, J.G.; Puls, J.; Najarro, F.

Nitrogen line spectroscopy of O-stars - I. Nitrogen III emission line formation revisited

Astronomy & Astrophysics, 2011, 536, A58

Vazdekis, A.; Ricciardelli, E.; Cenarro, A.J.; **Rivero Gonzalez, J.G.;** Díaz, L.A.; Falcón-Barroso, J.

MIUSCAT: extended MILES spectral coverage. I. Stellar populations synthesis models

Accepted for publication in Monthly Notices of the Royal Astronomical Society. Pre-print available at arXiv:1205.5496

Herrero, A.; Garcia, M.; Puls, J.; Uytterhoeven, K.; Najarro, F.; Lennon, D.J.; **Rivero Gonzalez, J.G.**

A peculiar Of star in the Local Group galaxy IC 1613

Accepted for publication in Astronomy & Astrophysics. Pre-print available at arXiv:1206.1238

Not refereed

Puls, J.; Sundqvist, J.O.; **Rivero Gonzalez, J.G.**

OB-stars as extreme condition test beds

Published at the "Active OB stars: structure, evolution, mass loss and critical limits", eds. C. Neiner; G. Wade; G. Meynet & G. Peters, Proc. IAU Symp. No. 272

Conferences

International Year of Astronomy 2009 Closing Ceremony, Padua, Italy, 9-10 January 2010

Visits to scientific institutions

- Instituto de Astrofísica de Canarias (IAC), Spain, September-October 2011

Languages

- Spanish: Native
- English: Very Good
- German: Basics
- French: Basics